BRNO UNIVERSITY OF TECHNOLOGY

VYSOKÉ UČENÍ TECHNICKÉ V BRNĚ

FACULTY OF MECHANICAL ENGINEERING

FAKULTA STROJNÍHO INŽENÝRSTVÍ

ENERGY INSTITUTE

ENERGETICKÝ ÚSTAV

CAVITATION INDUCED BY ROTATION OF LIQUID

KAVITACE VYVOLANÁ ROTACÍ KAPALINY

DOCTORAL THESIS

DIZERTAČNÍ PRÁCE

AUTHOR — Ing. Jiří Kozák

AUTOR PRÁCE

SUPERVISOR — doc. Ing. Pavel Rudolf, Ph.D.

ŠKOLITEL

BRNO 2019

ABSTRAKT

Tato disertační práce se zabývá experimentálním a numerickým výzkumem kavitace vyvolané rotací. Pro potřeby tohoto výzkumu byla využita transparentní osově symetrická Venturiho dýza, díky čemuž bylo možné zkoumat dynamiku kavitujícího proudění pomocí analýzy vysokorychlostních nahrávek.

KLÍČOVÁ SLOVA

Kavitace, vířivé proudění, OpenFoam, Venturiho dýza, CFD, POD, CT

ABSTRACT

This doctoral thesis deals with experimental and numerical research of cavitation induced by rotation of liquid. The transparent axisymmetric Venturi tube was exploited for this purpose. Thus, it was possible to investigate dynamics of cavitating flow using the captured high-speed records.

KEYWORDS

Cavitation, swirling flow, OpenFoam, Venturi tube, CFD, POD, CT

KOZÁK, Jiří. *Kavitace vyvolaná rotací kapaliny*. Brno, 2020. Dostupné také z: https://www.vutbr.cz/studenti/zav-prace/detail/122496. Dizertační práce. Vysoké učení technické v Brně, Fakulta strojního inženýrství, Energetický ústav. Vedoucí práce Pavel Rudolf.

PROHLÁŠENÍ

Prohlašuji, že svou dizertační práci na téma „ Kavitace Vyvolaná Rotací Kapaliny “ jsem vypracoval samostatně pod vedením školitele dizertační práce a s použitím odborné literatury a dalších informačních zdrojů, které jsou všechny citovány v práci a uvedeny v seznamu literatury na konci práce.

Brno …… ……

podpis autora

PODĚKOVÁNÍ

Předně bych rád poděkoval svému vedoucímu dizertační práce Ing. Pavlu Rudolfovi, Ph.D. za odborné vedení, konzultace a skvělý lidský přístup v průběhu celého studia na Odboru fluidního inženýrství Viktora Kaplana. Dále bych chtěl poděkovat své přítelkyni Janě Dostálové, která musela v jistých chvílích prokázat nesmírnou míru trpělivosti a pochopení. V neposlední řadě chci poděkovat rodičům za podporu během studia. A nakonec si dovolím poděkovat celému osazenstvu OFIVK, nejen za podporu, ale zejména za skvělé chvíle strávené v laskavém kolektivu.

CONTENT

1. Introduction

Cavitation is a complex physical phenomenon with crucial impact on many technical applications. When local value of the static pressure drops below certain level (i.e. value of the saturated vapor pressure) in the liquid volume, liquid changes its state. From the physical point of view, this process is similar to the boiling of the water. The main difference is the fact that the water is exposed to the ambient temperature, compared to the water boiling when temperature must exceed certain level depending on the ambient pressure. The creation, presence and decay of the cavitation bubble, which is filled mainly by the evaporated water and dissolved gasses, is associated with many consequences.

The most important effects of cavitation are erosion of the exposed surfaces, pressure fluctuations, vibrations and acoustic emission. These features of cavitation are usually undesirable, on the other hand they can be utilized in many technical applications. The erosion of the surfaces as well as pressure fluctuations lead to the reduction of the lifespan of the hydraulic machines, restrictions of the machine's operation and under certain circumstances they can cause the hydraulic machine destruction. All of the above-mentioned facts resulted in the comprehensive investigation of this phenomena.

Since there are several mechanisms which can lead to the pressure drop in the liquid, several types of cavitation are distinguished. The most important type of cavitation, from the energy industry point of view is so-called hydrodynamic cavitation. Assuming that the pressure drop is sufficient, the cavitation can occur in the liquid volume. This is a case of cavitation in hydraulic machines such as pumps, turbines, valves etc. The other example of the hydrodynamic cavitation is so-called vortex cavitation which is caused by the pressure drop in the core of the vortex.

Typical examples of the latter type of cavitation are so-called cavitating vortex ropes, which can be found downstream the hydraulic turbines runners in case of non-optimal operating conditions. Another type of vortex cavitation is found in case of the blade motion in the liquid. Thanks to the pressure difference on the both sides of the profile, so-called tip vortex is formed at the end of the blade. This type of cavitation is typical problem of the ship propellers, Kaplan and propeller turbines. Spiral vortex filament rolls from the rotating blade tip.

Typical example of the cavitation caused by the rotation of the liquid is so-called vortex ring, which appears downstream of the axisymmetric nozzles. If sufficient circulation and consequently pressure drop is established, then the circular vortex is filled with vapor.

This thesis will be focused on investigation of the cavitation caused by the rotation of the liquid, where most of the effort will be concentrated on experimental and numerical research of the cavitating vortices behind the swirl generator, which are similar to vortex ropes in the nature. For the purpose, the Venturi tube will be exploited. The cavitation will be investigated using the various methods including analysis of high-speed video, records of different transducers and also numerically using the multiphase simulations carried out using the computational fluid dynamics (CFD) software. Whole investigation will be done using the test section consisting of Venturi tube with and without the upstream-mounted swirl generator. Thus, it will be possible to investigate and compare different cavitation regimes as well as the influence of the vortex introduced by the swirl generator.

The experimental and numerical methods as well as necessary theoretical background are described in the following chapters.

1.1. Cavitation

Cavitation is a process of liquid evaporation, which is similar to the boiling of liquid. The main difference between the cavitation and boiling of the liquid is the fact that the evaporation is not driven by the temperature of the liquid, but the pressure drop. This pressure drop in the flow can be caused by various reasons, including flow exposure to ultrasound. The most common type of cavitation in hydraulic engineering is caused by the hydrodynamic behavior of the liquid flow, where pressure drop is caused by local increase of the liquid velocity. Thus, this phenomenon is referred to as hydrodynamic cavitation.

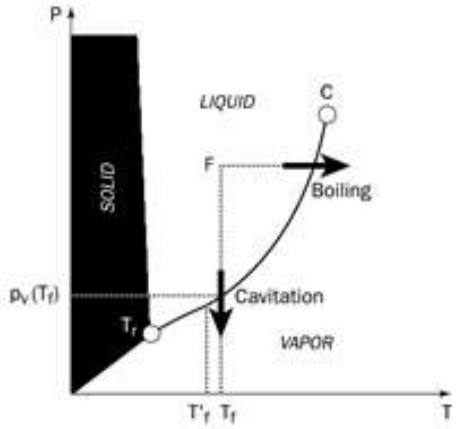

Figure 1 The comparison of boiling and cavitation of liquid in the phase diagram [1]

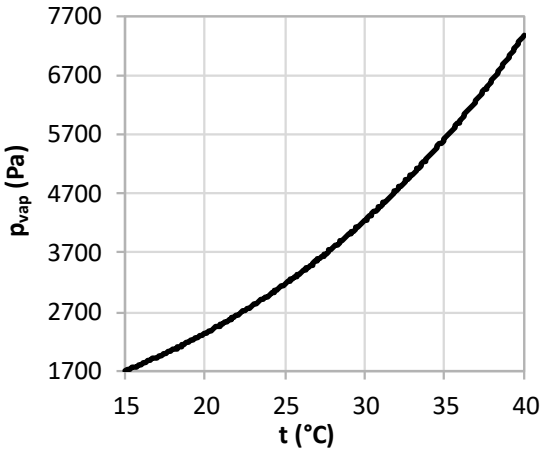

Figure 2 Saturated vapor pressure calculated according to equation (1)

On the other hand, even though cavitation is not driven by exceeding a certain temperature level, the pressure of the saturated vapor is highly affected by the temperature of the liquid, therefore the results of experimental measurement can be highly affected by the actual temperature of the liquid. Several equations expressing saturated vapor pressure p_{vap} as a function of temperature can be found in literature, for example modified Clausius-Clapeyron equation:

$$p_{vap} = 100 \cdot e^{53.6796 - \frac{6743.69}{T} - 4.8451 \cdot lnT} \tag{1}$$

where T is thermodynamic temperature. The values of the saturated vapor pressure obtained by this equation are depicted in the Figure 2.

Under certain conditions the cavitation bubble radius reaches critical value above which explosive growth of cavitation bubble is observed. This condition is described using the following equations. If the thermodynamics and diffusive effects are neglected, the static pressure within the spherical bubble p_B with radius r_B is expressed by equation

$$p_B = p_{sur} + \frac{2\sigma}{r_B} \tag{2}$$

Where p_{sur} is static pressure in liquid surrounding the cavitation bubble. Considering the cavitation bubble content composed of the undissolved gas and saturated vapor, the static pressure p_B can be expressed using the Dalton law:

$$p_B = p_{vap} + p_{gas} \tag{3}$$

Where p_{vap} is the saturated vapor pressure and p_{gas} is partial pressure of undissolved gas. Considering the equations (2) and (3), the condition of cavitation bubble stability is expressed by equation (4).

$$p_{vap} + p_{gas} = p_{sur} + \frac{2\sigma}{r_B} \tag{4}$$

In case that diffusive and thermodynamics effects are neglected as it was mentioned above, the static pressure of the liquid surrounding the cavitation bubble p_{sur} in case of cavitation bubble growth from initial radius of r_{B0} to final radius r_B can be calculated using the equation (5)

$$p_{sur} = p_{vap} + \left(p_{sur0} - p_{vap} + \frac{2\sigma}{r_B}\right)\left(\frac{r_{B0}}{r_B}\right)^3 - \frac{2\sigma}{r_B} \qquad (5)$$

Using the equation (5), the chart depicting reaction of spherical bubble of certain initial radius to change of ambient pressure can be constructed:

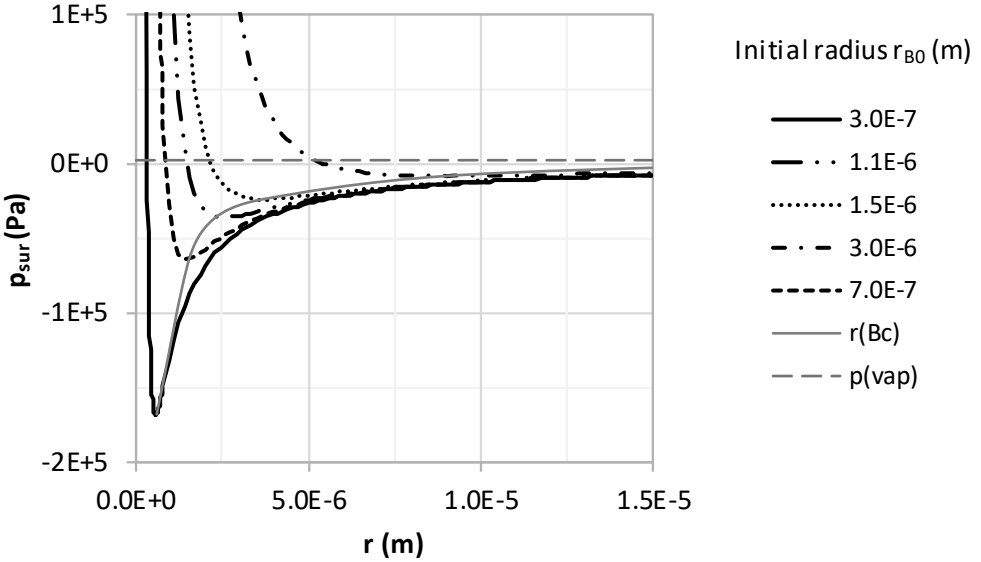

Figure 3 Behavior of spherical cavitation bubbles with different initial radius

Behavior of five spherical bubbles with different initial radius r_{B0} is depicted in the Figure 3, other parameters in equation (5) are constant. The minima of individual curves refer to the critical values of radius r_{Bc} and p_{surc}, where curve joining the critical points is dividing the diagram to the stable and unstable region.

Considering constant ambient pressure p_{sur}, response of the bubble to the sudden increase of its radius will be completely different in the region $r_B < r_{Bc}$ and $r_B > r_{Bc}$. In the first case, where the bubble radius is lower than critical, the ambient pressure in the liquid is higher, than the pressure within the enlarged bubble. Thus, the radius of the bubble will be reduced to the original value due to pressure equilibrium. In the second case, where bubble radius is larger than critical, the pressure within the enlarged bubble will be higher than ambient and the bubble will grow continuously.

Slight increase in radius of spherical bubble can be observed, when the bubble is exposed to decreasing ambient pressure until the critical ambient pressure p_{sur} is reached. The value of critical ambient pressure is the lower the lower is value of the initial bubble radius, which is clearly depicted in the Figure 3.

Dynamics of spherical cavitation bubble is described using Rayleigh-Plesset equation. This equation was derived by Rayleigh in 1917 [3] directly from Navier-Stokes equation and firstly applied to traveling cavitation bubbles by M.S. Plesset in 1949 [4], who also added the viscous term. The general form of R-P equation is usually written as:

$$\frac{p_B(t) - p_l(t)}{\rho_L} = r_B \frac{d^2 r_B}{dt^2} + \frac{3}{2}\left(\frac{dr_B}{dt}\right)^2 + \frac{4\nu_L}{r_B}\frac{dr_B}{dt} + \frac{2\sigma}{\rho_L r_B} \qquad (6)$$

Where:

$p_\infty(t)$ is the external pressure infinitely far from the bubble
ν_L, ρ_L are liquid the kinematic viscosity and density respectively
σ is the surface tension of the liquid

It is possible to calculate time-varying radius of the bubble $r_B(t)$ using this equation, if the $p_B(t)$ is known and $p_\infty(t)$ as well as initial bubble radius and velocity of its growth is given. It is possible to neglect the influence of surface tension and viscosity, assuming that in the equation (6), the influence of terms containing velocity and acceleration is dominant.[5] Then, so-called simplified Rayleigh-Plesset equation can be written down:

$$\frac{p_B(t) - p_l(t)}{\rho_L} = r_B \frac{d^2 r_B}{dt^2} + \frac{3}{2}\left(\frac{dr_B}{dt}\right)^2 \tag{7}$$

Further simplification, neglecting the non-linear term containing second derivative is commonly utilized, for the numerical models of cavitation in most of the CFD codes. The problem of numerical simulation of the cavitating flow is described separately in the chapter Cavitation modeling.

The presence of cavitation is connected with many side effects such as pressure fluctuations, noise emissions, vibrations and erosion of the materials subjected to the collapsing cavitation bubbles in the regions of higher pressure. All above mentioned effects are strongly linked to the cavitation type and its stage. Predispositions of the flow to the inception of cavitation within the flow can be described using dimensionless cavitation number σ. Value of cavitation number can be calculated using following equations:

$$\sigma_{vel} = \frac{p_{ref} - p_{vap}}{\frac{1}{2}\rho {v_{ref}}^2} \tag{8}$$

Where reference values of static pressure p_{ref} and velocity v_{ref}, should be representative for the investigated problem and type of cavitation (for example upstream pressure and velocity in the throat in case of nozzle).

Another definition of cavitation number is based on the pressure drop measured across the section affected by the cavitation:

$$\sigma_{pres} = \frac{p_{ref} - p_{vap}}{\Delta p} \tag{9}$$

1.1.1. Stages and types of hydrodynamic cavitation

The transition between cavitation-free flow and first occurrence of cavitation is usually called incipient cavitation. Detection of the first cavitation bubbles in flow can be quite challenging task, in case that the region of cavitation inception is not defined precisely (for example sharp edge of the nozzle throat) and investigation using high-speed photography is not possible. The inception of cavitation is not connected

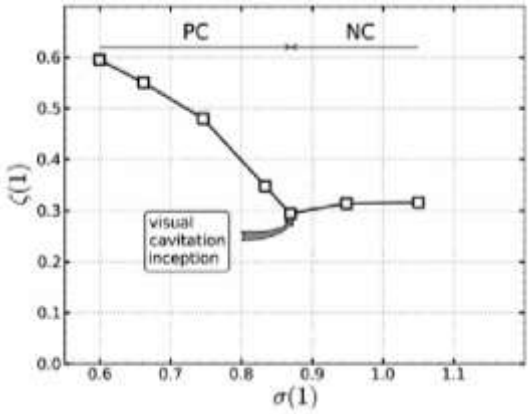

Figure 4 Q =5 l/s (NC – no cavitation, PC – partial cavitation) [8]

with loss of the efficiency, decrease of flow rate or with the significant erosion of the attached surfaces. On the other hand, as the amount and size of the cavitation bubbles increase, it is possible to observe slight decrease of hydraulic loss caused by decrease of friction between surfaces of the investigated

machine or device and surrounding flow. This decrease of the hydraulic loss was captured by Rudolf et al. during the experimental investigation of the cavitation in converging-diverging nozzle (Figure 4). [8]

With the further increase of the cavitation vapor amount within the flow, new regime called initial cavitation develops. Severe pressure pulsations accompanied by noise and massive erosion typically occur in this case. The cavitation void is usually highly unstable.

With further decrease of the cavitation number, it is possible to observe fully developed cavitation and then so-called supercavitation. The fully developed cavitation is accompanied by even more severe pressure pulsations and vibrations prior the transition to supercavitation as it will be described. The regime of supercavitation is characteristic by lower pressure pulsations compared to the partially or fully developed cavitation. According to other authors, it can be described as a flow regime where the downstream border of the stable, coherent cavitation zone is situated far beyond the investigated body. [1],[18] The comparison of the cavitation development stages in case of cavitation in Venturi tube and axial inflow is depicted in the following set of pictures.

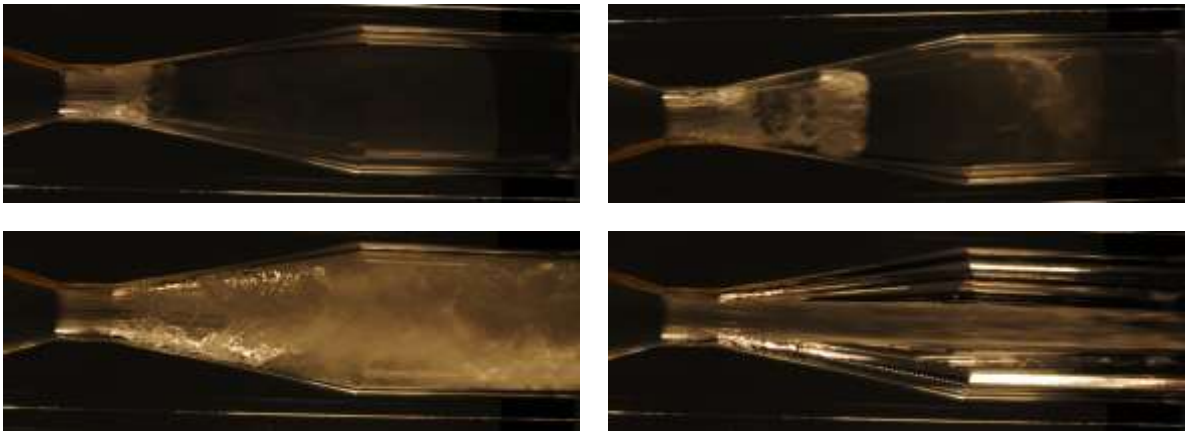

Figure 5 Stages of cavitation development in Venturi nozzle from initial phase of cavitation in upper left corner to supecavitation in bottom left corner

Several types of cavitation can be distinguished by the nature of cavitating structure. So-called attached or fixed cavitation is observed close to wetted surfaces. This type of cavitation is considered to be stable in quasi-steady sense. Further decrease of cavitation number makes this type of cavitation transient (or cycling). The cavity volume grows and then collapses. The maximum length of cavity depends on the system pressure.

In case of travelling cavitation, the cavitation bubbles or volume of the cavitation are drifted downstream by the main flow. Typical example of this type of cavitation is shedding of cavitation cloud over the hydrofoil. Re-entrant jet is created thanks to the presence of sufficiently thick attached layers of the cavitation. Cavitation sheet is separated by the re-entrant jet from the surface of hydrofoil and cavitation cloud is formed. Part of the cloud is dissociated and flows downstream to the region of higher static pressure, where it collapses.

The presence of swirl may result in creation of so-called vortex cavitation. This type of cavitation, its mechanisms and investigation of this phenomenon is the main aim of this thesis, so it will be described in detail in the following chapters. In general, vortex cavitation is caused by the pressure drop, which is observed in the vortex core. The following requirement has to be satisfied according to Noskievič [2]:

$$p_{vap} > p_{core} = p_{amb} - \frac{1}{2}\rho v_{core}^{\ 2} \tag{10}$$

Where p_{core} represents static pressure within the vortex core and v_{core} is computed using the following equation:

$$v_{core} = \frac{rv}{r_{core}} \tag{11}$$

where *r* represents the radius of vortex and *v* is the velocity related radius *r*.

Typical examples of this type of cavitation in technical praxis are vortex ropes, which may occur downstream the runner of hydraulic turbine for certain operation conditions or tip vortex cavitation in the spiral vortex filament created by the rotating propellers.

1.2. Mathematical models of vortex

Several mathematical types of vortex were proposed in order to describe the pressure and velocity profiles within the vortex. Alekseenko [10] put forward the pressure equation for swirling flow, where pressure is function of radial coordinate and tangential component of the velocity. The pressure equation is valid assuming several simplifications, namely steady and isotermic flow of the ideal liquid. The pressure equation is derived from the Euler equation and equation of continuity.

$$p = \rho \int \frac{{v_{tan}}^2}{r} dr + const \tag{12}$$

It is obvious, that the only unknown variable in the integral is the value of the tangential velocity, which can be estimated using a model of the vortex. It should be mentioned that more detailed description of the models can be found in literature, for example in the contribution written by Štigler [11] or in master thesis of Švaňhal [12].

1.2.1. Basic vorticity theorems

The vorticity of the fluid is defined by formula:

$$\boldsymbol{\Omega} = rot\, \boldsymbol{v} \tag{13}$$

Where nonzero value of the vorticity characterizes the rotational flow. It is possible to define the vortex or vorticity line, which is everywhere tangential to the local vorticity vector:

$$\frac{dx}{\Omega_x} = \frac{dy}{\Omega_y} = \frac{dz}{\Omega_z} \tag{14}$$

Vortex lines passing through given closed curve in the continuum form so-called vortex tube. If the definition of the vortex tube is considered, it is obvious that the flux of the vorticity through the wall of the tube is equal to zero. The flux of the vorticity through the cross section of the tube is equal to so-called vortex flux defined by the integral:

$$\mu = \int_A \Omega_n dA \tag{15}$$

Where Ω_n is component of the vorticity vector perpendicular to the cross-section *A*. The value of the vortex flux is constant within the whole vortex tube according to the second Helmholtz theorem. It is impossible to experimentally measure value of vorticity, on the other hand it is possible to compute circulation of the velocity Γ using the detected velocity field and then compute the vorticity indirectly using the Stokes theorem.

$$\Gamma = \oint_C \boldsymbol{v}\, d\boldsymbol{s} = \int_A rot\, \boldsymbol{v} \cdot \boldsymbol{n}\, dA = \int_A \boldsymbol{\Omega} \cdot \boldsymbol{n} dA = \int_A \Omega_n dA \tag{16}$$

1.2.2. Rigid body model of the vortex

The simplest model of the swirl motion assumes that the swirling flow can be described as a rotating rigid body. Thus, the tangential velocity is directly proportional to the distance to the axis of rotation and angular velocity.

$$v_{tan}(r) = \boldsymbol{\omega} \cdot r \tag{17}$$

It is possible to express pressure profile using the boundary condition (18) and substituting the tangential velocity in equation (12).

$$p = \rho \int \omega^2 \cdot r dr + const = \frac{\rho \omega^2 r^2}{2} + const \tag{18}$$

$$r = R \rightarrow p = p_r \tag{19}$$

The final expression for the rigid body profile of the pressure is defined by formula (5)

$$p = p_R - \frac{\rho \omega^2}{2}(R^2 - r^2) \tag{20}$$

1.2.3. Potential vortex

In case of the potential flow the motion of the particles must be irrotational. Thus, the particles do not rotate around their axis but move on the circular trajectory in case of potential vortex. The whole vorticity of the potential vortex is concentrated to the so-called vortex filament in the centre of the potential vortex. Rotation of this filament is the cause of the circular motion of the particles.

Velocity of the particle in a sufficient distance from the filament would be in good agreement with reality. On the other hand, the velocity magnitude rapidly increases with decreasing distance between the particle and filament. This rapid increase of the velocity magnitude does not correspond to the reality, where the tangential velocity drops to the zero due to the influence of viscosity near to the vortex core. [11] Profile of the tangential velocity can be described using following formula:

$$v_{tan}(r) = \frac{C}{r} \tag{21}$$

Where C is a constant. Substituting this expression to the formula (11), the pressure integral can be expressed.

$$p = \rho \int \frac{C^2}{r^3} dr + const = -\frac{\rho C^2}{2r^2} + const \tag{22}$$

The final equation of the static pressure can be obtained using the same boundary conditions as in case of rigid body model of the vortex.

$$p = p_R + \frac{\rho C^2}{2}\left(\frac{1}{R^2} - \frac{1}{r^2}\right) \tag{23}$$

1.2.4. Rankine vortex

The problem of increasing velocity in the vicinity of axis of potential vortex is partially solved by the Rankine model by introduction of vortex core.

The liquid continuum is divided by the vortex core. Within the vortex core, the liquid motion is described using the rigid model of vortex. On the other hand, the potential model of vortex is utilized outside this border. Therefore, the maximum magnitude of the tangential velocity is found at the vortex core radius. The most important con of this model is sharp change of the velocity profile derivation at the vortex core radius.

For $r < r_c$:

$$v_{tan}(r) = v_c \frac{r}{r_c} \tag{24}$$

And for $r \geq r_c$:

$$v_\varphi(r) = v_c \frac{r_c}{r} \tag{25}$$

It is possible to express pressure profile of Rankine vortex substituting these expressions to the pressure integral and using the boundary condition.

For $r \geq r_c$:

$$p = p_R + \rho \frac{{v_c}^2 {r_c}^2}{2}\left(\frac{1}{R^2} - \frac{1}{r^2}\right) \tag{26}$$

And for $r < r_c$:

$$r = r_c \rightarrow p(r_c) = p_c = p_R + \rho \frac{{v_c}^2 {r_c}^2}{2}\left(\frac{1}{R^2} - \frac{1}{{r_c}^2}\right) \tag{27}$$

$$p = p_R - \frac{\rho {v_c}^2}{2}\left(2 - \frac{{r_c}^2}{R^2}\right) + \frac{\rho {v_c}^2}{2}\frac{r^2}{{r_c}^2} \tag{28}$$

1.2.5. Lamb vortex

This model of the vortex is derived directly from the Navier-Stokes equation in case of planar motion considering the infinite space and incompressible liquid. Thus, the most significant restriction of this model is impossibility of the superposition principle utilization due to the non-linear terms of N-S equation.

Compared to the Rankine vortex, the velocity profile of the Lamb vortex is smooth along the vortex radius. Tangential velocity of the Lamb vortex is defined using the following expression. [10]

$$v_\varphi(r) = \frac{1{,}39 v_c r_c}{r}\left(1 - e^{\left(-1{,}26\frac{r^2}{{r_c}^2}\right)}\right) \tag{29}$$

Substituting this expression to the integral (12) the pressure integral of the Lamb vortex is obtained.

$$p = \rho \int \frac{1{,}39 v_c r_c}{r^2}\left(1 - e^{\left(-1{,}26\frac{r^2}{{r_c}^2}\right)}\right) dr + const \tag{30}$$

The pressure integral of the Lamb vortex is exponential, therefore the numerical integration had to be carried out to obtain the pressure equation. The final pressure function for the vortex with the radius discretely divided into n points is as follows:

$$p = p_r - \rho \sum_{i=1}^{n-1}\left(\frac{v_{tan}(r_{n-i+1})^2}{r_{n-i+1}} + \frac{v_{tan}(r_{n-i})^2}{r_{n-i}}\right)\frac{r_{n-i+1} - r_{n-i}}{2} \tag{31}$$

1.3. Computational Fluid Dynamics – theoretical background

The computational fluid dynamics has become one of the essential methods of the fluid flow investigation. Increase of the computational performance accompanied by the decrease of the computational resources cost lead to the utilization of the CFD methods not only in the academic sphere but also in the industry. CFD can be considered as important method of the hydraulic research from the theoretical investigation of the broad range of phenomena to the design and optimization of the hydraulic machines or whole hydraulic systems. The turbulent incompressible flow is described by Navier-Stokes equation and the continuity equation.

$$\frac{\partial v_i}{\partial t} + \frac{\partial v_i}{\partial_{x_j}} v_j = -\frac{1}{\rho}\frac{\partial p}{\partial x_i} + \nu \frac{\partial^2 v_i}{\partial x_j \partial x_j} + a_i \tag{32}$$

$$\frac{\partial v_i}{\partial x_i} = 0 \tag{33}$$

Unfortunately, the analytical solution of N-S equation can be obtained only for certain simple laminar flow problems. [1] The numerical solution is possible for the full spectrum of the complex hydraulic problems, if Reynolds Averaged Navier-Stokes (RANS) equation is employed. RANS equation is derived from N-S equation considering so-called Reynolds decomposition and Reynolds averaging rules, where instantaneous velocity and pressure are divided to the static and fluctuation components. The final form of RANS equation for incompressible liquid is given in following formula.

$$\frac{\overline{\partial v_i}}{\partial t} + \frac{\partial \overline{v_i}}{\partial x_j}\overline{v_j} = -\frac{1}{\rho}\frac{\partial \overline{p}_i}{\partial x_i} + \nu\frac{\partial^2 \overline{v_i}}{\partial x_j \partial x_j} - \frac{\partial}{\partial x_j}\left(\overline{v_i{}' v_j{}'}\right) \tag{34}$$

The averaged form of the continuity equation is as follows:

$$\frac{\partial \overline{v_i}}{\partial x_i} = 0 \tag{35}$$

So-called closure problem must be solved due to the fact, that there are four equations describing the problem and ten unknown parameters of the flow. This problem can be solved in two ways. The number of unknowns can be reduced or further equations describing the physical properties of the flow can be introduced to the system. Usually the combination of both approaches is exploited to close the system of equations. Thus, the proper choice of the turbulence model and appropriate near wall treatment is the crucial part of the numerical simulation.

The most appropriate numerical method for solution of partial differential equations of the fluid flow is Finite Volume Method. This method is utilized by most of the modern CFD codes.

1.3.1. Turbulence modelling

The averaged product of fluctuation velocity components in equation (36) multiplied by the density of the fluid is so-called Reynolds stress tensor:

$$\tau_{ij} = \rho\left(\overline{v_i{}' v_j{}'}\right) \tag{36}$$

The aim of the turbulence modelling is to compute or model Reynolds stress tensor. Two-equation models constitute one of the most commonly utilized groups of the turbulence models in engineering practice. These models usually provide reasonable compromise between computational cost and accuracy of the results. On the other hand, these models are based on so-called Boussinesque hypothesis, which introduces concept of eddy viscosity v_t:

$$2\nu_t S_{ij} - \frac{2}{3}k\delta_{ij} = -\overline{v_i{}' v_j{}'} \tag{37}$$

Where Sij is the mean rate of strain tensor (37), k is turbulence kinetic energy (38) and δ_{ij} is Kronecker delta.

$$S_{ij} = \frac{1}{2}\left(\frac{\partial \bar{v}_i}{\partial x_j} + \frac{\partial \bar{v}_j}{\partial x_i}\right) \tag{38}$$

$$k = \frac{1}{2}\left(\overline{v_i{}' v_i{}'}\right) \tag{39}$$

It is obvious that the Reynolds stress tensor including six unknown parameters is reduced to the scalar eddy viscosity. Thus, the isotropic turbulence is considered in case of the turbulence models based on Boussinesque hypothesis. This fact is the most important restriction of two-equation turbulence models, especially in case of highly swirling flows. Nevertheless, reasonable computational cost and numerical robustness compensate this restriction.

Two groups of two-equation models are the most common: k-ε and k-ω. These models are closing the system of equations by adding the transport equations for kinetic turbulent energy k and dissipation rate ε in case of k-ε model, or transport equation of k and specific rate of dissipation ω in case of k-ω model. Mathematical description of these models can be found in [7] or [19] for example. It should be

mentioned that the quality of the turbulence model implementation in CFD code considerably affects the obtained results.

The proper choice of the model of turbulence is crucial part of the numerical investigation of hydrodynamic problems. It was reported that in case of standard k-ε turbulence model, the numerical dampening was too large for creation of the helical vortex, while in case of realizable k-ε turbulence model the precessing helical vortex was created, but it was still too damped compared to the experimental data. On the other hand, Štefan et al. in [45] carried out single phase simulations of the vortex rope using OpenFoam employing realizable k-ε model of turbulence with good results compared to the experimental data.

Except the turbulence models based on the Boussinesque hypothesis considering isotropic turbulence, there are more complex approaches. Whole Reynolds stress tensor is computed in Reynolds Stress Model. The RSM demands considerably higher amount of computational resources and above that it is less robust compared to the two-equation models. The most important advantage of the RSM is resolution of turbulence anisotropy. Compared to the two-equation models, the results of the RSM are less damped as is shown in contribution of Rudolf et. al. [20], where results of cavitating vortex rope simulations were compared. In case of realizable k- ε turbulence model the cavitating vortex was not formed, whereas in case of RSM simulation the cavitating vortex rope occurred downstream the swirl generator.

1.3.2. Advanced methods of the CFD

The main disadvantage of the RANS equation, which is basis of the previous numerical models, is time averaging which suppresses some unsteady phenomena observable during the experimental research. Thus, the direct simulation of the N-S (DNS) equation can be favorable in some cases. Unfortunately, the required computational resources are still unacceptable in the field of the applied research and industry.

Turbulent flow is characterized by eddies with wide range of length and time scales. While size of the largest eddies is comparable with characteristic length of the mean flow and their interaction is nearly non-dissipative, the smallest eddies are responsible for the dissipation of the turbulent kinetic energy.

Another important difference between largest and smallest eddies is their versatility. Large eddies, which are responsible for the transport of the mass, energy and momentum transport (as well as other passive scalars), are highly influenced by the geometry of the domain and boundary conditions. Therefore, we can say that large eddies are problem-dependent, while small eddies are more isotropic and less influenced by the certain conditions of the investigated problem.

The above-mentioned fact leads to the crucial conclusion that it is easier to find universal model of turbulence applicable for the small eddies, than to find some universal model of large eddies. Thus, the spectrum of eddies can be divided into the two above mentioned groups to decrease the computational demands of the simulation. Compared to the DNS where no turbulence modeling is utilized, the small eddies are modeled by various turbulence models (so-called subgrid-scale models) in case of LES. This crucial difference offers many advantages.

While in case of DNS, where computational requirements of the simulation are proportional to Re_t^3, LES allows to use coarser mesh and timestep size. On the other hand, LES requires long computational time to obtain stable statistics of simulation. The much finer mesh compared to the RANS calculations is still required. This requirement is most significant in the region of the boundary layer where the scale of large eddies becomes small. These requirements lead to the higher computational requirements of the LES compared to the RANS simulations.

The governing equations of the LES are obtained by spatial filtering of the unsteady form of Navier-Stokes equations using filter width corresponding to size of the grid. The filtered variable is computed as follows. [6]

$$\bar{\phi} = \frac{1}{V}\int_V \phi(x)\, dx \tag{40}$$

Scales smaller than filter width are classified as so-called sub-grid scales (SGS). This part of flow is computed using the subgrid models of turbulence based on RANS equation (34) and averaged equation of continuity (35).

Using the Boussinesq hypothesis the subgrid-scale stresses can be written as follows:

$$\tau_{ij} - \frac{1}{3}\tau_{kk}\delta_{ij} = -2\mu_t \delta_{ij} \bar{S}_{ij} \tag{41}$$

Where τ_{kk} is not modeled but added to the filtered static pressure term. It is possible to split subgrid stress tensor τ_{ij} to its isotropic and deviatoric part:

$$\tau_{ij} = \underbrace{\tau_{ij} - \frac{1}{3}\tau_{kk}\delta_{ij}}_{\text{deviatoric}} + \underbrace{\frac{1}{3}\tau_{kk}\delta_{ij}}_{\text{isotropic}} \tag{42}$$

Deviatoric part of the subgrid stress tensor τ_{ij} is modeled using the Smagorinsky model:

$$\tau_{ij} - \frac{1}{3}\tau_{kk}\delta_{ij} = -2\mu_t \left(S_{ij} - \frac{1}{3} S_{kk}\delta_{ij} \right) \tag{43}$$

For example ANSYS Fluent 16 provides four different models of subgrid turbulent viscosity μ_t: Smagorinsky-Lilly [22], dynamic Smagorinsky-Lilly [23], WALE [24] and the kinetic energy subgrid-scale model [25].

1.3.3. Cavitation modeling

This chapter will be focused mainly on the theory of the numerical modelling of cavitation. Compared to the single-phase simulations, the simulations considering cavitation (e.g. multiphase simulations considering mass transfer between liquid and vapor phase in both directions) are more difficult due to their higher computational demands. Comprehensive summary of the mathematical methods of the cavitation simulation and their developments during last decades can be found in the work of Koop [26].

Cavitating flow can be simulated using the single-phase approach, where the border between liquid water and vapor is considered as a pressure isosurface referring to the value of saturated vapor pressure. This approach has its obvious advantages. Single-phase simulation of the turbulent flow demands lower computational effort and it is usually more stable. Therefore, the single-phase simulation of the cavitating flow is often utilized for the investigation of phenomena, which are not directly connected with presence of the second phase. The typical example can be investigation of the helical vortex rope downstream the turbine as it has been mentioned. The presence of the vortex is not conditional on presence of cavitation. Thus, it is possible to simplify problem to the single-phase simulation (for example Štefan et al. [45]).

On the other hand, this simplification is not applicable to the investigations of the problems or phenomena which are strongly connected to the presence of the second phase. Moreover, the presence of the vapor void within the liquid (e.g. density stratification) is the reason of so-called baroclinic vorticity production (equation (44)), which acts as an additional production term in vorticity transport equation.[8]

$$\frac{1}{\rho^2} grad(\rho) \times grad(p) \tag{44}$$

Mass transfer between phases can be modelled by various models of cavitation based on Raylegh-Plesset equation (6) , which is usually simplified for the purpose of the numerical modelling (equation (45)).

$$\frac{dr_B}{dt} = \sqrt{\frac{2}{3}\frac{p_B(t) - p_l(t)}{\rho_l}} \tag{45}$$

Several different approaches of the multi-phase flow modeling exist. Lagrange-Euler approach combines Eulerian approach of the main flow computation and Lagrangian approach for the computation of relatively small amount of the particles (bubbles) which are spread in the flow. The Eulerian multiphase model considers flow as an undisturbed continuum consisting of two or more phases. Each additional phase increases computational demands and decreases numerical stability of the simulation, because additional momentum transport equation is calculated for each of the phases.

The most proper approach, so-called full Eulerian model, computes whole system of equations for each phase. Unfortunately, this is usually too expensive from the computational point of view, regardless the increase of the computational performance of the computers during last decades.

The computational demands can be decreased when one set of equations describes the whole flow. In this case volume fraction α is introduced. Volume fraction of the phase describes how much of the computational cell is occupied by the phase. Sum of the volume fractions of all phases within the computational cell is equal to one and the total volume of the phase in the computational domain can be evaluated using the equation (46)

$$V_q = \int_V \alpha_q \, dV \tag{46}$$

$$\sum_{q=1}^{n} \alpha_q = 1 \tag{47}$$

The mass transfer between phases during the process of cavitation is governed by the vapor transport equation:

$$\frac{\partial}{\partial t}\left(\alpha_{vap}\rho_{vap}\right) + \frac{\partial}{\partial_{x_j}}\left(\alpha_{vap}\rho_{vap}\bar{v}_{vap\_j}\right) = R_e - R_c \tag{48}$$

Where terms R_e and R_c are the source terms connected to the growth (evaporation of the liquid) and collapse (condensation of the vapor) of the cavitation bubbles.

Modelling of the mass transfer between the phases is the main purpose of the cavitation models. Many of the cavitation models were developed during the time, but it is always necessary to consider restrictions of the chosen model and its suitability for the investigated problem. Brief overview of the chosen cavitation models will be given in the following text. Full derivation of the models can be found in the cited sources, or in documentation of the CFD software.

Singhal et al. proposed so-called full cavitation model. [9] This model accounts for all of the first-order effects in R-P equation including influence of noncondensable gases. The liquid-vapor mixture is assumed to be compressible. Singhal et. al proposed model where the vapor mass fraction f_{vap} is the dependent variable in the transport equation:

$$\frac{\partial}{\partial t}\left(f_{vap}\rho\right) + \frac{\partial}{\partial_{x_j}}\left(f_{vap}\rho\bar{v}_{vapj}\right) = \frac{\partial}{\partial_{x_j}}\left(\Gamma\frac{\partial f_{vap}}{\partial_{x_j}}\right) + R_e - R_c \tag{49}$$

Where Γ is diffusion coefficient. The source terms of evaporation and condensation are given by the following equations:

For $p \leq p_{vap}$

$$R_c = F_{vap}\frac{max\left(1.0,\sqrt{k}\right)\left(1 - f_{vap} - f_g\right)}{\sigma}\rho_l\rho_{vap}\sqrt{\frac{2}{3}\frac{\left(p^*_{vap} - p\right)}{\rho_l}} \tag{50}$$

For $p > p_{vap}$

$$R_c = F_{cond}\frac{max(1.0,\sqrt{k})f_{vap}}{\sigma}\rho_l\rho_l\sqrt{\frac{2}{3}\frac{(p^*_{vap}-p)}{\rho_l}} \quad (51)$$

Where F_{vap} and F_{cond} are empirical constant and p^*_{vap} is corrected using the following equation by an estimation of the local values of the turbulent pressure fluctuations:

$$p^*_{vap} = p_{vap} + \frac{1}{2}(0.39k) \quad (52)$$

The main disadvantage of this model is its lower numerical robustness, on the other hand the model was utilized in many successful simulations. For example, study of the cavitation behavior of a centrifugal storage pump utilizing this model of cavitation has been done by Stuparu et al.[13]

Zwart-Gerber-Belamri model of cavitation is based on assumption that the size of the bubbles is constant in the whole system. [14] The final form of this model as follows:
For $p \leq p_{vap}$

$$R_e = F_{vap}\frac{3\alpha_{nuc}(1-\alpha_{vap})\rho_{vap}}{r_B}\sqrt{\frac{2}{3}\frac{(p_{vap}-p)}{\rho_l}} \quad (53)$$

For $p > p_{vap}$

$$R_c = F_{cond}\frac{3\alpha_{vap}\rho_{vap}}{r_B}\sqrt{\frac{2}{3}\frac{(p-p_{vap})}{\rho_l}} \quad (54)$$

Where F_{vap} and F_{con} are empirical coefficients and nucleation site volume fraction α_{nuc} is introduced to the model due to the limitation of the assumption that the cavitation bubbles do not interact with each other (which is physically correct only during the initial phase of cavitation).
Schnerr and Sauer proposed model of cavitation where, similar to the Singhal model of cavitation, the exact expression of the net mass transfer from liquid to vapor is derived. [15] The general form of volume fraction transport equation is as follows:

$$\frac{\partial}{\partial t}(\alpha_{vap}\rho_{vap}) + \frac{\partial}{\partial_{x_j}}(\alpha_{vap}\rho_{vap}\bar{v}_{vap\_j}) = \frac{\rho_{vap}\rho_l}{\rho}\frac{D\alpha_{vap}}{Dt} \quad (55)$$

It should be noted that the right side of the equation (54) represents the net mass source R. The vapor volume fraction is connected to the number of bubbles per volume of liquid:

$$\alpha_{vap} = \frac{n_B\frac{4}{3}\pi r_B{}^3}{1+n_B\frac{4}{3}\pi r_B{}^3} \quad (56)$$

Mass transfer rate is defined by following equation:

$$R = \frac{\rho_{vap}\rho_l}{\rho}\alpha_{vap}(1-\alpha_{vap})\frac{3}{r_B}\sqrt{\frac{2}{3}\frac{(p_{vap}-p)}{\rho_l}} \quad (57)$$

Where bubble radius:

$$r_B = \sqrt[3]{\frac{\alpha_{vap}}{1-\alpha_{vap}}\frac{3}{4\pi}\frac{1}{n}} \quad (58)$$

It is evident, that the only parameter, which must be determined is number of spherical bubbles per unit volume of liquid. The final form of the model is as follows:

For $p \leq p_{vap}$

$$R_e = \frac{\rho_{vap}\rho_l}{\rho}\alpha_{vap}(1-\alpha_{vap})\frac{3}{r_B}\sqrt{\frac{2}{3}\frac{(p_{vap}-p)}{\rho_l}} \tag{59}$$

For $p > p_{vap}$

$$R_c = \frac{\rho_{vap}\rho_l}{\rho}\alpha_{vap}(1-\alpha_{vap})\frac{3}{r_B}\sqrt{\frac{2}{3}\frac{(p-p_{vap})}{\rho_l}} \tag{60}$$

The cavitation model proposed by the Kunz et al [16] is utilized for the numerical investigation which will be presented in this thesis. The choice was based on the reasonably accurate results of the previous numerical investigation considering axial inflow into the Venturi tube [51]. In case of Kunz cavitation model, the source terms R_e and R_c are computed using the formulas (61) and (62). Where R_e and R_c represent the source terms of evaporation and condensation respectively.

$$R_e = C_v\frac{\rho_v\alpha}{t_\infty(0.5\rho_l U_\infty{}^2)}min[0, p-p_v] \tag{61}$$

$$R_c = C_c\frac{\rho_v\alpha^2(1-\alpha)}{t_\infty} \tag{62}$$

Where t_∞ is mean flow time scale and U_∞ represents mean stream velocity [16]. Values of the empirical constants C_v (900) and C_c (12000) were set-up based on [51].

Four different cavitation models were mentioned and briefly described in the chapter. It should be noted, that there are many others, which can be found in literature. For example, model proposed by Merkle [17]. It is always necessary to consider not only the suitability of the cavitation model, but also its implementation in the chosen CFD solver.

1.3.4. High-speed video processing

Cavitation is phenomenon with short time scale. Thus, the frame rate has to be sufficient in order to capture its dynamics. This fact leads to the utilization of high-speed camcorders in this field of cavitation research.

Cavitation can be observed and captured due to the fact, that the light is reflected by the interface between phases. Nevertheless, the experimental research has to be adapted for the purpose of the video capturing. Thus, the part of the hydraulic circuits must be transparent, and the captured scene has to be lighted properly.

Output of the digital high-speed cameras is usually captured in grayscale. The picture is represented by the matrix of pixels. In case of grayscale each pixel of the image is described by its position and intensity, where 0 refers to black and maximum value of the chosen depth refers to white (255 in case of 8-bit image depth).

Record of the pixel or group of the pixels intensities, which is affected by the cavitation process can be successfully correlated with dynamics of the phenomenon as it will be shown. Thus, good agreement between dominant frequencies of the cavitation identified using the pressure transducers and high-speed video can be found in literature. For this purpose, the spectral analysis using Fourier Transformation is usually utilized. This method will be described in the following chapter.

Sedlář et. al. [27] investigated dynamics of the cavitation cloud shedding in case of NACA 2412 hydrofoil. The results of numerical and experimental investigation were compared in broad range of operation points, while the dominant frequencies obtained by high-speed video analysis were in good agreement with the results of the pressure records analysis. Beside this type of the analysis also the results obtained by the Proper orthogonal decomposition (POD) will be analyzed and discussed in the chapter 3.2.

The most crucial disadvantage of the pixel intensity spectral analysis is the fact that it is not possible to obtain amplitude of the pressure pulsations. Even the comparison of the intensity amplitude between various operating points may be quite misleading, thanks to the fact that values of the pixel intensity are highly affected by the local interfacial boundary instabilities.

1.3.5. Fast Fourier Transform

Fourier transform (FT, also called frequency domain representation of the original signal) is a mathematical method based on assumption, that it is possible to decompose any given continuous function *f* into the series of sinusoidal functions. Fourier transform of function of time is a complex valued function of frequency. The absolute value of this function provides the frequency spectrum of analyzed signal (original function), while the complex argument holds information about phase offset. Majority of analyzed outputs in technical applications do not consist of continuous signals but discrete values of measured quantity, therefore Discrete Fourier Transform was developed. The sampling frequency f_{samp} of the discrete function should meet so-called Nyquist theorem (63), otherwise the results of DFT are distorted by aliasing. [52]

$$f_{samp} \geq 2f_{max} \tag{63}$$

Fast Fourier Transform (FFT) is numerical method based on DFT. In case of FFT algorithms decreasing computational demands of the signal processing are introduced. Thus the computational demands are decreased from $O(N^2)$ arithmetic operations in case of DFT to O(N log(N)) operations of FFT. Fourier transform is implemented in many software (for example Matlab, Excel, ANSYS Fluent) and in mathematical libraries of programming languages (Python). Thus, it should be emphasized, that complex description of the Fourier transforms and utilized algorithms theory is beyond the scope of this text, but it can be found in literature. This method will be utilized for the analysis of the static pressure records as well as for the analysis of the high-speed videos. The example of spectral analysis of synthetic signal $p = 310 \cdot \sin(2 \cdot \pi \cdot 20 \cdot t) + 215 \cdot \cos(2 \cdot \pi \cdot 50 \cdot t)$ is depicted in following picture:

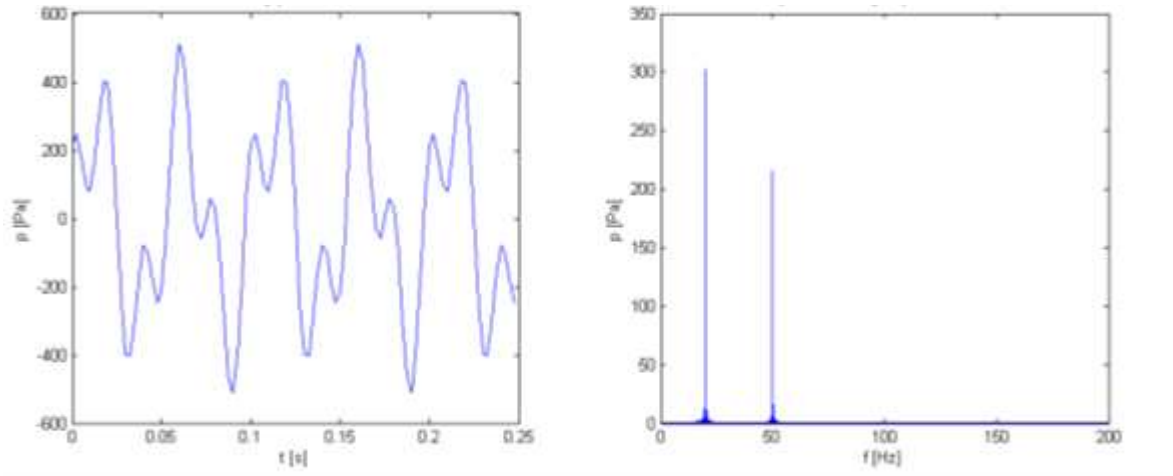

Figure 6 Spectral analysis of the synthetic signal

1.3.6. Computed tomography in cavitation field of study

Above mentioned analysis of the high-speed video can provide wealth of information about dynamics of cavitation, its inception and lot of other attributes related to the cavitation presence. Unfortunately, the light is scattered on the water-vapor interface, thus it is not possible to investigate distribution of cavitation behind its outer border (e.g. cross-sectional distribution of cavitation). It is possible to utilize so-called tomographic imaging for this purpose. The exhaustive description can be found in medicine literature (for example [31]). Bauer in his paper Measurements of void fraction distribution in cavitating

pipe flow using x-ray CT summed up the basics of tomography sufficiently for the technical purposes. [30]

Tomography has been originally developed for medical purposes. The mathematical background of this method has been derived by Johann Radon at the beginning of 20th century. [28] Radon concluded that it is possible to exactly describe property of 2D object, if an infinite number of line integrals about the property are defined in various directions. These line integrals can be directly measured if some kind of radiation absorbed by matter is captured by detector behind the irradiated object. In this case the captured value (e.g. amount of radiation) corresponds to the line integral of the attenuation coefficient along trajectory of the beam inside the object. It should be mentioned that the different kinds of radiation (light, radio waves, microwaves, etc.) can be utilized for this purpose.

The most common type of radiation used in computed tomography are X-rays thanks to their hardness (e.g. capability to penetrate objects without significant scattering). On the other hand, x-ray beam is weakened by the matter inside the irradiated object, whereas the attenuation coefficient along the trajectory of the beam depends on density of material.

It should be mentioned that the final picture of the slice is not 2D, but thanks to the certain depth in the 3rd direction it consists of so-called voxels (e.g. 3D pixels). The final image of the slice in grayscale corresponds to the attenuation coefficient μ distribution using so-called Hounsfield number (HU, in some literature also called as CT_{number}):

$$HU = 1000 \cdot \frac{\mu - \mu_{H_2O}}{\mu_{H_2O}} \tag{64}$$

It is obvious that value of *HU* is equal to 0 in case of water (equation (64)). Attenuation coefficients of gases are close to 0, thus the *HU* values range from -1000 to 0 within the cavitating flow. Therefore, void of cavitation in the reconstructed image will be darker than undisturbed liquid flow. The quality of results is highly influenced by the selection of the materials in the monitored area. Materials with significantly higher density (which is strongly connected to the attenuation coefficient) compared to the rest of test rig and liquid should not be used. Presence of such materials may cause artifacts. [30]

Important part of computed tomography is reconstruction of the results, while chosen algorithm can significantly improve the final image quality. Comprehensive description of four different reconstruction algorithm can be found in books of W. Hendee. [29][32]

Simple projection algorithm is the simplest method, which considers equally spaced division of each x-ray path through the examined object, where each element of the path contributes the same to the total attenuation along the x-ray path. The final attenuation of the element is obtained using the x-ray path with different angular orientation. The final slice of examined object is composite image of attenuation coefficients of elements in cross-section. This method is simple and straightforward. On the one hand the results of simple projection algorithm are usually blurred.

Filtered back projection algorithm produces sharper images. This algorithm is also called convolution method and it is most popular way how to reconstruct results of computed tomography. Most common filter removes the frequency components of the x-ray transmission data, which are responsible for the most of composite image blurring. Frequency of convolution filter influences the results. The high frequency convolution filter can be utilized in order that it reduces noise and makes the final image smoother. Low frequency filter produces sharper results.

Several papers discussing utilization of the CT in the cavitation field of study have been published. The above-mentioned paper of Bauer et al. [30] deals with CT measurement of cavitation distribution in purpose-built nozzle made of Perspex (transparent polymer, Figure 7). The results of CT measurement have been complemented with photographic images to obtain more complex information about cavitation patterns. Bauer mentioned that it is not possible to capture phenomena of short time scale using CT due to the time averaging over 1 second. Thus, only time averaged structures or quasi steady cavitation can be captured correctly. Bauer concluded that x-ray CT can be powerful tool in cavitation research, based on the results of various types of cavitation (film, bubble and cloud cavitation) investigation.

Compared to the work of Bauer, which is based on cavitation study in special nozzle, the paper written by Brett et al. [33] deals with cavitation in common PVC butterfly valve. The results of CT are compared with numerical simulation using the ANSYS Fluent considering Schnerr and Sauerr model of cavitation. The CT served the purpose of the cavitation model verification.

The investigation was carried out for four operating points referring to different cavitation regimes and constant butterfly valve opening angle of 30°. The results of steady-flow simulations have not been successful regardless the introduced adjustments.

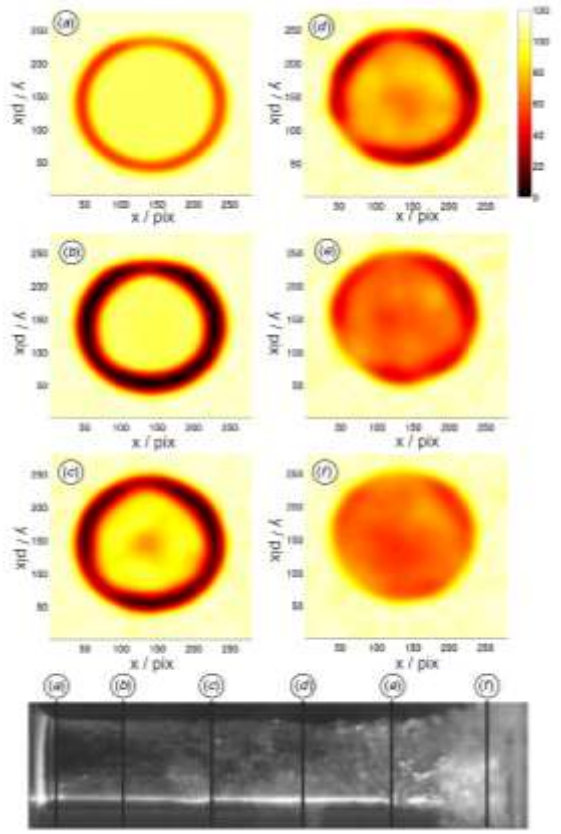

Figure 7 Cross sectional CT images at different axial positions labeled from (a)–(f) [30]

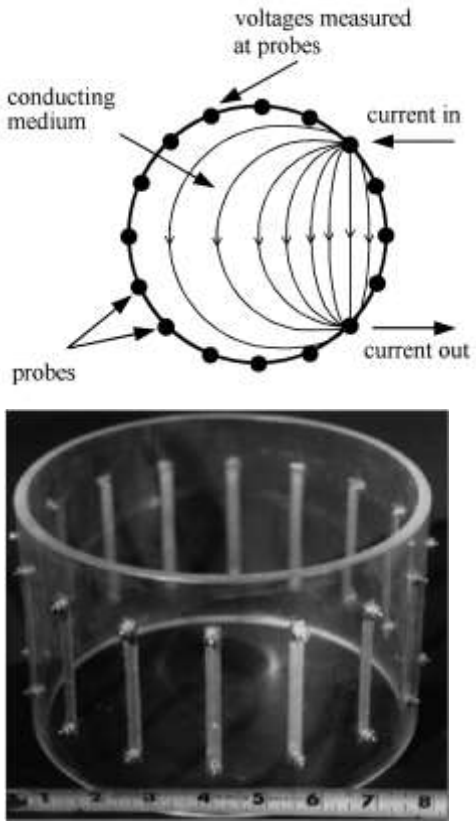

Figure 8 Principle of EIT measurement (top), EIT strip electrode array(bottom)[34]

Convergence of steady-flow simulation was particularly improved by the inclusion of non-condensable gas in the water vapor. Results of transient simulations were better. Converged results were obtained after about 0.44 s of simulation, additional calculations continued for a total time of 1.514 s. It should be mentioned that the water temperature increased about 5-10 °C during each measurement. Brett concluded that results of x-ray CT can be successfully utilized for averaged density variation capturing. Thanks to the fact that the density is directly connected to the local void fraction, the time averaged distribution of cavitation has been evaluated and compared with numerical simulation. Brett pointed to the importance of non-condensable gas measurement during the experiments as a background data for the following numerical simulations.

However, x-ray computed tomography has some obvious disadvantages. This type of radiation constitutes a health risk and the experimental apparatus is relatively complicated. Thus, other methods of computed tomography can be more beneficial in case of hydraulic research. Electrical-impedance tomography (EIT) seems to be promising method. Validation of this experimental method for two-phase flow is scope of the paper written by George et al. [34]

The basic principle of the EIT measurement is depicted in the Figure 8. Electrodes are mounted to the surface of the investigated domain. All electrode voltages are measured relatively to the ground, while prescribed current is injected into the domain at one electrode and withdrawn at another electrode.

It is possible to reconstruct the impedance within the domain and infer the phase distribution using these measurements. It should be noted that the resolution of the reconstructed conductivity field is strongly related to the number and location of the electrodes. The investigated domain can be modeled as N-port impedance network, where *N* is the number of the utilized electrodes. The current source and sink are placed on two of the ports. The current sink is often referenced to ground. The results of EIT were validated using the gama-densitometry tomography (GDT) to confirm its ability to measure spatial distribution of the phases in case of solid-liquid and gas-liquid flow.

The investigation of the gas-liquid flow was done using bubble flow within the transparent column made of lexan, which was filled by water. Air was introduced through the spargers at the base of the column. The measurement was done for several flow rates of gas. Discrepancy of the average gas volume fraction and radial gas volume fraction obtained using the EIT was negligible compared to the GDT.

1.4. Vortex rope within the draft tube

Vortex rope (example of the one form of so-called vortex breakdown) can be observed during the non-optimum operation of certain types of hydraulic turbines. The presence of the vortex rope does not necessarily lead to cavitation, but the static pressure within the vortex core can drop below the pressure of the saturated vapor. Despite the fact, that the draft tube vortex rope is not exactly the scope of the presented investigation, the similar structures were observed during the research. However, the nature of this type of cavitating flow is similar to the nature of the flow structures observed within the Venturi tube as it will be described. Therefore, the brief description of the phenomenon as well as its investigation is provided in this chapter.

The extensive research of this phenomenon during the last decade has been motivated by the increasing demands to control the power grid using the water energy, which is caused by the onset of renewable sources of the energy. These sources, such as wind or solar energy, are strongly influenced by the actual weather conditions. Therefore, it is necessary to compensate fluctuations of the energy in the electrical grid. Beside the other sources of energy, the hydropower plants are suitable for this purpose. On the other hand, the regulation of the grid using the hydropower often requires operating of the water turbines under the off-design conditions, which can lead to creation of the vortex rope. The following text will be focused on the theoretical and experimental research of this phenomenon.

Off-design operation of the Francis turbine is often connected with the presence of this phenomenon as a result of high residual swirl downstream the runner of the turbine. This is a result of the mismatch between the swirl generated by the guide vanes and the angular momentum extracted by the turbine.[35] The orientation and shape of the swirl downstream the Francis turbine is determined by the velocity triangle at the runner exit. Thanks to the constant pitch of the runner blades, the angle between circumferential velocity u and relative velocity w remains constant, regardless the actual flow rate. Significant circumferential component of the relative velocity deforms the velocity triangle in case of off-design condition (Figure 9). On the other hand, it should be mentioned that the relatively small swirl downstream the runner is plausible for the flow in the draft tube.

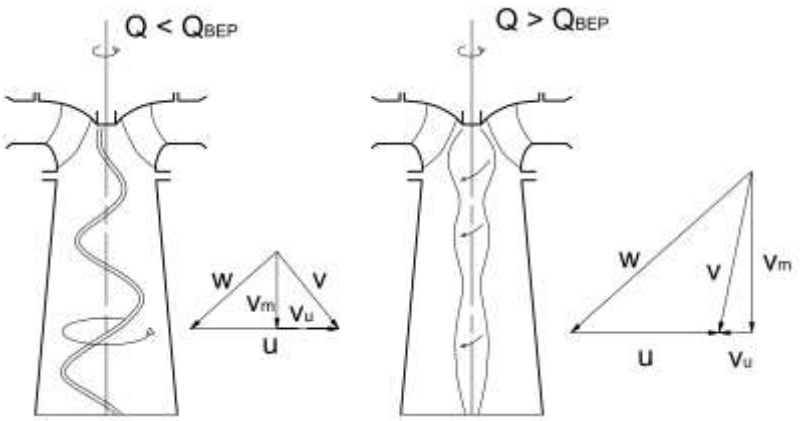

Figure 9 Partial load (left) and full-load (right) of Francis turbine with corresponding velocity triangles

Susan-Resiga et al.[35] concluded that the spiral vortex with central quasi-stagnant region in the draft tube, which occurs if circumferential momentum is large enough compared to the flux of axial momentum is a mechanism limiting the increase of the swirl number *Sn*.

$$Sn = \frac{1}{R} \cdot \frac{\int_0^R v_{ax} \cdot v_{tan} \cdot r dr}{\int_0^R {v_{ax}}^2 \, dr} \tag{65}$$

In other words, it is possible to prevent creation of the vortex rope by keeping the swirl number under the critical value. It is very useful knowledge, nevertheless in case of the Francis turbine it can be achieved only by the external intervention modifying flow in the draft tube.

Presence and motion of the vortex structure relates to the low frequency pressure pulsations, which can lead even to the destruction of the hydro plant facility, if the resonance is achieved. Therefore, it is necessary to restrict operation under the off-design conditions, which is inappropriate and uneconomic if the water turbine serves to regulation of the grid. These reasons lead to the extensive experimental and numerical research of this phenomena.[36]

Flow within the draft tube can be divided into the two different zones. The quasi-stagnant zone (or recirculation zone) is situated along the draft tube axis. Shape of the stagnant zone is influenced by the draft tube inlet flow properties. Generally, the quasi-stagnant zone is the wider, the higher is value of the swirl number (e.g. the lower is the flow rate according to equation 19(65)). This zone is surrounded by the zone of the main flow. Precessing vortex core laid on the boundary of main flow and quasi-stagnant region. [36][37]

Operating of the Francis turbine in the partial load is characterized by the presence of the helical vortex. Behavior and induced pressure pulsations of the vortex rope are influenced by the operating distance from the design point.

If the discharge drops to 70-80 % of Q_{11opt} (also called upper partial load) the spiral vortex precessing with the same direction as a runner is observed in the draft tube. It is possible to detect pressure pulsations with frequency corresponding to the rotation of the vortex rope. Beside these dominant pulsations It is also possible to identify pulsations with frequencies close to the dominant frequency multiples. Some authors suggest that the higher frequency pulsations may be caused by the rotation of the elliptical cross section of the vortex rope. [36]

With the further discharge decrease down to 50 % of Q_{11opt} the helical vortex rope precessing with the same direction as a runner is still observable in the draft tube. Frequency of the vortex precession is 20-40 % of the runner rotation frequency. Within the range of 40-50 % Q_{11opt} the helical vortex structure decays to the significant number of small vortices. Thus, the pressure pulsations lost their periodicity.

Certain conditions favor development of two separated vortex ropes. Inception of this flow regime is accompanied by sudden change of pressure pulsations.[36]

The vortex rope has usually completely different shape (as is shown in the Figure 9) in case of full load, when the position of the vortex is stabilized along the axis of the draft tube. The vortex rotates in the opposite direction than the runner. Mechanism of the pressure pulsations origin is different. So-called self-induced oscillations arise, which are connected with presence of the cavitating phase (vapor) and so-called mass flow gain factor:

$$\chi = \frac{\partial V_{cav}}{\partial Q} \tag{66}$$

The research of the flow within the draft tube can be realized on the complex models with turbine runners or using different types of swirl generators, which are cheaper. On the other side utilization of the simplified generators can lead to neglecting of some physical properties of the flow compared to the real turbines. Large database of the experimental results was created in research project FLINDT (Flow Investigation in Draft Tubes), which was conducted at EPFL Lausanne. The experimental measurement of Francis scale model has been carried out for wide range of the operating points. Results of these experiments were used for the further experimental, theoretical and numerical investigation of the swirling flow in the draft tube. [38]

Another large project Francis-99 conducted under the patronage of Norwegian University of Science and Technology and Luleå University of Technology is more up to date. The series of three planned workshops is based on experimental measurement of a high head Francis turbine. [39] The scopes of the workshops are as follows: Steady operation of Francis turbines (December 2014), Transient operation of Francis turbines (December 2016) and FSI of Francis turbines (December 2018).

The comparison of the experimental results with numerical simulation of the vortex has been done by Kirschner et.al.[40] to investigate properties of the flow. Three investigated operating points (part, optimal and full load) of the pump turbine in turbine mode were investigated using the simplified 2D axisymmetric computations. Results of simulations were compared with the PIV measurements where good agreement in time averaged velocity field was obtained in case of part load and optimum load. The results of full load were influenced by the inaccuracy of the inlet boundary condition. Correction of this discrepancy lead to the improvement of the numerical results. Kirschner confirmed that simplified computation is useful, and it is possible to detect separation of the flow from the diffuser walls in case of the optimum load or creation of the recirculation zone in case of part load.

The influence of the computational mesh refinement and model of turbulence on the pressure pulsations downstream the Francis turbine was scope of the investigation carried out by Jošt et al. [41] It was concluded, that density of the computational mesh strongly influenced the value of the pressure pulsations amplitudes. While the difference between numerical and experimental amplitudes were around the 50 % in case of coarser mesh, the finer mesh showed error about 10 %. Comparison of the RSM, SAS-SST models of turbulence and LES lead to the conclusion that quality of results is comparable. It should be mentioned, that Jošt obtained worse results using the multiphase simulation, than in case of single-phase computations neglecting the presence of cavitation. Jošt proposed that this result can be caused by insufficient density of the mesh or by the cavitation model uncertainty.

Flemming et al. [42] obtained more realistic results considering the multiphase simulation, which is depicted in the following picture.

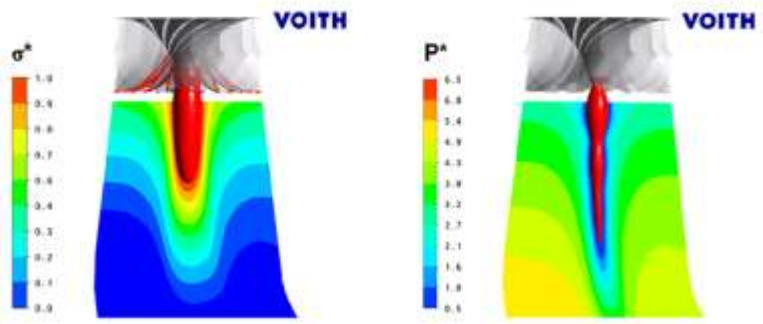

Figure 10 Comparison of the vortex rope using the single-phase (left) and multiphase (right) simulation, Flemming [42]

The same result was conclusion of the investigation carried out by Dörfler et al [43] using simplified 2D axisymmetric computation.

1.4.1. Swirl generator with fixed blades

Hydraulic laboratory of V.K. Dept. of Fluid engineering has considerable experience with the utilization of the swirl generators with fixed blades. The swirl produced by the guide vanes has a defined strength and distribution of the circumferential velocity. The main advantages of the conception are the reasonable price of the swirl generator, which can be 3D printed and its compactness. It is possible to modify the experimental set-up in short time and with reasonable cost.

Swirl generator has been employed for detailed analysis of the swirling flow within the diffuser by David Štefan and Pavel Rudolf, who had published several contributions aiming to the experimental and numerical evaluation of the vortex rope dynamics. [44], [45], [48]

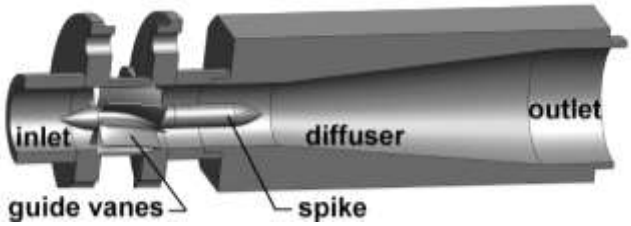

Figure 11 Swirl generator with fixed blades – older model

Štefan concluded that LES single-phase simulation brought significantly better results of the decelerated swirling flow compared to RSM calculation through the POD analysis of the obtained results. [44] In another contribution Štefan et al. [45] presented the comparison of experimental data and numerical simulation carried out by OpenFoam code considering single-phase computations. It has been concluded that experimentally observed helical vortex unsteadiness can be well-captured using the utilized CFD set-up and above that Štefan proposed that the periodically decaying vortex decreases the magnitude of the asynchronous pressure pulsations downstream the diffuser which were observed in experimental as well as in the numerical results.

Another utilization of the swirl generator is connected with downstream converging-diverging nozzle replacing the diffuser. This set-up can be exploited for the water disinfection, where the number of cyanobacteria within the water can be significantly reduced using the hydrodynamic cavitation, respectively the pressure pulsations induced by this phenomenon. The comprehensive study of the flow in the Venturi nozzles considering two different diameters of the throat, with and without the generator is the main scope of the diploma thesis written by M.Gríger.[46] The thesis was focused on the experimental measurement of the hydraulic loss in converging-diverging nozzles in wide range of cavitation regimes, with and without the swirl generator. The second main scope of the thesis was to investigate dynamics of cavitation using the high-speed video records and records of the static pressure.

The experimental data obtained by Gríger were investigated by Rudolf et al. [8] and Kozák et al. [51] in more details.

The CFD simulation of the similar experiment has been done by Rudolf et al.[47] Results of realizable k-ε, RSM and LES single-phase computations were correlated with experimental data. It was shown that realizable k-ε model of turbulence is not suitable for this purpose. On the other hand, RSM and LES are fully comparable in time averaged characteristics, nevertheless the Reynolds stress model of turbulence was not able to capture the unsteady behavior of the flow with spiral vortex breakdown. Comparison of the LES investigation and the experiment is depicted in the following figure.

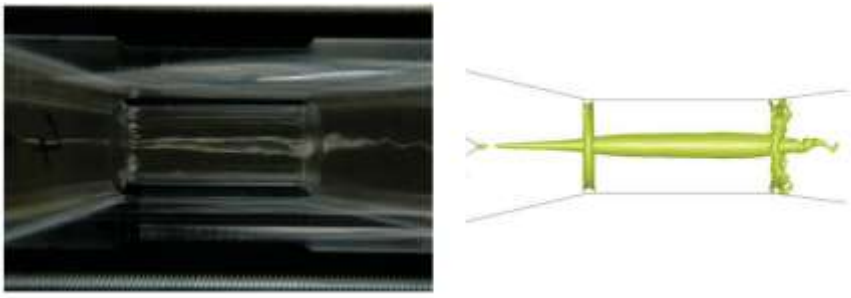

Figure 12 Comparison of the vortex rope in the C-D nozzle downstream the swirl generator, experiment vs. single-phase LES calculation, isosurface of vapor pressure is depicted [47]

Profiles of the tangential and axial components of velocity were captured in the middle section of the nozzle using the Laser Doppler Velocimetry (LDV) in case of non-cavitating operation regimes. The results of LDV were compared with CFD calculations utilizing the above-mentioned turbulence models (Figure 13).

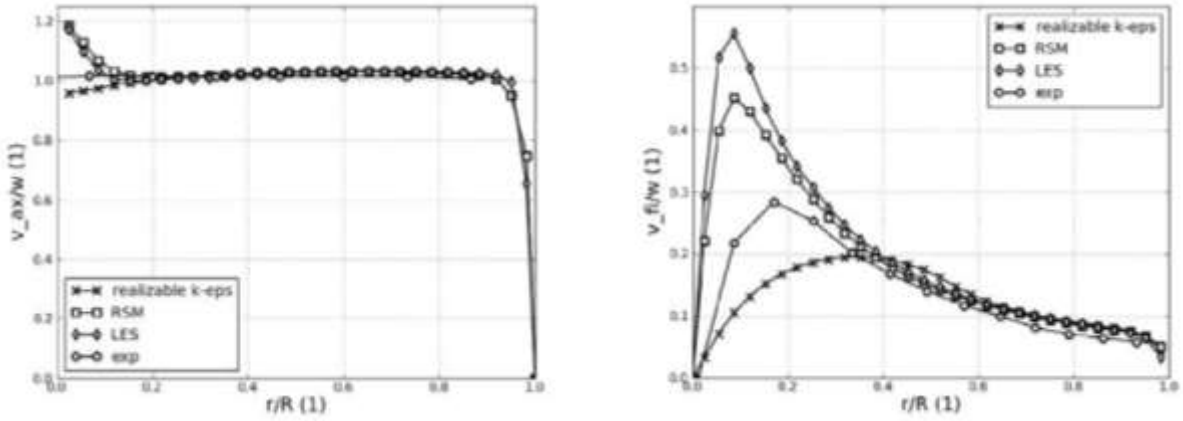

Figure 13 Comparison of predicted axial (left) and tangential (right) component of velocity with results of LDV measurement in case of non-cavitating regime (Q = 4.56 l/s)[47]

1.5. Utilization of cavitation

Mainly the undesirable effects of cavitation were mentioned in the previous text, on the other hand there are many positive ways of the cavitation utilization in branches such as medical, food-processing or chemical engineering. This chapter is devoted to the brief summary of the utilization of cavitation effects in water processing and its disinfection.

Kalumuck, Chahine and other members of Dynaflow INC [49] presented wide range of water disinfection possibilities using their Dynajet cavitationg jets. Two different cavitating jets were described. StratoJet produces cavitating vortex ring, while DynaSwirl was capable to produce central cavity, with vortex breakdown at the end. Laboratory experiments were carried out to prove ability of the hydrodynamic cavitation to destroy microorganisms and oxidize a broad range of harmful compounds such as pesticides and their mixtures, volatile organic compounds and arsenic. It was concluded that cavitating water jet is highly efficient compared to the standard oxidation using the ultrasonic horn. Ultrasonic devices have limited efficiency of the cavitation production, which occurs only in a thin layer near the surface of the sonifier.

The similar result was proposed by Jančura et al. [50], in case of selective cynobacterial bloom removal. The experimental part of this contribution has been done in hydraulic laboratory of V. Kaplan Department of Fluid Engineering, where the water containing specified amount of cyanobacteria and green algae was exposed to the hydrodynamic cavitation within the converging-diverging nozzle. It was concluded that the cavitation treatment of cyanobacteria is capable to selectively disintegrate their gas vesicles with no effect on cyanobacterial membrane integrity, thus there is no risk of cyanotoxin release into the water column. Moreover, green algae were not affected by the cavitation, thus it can act as the natural nutrient competitors of the cyanobacteria even after the explosion to the cavitation.

Balasundaram et al [56] has published experimental investigation of the brewer's yeast disruption using the hydrodynamic cavitation. The influence of several parameters including the cavitation regime, initial concentration of yeast and number of the exposures to the cavitating conditions was investigated. Balussundaram identified optimal conditions (σ = 0.13) corresponding to the extensive cavitation. Nevertheless, it was concluded that the further decrease of cavitation number value lead to the decrease of disruption efficiency, which was identified as consequence of cavitating bubbles fusion.

1.6. Overview of the exploited methods of investigation

Following text will be structured into the logical sections based on the purpose and methods of the investigation. The brief overview is provided bellow:

Visualization of the cavitating structures using the high-speed video records

- Description of the typical patterns and cycles of the cavitation
- Spectral analysis of the cavitation dynamics using the pixel intensity fluctuations
- Proper orthogonal decomposition of the captured records

Experimental measurement of cavitation characteristics

Using the acquired data, the dynamics as well as tie averaged characteristics including the hydraulic losses will be discussed. Following physical quantities were recorded during the test campaign in order to provide baseline for further discussion (this is not meant to be full list of exploited transducers):

- Static pressures
- Pressure pulsations
- Pipe-wall acceleration
- Acoustic emission
- Noise

Numerical investigation of the cavitating flow

- Unsteady multiphase simulations carried out using the OpenFoam

Computed tomography

- EIT tomography was utilized as an attempt to describe distribution of the gaseous phase within the flow during the cavitation.

Experimental investigation of the cavitation within Venturi tube

Content of the following chapter:

1. Description of the experimental facility
2. Analysis of the high-speed video records
3. Analysis of the experimental acquired data

2. Experimental investigation of the cavitation within Venturi tube

The experimental research was focused on the investigation of the wide range of cavitation regimes and influence of the induced swirl. A great deal of effort was devoted to the description of the cavitating flow characteristics using the analysis of the HS (high-speed video) records. Also the results of pressure fluctuations, pipe-wall acceleration, noise and acoustic emission will be discussed and correlated in order to describe the individual cavitation regimes, influence of the flow rate magnitude and the influence of the swirl induced by the upstream mounted generator. The dynamics of the cavitating structures will be discussed together with the analysis of the time-averaged properties of the cavitating flow. The specific variations of these properties and typical cavitating structures connected with the transition between the cavitation stages will be identified.

2.1. Cavitation circuit

Cavitation circuit of the Victor Kaplan Dept. of Fluid Engineering was exploited for the purpose of the experimental measurement. Since the image analysis was one of the crucial parts of the investigation, the Venturi nozzle was manufactured from the transparent plexiglass and surfaces of the Venturi nozzle were polished. The main dimensions of the Venturi nozzle are depicted in the Figure 14.

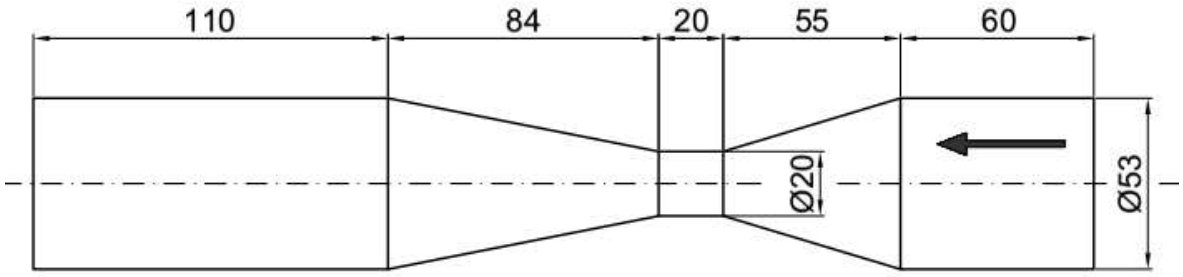

Figure 14 Scheme of the Venturi nozzle

The 3D printed swirl generator (SG) was used in order to introduce the swirl into the flow during the main part of the investigation. Swirl generator consists of 9 fixed blades with the linear change of the exit angle from axial direction (30° to 50°, from hub to shroud). It was necessary to caulk the surface of the SG prior the measurement. This was done using the epoxy coating of the outer surfaces and subsequent coating with spray paint, while the SG was evacuated. The 3D model of the swirl generator is depicted in the Figure 15.

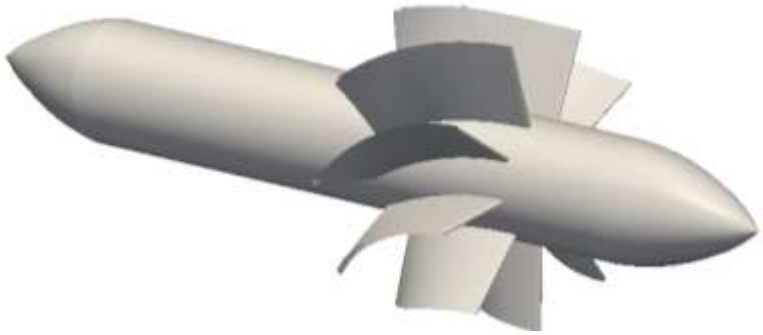

Figure 15 Swirl generator

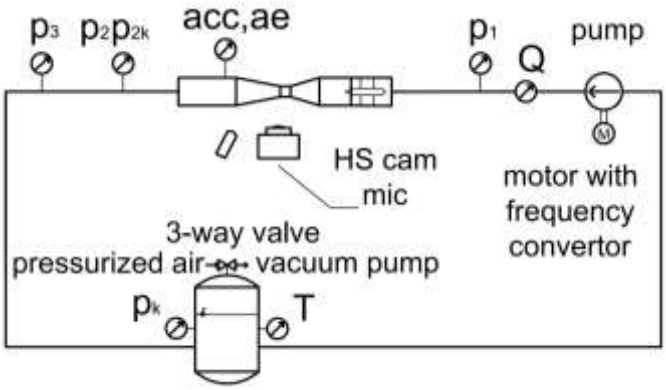

Figure 16 Cavitation rig considering presence of SG upstream the Venturi nozzle

Cavitation rig was equipped with the pressure tank. Thus, it was possible to investigate different cavitation regimes of the flow for the constant discharge. Several physical properties of the water and investigated flow have been captured during the experiment as it has been mentioned. The cavitating flow has been recorded using the HS camera HS Photron FastcamSA-X2 1000K. Scheme of the cavitation circuit including placement of the transducers is depicted in the Figure 16. Information of the utilized transducers and other equipment is provided in the Table 1. It should be also noted that the swirl generator was replaced by the straight pipe section in case of the axial inflow investigation to preserve constant distance between the nozzle and pressure transducers.

Symbol	**Equipment**	**Type**	**Accuracy**
Pump	Single-stage Centrifugal pump	SPP KP06C	-
M	Drive	SDS112 S603	-
HS Cam	High speed camera	SA-X2 1000K	-
p_1, p_2, p_3, p_k	Pressure transducer	BD DMP 331	± 0.35 %
p_{2k}	Pressure transducer	Kistler 211 B4	± 1 %
Q	Flow meter	ELA MQI 99 SN	± 0.3 %
T	Thermometer	Rawet PTP 55	± 0.3 %
Acc	Accelerometer	Aura SV 129	± 0.4 - 3 %
AE	Acoustic emission transducer	UT 1000	± 1.5 dB
Mic	Microphone	PCB 378B02	± 1.5 dB

Table 1 List of experimental equipment

2.1.1. Eigenfrequency of the test bench

The eigenfrequency of the test bench has been evaluated using the modal analysis (bump test) and subsequent analysis of the pipe-wall acceleration records. The test was done on the flooded test bench under the steady state conditions (flow-rate equal to zero) considering the measurements of vertical and horizonal shock as it is depicted in the Figure 17.

Figure 17 Position of the accelerometer during the measurement of the eigenfrequency of the test bench in vertical (left) and horizontal direction(right).

Eigenfrequency of the test bench was investigated for both experimental configurations to capture the influence of the swirl generator. The gradual decrease of the measured acceleration after the vertical impulse is depicted in the Figure 18 (vertical shock). The measured acceleration was decreasing relatively fast after the initial impulse regardless the configuration of the test bench.

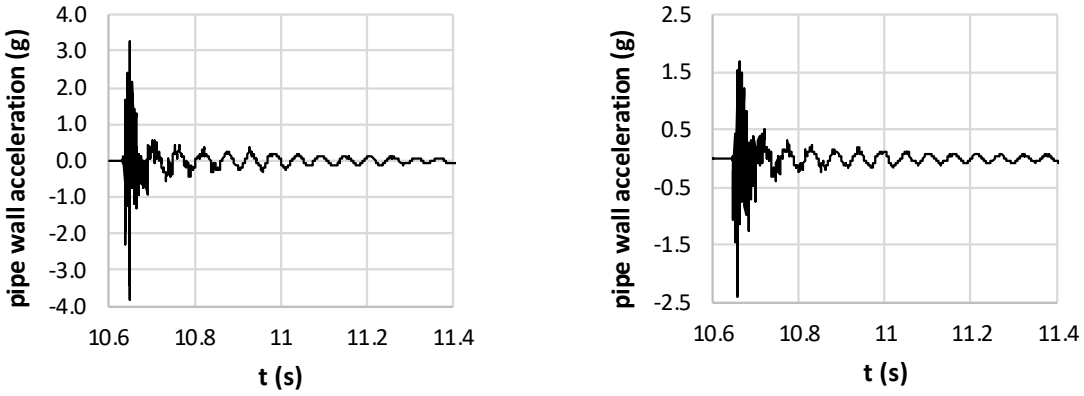

Figure 18 The pipe-wall acceleration measured during the bump test in order to determine eigenfrequency of the test bench. Axial inflow – right, Swirl generator – left

The frequency spectra of the signals are depicted in the following figure. As it is clearly depicted, the eigenfrequencies obtained by the analyses are nearly the same, regardless the presence of the swirl generator. In other words, the presence of the swirl generator had negligible influence on the value of the determined eigenfrequency of the test bench after the vertical shock. The actual value of the eigenfrequency was close to 18 Hz.

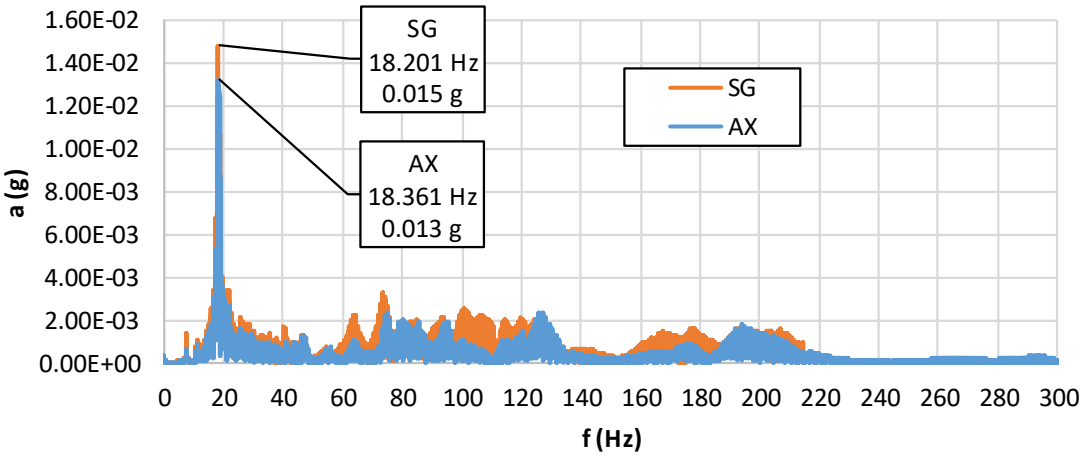

Figure 19 Frequency spectra obtained by the analysis of the acceleration records captured after the vertical impulse which was applied on the test bench.

The same analysis was done considering the horizontal shock. The obtained frequency spectra are depicted in the Figure 20. The dominant frequencies are slightly lower compared to the vertical impulse. The most significant frequency is close to the 11 Hz regardless the experimental configuration. Nevertheless, the significant peak of the acceleration amplitude was also observed close to 7.4 Hz. The lower values of the observed frequencies can be devoted to the lower stiffness of the pipeline mounting in the horizontal direction.

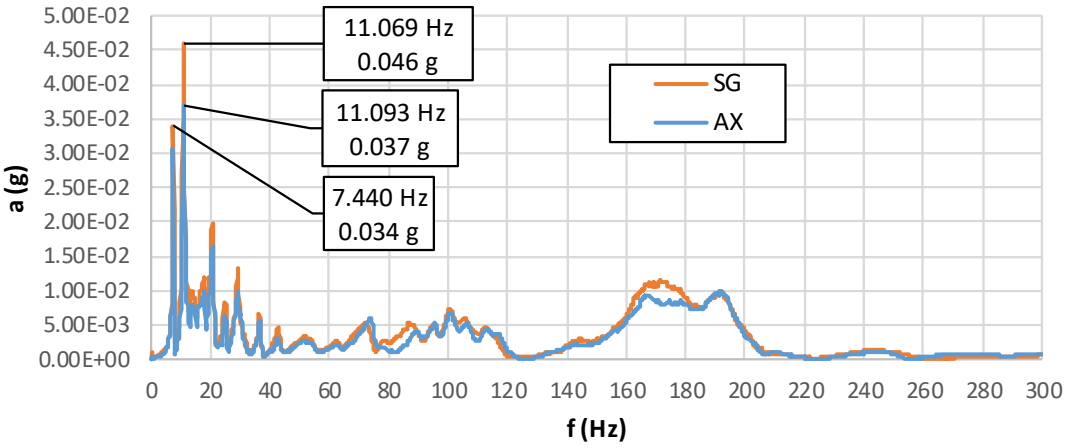

Figure 20 Frequency spectra obtained by the analysis of the acceleration records captured after the horizontal impulse which was applied on the test bench.

2.1.2. Pump shaft and blade passing frequencies induced by the operation of the pump

To describe the frequencies induced by the operation of the pump during the test campaign, the charts of blade passing frequencies are depicted in the Figure 21 and the pump rotating frequencies in the Figure 22.

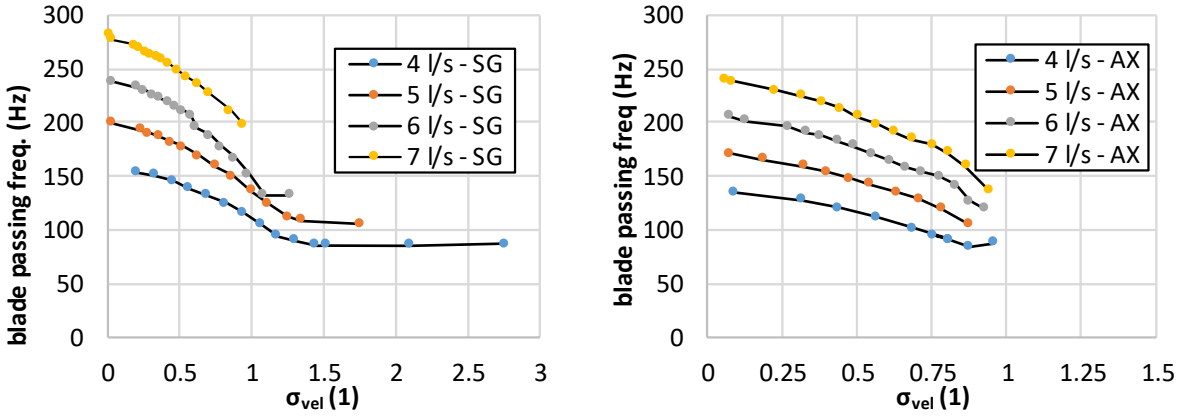

Figure 21 Informative charts of the blade passing frequency induced by the operation of the pump in case of the SG presence (left) and axial inflow (right)

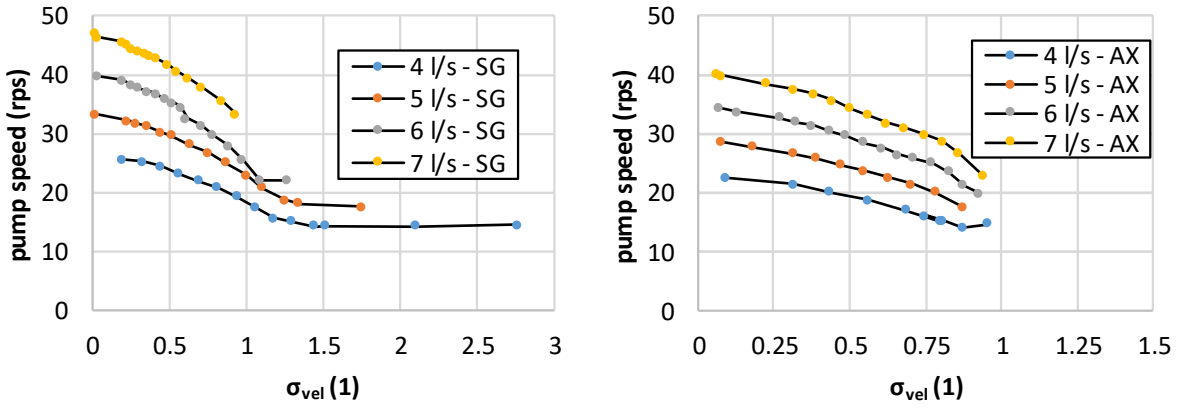

Figure 22 Informative charts of the pump rotating speed in case of the SG presence (left) and axial inflow (right)

High speed video records analysis

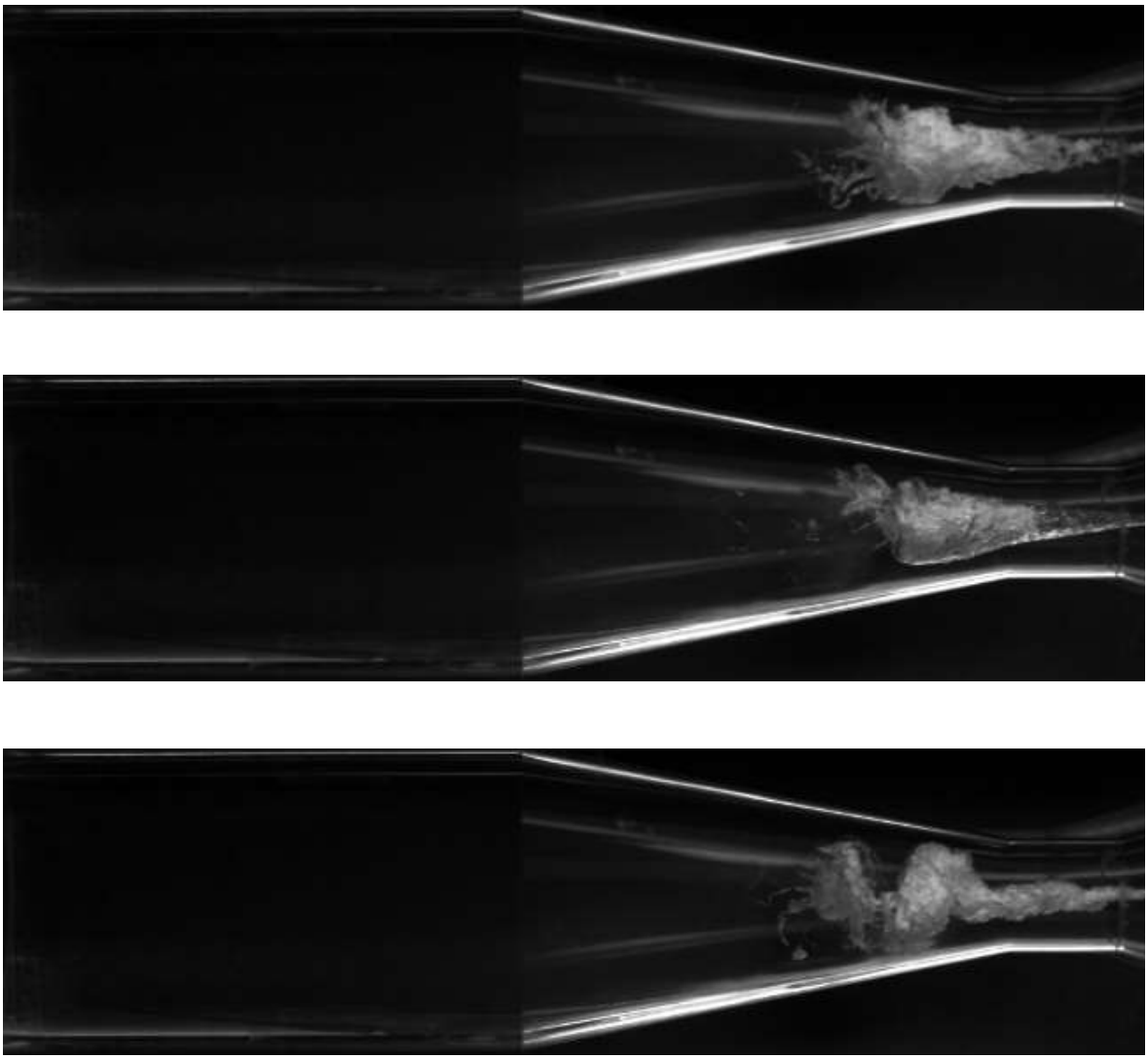

Content of the following chapter:

4. Description of the characteristic cavitation cycles
5. Spectral analysis of the cavitation dynamic based on the pixel intensity fluctuations
6. Analysis of the cavitation cycles using the proper orthogonal decomposition

The high speed (HS) video records provide a rich source of information characterizing cavitation dynamics, typical cavitation patterns and allows to quantify presence of gaseous phase within the flow to certain extent. The following chapter provides analysis of the captured records. Special attention will be paid to study of the induced swirl influence on the cavitating flow properties.

The study of the cavitation dynamics will be done exploiting the spectral analysis of the pixel intensity and proper orthogonal decomposition of the data recorded within the selected region of interest.

Extensive study of the cavitation dynamics and the mechanisms causing the shedding of cavitating structures has been published by Saad et al. [67]. The study has been carried out using the asymmetrical Venturi nozzle (considering the axial inflow). Two major mechanisms causing the periodical shedding were identified based on the value of cavitation number. While in case of the relatively high values of the cavitation numbers so-called re-entrant jet was identified as the phenomenon causing the shedding of cavitating structures, the prevalent mechanism for periodic cavity shedding was found to be the bubbly shock mechanism in case of lower cavitation numbers.

2.2. Experimental set – up

The grayscale records were captured using the camera FASTCAM SA-X2 type 1000K-M2. List of the most essential camera settings is provided in the following table. Sampling frequency of 20 000 frames per second (fps) guaranteed sufficient temporal resolution of the captured records due to the expected time-scale of the cavitation structures fluctuations.

Sampling frequency	20 000 fps
Shutter time	1/40000 s
Color pallete	8 bit grayscale
Image resolution	1024 by 296 px
Record length	0.5 s

Table 2 Camera settings utilized during the experimental measurement

Venturi tube was illuminated using two panels of led diodes. This type of illumination provides reasonable performance, while the produced heat remains relatively low. On the other hand, the matrix of led diodes can be visible in the captured images under certain circumstances. Moreover, the flickering of the diodes with the frequency of 3000 Hz was observed. The flickering was limiting the applicable shutter speed of the camera.

Three types of the scene arrangement were tested prior the main experimental measurement. The least appropriate scene setting consisted of the front illumination of test section with the white background behind the transparent nozzle (Figure 23, left). Alongside with the relatively low contrast of the cavitating structures, the surface imperfections of the white background were significant.

The second tested scene setting was illuminated using the backlit behind the white background which was made out of tracing paper (Figure 23, middle). In case of this type of the scene setting, the contrast of the cavitating structures was excellent. The cavitation structures represented dark regions within the very light image as the result of the light reflection. On the other hand, it was very difficult to study dynamics and motion of the observed structures, because a lot of information was lost since only the silhouettes of the most significant structures were captured. Furthermore, it was not possible to guarantee uniform backlight intensity over the whole investigated region. Nevertheless, this type of the scene illumination would be highly appropriate for the future investigation in case of larger led diode panel availability.

The last scene setting, which was chosen for the further experimental measurement consisted of front light utilizing the two led panels and black background (Figure 23, right). Threaded rods were covered by the black paper to minimize the reflections. The interface between liquid and gaseous phases was reflecting the light back to the camera, therefore the cavitating structures are represented by light regions in front of the dark background. The image contrast of this configuration is sufficient, while it is still possible to gather more information of the cavitating structure motion and its dynamics. The most

significant disadvantage of this type of scene setting is intermittent occurrence of the overexposed regions and uneven scene illumination.

Figure 23 Comparison of the images obtained using the different scene setting

2.3. Cavitating flow – comparison of cavitation regimes

Since the description and comparison of the cavitation patterns will be done over the wide range of cavitation regimes, it seems to convenient to divide the whole range of the investigated operating points to the several characteristic subsections. Mean values of the magnitude of the pipe wall acceleration fluctuations *a* was exploited for this purpose as it can be seen in the Figure 24 (this quantity will be referred as an acceleration in the following text).

While the comprehensive analysis of the whole range of the investigated flowrates will be described in the chapter devoted to the analysis of the records of transducers, only the results of 6 and 4 l/s are depicted in this chapter. It can be stated that the magnitude of acceleration in case of the higher cavitation numbers (region 1 and partially 2) was higher when the flow was affected by the induced swirl. In contrast, the vibrations were considerably more severe in case of the axial inflow within the region of lower cavitation number. It should be noted that this observation is dependent on the investigated discharge. It is clearly depicted, that the acceleration induced by the axial inflow becomes higher compared to results corresponding to the presence of swirl generator earlier in case of 6 l/. Considering the flowrate of 4 l/s, the pipe wall acceleration induced by the swirling flow remain dominant down to the considerably lower value of cavitation number.

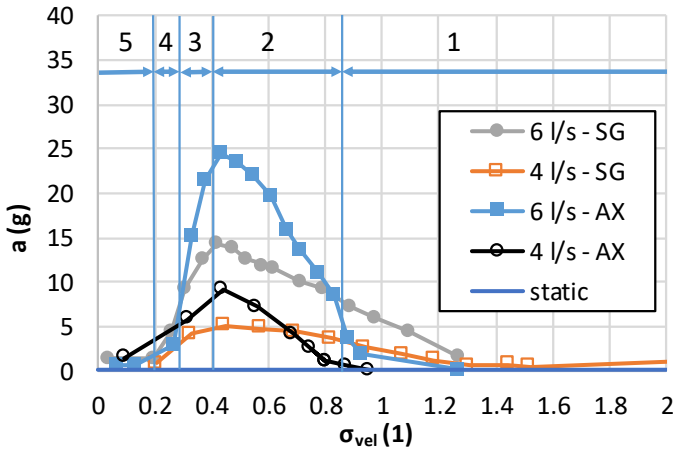

Figure 24 Mean value of the pipe wall acceleration fluctuations magnitude induced during the different stages of cavitation development in case of swirl generator presence (SG) and axial inflow (AX). Static line corresponds to the measurement under the static conditions (0 l/s)

The typical cavitation patterns characterizing individual regimes as well as the discussion of the induced swirl influence are provided in the following text. Individual subsections are introduced by the general description of the observed cavitating structures supplemented by the set of images. Detailed description of the cavitating flow cycle will be provided separately based on the experimental configuration (SG and AX) exploiting the provided images.

2.3.1. Region 1 – Initial cavitation I

Initial regime is characteristic by the relatively small amount of the cavitation within the flow. The observed cavitating structures were completely different based on the presence of the swirl generator due to the distinct redistribution of the flow within the Venturi tube.

The narrow cavitating vortex filament was observed downstream the spike of the generator in case of the flow affected by the induced swirl. The length of filament was increasing with the decreasing value of cavitation number. When the filament reached the diffuser downstream the throat of the nozzle, the helical vortex breakdown occurred (see Figure 25, left). Observed scale of this phenomenon was relatively small with respect to the resolution of the captured records.

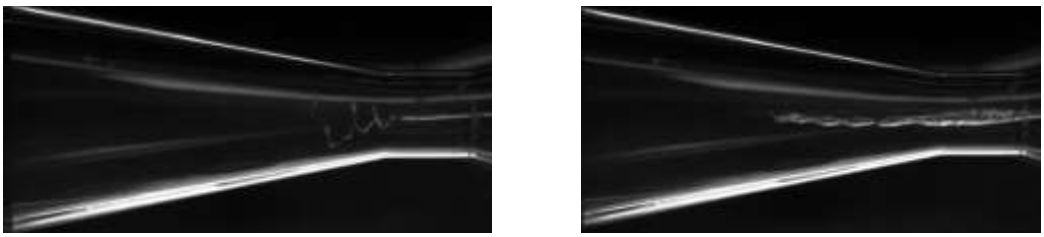

Figure 25 Detail of the helical vortex breakdown at the end of the straight filament (left) and axisymmetric cavitating vortex consisted of connected cavitating voids.

With the decreasing value of cavitation number, the vortex filament was extending in the diffuser downstream the throat of the nozzle. The vortex structures became similar to so-called full load cavitating vortex, which can be found downstream the runners of Francis turbines operating under the off-design conditions (see Figure 25, right). The vortex gained shape of connected voids of cavitation, while it was possible to observe slow precession of the structure within the diffuser. The void in the throat of the nozzle was considerably more massive and longer compared to the voids closer to the tip of the vortex. With the further decreasing value of cavitation number, the backflow regions occurred within the voids of the vortex and cavitating structure became unstable. This structure transforms into the conical vortex (see left column of Figure 27). Cavitating vortex was the more massive, the lower was cavitation number. It was possible to observe helical type of the vortex breakdown at the end of the conical structure. The creation of the backflow region was observed. The upstream motion continued up to the inlet part of the throat of the nozzle. After that, the partial collapse of the conical vortex accompanied by the helical type of the vortex breakdown followed. It should be noted that consequent re-establishment of the conical vortex was relatively fast.

In case of the axial inflow (see right column of Figure 27), the first occurrence of the cavitation was observed downstream the leading edge of nozzle throat wall. The length of the cavitating structure was the longer, the lower was cavitation number. Cavitating boundary layer was highly unstable with the typical fast longitudinal pulsations. When the cavitating structure reached the diffuser downstream the throat, it disintegrated to the considerable amount of highly stochastic cavitating vortices. So-called re-entrant jet plays significant role in the fluctuations of the cavitating boundary layer in case of this experimental configuration. This phenomenon is captured in set of images provided in Figure 26, where chosen structure is highlighted by the yellow contour. It was possible to observe upstream motion of the flow structures on the wall of the throat during the growth of the cavitating boundary layer (0-5 ms). The cavitating boundary layer was shortening back to the leading edge of the throat in the last part of the cycle (7.5 ms).

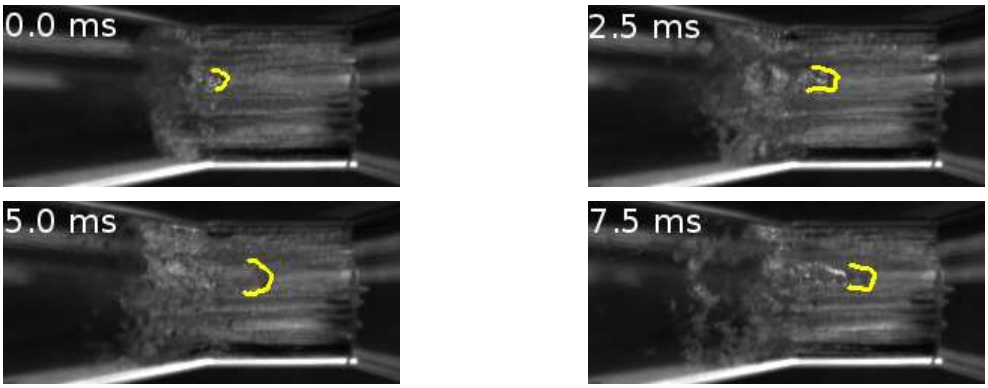

Figure 26 Re-entrant jet – upstream motion of the liquid structure on the wall of the nozzle throat. Defects of the leading edge of the throat are clearly depicted.

The experimental measurement was influenced by the small imperfections of the leading edge of the throat. These defects were created as a result of cavitation erosion and consequently these defects played a role as source of cavitation nucleation. Thanks to this fact, it was impossible to reach the cavitation free regime prior the aeration of the test rig. The cavitation cycles of the both of investigated experimental configurations are depicted in the following set of images.

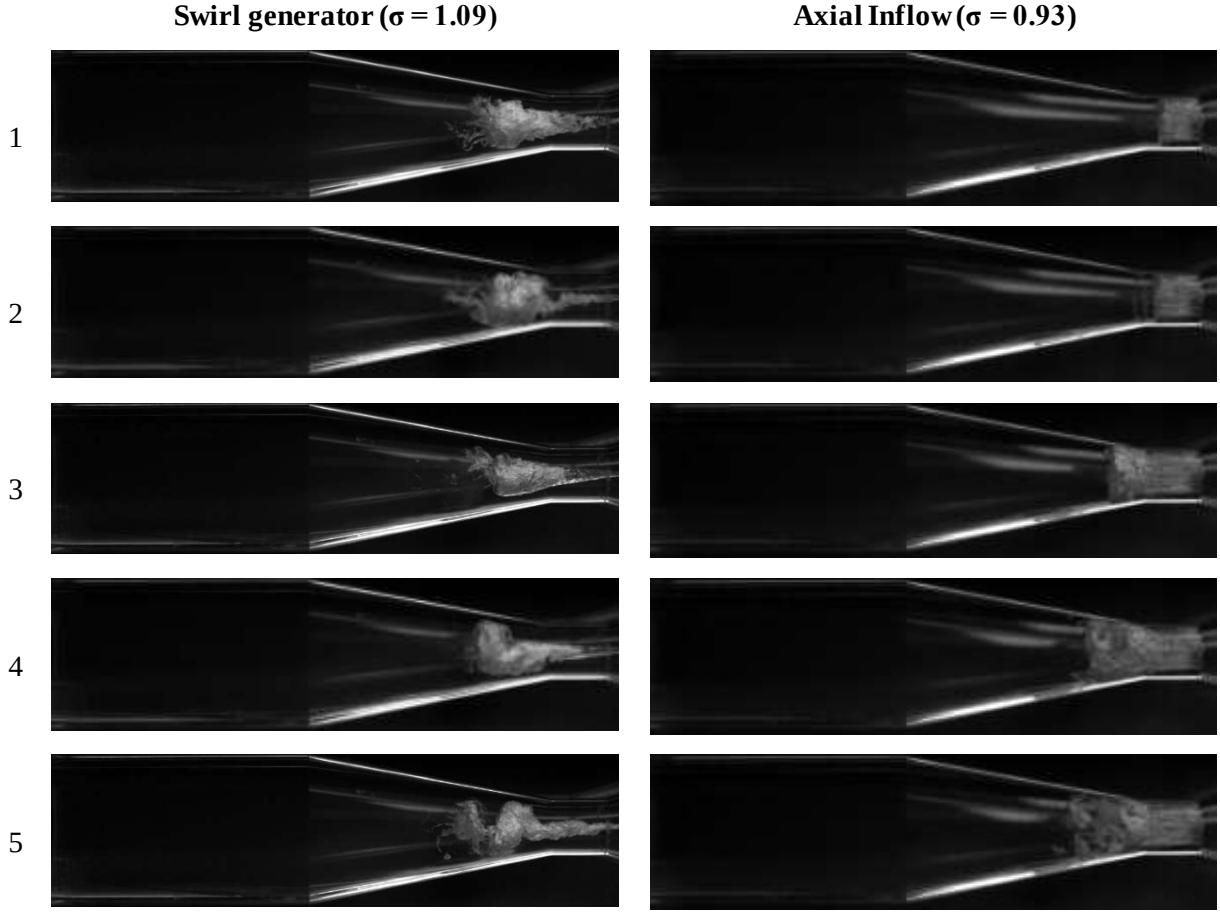

Figure 27 Representative sets of images depicting cavitation cycles in case of the 1st region.

Cavitation induced by the swirl – left column of Figure 27

The initial phase of the cavitating vortex stabilization after the end of previous cycle is depicted in the row 1. The length of the conical structure was increasing relatively fast (row 2) until the maximum length of the cavitating vortex was reached (row 3). Short but distinguishable helical end of the vortex

is clearly depicted in the image. Backflow region causing the destabilization of the vortex was observed (row 4). Growth of the backflow region was relatively slow until the moment, when the region reached throat off the nozzle. Then the rapid collapse of the vortex occurred (row 5).

Cavitation in case of the axial inflow – right column of Figure 27

Cavitation cycle started with the growth of the cavitating boundary layer length downstream the leading edge (row 1). The cavitation on the trailing edge of the throat occurred prior the growing cavitating boundary layer reached the end of the throat (row 2). The cavitating structure was getting longer towards to the inlet part of the diffuser. It should be noted that the interface between liquid and gaseous phase was highly unstable due to the presence of the imperfections of the leading edge of the throat (row 3). The partial collapse of the relatively short cavitating structure occurred downstream the throat with the consequent separation of the significant amount of the minor cavitating structures (row 4). The relatively long-lasting effervescence of these vortices preceded the final collapse of the cavitation (row 5). It should be noted that the cavitation never decayed completely and even the contraction of the cavitating boundary layer upstream the trailing edge of the nozzle, which is depicted in the first row, was relatively seldom.

2.3.2. Region 2 – Fully developed cavitation I

The cavitation affected by the swirl generator has the same character as in case of the region 1 (see left column of Figure 29). The vortex is more massive and longer compared to the first region due to the lower level of static pressure (e.g. lower value of cavitation number). It was clearly visible that the cavitation occurred in the shear layer between the inner backflow (or quasi-stagnant) region and region of the downstream flow close to the walls of Venturi tube. The partial collapse in form of the helical vortex breakdown was observed when the backflow reached the inlet part of the nozzle throat similarly to the region 1.

It should be noted that the cavitation was relatively compact. No significant separation of the cavitating structures from the vortex was detected. However, considerable amount of the small cavitating vortices was observed close to the cavitation closure region. The length of the coherent conical structure did not exceed the length of the diffuser in the whole region 2. On the other hand, it was possible to find minor amount of small cavitating structures entrained by the flow into the straight pipe downstream the diffuser of the nozzle. Moreover, the significant amount of the micro bubbles (close to, or under the resolution of the captured images) in the whole section downstream the throat was detected, mainly thanks to the fluctuations of the image brightness caused by the light reflection from interfaces of these bubbles, which were slightly changing their scale with the pressure pulsations.

In contrast to the cavitation affected by the induced swirl, the character of the cavitating flow in case of the axial inflow was different compared to the region 1 (see right column of Figure 29). The cavitating boundary layer was rolling up in form of the coherent cavitating vortex ring which was entrained by the flow. Vortex rings were the larger, the lower was cavitation number. Even in case of relatively high values of the cavitation number the rings were able to travel long distance within the straight pipe downstream diffuser prior their decay. In case of the operating points close to the region 3, it was possible to observe creation of the secondary and sometimes even the tertiary vortex ring directly after the separation of the massive and coherent primary vortex ring (see Figure 28, left). These structures were significantly smaller, less coherent and they were collapsing relatively fast into the considerable amount of the cavitating vortices close to the axis of the nozzle. From time to time the secondary ring was sucked and absorbed by the primary vortex ring as is depicted in the Figure 28.

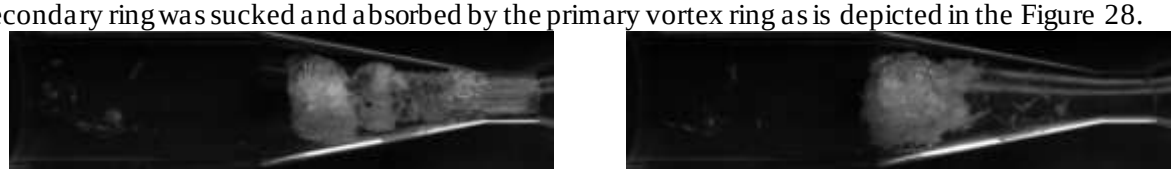

Figure 28 Separation of the secondary vortex ring (left) and its absorption by the primary vortex rings (right) captured in case of axial inflow

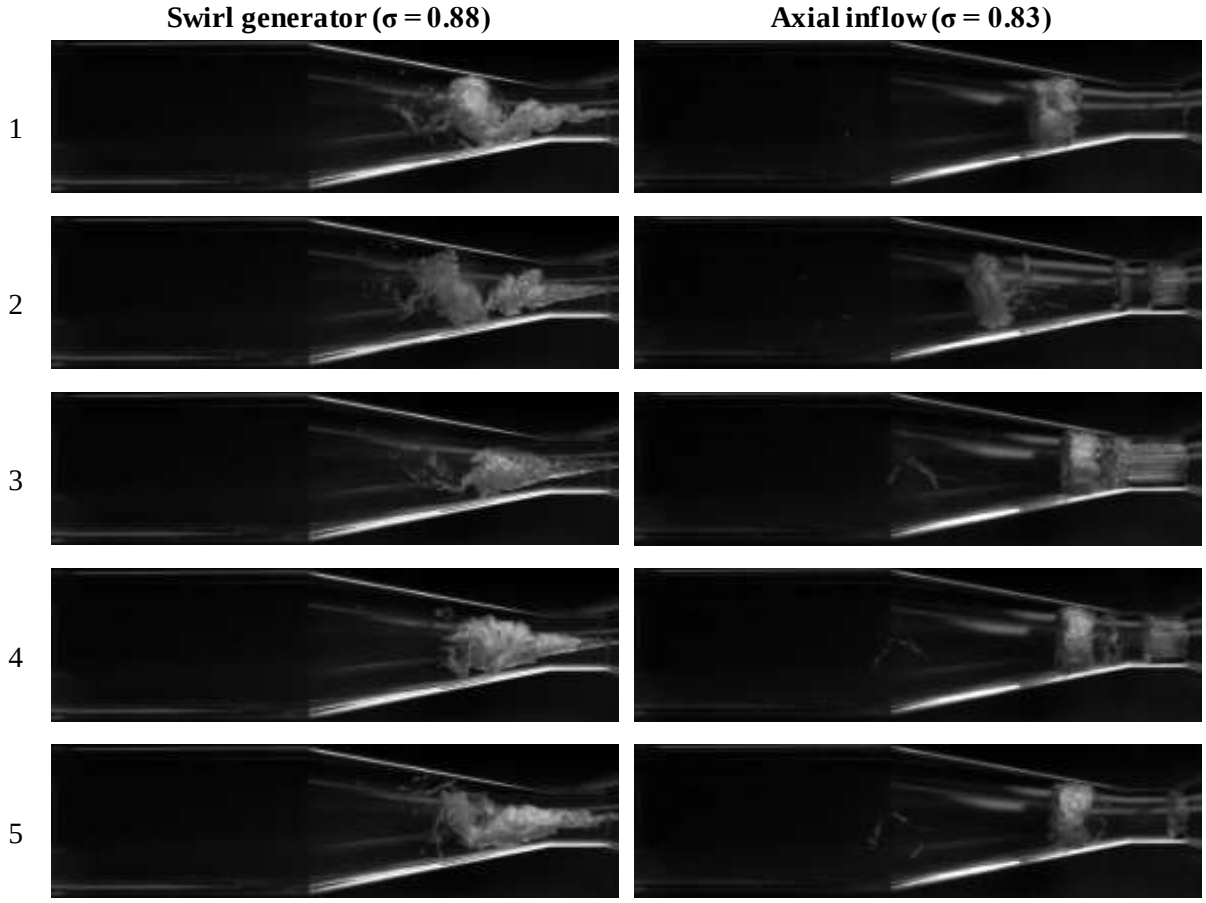

Figure 29 Representative sets of images depicting cavitation cycles in case of 2nd region.

Cavitation induced by the swirl – left column of Figure 29

The initial part of the cavitation cycle depicted in the row 1 consisted of the resumption of stable conical vortex within the throat of the nozzle after the end of the previous cycle. The length of this structure was growing downstream the throat (row 2) up to the moment when the cavitating vortex reached its maximum length (row 3). The consequent occurrence of the growing region of backflow was observed. The occurrence of the backflow related to the gradual destabilization of the cavitating structure as it is depicted in the row 4. The process of the vortex collapse was relatively slow, until the throat of the nozzle was reached by the backflow region when sudden collapse of the frontal part of cavitating vortex occurred. It should be emphasized that the void of the cavitation was remaining relatively compact during the whole cycle, no significant separation of the cavitating structures was observed.

Cavitation in case of the axial inflow – right column of Figure 29

Several significant differences can be described comparing the cavitation cycle with the first region. Contrary to the initial stage of cavitation, there is no visible cavitation within the throat of the nozzle at the beginning of the cavitation cycle. Clearly visible previous cavitating vortex ring entrained by the flow within the diffuser was observed at the beginning of the new cycle (row 1). The cavitation occurred at the leading edge of the throat. Nevertheless, the creation of the smaller amount of cavitation close to the trailing edge of the throat was detected only with a short delay (row 2). The cavitating boundary layer rolled up to the form of the vortex ring within the diffuser (row 3). The cavitating boundary layer started to shorten upstream to the leading edge of the throat (the re-entrant jet was clearly visible), while the separated vortex ring was entrained downstream to the region of higher pressure (row 4). The cavitating boundary layer reached the leading edge and the cycle of the creation of the new vortex ring began (row 5). Seeing the rows 3, 4 and 5 the remainder of the previous vortex ring can be found downstream the diffuser prior its complete decay.

2.3.3. Region 3 – Fully developed cavitation II

The cavitating vortex induced by the swirl generator was extended into the straight part of the Venturi nozzle (see Figure 30, left). The observed structures became more stable compared to the region 2. Nevertheless, it was still possible to clearly detect the creation and slow progression of the backflow region within the core of the vortex. Subsequent partial collapse of the vortex was limited mainly to the frontal part of the cavitating structure, while the cavitation farther away from the throat remained stable. The helical vortex breakdown occurred during the cycle. Fluctuations of the cavitation vortex length were detected; whereas the cavitating structure remains relatively compact (no significant structures were separated and entrained by the flow downstream the vortex during the cycle). When the cavitation number decreased (closer to the 4th region), the cavitating vortex was reaching and exceeding the length of the transparent section of the experimental rig.

The cavitating vortex rings transformed to the large cavitating clouds in case of the axial inflow (see Figure 30, right). While the presence of secondary vortex ring was identified in case of 2nd region, considerable amount of the small cavitating vortices were surrounding the inner core of the flow behind the vortex rings in the third region. The cycle was finished by the collapse of the cavitating boundary layer within the throat of the nozzle, while the separated cavitation cloud was entrained by the flow downstream the transparent section of the test rig.

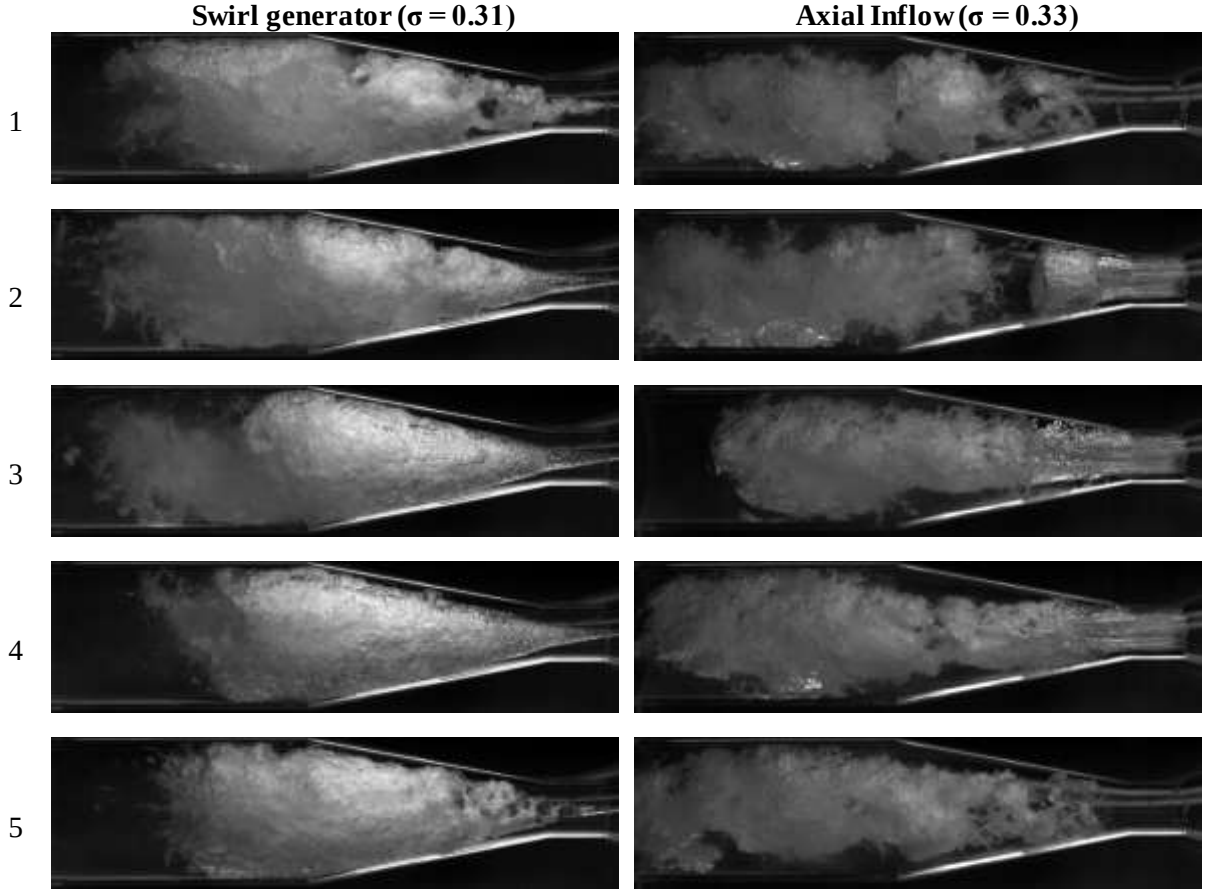

Figure 30 Representative sets of images depicting cycles cavitation in case of 3rd region.

Cavitation induced by the swirl – left column of Figure 30

While the captured amount of the cavitation is significantly larger, the overall character of the cavitation cycle persists relatively similar to the third region. The cavitation cycle started with the recovery of the stable vortex structure within the throat of the nozzle. The presence of the cavitating vortex of the previous vortex cycle was still considerable as it is depicted in the 1st row. Length of the new vortex was growing downstream to the cloud of cavitation remaining from the previous cycle (row 2). The maximum length of the cavitating vortex of the selected operating point is depicted in the row 3. The

end of cavitating vortex nearly reached the end of the transparent section. The observed backflow region proceeded slowly towards to the throat, while the length of the cavitating structure within the straight pipe was shortening towards to the diffuser (row 4). The cavitation cycle was completed by the collapse of the of the cavitating vortex in the throat of the nozzle and partial separation of the cavitating structure within the diffuser (row 5).

Cavitation in case of the axial inflow – right column of Figure 30

As it is clearly depicted in the row 1, the new cycle of cavitation began at the edges of the throat, where no cavitation was detected after the end of the previous cycle. On the other hand, the massive cavitating cloud was present downstream the throat at the same time. The formation of the cavitating vortex ring is depicted in the row 2. This ring collapsed relatively fast in the form of cavitating cloud (row 3). At the certain moment, the massive cavitation cloud detached (row 4). It was subsequently entrained downstream while the cavitating boundary layer started to collapse. The cavitation collapsed totally within the throat of the nozzle at the end of the cycle (row 5).

2.3.4. Region 4 – Transition to the supercavitation

The length of the cavitating structures exceeded the length of the transparent section in case of the transition regime considering the presence of the swirl generator as it can be seen in the left column of Figure 31. The void of the cavitation was considerably more stable compared to the previous regimes. On the other hand, it was still possible to observe creation of the backflow region and occasional collapses of the frontal part of the cavitating vortex (helical vortex breakdown).

In case of the axial inflow, the small instabilities described in the 3rd region became more significant (see Figure 31, right column). These small cavitating vortices were gradually merging together up to the state, when the liquid jet surrounded by the vapor was created. This flow pattern, typical for the supercavitation, was alternating with the presence of massive cavitation clouds. It should be noted that the lower cavitation number was, the more dominant and stable was the presence of the liquid jet.

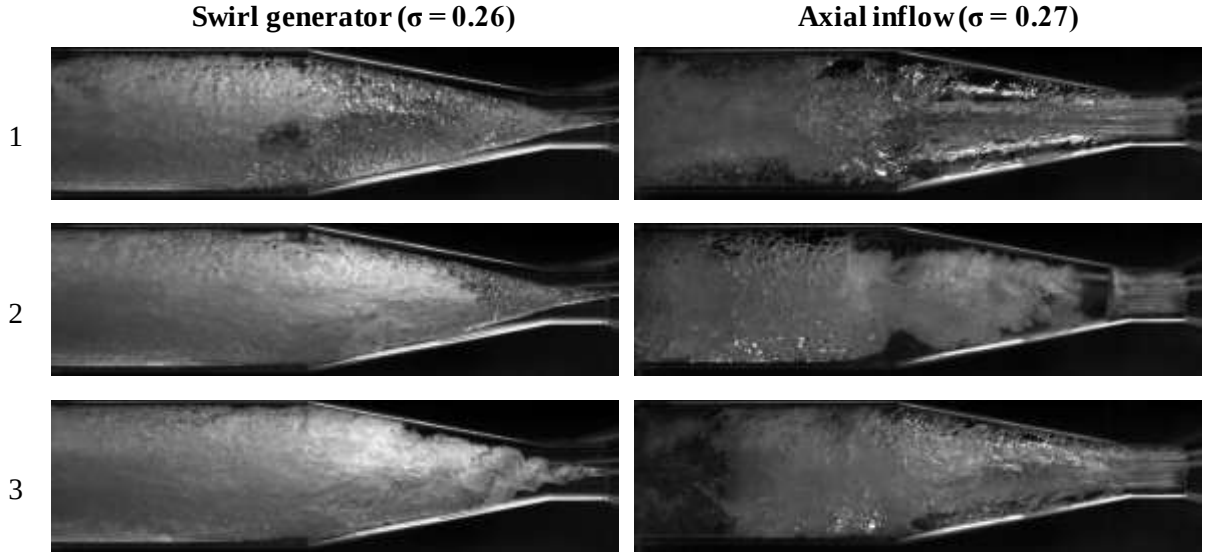

Figure 31 Representative sets of images depicting cycles cavitation in case of 4th region.

Cavitation induced by the swirl –left column of Figure 31

Cavitating vortex exceeds the whole length of the transparent section. Seeing the colour of the structure in the first row, it can be assumed that the coherence of the cavitation is higher compared to the previous regime, but still not as coherent as in case of supercavitation (as it will be shown in the Figure 32 depicting supercavitation regime). The relatively stable vortex was disturbed by the presence of the backflow region (row 2). It was possible to observe occasional partial collapse of the front part of the cavitating vortex, when the backflow reached the throat of the nozzle (row 3).

Cavitation in case of the axial inflow – right column of Figure 31
The first row is also depicting the state, when the flow pattern almost corresponded to the supercavitation regime in case of the axial inflow. The coherent jet is clearly depicted within the throat and diffuser of the Venturi nozzle. The jet was partially decaying within the straight part of the test section. The collapse of the jet is depicted in the row 2. When the jet collapsed the cavitating boundary layer started to move upstream to the trailing edge of the nozzle. After this collapse the cavitation cloud similar to the region 4 occurred (row 3).

2.3.5. Region 5 - Supercavitation

The flow became stable in both investigated configurations after the complete transition to the supercavitation regime (see Figure 32). The pressure pulsations as well as vibrations were minimal compared to the other regimes. It should be noted that the supercavitation affected by the induced swirl was less noisy compared to the configuration considering axial inflow.

The cavitating vortex became highly coherent while it was surrounded by the liquid flow attached to the walls of the Venturi nozzle in case of swirl generator presence. Separation of the cavitating boundary layer downstream the throat of the nozzle was observed during this regime. This separation was the more significant, the higher was investigated discharge.

As it was mentioned in the description of the transition regime, the supercavitation considering the axial inflow is typical by the presence of the stable liquid jet surrounded by the water vapor. Nevertheless, due to the design of the experimental rig, the liquid water with the free surface occurred within the lower part of the pipe downstream the diffuser of the nozzle which is clearly depicted in the bottom right corner of the Figure 32. Also, the walls of the diffuser were covered by the thin film of the liquid layer.

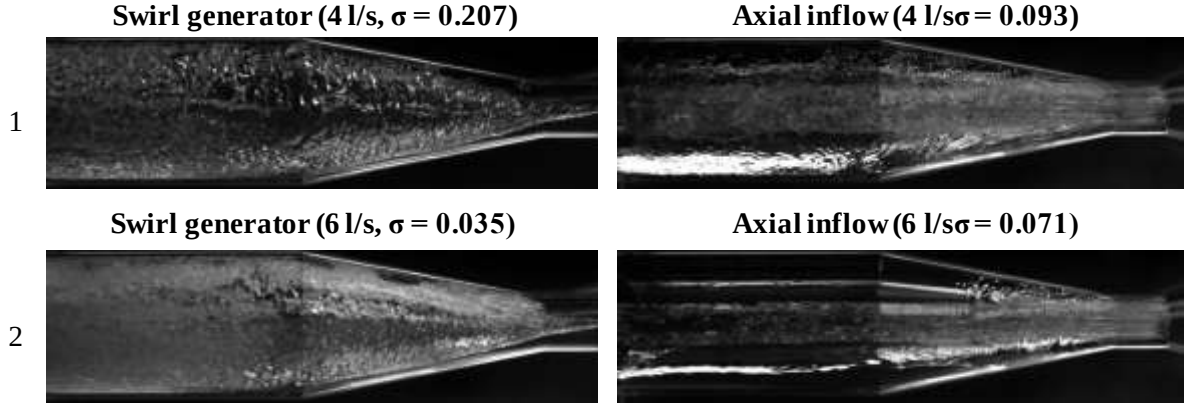

Figure 32 Representative sets of images depicting cycles cavitation in case of 5th region.

Cavitation induced by the swirl – left column of Figure 32
The cavitating structures are quasi-stable during the supercavitation. Thus, it is not possible to speak about the cavitation cycle. In case of the of the swirl generator presence the comparison of the 4 l/s (row 1) and 6 l/s (row 2) is depicted. While the shape of the cavitating vortex is similar, several differences can be described. First of all, the cavitation number is slightly higher in case of the 4 l/s discharge. Nevertheless, the cavitating vortex seems to be more coherent regardless higher cavitation number. The cavitating boundary layer in the diffuser is captured in case of the higher flow rate. This phenomenon can play a role in disruption of the interphase region and subsequent higher amount of reflected light in case of this operating point.

Cavitation in case of the axial inflow – right column of Figure 32
The comparison of the same discharges as in the case of the swirl generator presence is shown in the right column of the Figure 32. Coherent jet surrounded by the saturated vapor is clearly depicted in both cases. The more significant presence of the liquid film covering the wall of the nozzle in case of 4 l/s (row 1) was probably caused by the higher value of the cavitation number compared to the 6 l/s (row 2).

The free surface of the liquid water at the bottom of the nozzle was clearly captured. This is particularly distinguishable in case of 6 l/s thanks the reflection of light on the water surface (row 2).

2.4. Time-averaged analysis of the records

While description of characteristic cavitation cycles was provided in the previous section and the analysis of cavitation dynamics will be provided in the last part of this chapter, considerable amount of interesting results can be found and discussed using the time-averaged images.

Several limitations of the image analysis should be described to avoid misleading conclusions. First, the analysis will be done by the investigation of the pixel intensity values of the time-averaged images. The intensity of the pixel is given by the reflection of the light incidents on the interface between the phases. Thus, it can be assumed that the pixel intensity does not refer to the amount of the gaseous phase within the liquid flow directly, but it is highly affected by the nature of the investigated operating regime. This can be explained by the comparison of two images depicting fully developed cavitation and supercavitation affected by the swirl (Figure 33). It can be legitimately assumed, that the amount of the cavitation within the diffuser is higher in case of supercavitation regime (see Figure 33, right). Nevertheless, it is obvious that the image depicting the fully developed cavitation is significantly brighter than the image of supercavitation (see Figure 33, left).

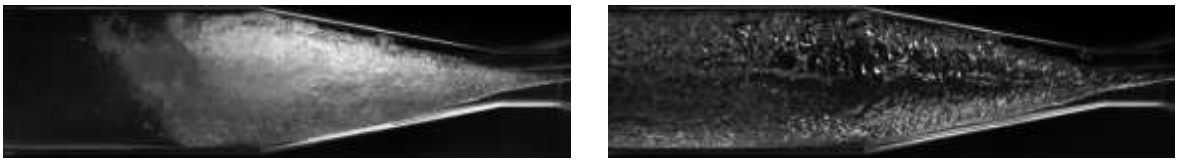

Figure 33 Direct comparison of the image brightness based on the cavitation regime in case of the SG presence. Fully developed cavitation (left), supercavitation (right)

This is caused by the highly coherent nature of supercavitation regime, where the main source of the light reflection is represented by the interface between cavitating vortex core and liquid flow surrounding the gaseous core. In contrast, the cavitating flow is considerably more "bubbly" in case of the fully developed regime as it is depicted in left part of Figure 33. Thus, the reflecting surface of interface is considerably larger. Therefore, the image depicting fully developed cavitation is significantly brighter.

The second limitation which should be mentioned results from scene (cavitation section) lightning solution. First of all, it was not possible to fully avoid the light reflection on the inner walls of the Venturi tube. This was considered and the images were cropped to minimize the presence of these light reflections during the analysis. The second problem results from the different distribution of cavitation depending on experimental configuration. While the exploited lights were adjusted and positioned similarly during the two days of experimental campaign, it is clearly visible that the images of the cavitation affected by the induced swirl are considerably brighter compared to the images corresponding to the axial inflow. This is apparently obvious downstream the throat of the nozzle (see Figure 30).

These limitations should be taken into account before making any conclusions.

2.4.1. Statistical analysis of the pixel intensity

The pixel intensity was investigated using the cropped regions of interest in order to minimize presence of overexposed areas. The location of the selected region of interest (ROI) was slightly different based on the investigated experimental configuration. However, other properties of the selected regions were consistent. The whole length of the averaged image was investigated using the narrow rectangular area with the size of 1024 by 22 pixels. The selected regions of interests of the both of investigated configurations are depicted in the Figure 34.

Figure 34 Regions of interests (white rectangles) exploited for the investigation of the statistical properties of the recorded cavitating flows. SG – left, AX - right

The mean pixel intensity and standard deviation of the pixel intensity fluctuations based on the RMS image analysis have been investigated. Various properties of the different cavitation regimes can be discussed using these data. The cavitation presence over the investigated domain can be examined using the analysis of the pixel intensity. For this purpose, the pixel intensity was spatially averaged. Using the averaged pixel intensity along the full length of the investigated region, it is possible to discuss presence of the cavitation, length of the cavitating structure and compactness of the cavitating structures as it will be shown. It is also possible to discuss the amount of cavitation to a certain extent. In case of the cavitation amount investigation, the fact that the pixel intensity is influenced by the interface surface (e.g. character of cavitation) must be considered.

The regions of the most severe fluctuations of cavitation presence can be identified using the analysis of the pixel intensity standard deviation (RMS images). For illustration, the process of the analysis will be described step by step. As it has been mentioned, only the selected region of interest was analysed. Thus, the time-averaged image and RMS image were obtained (Figure 35 - top) and this data were averaged across y-axis direction (Figure 35 - bottom).

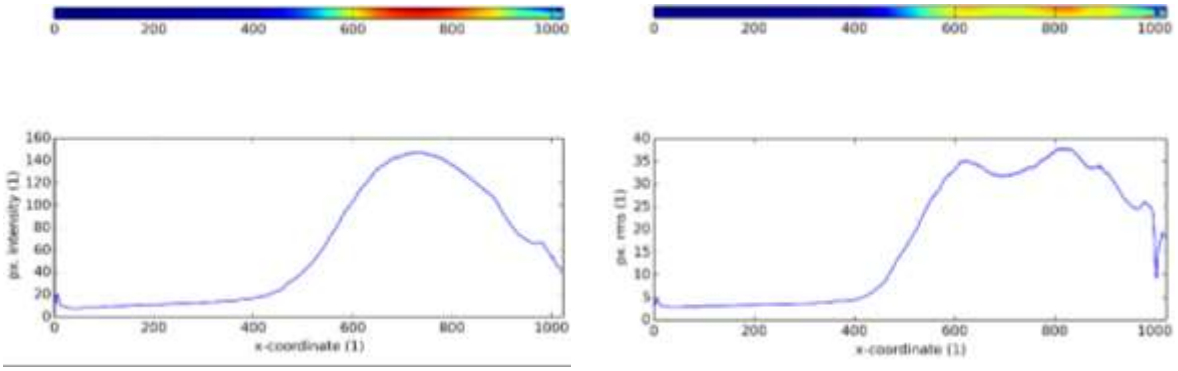

Figure 35 Example of the time averaged intensity (upper left) and standard deviation of the pixel intensity (right right) of the region of interest with corresponding charts depicting spatially (along y-axis) averaged values of these quantities (bottom)

This process was applied on the whole spectrum of investigated regimes, which is depicted in the Figure 36. The drop of the pixel intensity value in case of the supercavitation is caused by the transition between the diffuser and the straight pipe of the transparent section. This drop is observable, but far more marginal, in most of the depicted pixel intensity curves (see Figure 36, left, x -coordinate close to 400). The similar behaviour of the pixel intensity is also observable close to the beginning of the throat of the nozzle where sudden change of the pixel intensity RMS can be also found (e.g. x-coordinate value of 978). This drop is caused by the presence of pitting caused by cavitation erosion. Surface imperfections were nearly opaque, thus the pixel intensity in this area was significantly steadier.

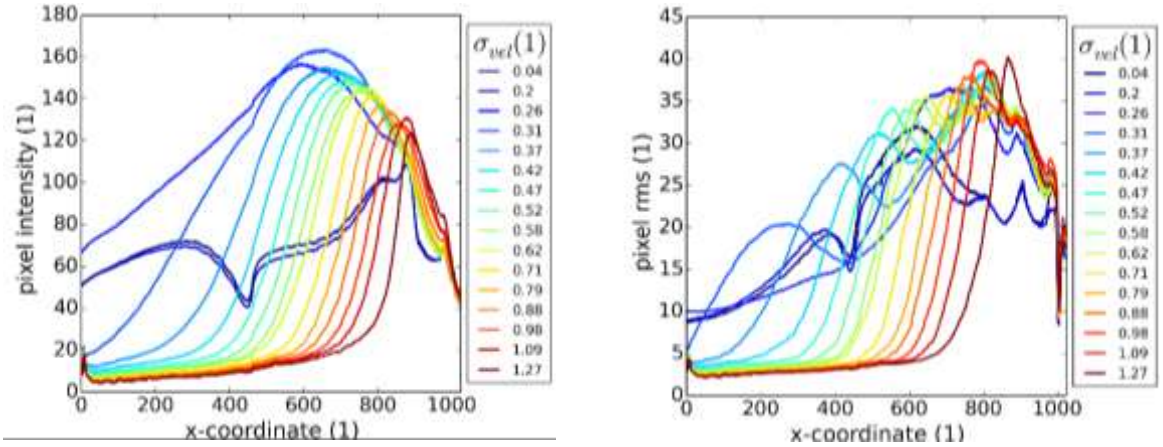

Figure 36 Profiles of the time-averaged values of the pixel intensity (left) and standard deviation of the pixel intensity (right) - 6 l/s, SG presence

Using the obtained values of the pixel intensity and pixel intensity RMS (standard deviation), it was possible to create maps of these properties corresponding the individual investigated flow-rates. The 3D representations of these results are depicted in the Figure 37.

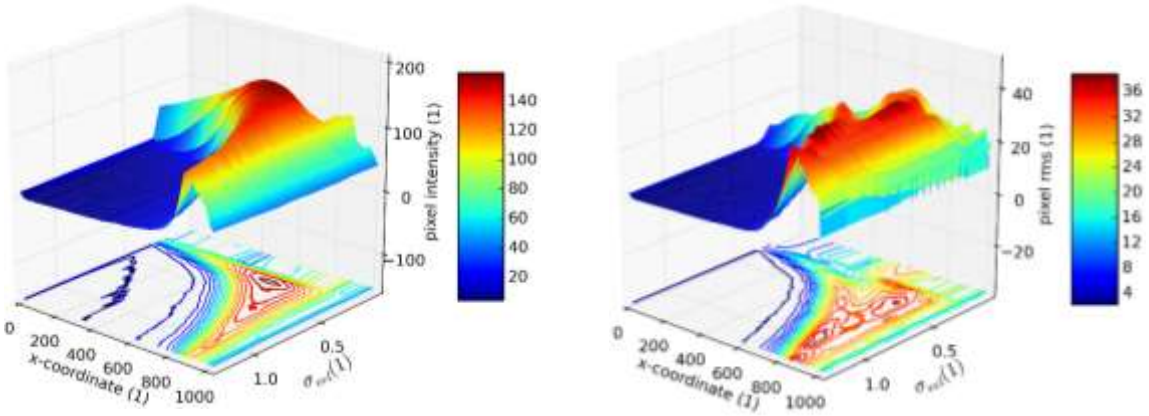

Figure 37 3D representation of averaged values of the pixel intensity (left) and standard deviation of the pixel intensity (right) - 6 l/s, SG presence

The 2D contour plots of these characteristics are more convenient for the discussion of the results. It should be emphasized that range of the investigated cavitation regimes (e.g. range of the cavitation numbers) varied based on the investigated flow rate and experimental configuration due to the operational restrictions of cavitation rig.

The 2D contours will be described in detail for both investigated configurations considering discharge of 6 l/s. Large dark blue area labelled as region A in Figure 38 (induced swirl) and 39 (axial inflow) corresponds to the region where no significant presence of cavitating structures was captured. In case of the flow affected by the presence of the induced swirl , the transition (see region B in Figure 38) between this region and the region of the significant cavitation presence (see region C in Figure 38) is relatively narrow. This is particularly significant by comparison with the Figure 39 depicting the results corresponding to the axial inflow. The transition (see region B in Figure 39) is gradual in case of the axial inflow. This fact corresponds to the observation that the cavitating flow affected by the induced swirl is considerably more compact, compared to axial inflow, where the separation and subsequent motion of the large cavitating structures were observed.

This is clearly captured in case of the transition between regions 1 and 2 in case of axial inflow. As it was described the cavitating boundary layer within the throat is very stable in case of the initial stage of the cavitation and its complete decay was occasional. Thus, the time-averaged value is relatively

high (see region 1 in Figure 39) compared to beginning region 2, which is typical by strong fluctuations of the cavitating boundary layer length within the throat of the nozzle. The sudden increase of the pixel intensity value corresponds to transition of cavitation pattern from the thin cavitating filament to the straight vortex consisting of the connected cavitating voids in case of the swirl generator (SG) presence. This transition was not captured in case of the 6 l/s discharge, but it is clearly depicted in case of the lower discharges (e.g. 4 and 5 l/s in the Figure 42).

The inception of the vortex rings separation connected with the fluctuations of the cavitating boundary layer in case of the axial inflow is also clearly depicted close to the σ_{vel} value of 0.8.

The different character of the cavitating flow depending on configuration of experiment is clearly visible comparing the pixel intensity within and upstream the throat of the nozzle. While the pixel intensity increases at the beginning of the region of interest (labelled as Th.) gradually, due to the presence of the cavitating vortex downstream the spike of the swirl generator (see Figure 38), the change of the pixel intensity is sudden in case of the axial inflow, where the inception of the cavitating boundary layer at the leading edge of the throat represents significant source of the pixel intensity increase (see Figure 39).

Maximum length (e.g. whole length of the transparent section) of the cavitation structure has been reached close to the σ_{vel} value of 0.26 (region 3) regardless the configuration of experiment and the investigated discharge. This corresponds to the fully developed cavitation right before the beginning of the transition to the supercavitation regime (region 4).

The supercavitation regime (region 5) is clearly distinguishable regardless the configuration. As it was described, the value of the pixel intensity is reduced due to the highly coherent nature of the cavitation structures. The relatively high value of the pixel intensity within the throat and in the diffuser downstream the throat of the nozzle is caused by the significant amount of the interface instabilities as well as due to the presence of the imperfections of the liquid film covering the walls of the nozzle in case of the axial inflow.

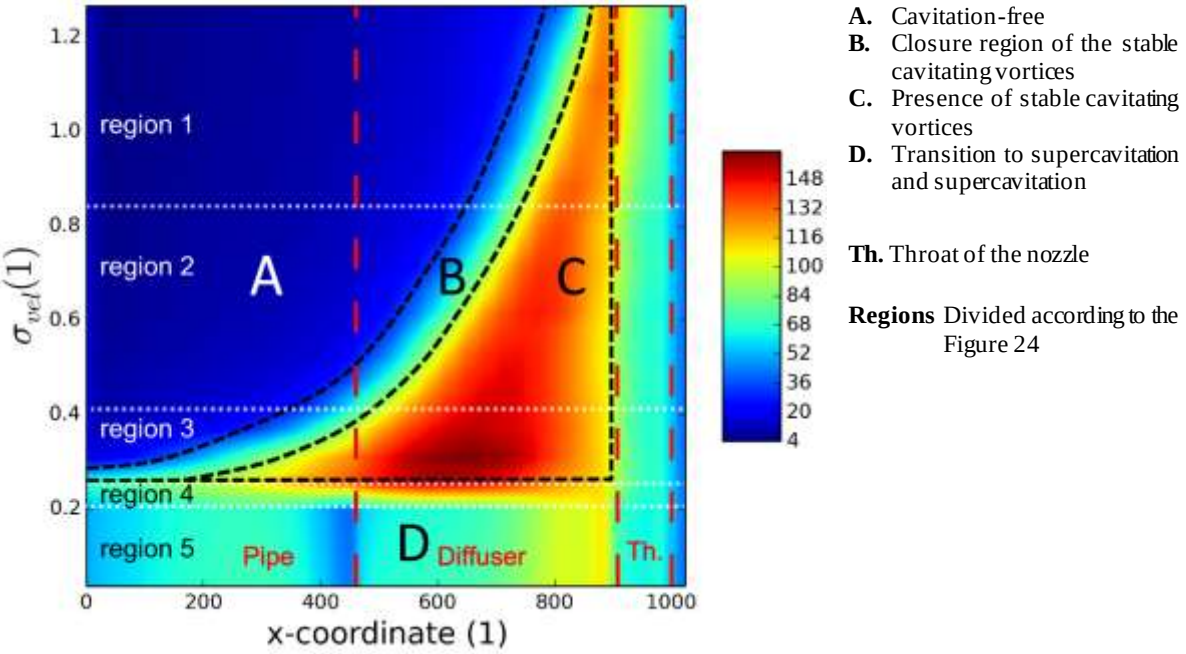

Figure 38 Map of the time-averaged pixel intensity considering 6 l/s flow-rate and presence of swirl generator (SG)

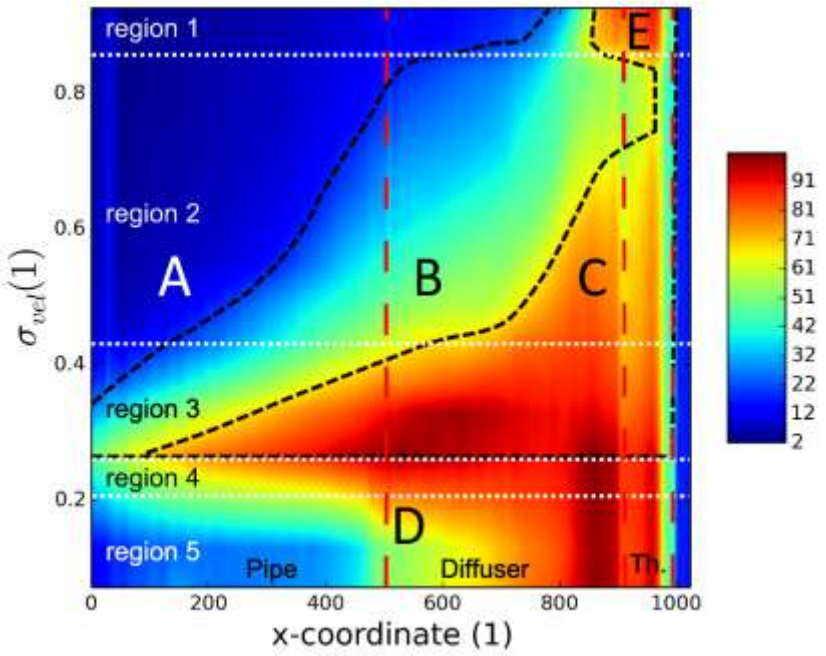

A. Cavitation-free
B. Fluctuations of the large cavitating structures
C. Presence of stable structures (prior the separation)
D. Transition to supercavitation and supercavitation
E. Presence of the quasi-stable cavitating boundary layer within the throat

Th. Throat of the nozzle

Regions Divided according to the Figure 24

Figure 39 Map of the time-averaged pixel intensity considering 6 l/s flow-rate and axial inflow (AX)

While the above discussed maps of the pixel intensity provide description of the cavitating structures presence, the regions of the most significant fluctuations of the cavitating structures can be described using the maps of the pixel intensity standard deviation (pixel RMS). First of all, the maximum values of the computed RMS are very similar regardless the experimental configuration, which is in contrast to the time-averaged pixel intensity values.

In case of the swirl generator presence (see Figure 40), it is possible to find two regions of the higher RMS values. The first one corresponds to the closure region of the cavitating vortex, where the short helical type of the vortex breakdown occurred from time to time. The second region corresponds to the partial collapses of the cavitating vortex within the diffuser of the nozzle.

The image of the pixel intensity RMS values considering the axial inflow (Figure 41), shows the large area of the significant values, which corresponds to the region of the vortex rings separation and the region of the large cavitation clouds presence. The supercavitation regimes show significant rms value drop, which corresponds to the high stability of this regime.

In case of the swirl generator presence and discharges of 4 and 5 l/s it is possible to find regions of the higher RMS values close to the σ_{vel} 1.5, which corresponds to observation of the long axisymmetric cavitating vortex (see Figure 42).

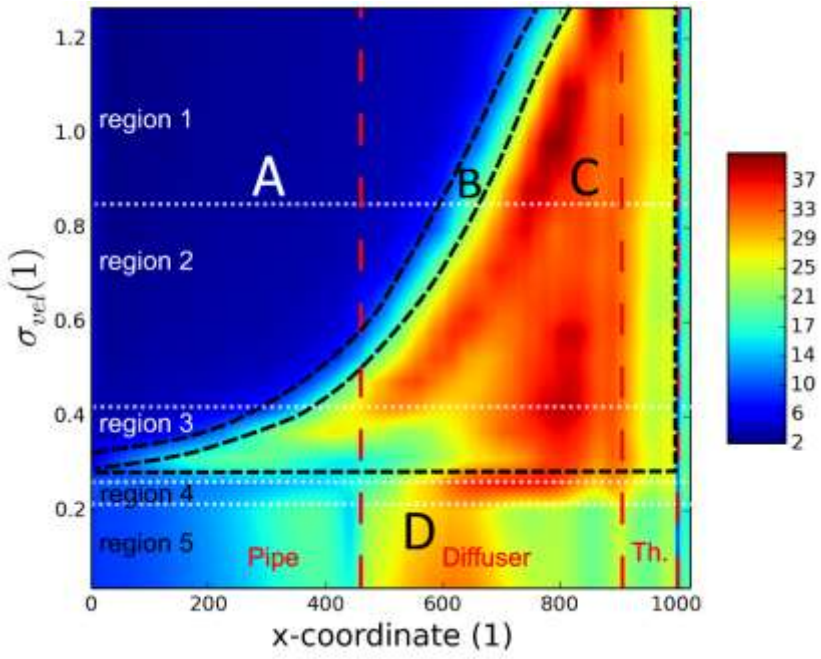

A. Cavitation-free
B. Closure region of the stable cavitating vortices
C. Presence of stable cavitating vortices
D. Transition to supercavitation and supercavitation

Th. Throat of the nozzle

Regions Divided according to the Figure 24

Figure 40 Map of the standard deviation of pixel intensity fluctuations considering 6 l/s flow-rate, swirl generator (SG)

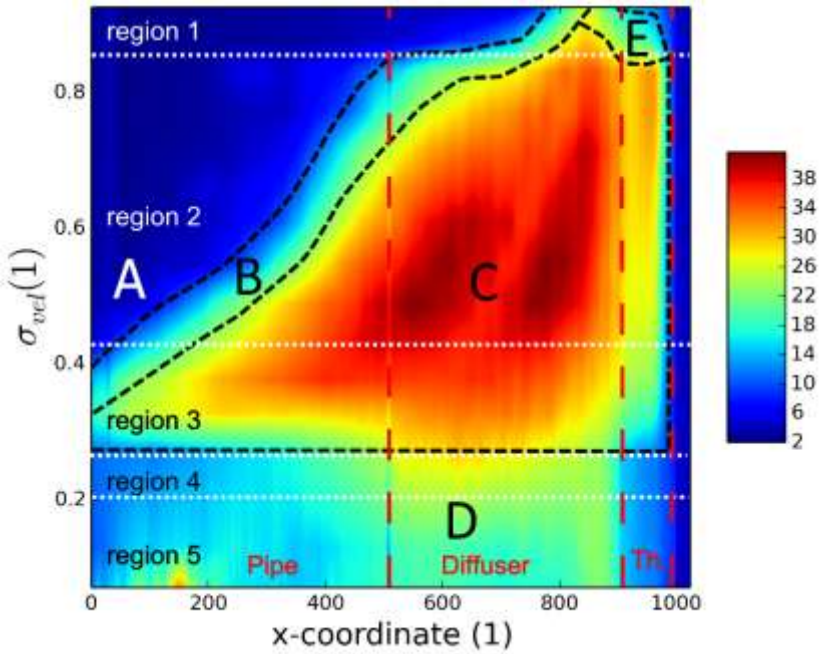

A. Cavitation-free
B. Fluctuations of the large cavitating structures
C. Presence of stable structures (prior the separation)
D. Transition to supercavitation and supercavitation
E. Presence of the quasi-stable cavitating boundary layer within the throat

Th. Throat of the nozzle

Regions Divided according to the Figure 24

Figure 41 Map of the standard deviation of pixel intensity fluctuations considering 6 l/s flow-rate and axial inflow (AX)

The results obtained by the analysis of the various flow-rates show similar results compared to the flow-rate of 6 l/s as it is depicted in the Figure 42 in case of the time-averaged values of pixel intensity and in the Figure 43 showing the maps of standard deviation of the pixel intensity fluctuations.

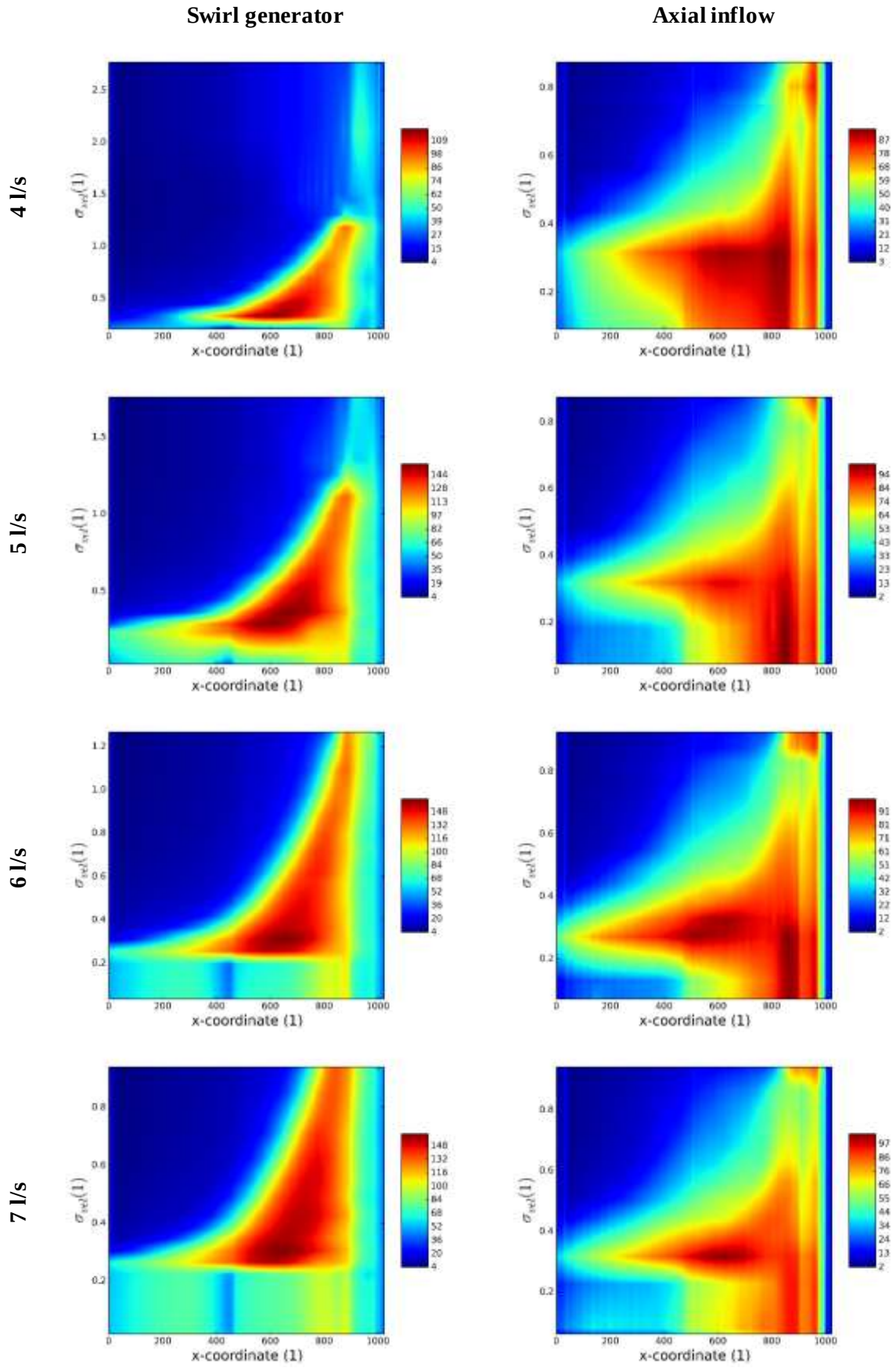

Figure 42 Time-averaged values of the pixel intensity over the whole region of interest corresponding to the various investigated flow-rates

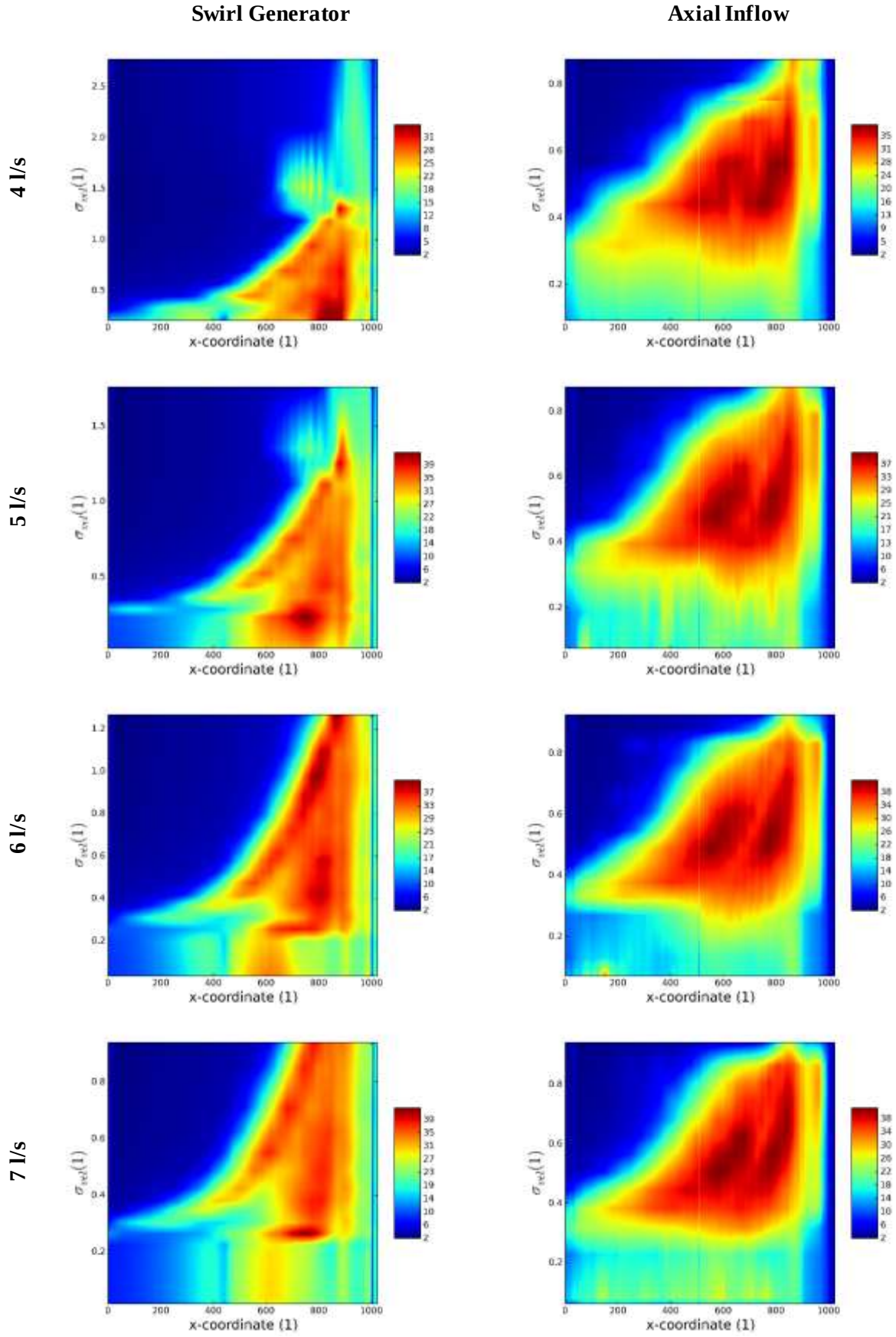

Figure 43 Values of pixel intensity standard deviation over the whole region of interest corresponding to the various investigated flow-rates

3. Analysis of the cavitating structures dynamics using the highs-speed video records

Dynamics of the observed cavitating structures was investigated using the two methods of the high-speed video records (HS) analysis: spectral analysis of the pixel intensity fluctuations and proper orthogonal decomposition (POD) of the selected region of interests (ROI).

The spectral analysis of the pixel intensity is relatively fast and well-established method. Nevertheless, it can be relatively difficult to obtain robust results in case of small values of cavitation number (e.g. close to the transition from the fully developed cavitation to the supercavitation). On the other hand, the POD represents considerably more complex method, which can provide robust results dominant frequencies of the captured cavitating structures analysis. Furthermore, the POD provides rich source information about the nature of the investigated phenomenon.

Therefore, the spectral analysis of the selected flow rates will be exploited as reference method to verify the results of the POD analysis. It should be mentioned that the analysis was done using the in-house developed software written in Python. These tools were exploited for the study of cavitation shedding over the hydrofoil as well as for the investigation of the various regimes of cavitation within the Venturi tube as it will be described.

3.1. Spectral analysis of the pixel intensity fluctuations

The spectral analysis of the pixel intensity fluctuations will be done only for the selected discharge of 6 l/s, in order to provide data for the POD analysis validation. These results were published by author in [54], where the main scope of the contribution was to describe the influence of the generated vortex on the cavitation dynamics within the Venturi tube using the analysis of the H-S records and its correlation with the experimental data including the analysis of the pipe wall acceleration and pressure pulsations.

The source of the data for the spectral analysis is represented by the fluctuations of the pixel intensity (brightness) which vary from 0 to 255 in case of grayscale HS video. The presence of interface between liquid and gaseous phase leads to a reflection of the light and consequently increases captured brightness of the region affected by the cavitation. The previous results of the HS video analysis correlations with pressure fluctuations, which lead to the utilization of this method during the investigation can be found in [27] and [53], where cavitation over NACA 2412 profile was investigated or in [51] where analysis of wide range of operating regimes within the Venturi nozzle considering axial inflow was carried out. It should be emphasized that results of the HS records analysis were in good agreement with the pressure pulsations analysis in these examples. In case of the pipe-wall acceleration analysis, the agreement of the frequencies was partial. As it will be mentioned in this chapter, it was possible to distinguish the peaks corresponding to the dominant frequencies of the pixel intensity fluctuations within the frequency spectra of the pipe wall acceleration. On the other hand, these peaks or rather frequencies of the pipe wall acceleration, were not dominant by no means.

The proper choice of the source pixel does not pose a problem in case of the initial stages of cavitation (e.g. higher values of the cavitation number). On the other hand, it became problematic with the fully developed stage of cavitation regime and its transition to the supercavitation. These regimes are characterized by the significant amount of small and highly stochastic instabilities within the cavitating flow, as well as with the significant amount of the gaseous phase. This complicate proper illumination of the region of interest. It is usually not possible to fully suppress occurrence of the over- and underexposed regions during recording of the cavitation. The improper choice of the pixel intensity can represent source of the corrupted or even misleading results.

Manual choice of the proper source pixel can be time consuming process and, moreover, it can be biased by of human factor. Thus, the semi-automated method of the source pixel choice has been exploited. The method was proposed based on the cooperation with Matouš Zaremba et al [55] who utilized the similar method for the analysis of spraying processes. In contrast to Zaremba, the source pixel is selected automatically based on the analysis of the whole length of captured record. As the

criterion for the source pixel choice, the value of the pixel intensity standard deviation (e.g RMS image) within the selected region of interest was exploited. Therefore, the entire record had been cropped prior the analysis. The cropping reduced the computational effort demanded by the process of the RMS image generation. Furthermore, it is possible to avoid the strongly overexposed or underexposed regions of records. It should be mentioned that the regions were set manually within the Python script using the dedicated function.

Since the whole spectrum of the cavitation regimes was investigated, the two different regions of interests were exploited as it is depicted in the Figure 44.

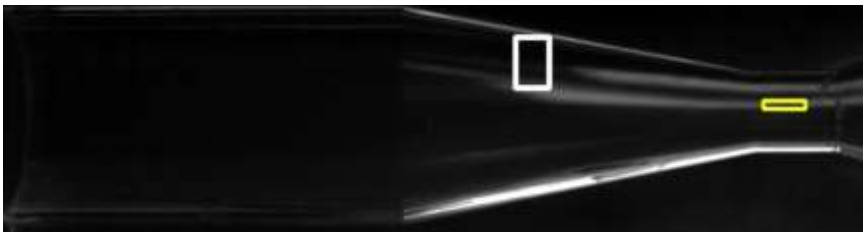

Figure 44 Regions of interest which were utilized for the spectral analysis of pixel intensity fluctuations. Yellow – ROI 1, White – ROI 2

The yellow and narrow region of interest (ROI 1, 50 by 10 px.) within the throat of the nozzle was exploited for the analysis of the higher values of cavitation number, where no significant presence of the coherent cavitation structures was observed downstream the throat of the nozzle. Larger white region (ROI 2, 40 by 160 px.) within the diffuser was exploited for the analysis in order to capture motion and decay of the larger cavitating structures observed during the fully developed regime of cavitation.

The final RMS images obtained by the analysis of the records are depicted in the following sets of images. Figure 45 is devoted to the ROI 1, while the results obtained using the ROI 2 are shown in the Figure 46. It should be noted that the actual values of the standard deviation were not important. Thus, only the structure of the RMS images without the color bars are depicted.

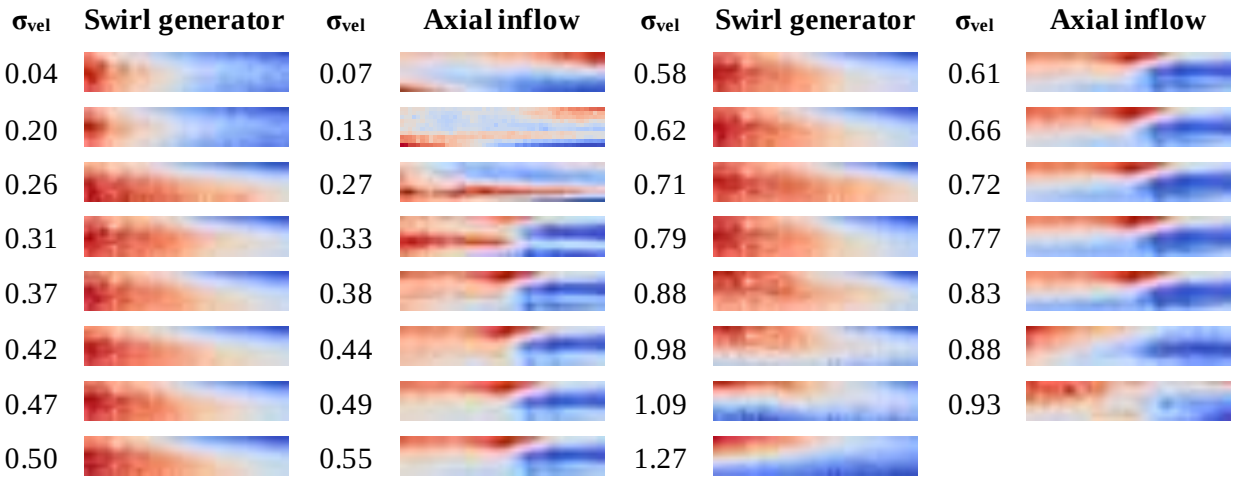

Figure 45 Standard deviations of the pixel intensities obtained using the ROI 1

;

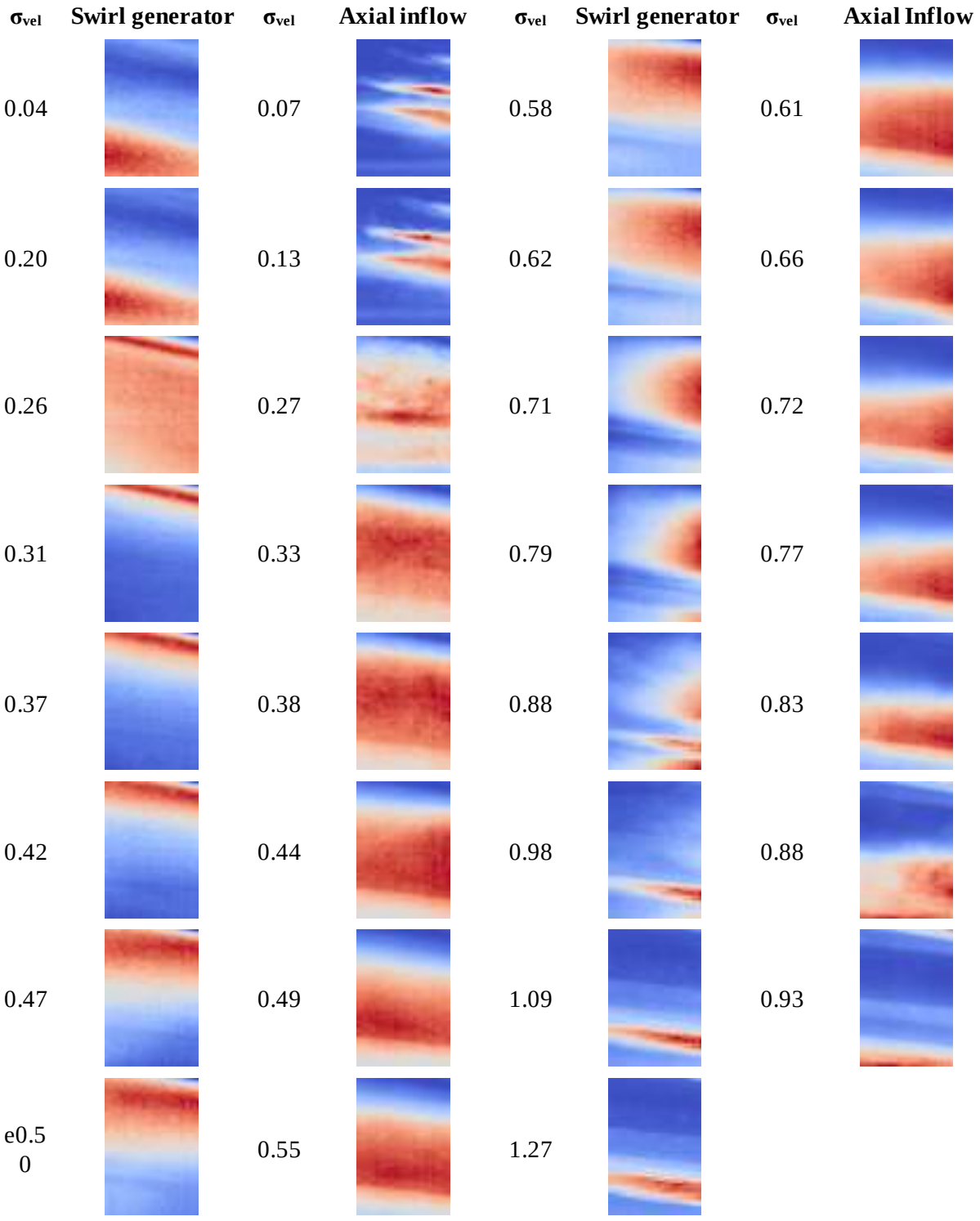

Figure 46 Standard deviations of the pixel intensities obtained using the ROI 2

The RMS images should be briefly described and discussed. The character (i.e. structure) of the RMS images remains relatively stable after the transition to the fully developed stage of cavitation (σ_{vel} 0.87) and prior the beginning of the transition to the supercavitation regime (σ_{vel} 0.22) in case of the ROI 1 placed in the throat of the nozzle regardless the investigated configuration (see Figure 45).
On the other hand, the significant changes of the RMS images obtained by the analysis of the ROI 2 can be found within the same range of the cavitation regimes, as it is clearly depicted in the Figure 46. The

transition regime of cavitation is nicely captured using the RMS images of the cavitation affected by the swirl (0.26) as well as in case of the axial inflow (0.27) considering ROI2. The character of these images is different compared to the previous and following investigated regimes (see Figure 46).

It should be also noted, that in case of the higher values of the cavitation number, where the presence of the cavitation within the ROI 2 was minor or it was not detected at all, the regions of light reflections became clearly visible in the RMS images. Nevertheless, since the strongly overexposed regions of the captured scene were not included into the investigated ROIs, the results were still acceptable in case that the cavitation structures reached the investigated ROI.

When the source pixel was selected within the ROI based on its intensity standard deviation value, it was possible to create signal for the following spectral analysis by collecting source pixel's intensities during the time of the record. It should be noted that there was no tight connection between the characteristic frequencies of the observed cavitation structures fluctuations and the frequencies induced due to the nature of the experimental measurement, such as blade pass frequencies of the exploited pump during the experimental analysis as it will be shown.

The fact that the investigated fluctuations of the cavitation structures are mostly self-induced, together with the considerable amount of the smaller instabilities of the interface between the liquid and gaseous phase lead to the noisy nature of the processed signals. This is particularly significant in case of the initial and supercavitation regimes of cavitation, when the main sources of the pixel intensity fluctuations are represented by the highly stochastic and small instabilities of the observed cavitating structures. Comparing the signals of the pixel intensity fluctuations depicted in the Figure 47 (ROI 2), several observations can be described prior the actual spectral analysis. Signal length of 0.05 s is exploited for the better visualization of the pixel intensity variation during the cavitation cycle. Whole length of signal records (0.5 s) was analysed as it will be shown.

Periodic fluctuations of the cavitating structures were captured for both experimental configurations, except the highest value of the cavitation number. In this particular case, the pixel intensity signal is nearly constant considering axial inflow (see Figure 47, σ_{vel} 0.93), while several drops of the intensity value can be found in case of the SG presence as it can be seen in the Figure 47 (SG, σ_{vel} 0.98). This fact was caused by the presence of the small cavitating vortices, which were entrained by the flow through the investigated region. Nevertheless, comparing the intensity signals with the corresponding RMS images depicting standard deviation of the pixel intensity fluctuations within the selected region of interest, it is obvious that the source pixel was located in the region of the light reflection on the wall of the nozzle, where no significant presence of cavitation had been detected. Therefore, the mean value of the signal is relatively high comparing the signals corresponding to the lower values of σ_{vel}.

Comparing the signals corresponding to more developed regimes of cavitation, it is obvious that the nature of the pixel intensity signal is highly influenced by the configuration of the experiment. While the main fluctuations of the cavitating structures are clearly distinguishable regardless the configuration, the frequency of the fluctuations is evidently higher in case of the SG presence. This is clearly visible by the comparison of the signals depicted in the second row of Figure 47. Above that, the relatively long periods of the intensity drops can be found in case of the axial inflow. This agrees with the observed cavitation patterns. While the cavitating structures are represented by the vortex rings in case of the axial inflow, the cavitation induced by the SG represented by the conical cavitating vortex is considerably more compact and stable. It can be also mentioned that the recovery of the cavitating structure after the collapse is significantly faster in case of the swirl generator presence by the comparison of the depicted signals.

The penultimate observation, which should be emphasized is the fact that the signal obtained by the analysis of the pixel intensity is significantly noisier in case of the swirl generator presence.

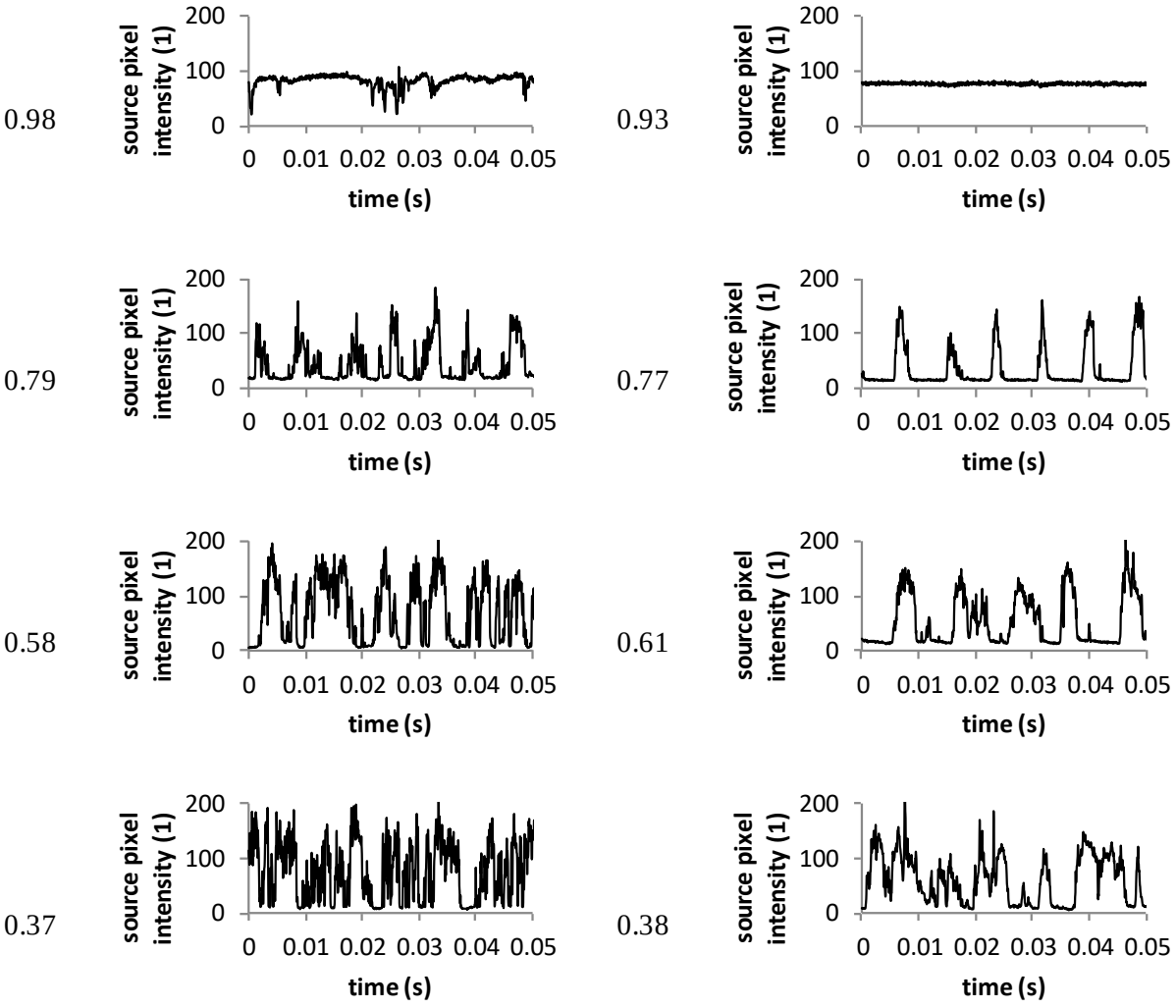

Figure 47 Signals of the pixel intensities obtained using the semi-automated choice of the source pixel using the ROI 2. Swirl generator – left, Axial inflow - right

The last observation based on the pixel intensities signals is the comparison of the pixel intensity values. As it was mentioned, the scene lightning was very similar during the days of the test campaign. Nevertheless, the brightness of the captured images differed considerably mainly due to the different nature of the cavitation based on the investigated configuration. Thus, the Figure 48 is depicting the mean values of the pixel intensities together with the ratio between mean and maximum values of the signal.

Based on the results corresponding to the initial stage of cavitation (e.g highest values of σ_{vel}), the abovementioned comparison of the intensity signals is confirmed. Mean values are significantly higher compared to the more developed stages of cavitating flow, the ratio between the mean and maximum pixel intensity of the investigated signals is considerably lower in case of the SG presence compared to the axial inflow. As it was mentioned, this ratio drop is caused by the occasional presence of the minor cavitating vortices entrained by the flow through the ROI 2. While the presence of the cavitation usually leads to the increase of the pixel intensity, in this case the intensity drop is caused by the shades on the vortices together with the presence of the light reflection from the nozzle wall. On the other hand, the high value of 0.93 of the ratio (e.g. close to the 1) corresponding to the σ_{vel} 0.93 of axial inflow analysis is caused by the absence of the cavitation within the ROI 2(see Figure 48).

Seeing the mean values of the investigated signals depicted in the Figure 48, it is clearly visible that the brightness of the records is generally higher in case of the swirl generator presence. Comparing these

values with the axial inflow, significant difference of the mean intensity behaviour can be described. The increase of the intensity value with the decreasing σ_{vel} is gradual in case of the axial inflow . In contrast, the sudden increase of the mean intensity value can be found between the σ_{vel} 0.79 and 0.58 considering the presence of the swirl generator. While the value remains nearly constant during the transition from the σ_{vel} of 0.79 to the 0.37. It is in good agreement with the described flow patterns during the cavitation cycles.

The cavitating vortex rings typical for the high values of σ_{vel} transform into massive cavitating clouds, with the significant axial pulsations in case of the axial inflow. The cavitating structures are considerably more stable in case of the SG presence. Therefore, when the selected ROI of the image has been reached by the cavitating structure, the presence of this structure within the ROI was remaining relatively constant during the cycle. The values of the mean pixel intensity are also influenced by the faster stabilization of the cavitating vortex after the collapse, in case of the SG presence.

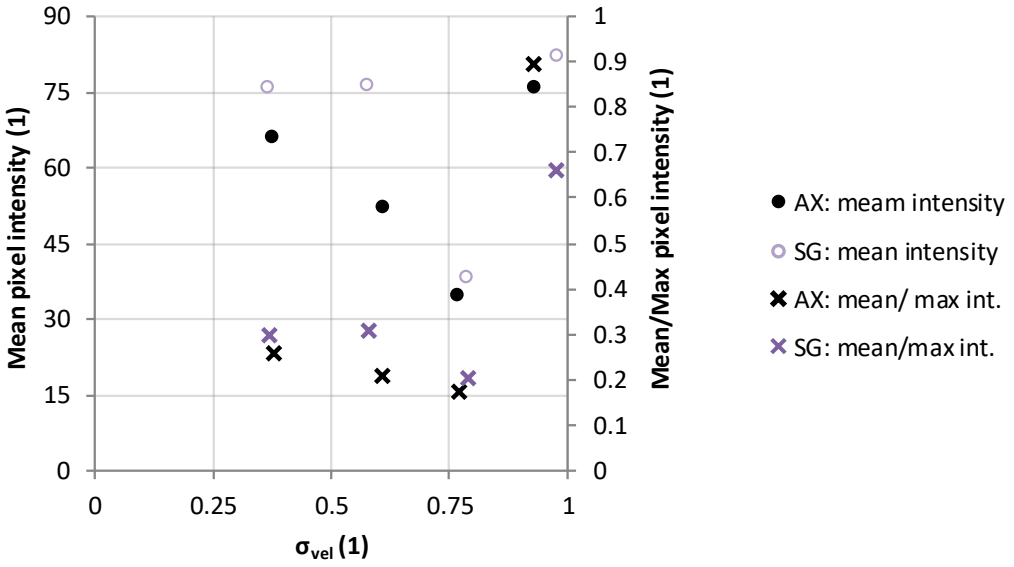

Figure 48 Mean values and ratios between the mean and maximum value of the pixel intensity of the signals

The obtained signals were analyzed using the DFT algorithm implemented as the numpy (Python library for the scientific computing) function *numpy.fft*. The obtained frequency spectra can be compared in the set of images provided in the Figure 49 and Figure 50. It should be noted that the depicted results correspond to the previously described signals obtained using the analysis of the selected operating points and considering the ROI 2. Nevertheless, all of the captured records were analyzed to obtain the frequencies of cavitation fluctuations corresponding to the wide range of the regimes. The results of the ROI 2 were compared and complemented by the results of the ROI 1, when it was necessary due to the nature of the captured cavitation patterns.

Prior the main investigation of the dominant frequencies, the influence of the exploited region of interest will be described using the frequency spectra corresponding to the initial stage of cavitation (see Figure 49). The analyses corresponding to the σ_{vel} of 0.98 in case of the SG presence and 0.93 in case of the axial inflow are showing the flickering of the led panels with the fundamental frequency of 3010 Hz and its second and third harmonics regardless the investigated ROI. It is also clearly depicted that the nature of the obtained frequency spectra differs significantly based on the experimental configuration and analyzed region. While in case of the ROI 2 (e.g. within the throat of the nozzle), the frequency spectrum obtained by the analysis considering axial inflow contains mainly the fluctuations of the light intensity, in case of the SG presence the significant noise up to the frequency of 2000 Hz can be found.

The results of the ROI 1 (e.g region of the throat of the nozzle) analysis are considerably different, whereas it is possible to state that the obtained frequency corresponds to the nature of the cavitating

patterns of the different experimental configuration. It is clearly visible that the noise contained within the signal corresponding to the axial inflow is considerably more significant compared to the analysis of the cavitation induced by the SG (see bottom row of the Figure 49). As it was mentioned, the cavitating boundary layer within the throat of the nozzle was relatively stable from the axial pulsation point of view in case of axial inflow. On the other hand, the interface between the gaseous and liquid phase was disturbed by the imperfections of the leading edge of the throat. These facts are in good agreement with the frequency spectrum obtained by the analysis of the ROI 1 considering axial inflow.

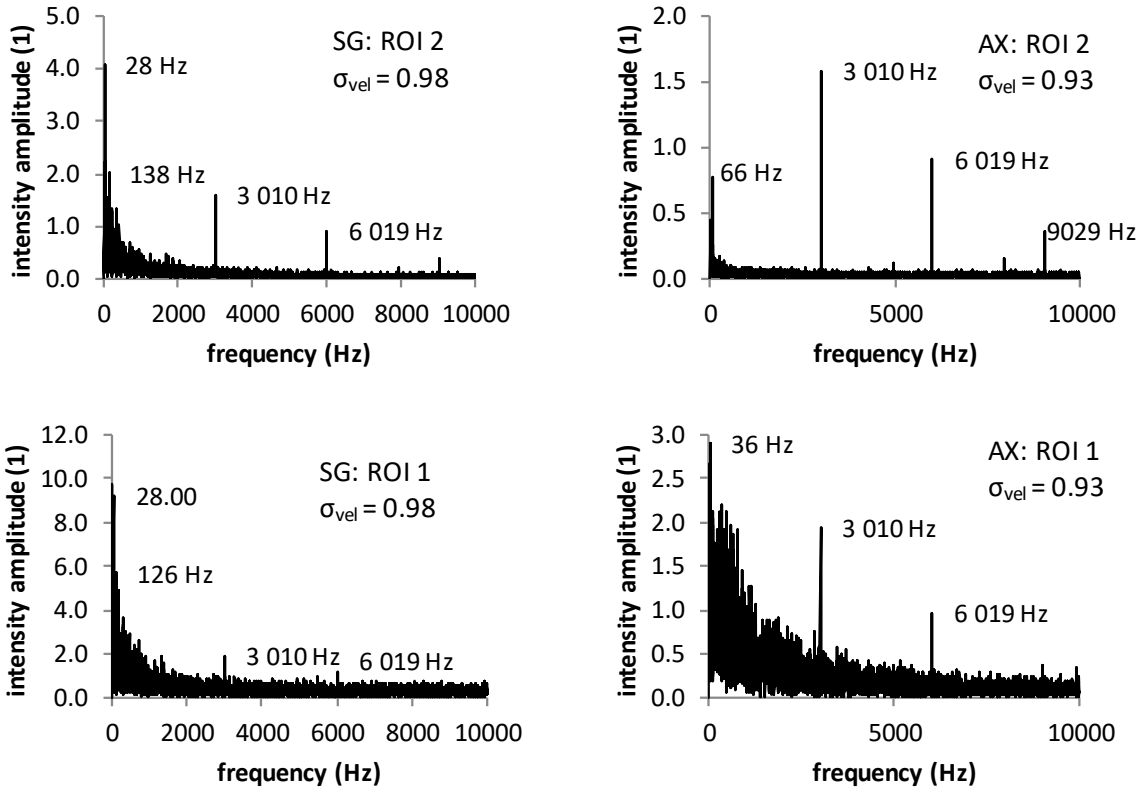

Figure 49 Influence of the selected region of interest on the results of the spectral analysis in case of the initial regime of cavitation

In contrast, the frequency spectra obtained by the analysis of the cavitating flow induced by the swirl is containing significantly smaller amount of the wideband noise. Again, it is in good agreement with the nature of cavitating vortex. The cavitating vortex has been relatively stable, with the occasional partial collapses. Thus, the instabilities of the interface region cannot represent as significant source of the stochastic pixel intensity fluctuations.

Together with the frequency of the led diodes flickering, it is possible to find relatively significant low frequencies. In case of the swirl generator it is possible to distinguish the frequency of 28 Hz in both of the investigated regions, this frequency roughly corresponds to the frequency of the observed separation of the small helical cavitating vortices from the end of the main conical vortex. At the same time, the frequency 28 Hz is close to the pump rotation frequency of 25.4 Hz. The higher frequencies slightly differ based on the investigated region of interest (138 and 126 Hz). Nevertheless, the source of these frequencies has not been identified yet. The blade passing frequency corresponding to this operating point was higher (152.4 Hz).

The frequencies of 36 Hz and 66 Hz were distinguishable in case of axial inflow. While the lower frequency was more dominant in case of the ROI 1, in case of the ROI 2 was the situation opposite and amplitude of the lower frequency was higher. These frequencies do not match with the rotating frequency of the pump. It can be assumed that the frequency of 36 Hz obtained by the analysis

considering ROI 1 corresponds to the occasional collapse of the cavitating boundary layer within the throat of the nozzle.

Since the cavitating structures became more coherent and more periodical with the decreasing value of the σ_{vel}, the dominant frequencies of the longitudinal oscillations of the observed structures are clearly visible in the frequency spectra in the Figure 50. The obtained results are depicted up to frequency of 500 Hz in order to clearly visualize the frequency range of the expected fluctuations of the cavitating structures.

Several observations can be stated based on these results. First, the dominant frequencies corresponding the experimental configuration considering SG are slightly higher compared to the axial inflow. This can be observed in the whole range of the examined operating points as it will be described at the end of this section. The dominant frequency was the higher, the lower was the cavitation number, regardless the experimental configuration.

On the other hand, amplitudes of the dominant fluctuations are considerably higher in case of the axial inflow. This result corresponds to the observed cavitation patterns, which were described at the beginning of this chapter. While the cavitation induced by the swirl generator was compact and stable, with partial collapses followed by the fast stabilization of the cavitating structure, the collapses were far more complete in case of the axial inflow. The frequency magnitude, which was the lower, the lower was cavitation number of the investigated operating point. The observed amplitudes increased only to a certain moment as it can be seen by comparison of second and third row of the Figure 50.

Due to the nature of the cavitating patterns influenced by the induced swirl, the signal corresponding to the SG presence contained higher amount of the noise as it was described. This is clearly depicted in the frequency spectra. Nevertheless, the dominant frequencies are still clearly distinguishable.

Amplitudes of the observed fluctuations of pixel intensity corresponding to the cavitating structures oscillations (15-50) are several times higher compared to the amplitudes corresponding to the LED diodes flickering (1.5-2, see Figure 49).

It should be also noted that the frequency spectra contain significant second and even the third harmonics of the fundamental frequency in case of the axial inflow.

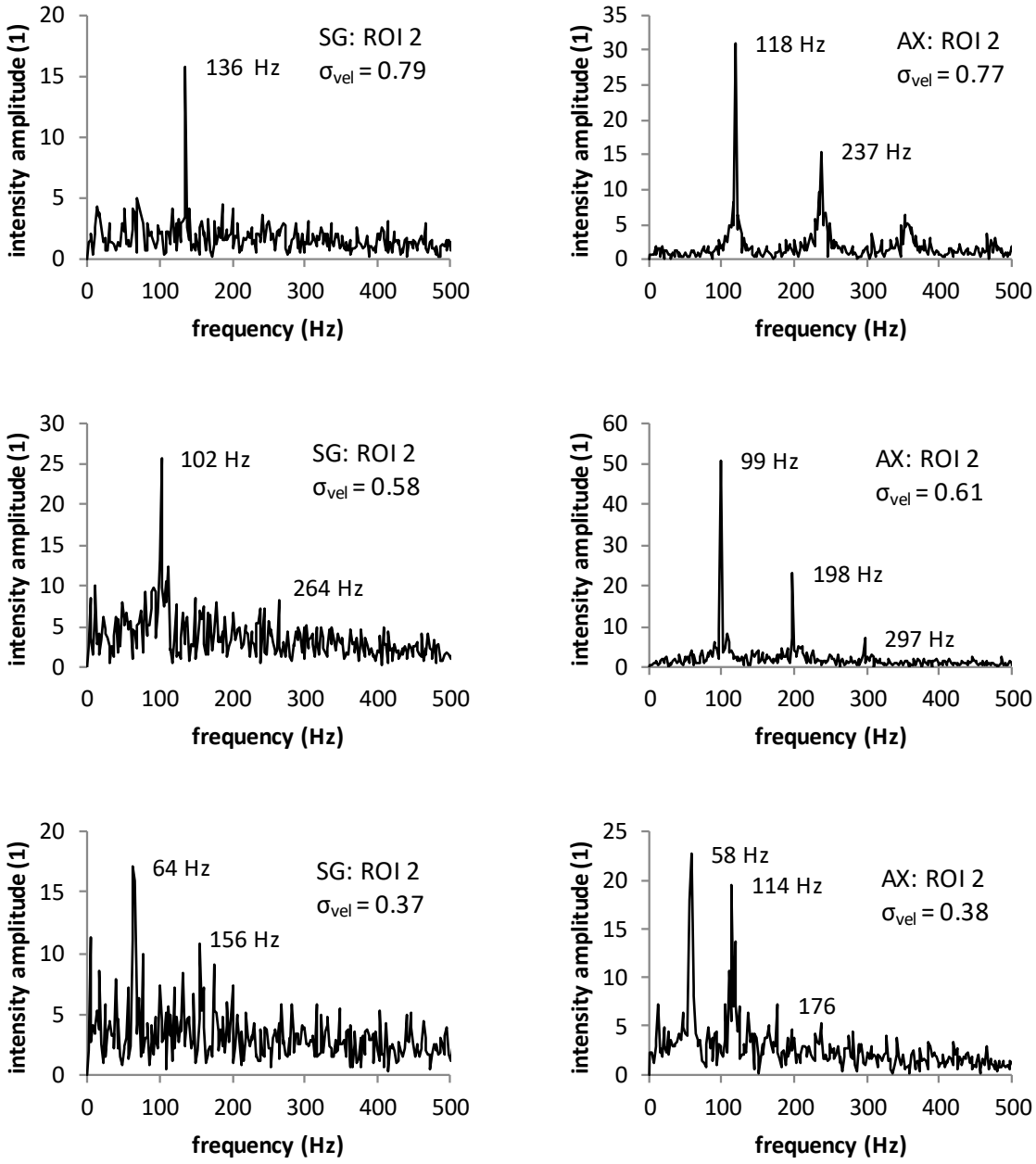

Figure 50 Results of the spectral analysis of the pixel intensity signals in case of fully developed cavitation

Using the obtained data, it was possible to create charts of the dominant frequencies and corresponding values of the mean pixel intensities.

The analyses of dominant frequencies corresponding to the different investigated operating points are compared with the result of the pressure fluctuations and pipe wall acceleration analyses to prove the reliability of this method (see Figure 51).

Provided results of the image analyses were obtained mainly using the ROI 2. However, in case of the SG presence, the dominant frequencies corresponding to the three operating points with the highest values of cavitation number were not dominant. Nonetheless, it was possible to find these frequencies within the spectra as the locally significant frequencies, which corresponded to the analysis of the pressure fluctuations. In case of the 4th operating point considering the SG presence (σ_{vel} 0.88) the depicted frequency corresponds to the ROI 1.

The results of the pixel intensity fluctuations are in good agreement with the analyses of the pressure fluctuations regardless the investigated configuration as it is clearly depicted in the Figure 51. It was also possible to find some of the characteristic pixel intensity frequencies within the frequency spectra of the pipe-wall acceleration as local peaks. Nevertheless, it must be emphasized that frequencies of pipe wall acceleration depicted in the charts were not the dominant ones by no means.

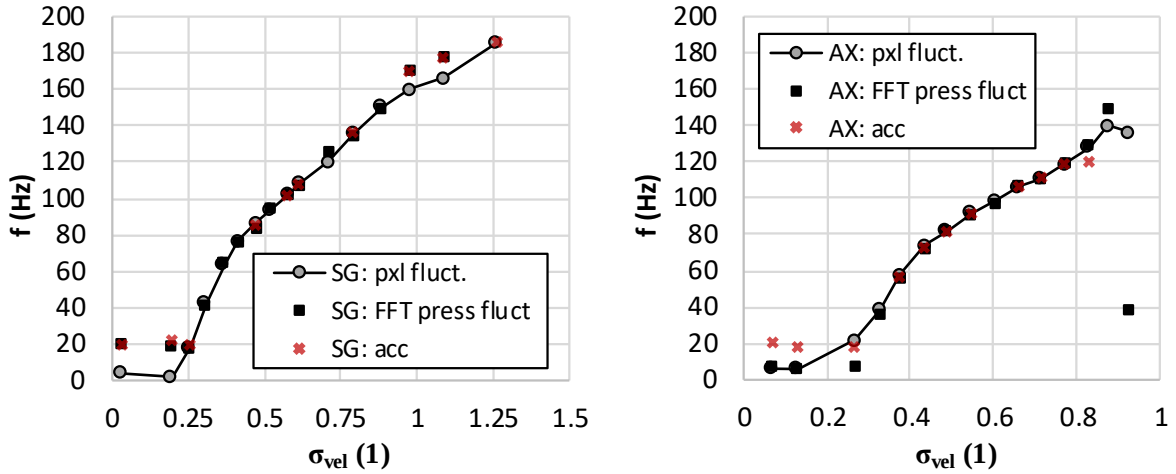

Figure 51 Frequencies obtained by the analysis of the pixel intensity fluctuations in comparison with results of the pipe-wall acceleration and pressure fluctuations analysis (ROI 2 - mainly)

Based on these comparisons, it is possible to state that the results of the pixel intensity analysis are reliable when the investigated ROI is selected properly. It was possible to obtain results corresponding to analysis of the pressure fluctuation records in wide range of the operating points using the semi-automated choice of the source pixel based on the maximum value of the pixel intensity standard deviation (RMS images). It was possible to extend the range of the pixel intensity analysis by the proper choice of ROI location, but at the certain moment the dominant frequencies of the pixel intensity fluctuations ceased to correspond to the pressure fluctuations analysis. On the other hand, it was still possible to find the characteristic frequencies of the pressure pulsations within the spectra of the pixel intensity fluctuations.

The comparison of characteristic frequencies of the both of the investigated experimental configurations is depicted in the Figure 52.

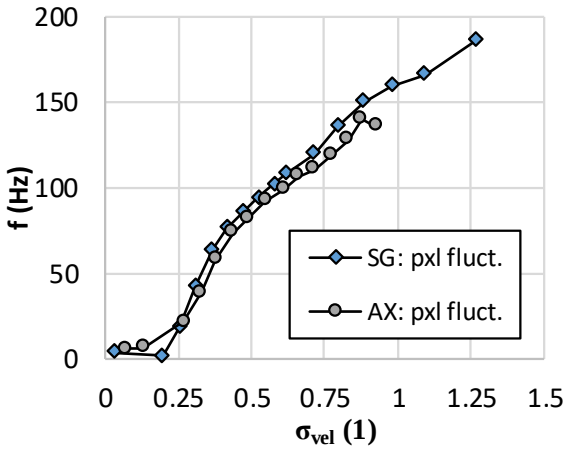

Figure 52 Results of the dominant frequencies – comparison of the investigated experimental configuration (ROI 2 - mainly)

Dominant frequencies corresponding to the experimental configuration considering presence of the swirl generator are slightly higher compared to the axial inflow in the whole range of the investigated

cavitation regimes. Seeing the results, is clearly visible that the decrease of the frequency with the decreasing value of the σ_{vel} is nearly piecewise linear regardless the investigated configuration.

Due to the fact, that the dominant frequency is decreasing with the increasing compliance of the medium (e.g. with the increasing amount of the gaseous part of the flow), it can be assumed that the increase of the cavitation (gaseous phase) presence becomes to be faster close to the σ_{vel} value of 0.44.

In order to amend results of the spectral analysis, the charts of the static components and amplitudes of the dominant frequencies are provided in the Figure 53.

Seeing the mean values of the pixel intensity signals (see left part of Figure 53), the sudden drop of the obtained values can be found close to the σ_{vel} value of 0.93. This was caused by the presence of the light reflection on the wall of the nozzle as it was described in the previous chapter. Further increase of the mean pixel intensity is gradual up to the σ_{vel} value of 0.44 in case of the axial inflow.

In the same range of the operating regimes, the increase of the mean pixel intensity was steeper when the additional swirl was introduced to the flow. The mean value increased gradually up to the σ_{vel} 0.47.

The courses of the mean pixel intensities with the further decreasing σ_{vel} are considerably different based on the experimental configuration. While in case of the SG presence the gradual decrease of the mean pixel intensity up to the transition to the supercavitation regime was observed, the sudden increase of the pixel intensity can be found in case of axial inflow and the operating point corresponding to the transition regime between fully developed and supercavitation regime of the cavitating flow. These observations correspond to the nature of the cavitation patterns described in the previous chapter.

Seeing the amplitudes of the observed dominant frequencies (right chart in the Figure 53), it is obvious that the maximum values of the pixel intensity fluctuations were considerably higher in case of the axial inflow. It might be also noted, that during the experimental measurement of the axial inflow, the cavitating regimes characteristic by the separation of the distinctive vortex rings prior the transition to the oscillations of the massive cavitating clouds were the noisiest from the subjective point of view. This agrees relatively well with the maximum amplitudes of the pixel intensity fluctuations in case of this experimental configuration.

Values of the characteristic pixel intensity amplitudes are significantly more stable in case of the SG presence compared to the axial inflow. It is in good agreement with the observed cavitating patterns which were far more uniform over the whole range of investigated cavitation regimes when the additional swirl was introduced to the flow by the swirl generator.

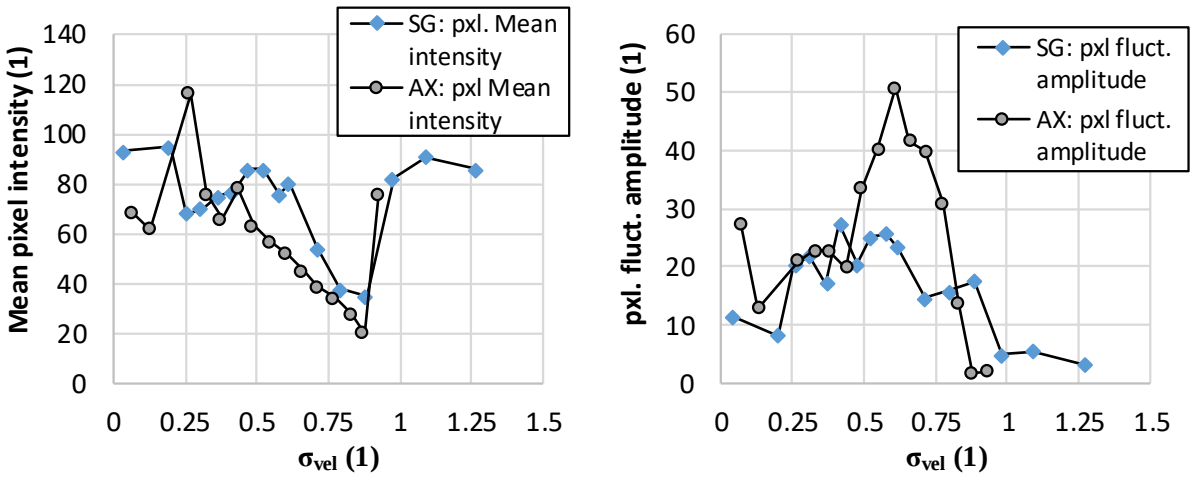

Figure 53 Mean pixel intensities right and amplitudes of the observed dominant frequencies depicted as functions of cavitation number

Partial conclusions – Spectral analysis of the pixel intensity fluctuations

The dynamics of the cavitating flow in case of the 6 l/s discharge has been investigated using the spectral analysis of the pixel intensity fluctuations. The following preliminary conclusions can be stated:

I. Dominant frequencies of the pixel intensity fluctuations are decreasing with the increasing amount of the cavitation within the flow, regardless the experimental configuration.
II. The observed decreases are gradual. The decrease is steeper in case of the large cavitating structures presence (considering decreasing value of cavitation number)
III. Dominant frequencies of the pixel intensity fluctuations are in good agreement with the results of the pressure fluctuations analysis. The partial match of the frequencies can be also found in case of the pipe-wall acceleration fluctuations.
IV. The dominant frequencies are slightly higher in case of the swirl generator presence. In contrast, the amplitudes corresponding to the dominant frequencies are higher in case of the axial inflow. The highest amplitudes are induced by the distinctive cavitating vortex rings.
V. The processed signals were considerably noisier in case of the swirl generator presence. It was caused by the nature of the cavitation patterns as they were described in the chapter 2.3.
VI. The higher harmonics of the fundamental frequencies were observed in case of the axial inflow.
VII. The results obtained using the semi-automated selection of the source pixel (based on the maximum value of the pixel intensity standard deviation within the manually selected region of interest) are reliable in wide range of the operating points. The region of interest must be selected properly to capture the investigated structures on the one side and to avoid the overexposed areas as well as the areas of the significant light reflections on the other side.

3.2. Proper orthogonal decomposition of the cavitating structures

POD represents an effective way how to decompose a complex physical phenomenon captured in the time domain into the modes in form of spatio-temporal eigenfunctions. Due to the process of decomposition, it can be assumed that most of the information related to the dominant instabilities captured within the decomposed record is contained in the first several POD modes. In other words, the most coherent flow structures of the investigated phenomenon can be easily identified. Although the fact that this method can be exploited for the analysis of the vector quantities and provide deeper insight in the physical nature of the phenomenon, the utilization of POD is confined to the processing of the scalar pixel intensity of the HS records in this chapter. Thus, the description of this method will be limited to the analysis of scalar quantities.

Exhaustive description of this method can be found in [59] for example. The k^{th} POD mode obtained by the decomposition consists of the time temporal eigenfunction $\boldsymbol{a_k}(t_k)$ (i.e. temporal mode) and orthogonal spatial basis function $\boldsymbol{\phi_i^k}(\boldsymbol{x})$(i.e. spatial mode), where i = 1,2,3,…,N (N is the amount of points within the investigated region of interest) and k = 1,2,3,…,M (M represents the number of snapshots of the processed record). These modes are computed to find an approximation of a spatio-temporal dependent variable, in this case pixel intensity $\boldsymbol{I}$ ($\boldsymbol{x}$, t_k), where $\boldsymbol{x}$ represents the spatial coordinates and t_k corresponds to the discrete temporal nature of the analyzed function. Since the amount of the snapshots is considerably higher compared to the number of intensity values within the region of interest it is plausible to exploit so-called snapshot variant of the POD. This method was proposed by Sirovich [59] to reduce the NxN eigenvalue problem to the size of M x M.

For this purpose, the temporal correlation matrix $\boldsymbol{C_{ij}}$ is constructed as an inner product between every pair of snapshots (i.e. fields of pixel intensity) as is shown in the discrete form in the formula (67).

$$\boldsymbol{C}(t_k', t_k) = M^{-1}\boldsymbol{I}'(\boldsymbol{x}, t_k)\boldsymbol{I}(\boldsymbol{x}, t_k) \tag{67}$$

Where $\boldsymbol{I}(\boldsymbol{x}, t_k)$ represents the matrix contained all of the processed snapshots in form of columns of the corresponding pixel intensities $\boldsymbol{i}(\boldsymbol{x}, t_k)$.

$$\boldsymbol{I}(\boldsymbol{x}, t_k) = \begin{bmatrix} i_{x_1,y_1,t_1} & \cdots & i_{x_1,y_1,t_M} \\ \vdots & \ddots & \vdots \\ i_{x_N,y_N,t_1} & \cdots & i_{x_N,y_N,t_M} \end{bmatrix} \tag{68}$$

Solving the eigenvalue problem of the correlation matrix $\boldsymbol{C}(t_k', t_k)$, the eigenvalues λ and eigenvectors $\boldsymbol{e}$ are obtained. Considering that the eigenvalue is paired with corresponding eigenvector and the fact that its value is directly connected with energetic contribution of the corresponding POD mode, the eigenvalues and eigenvectors are sorted by the magnitude of the eigenvalues.

Temporal coefficients a_k and spatial eigenmodes $\boldsymbol{\phi_k}$ are then computed using the following expressions:

$$\boldsymbol{a_k} = \boldsymbol{e_k}\sqrt{N\lambda_k} \tag{69}$$

$$\boldsymbol{\phi_k} = \boldsymbol{U}\frac{\boldsymbol{e_k}}{\sqrt{N\lambda_k}} \tag{70}$$

The approximation of the pixel intensity is carried out by the backward reconstruction using the certain number K of the obtained POD modes as it follows.

$$\hat{\boldsymbol{I}}_{\boldsymbol{i}}\,(\mathbf{x};\, \mathrm{t}_k) = \sum_{k=1}^{K} a_k(t_k)\,\boldsymbol{\phi}_i^k(\boldsymbol{x}) \tag{71}$$

Dominant frequency of the selected mode k can be evaluated using the spectral analysis of the correspondent temporal coefficient $\boldsymbol{a_k}$.

Several applications of POD for the purpose of cavitating flow dynamics investigation can be found in the literature. POD was introduced to the field of turbulent flow dynamics investigation by Lumley [60], [61]. It was concluded that this method represents effective tool for this type of investigation. Ever since this method has been exploited in several contributions devoted to the investigation of the swirling flows as well as the cavitating flows investigations.

Comprehensive study of the cavitating spiral vortex within the draft tube was done by Štefan et al [62], [66]. The POD analysis of the HS video capturing cavitation cloud over NACA profile was done by Rudolf et al [63]. Influence of the aeration on the cavitation patterns downstream within the Venturi tube was the scope of investigation which has been done by Tomov et al [64]. The operation regimes in this study corresponded to the partially developed stage of cavitation. POD study of the cavitation regime detection in case of grooved C-D nozzle was done by Danlos et al [65]. Kozák et al exploited the POD for the investigation of the hysteresis presence during the transition between the fully developed cavitation to supercavitation and vice versa in case of the cavitation within the Venturi tube considering the axial inflow in [57].

The proper orthogonal decomposition has been implemented into the Python script. The functionality of the script is similar to the above described script exploited for the processing of the pixel intensity fluctuations using the DFT. Prior the main spectral analysis of the temporal coefficients corresponding to the most significant modes, it was necessary to process the input data.

It should be mentioned that each 10^{th} image of the captured record was exploited for the decomposition. This led to the decrease of the sampling frequency from the originally captured 20 000 frames per second to the 2 000 fps. To support this approach, the reduced sampling frequency can be compared with the Nyquist - Shannon sampling theorem.

According to the theorem, the sampling frequency f_s must be at least two times higher compared to the maximum frequency of the investigated discrete function. Since the maximum dominant

frequency obtained by the spectral analysis of the pixel intensity fluctuations was 185 Hz as it was shown in the previous chapter, it can be assumed that the decreased sampling frequency of 2000 Hz is more than sufficient for the purpose of the cavitation dynamics investigation.

This reduction of the processed image amount together with the image cropping lead to the significant reduction of the correlation matrix $\boldsymbol{C}$ size. Nevertheless, the influence of the input image cropping will be discussed at the end of this chapter.

Beside the analysis of the cavitating flow dynamics, the coherence of the captured structures will be discussed using the analysis of the POD modes significance distribution using the corresponding eigenvalues. The analysis will be complemented by the backward reconstruction of the source images using the specific amount of the POD modes.

Some of the presented results will be described using the selected flow rates. Nevertheless, the results will be provided for the full range of the investigated operating points (from the cavitation regime as well as from the flow rate magnitude points of view).

3.2.1. Regions of interests exploited for the POD

The dynamics of dominant cavitating structures has been analysed using two different regions of interest to discuss the influence of the selected region as well as the robustness of the obtained results. The regions of interests which were exploited for the POD analysis are depicted in the Figure 54. The ROIs are labelled alphabetically to distinguish them from the regions utilized in case of the pixel intensity fluctuations spectral analysis.

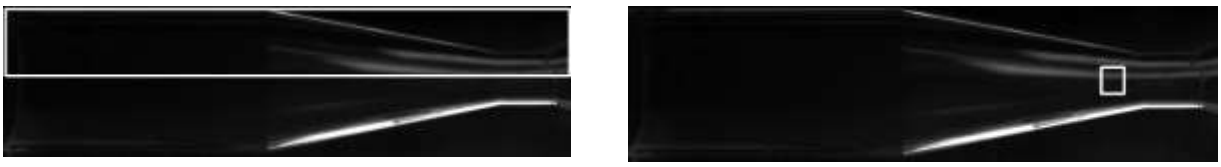

Figure 54 Regions of interests (white-lined rectangles) utilized for the comparison of the results obtained by the proper orthogonal decomposition. ROI A – left, ROI B – right

As it can be seen the ROI B is significantly smaller compared to ROI A, which lead to the significant reduction of the computational cost. It should be also noted that the ROI A is containing part of the scene out of the Venturi nozzle in contrast to the ROI B which is restricted to the region close to the axis of the nozzle. The size of the regions utilized for the decomposition including the number of the correlation matrices elements is listed in the following table.

	Size of the ROI	Size of the correlation matrix $\boldsymbol{C}$
ROI A	119 x 1023 px	121 737 000
ROI B	45 x 39 px	1 755 000

Table 1 Properties of the regions of interest

3.2.2. POD modes – Spatial modes

The final mode obtained by the decomposition consists of the spatial mode and temporal coefficient, whereas the number of the modes corresponds to length of the analyzed record (e.g. number of the snapshots). Since the most coherent structures are captured by the lowest modes, the first ten modes will be depicted and discussed in details for the flow rate of 6 l/s. The spatial coefficients corresponding to the first ten modes of the selected operating points obtained by the POD analysis utilizing ROI A are depicted in the Figure 55. As it is clearly depicted the 0^{th} modes correspond to the static information (i.e. their structure is the same as in case of the time-averaged image). The higher modes correspond to the dynamics of captured cavitating structures. The nature of the POD modes can be also discussed based on the images. The lower order of the observed mode is, the simpler is the structure. In other words, the

lowest POD modes are corresponding to the dominant dynamic structures captured by the HS records. This is particularly visible by the comparison of the 1st and 19th modes as are shown in the Figure 55. While the first mode corresponds to the axial pulsations of the cavitating structures, the 19th mode includes the stochastic instabilities of the interface region. It should be also noted that the dynamic modes of the axial inflow are extended to a greater distance from the throat of the nozzle, even though the cavitation number is nearly the same regardless the configuration of experiment. This corresponds to the observed separation and motion of the cavitating vortex rings in case of this configuration.

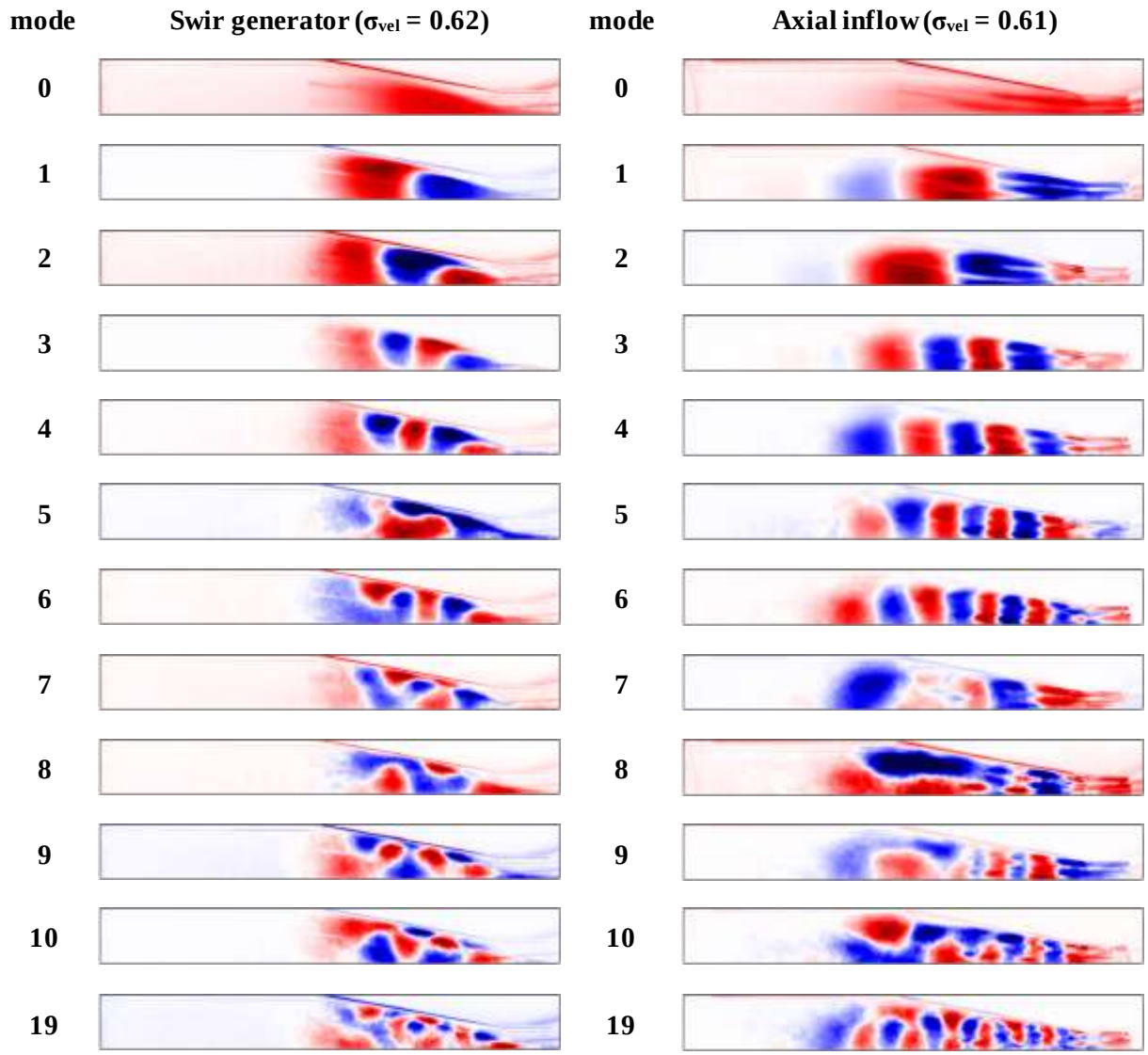

Figure 55 Comparison of the spatial modes corresponding to the same decomposed record for ROI A. SG – left, Axial inflow - right

The wall of the diffuser is distinguishable as it can be seen in the depicted modes. This is caused by the light reflection. The information about potentially captured flow patterns dynamics can be lost in this region, because the values of the obtained spatial mode are constant close to this overexposed region. Nevertheless, it can be stated that in case of the investigated cavitating structures this region does not play important role.

The similar observations can be described in case of POD modes obtained by the analysis of ROI B depicted in the Figure 56. In case of the 1st POD mode corresponding to the axial inflow, the most significant fluctuations captured in this region correspond to the flickering of the light reflection. Nevertheless, it should be noted that the intensity of the reflected light is tightly connected to the

presence of the cavitation, obtained dominant frequency of this mode is in good agreement with the axial pulsation of the cavitating structures. The structures captured by the lower spatial modes correspond to the most significant (i.e. important) fluctuations, while the more stochastic fluctuations such as interface regions instabilities are captured by the higher modes similarly to the ROI A. The significance of these modes will be discussed using the analysis of the corresponding eigenvalues in the following part of this chapter.

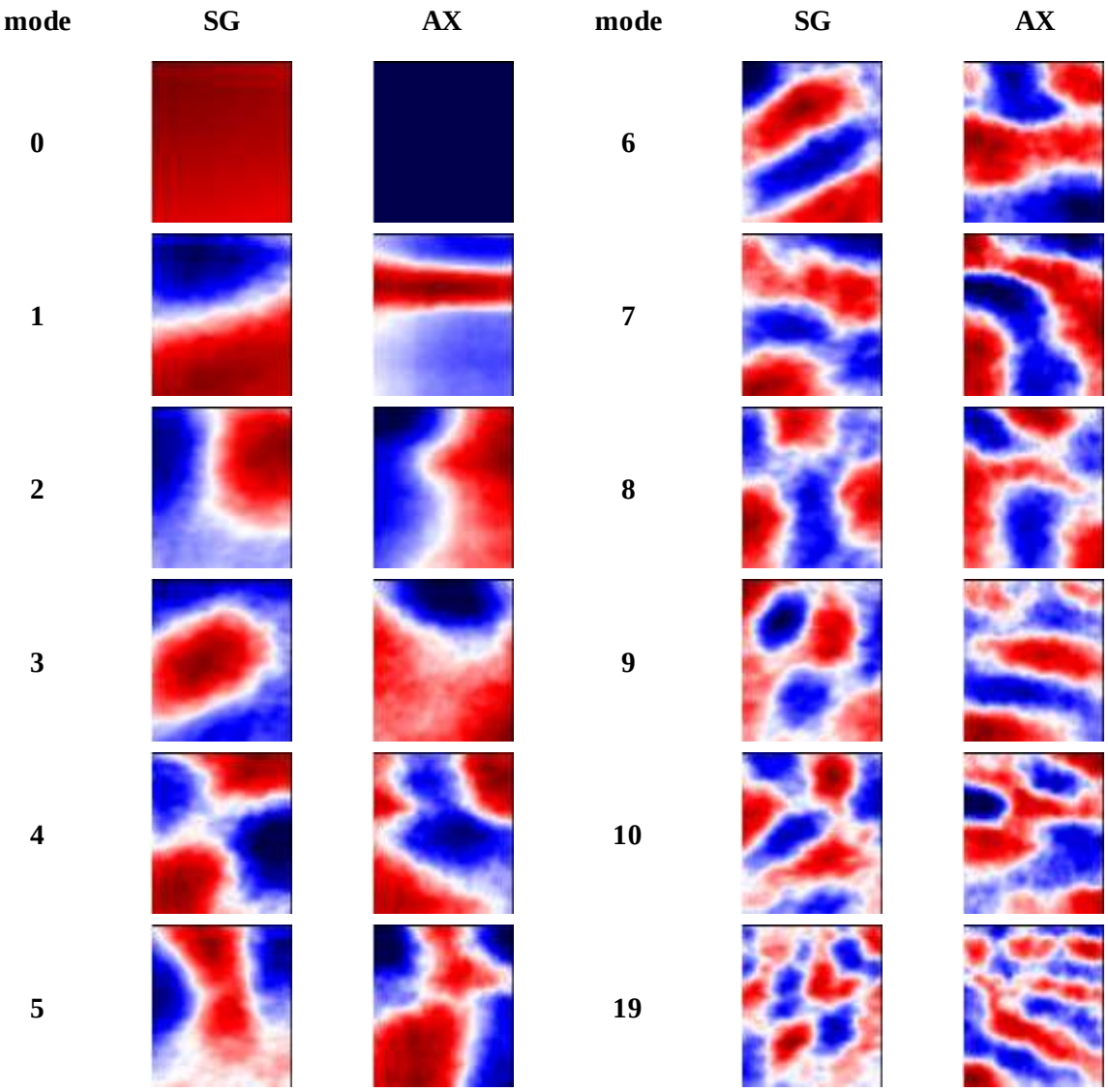

Figure 56 Comparison of the spatial modes corresponding to the same decomposed record considering ROI B. SG σ_{vel} = 0.62, Axial inflow: σ_{vel} = 0.61

Prior the analysis of the POD modes significance distribution and the dynamics of investigated cavitating structures using the spectral analysis of the temporal coefficients, it will be convenient to depict the comparison of the most significant dynamic modes corresponding to the different stages of the cavitation development. Due to the fact, that the results are in good agreement regardless the selected region of interest, this comparison is shown only for the ROI A and the discharge of 6 l/s (see Figure 57).

Several observations can be stated by the comparison of the modes depicting the wide range of the cavitation regimes. It is possible to identify particular cavitation regime and even the transitions between the regimes, based on the depicted modes. This is valid for both of the investigated experimental configurations.

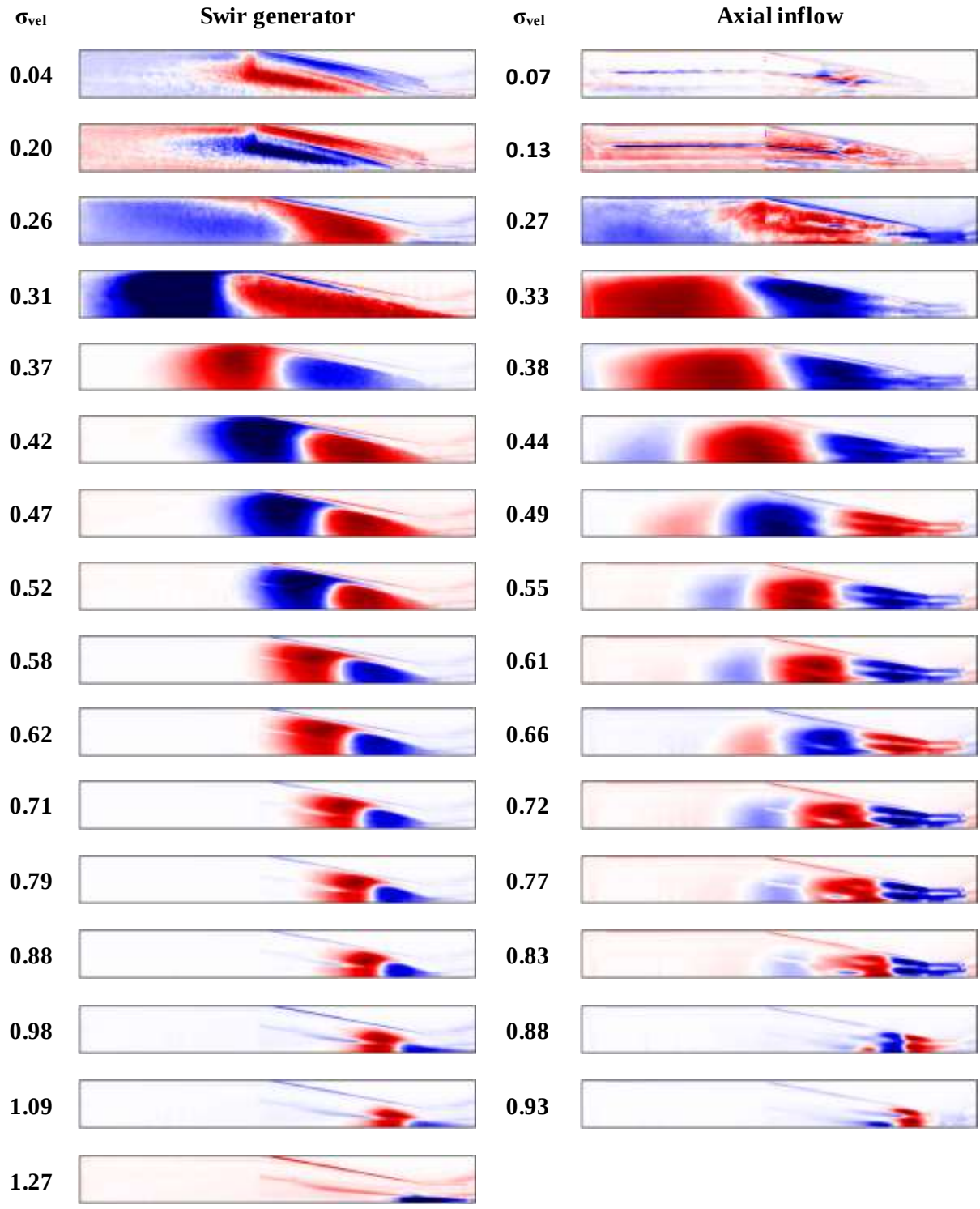

Figure 58 Most significant spatial modes corresponding to the different regimes of cavitating flow, red –max value, blue – min value, white - zero

The modes corresponding to supercavitation regimes depicted in the first two rows of the Figure 58 mostly capture the highly stochastic instabilities of the interface region, because the obseved cavitating structures were stable and neither significant fluctuations nor collapses were captured during the experimental measurement. The spatial modes corresponding to the supercavitation affected by the upstream mounted swirl generator clearly shows the shape of the conical cavitating structure within the diffuser of the nozzle. In case of the axial inflow, the interface between the liquid jet close to the axis of

the nozzle and surrounding void of cavitation can be found in the straight pipe section downstream the diffuser of the nozzle. Under this regime the liquid film on the walls of the diffuser was observed. While the liquid film had not been stable, it was possible to track the motion of the small instabilities. This is reflected to the higher values of the spatial coefficient within the diffuser in case of the axial inflow. It should be also noted that spatial modes corresponding to the supercavitation are considerably grainier, compared to the fully developed stage of cavitation, regardless the presence of the swirl generator.

Transition between the supercavitation and the fully developed stage of cavitation can be also identified based on the structure of dominant POD modes (see the 3rd row of the Figure 58). It can be seen that the spatial modes corresponding to the transition are completely different compared to the coefficients of the supercavitation. The captured shapes of the coefficients are considerably more coherent, and the captured structures are considerably larger compared to supercavitation. On the other hand, the images depicting these coefficients are still obviously grainier compared to the spatial modes depicting fully developed regime of cavitation.

The shape of the spatial modes is relatively stable in wide range of σ_{vel} corresponding to the fully developed cavitation. Length of the regions of the higher spatial modes magnitude is the longer, the lower corresponding cavitation number is, similarly to the length of the decomposed cavitating structures. As it was mentioned in the previous part of this section, it is possible to observe that the length of the structures captured within the dominant dynamic coefficients is longer in case of the axial inflow. This statement is valid for the whole range of the depicted operating points. The reason arises from the different nature of the observed cavitating patterns. Where the separation and subsequent motion of the separated cavitating vortex rings was observed in case of the axial inflow, the cavitating structures were considerably more stable, when the additional swirl was introduced to the flow. Thus, the motion of the captured structures covers longer region in case of the axial inflow.

The initial stage of the cavitation is distinguishable from the fully developed stage of cavitation (see the last three rows in Figure 58). As it can be seen, the magnitude of the spatial coefficient approaches to zero within the throat of the nozzle in contrary to the more developed stages of cavitating flows in case of the axial inflow. The axial inflow was characteristic by the quasi-stable boundary layer during the initial stage. In other words, only the minimum amount of significant collapses of the cavitating boundary layer were observed within the throat of the nozzle during this regime. This behavior was completely different in case of the operating regimes corresponding to the lower values of σ_{vel}, where the complete decay of the cavitating boundary layer occurred at the beginning of cavitation cycle.

Also, in case of the of the swirl generator presence, relatively significant difference between the fully developed and initial stage of cavitation can be found. As it can be seen, the "cone" of the vortex close to the axis became significantly narrower in case of the initial stage of cavitation.

To complete the analysis of the spatial modes obtained by POD, it is necessary to discuss the influence of the investigated flow rate. Whereas the considerable amount of the operating points was investigated, the discussion will be focused on the comparison of the selected operating points corresponding to the fully developed cavitation as it is shown in the Figure 59. Since the shape of the most important dynamic POD modes is nearly the same, regardless the investigated discharge, it can be assumed that the most important sources of the image fluctuations remain unchanged over the whole spectrum of investigated discharges. The minor changes of the length can be devoted to the slight variation of the corresponding values of cavitation number.

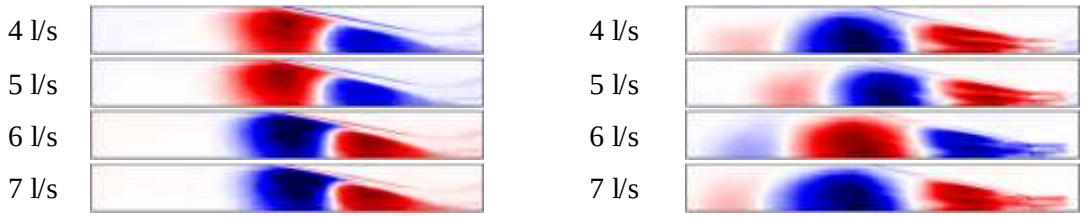

Figure 59 Most significant spatial modes corresponding to the different flow-rates, SG – left, AX – right

3.2.3. POD modes – investigation of the cavitation dynamics

Spatial modes obtained by the proper orthogonal decomposition have been described to discuss to influence of the cavitation stage and the investigated discharge as well as to identify the most important sources of the captured instabilities. Temporal coefficients description and their analysis will be provided in this chapter to investigate dynamics of the analyzed cavitating structures.

The POD mode consisted of the temporal and spatial modes. Thus, some of the essential properties of the corresponding coefficients are similar. The lower POD modes are containing the information about the most important (e.g. coherent) instabilities. This was clearly depicted by the comparison spatial modes depicted in the Figure 55. Similar conclusion can be stated in case of the temporal coefficients corresponding to the different POD modes. This can be shown using the images of the spatial modes, corresponding temporal coefficient and the frequency spectra obtained using the spectral analysis. For this purpose, the operation points corresponding to the fully developed cavitation and the discharge of 6 l/s were chosen.

Figure 60 and Figure 61 are depicting three different POD modes corresponding to the similar cavitation regimes of the flow affected by the swirl generator and axial inflow, respectively. The higher temporal coefficients are noisier regardless the experimental configuration. Although it is worth to mentioned, that the temporal coefficient corresponding to the 1st POD mode is considerably noisier in case of the SG presence (1st row in Figure 60) compared to the signal corresponding to axial inflow (1st row in Figure 61). It can be stated that the dominant frequency of the 1st POD mode is slightly higher in case of the SG presence even though the cavitation number value is slightly higher in case of the axial inflow (by 4.8 %). Dominant frequency of the 1st mode (94 Hz) considering the presence of the SG can be found also in frequency spectrum of the 4th mode. Besides that, the significant frequency of 266 Hz is contained within the temporal coefficient of the 4th POD mode (2nd row in Figure 60). This frequency is close to the significant frequency of the pressure fluctuations induced by the cavitating flow as it will be shown in the chapter devoted analysis of the pressure signals. The frequency spectra corresponding to the 19th POD modes are noisy regardless the experimental configuration. It is in good agreement with the statement that the higher modes are containing mainly the information about the highly stochastic minor instabilities of the interface.

Comparing the amplitudes corresponding to the dominant frequencies, it is visible that this value is more than two times lower in case of the swirl generator presence (1765) compared to the axial inflow (4046). This observation is in good agreement with the observed flow patterns and as it will be shown, the similar results will be obtained by the analysis of all the investigated flow characteristics.

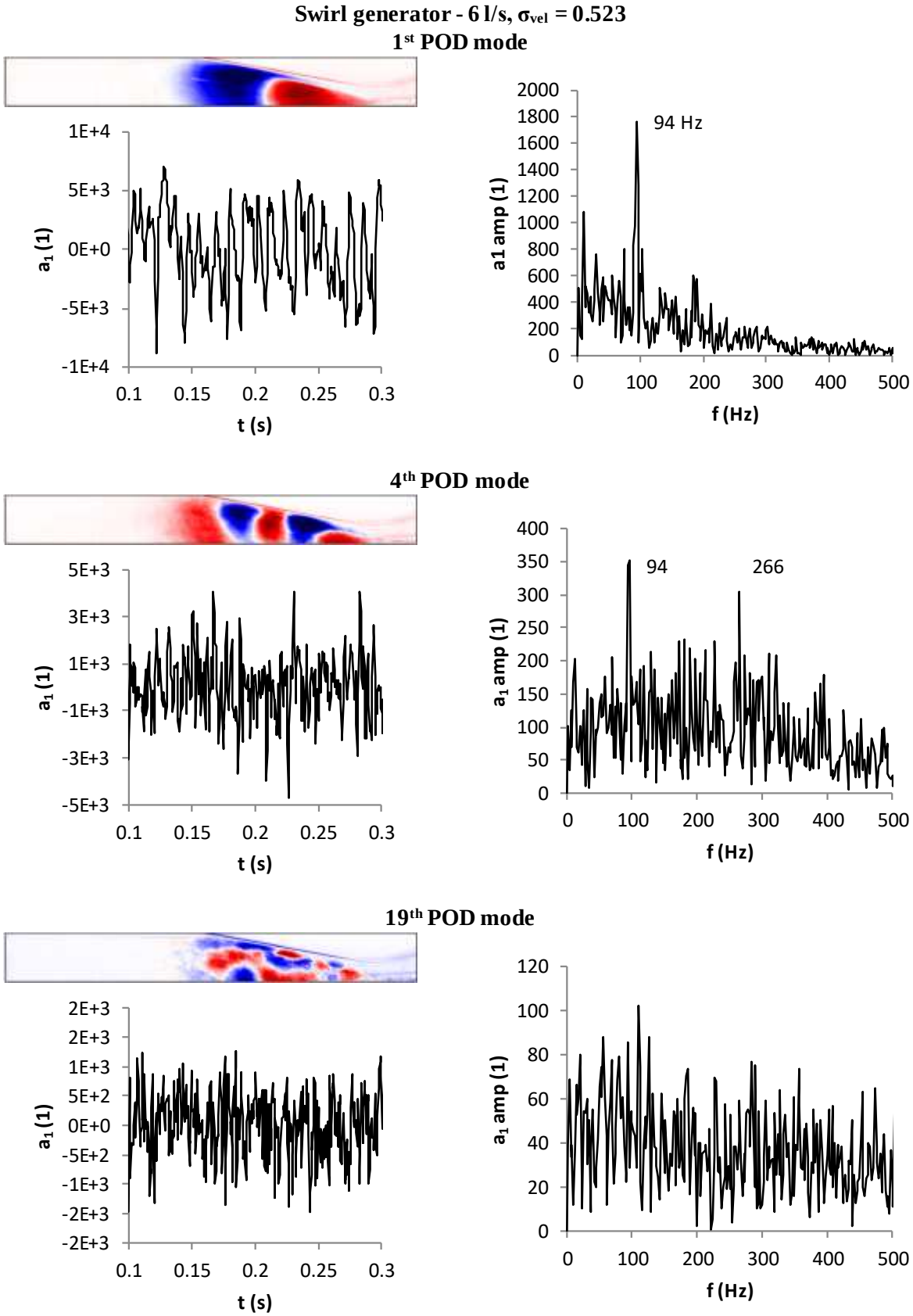

Figure 60 POD spatial modes depicted with the temporal coefficients and their frequency spectra in case of SG presence

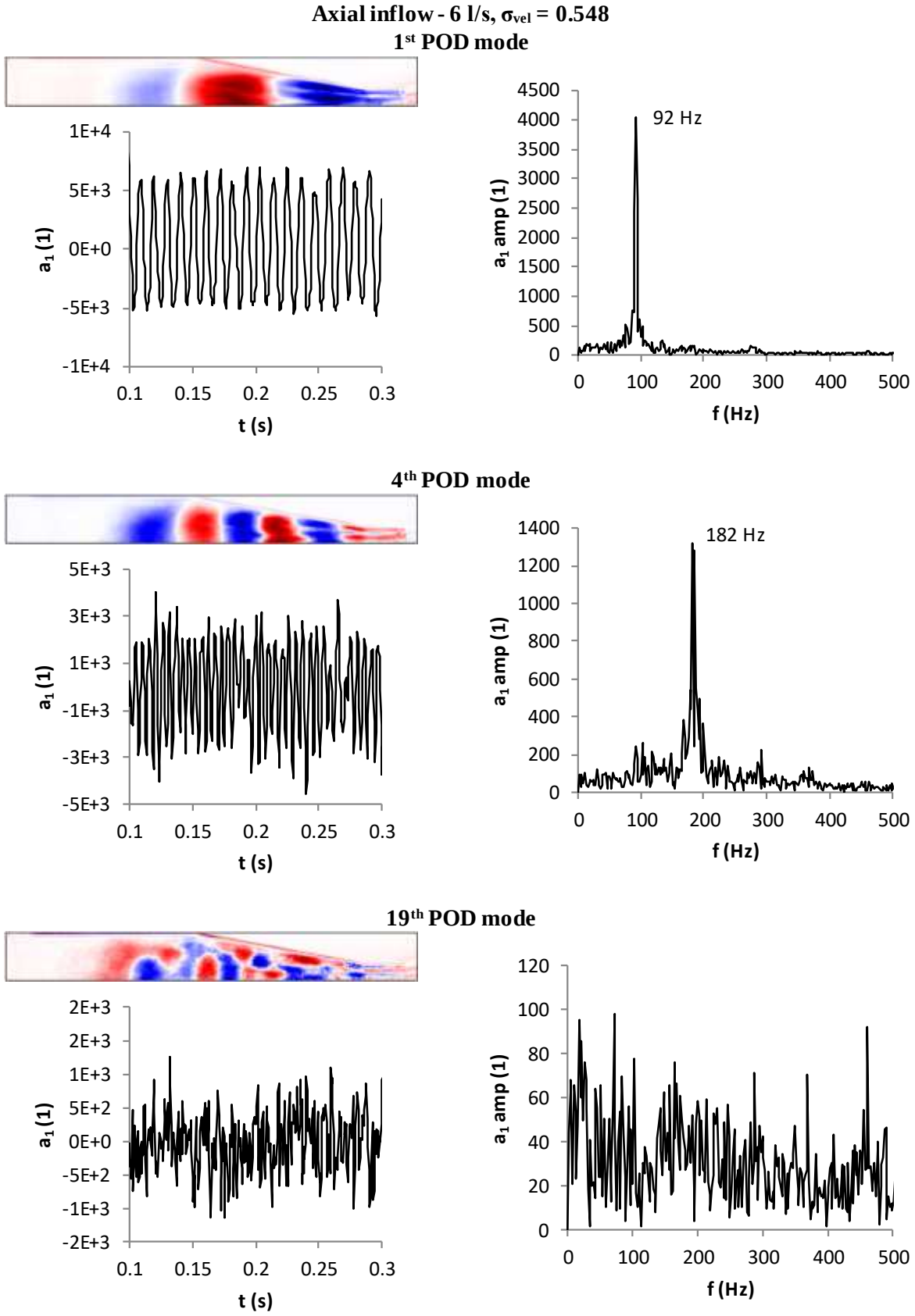

Figure 61 POD spatial modes depicted with the temporal coefficients and their frequency spectra in case of axial inflow

Dominant frequencies obtained by the POD analysis of 6 l/s are compared with the analysis of the pixel intensity fluctuations in the Figure 62. As it has been shown in the chapter 3.1, this method is in good agreement with the results of the analysis of the pressure fluctuations. Thus, it is possible to exploit the DFT of the pixel intensity signals for the verification of the results obtained using the POD.

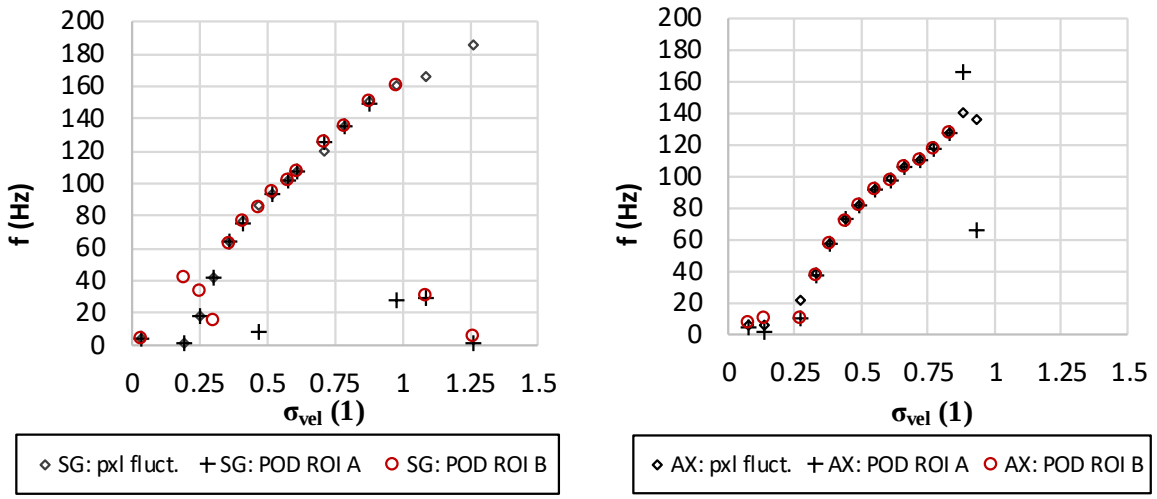

Figure 62 Dominant frequencies obtained using the different regions of interest in comparison with the results of the pixel intensity fluctuations. SG – left, AX - right

Results of the POD analysis are in good agreement with the spectral analysis of the pixel intensity fluctuations in general. Nevertheless, the agreement is the best in the region of fully developed cavitation regardless the investigated configuration and selected region of interest.

Significant discrepancy between the results obtained by the different regions of interest can be found in close to σ_{vel} 0.25 (e.g. during transition between the fully developed regime and supercavitation) considering the presence of swirl generator (Figure 62, left). The frequencies obtained using the region B are increasing close to the supercavitation regime, while the completely opposite behavior can be found in case of the ROI A of POD analysis and DFT analysis of the pixel intensity fluctuations. On the other hand, it is possible to identify the dominant frequency of 161 Hz corresponding to σ_{vel} of 0.98 using the ROI B. This frequency has been found using the spectral analysis of the pressure fluctuations as well as in case of the pixel intensity fluctuations investigations. However, the analysis of the three operating points corresponding to the highest values of the σ_{vel} using the pixel intensity signals were not reliable, as it has been mentioned. From this point of view, the analysis using the POD seems to be more appropriate.

Using these observations, it is possible to state, that the analysis of the cavitating flow dynamics using the spectral analysis of the temporal coefficients corresponding to the most significant POD modes is reliable. The choice of the analyzed ROI played a role to a certain extent. On the other hand, the obtained dominant frequencies corresponding to the fully developed cavitation were consistent regardless the selected ROI for both investigated configurations. It was possible to slightly extend the range of the analyzed dominant frequencies by the choice of appropriate ROI in case of initial cavitation. Nevertheless, the nature of cavitating structures fluctuations is the more stochastic; the higher is cavitation number. The question is to what extent these results can be trusted in case of the HS records analysis.

The further analysis of the cavitation dynamics will be discussed exploiting the ROI A, the results will be corrected and complemented by the results obtained using the ROI B in case of necessity. Results exploiting σ_{vel} are described in the following set of figures. The Figure 63 is depicting the whole spectrum of investigated flowrates. Identified dominant frequencies of the cavitating structures pulsations are the lower, the lower σ_{vel} is regardless the investigated configuration of experiment. It should be also noted

that the obtained frequencies are depicted up to the σ_{vel}, when the sudden drop of the identified frequency occurred.

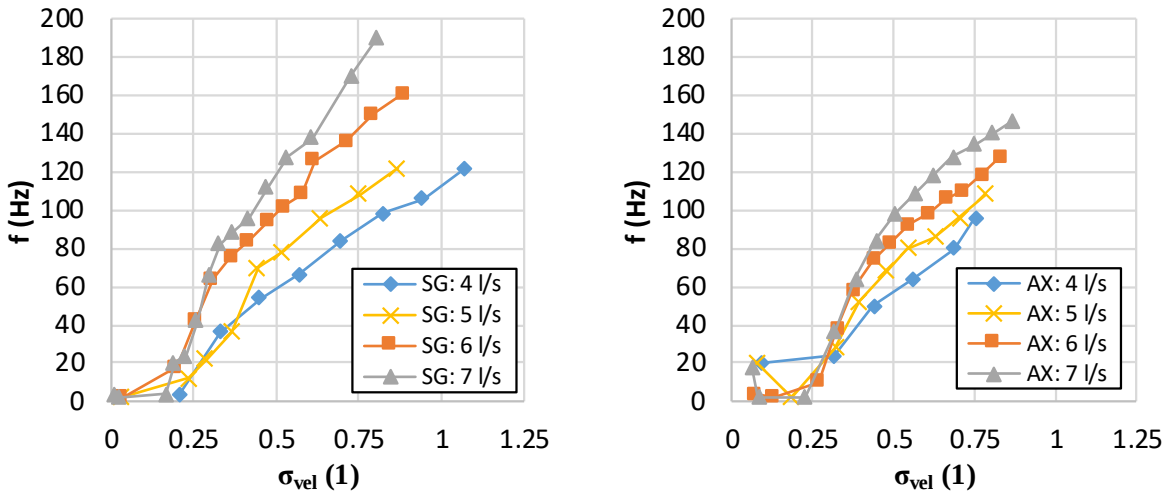

Figure 63 Dominant frequencies of the axial pulsations obtained by the POD analysis for the whole range of investigated operating regimes. SG-left, AX-right.

The comparisons of dominant frequencies corresponding to the same nominal flow-rates and different experimental configurations are provided in the following figures. Direct comparison of the identified frequencies shows that these frequencies are higher in case of the swirl generator presence. While in case of the lower discharges (4 l/s and 5 l/s depicted in Figure 64) the difference is relatively minor, it became clearly noticeable in case of the 6 l/s and 7 l/s (see Figure 65).

As it has been described the decrease of the identified frequencies of the cavitating structures pulsations became significantly more rapid within the region 3 (e.g. in the region of the massive cavitation, close to the σ_{vel} 0.41 and lower). This observation has been captured in the whole spectrum of the investigated flowrates. Nevertheless, this rapid decrease of the dominant frequencies within the region 3 is most evident in case of 6 and 7 l/s discharges.

The cavitating structures became stable during the transition to the supercavitation regime. Thus, the identified frequencies approach the value of 0 Hz.

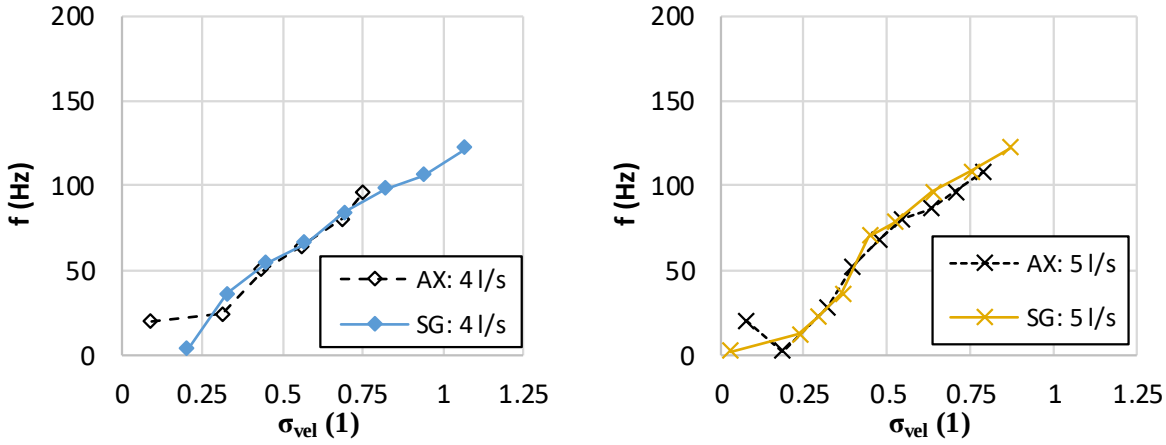

Figure 64 Comparison of dominant frequencies based on the experimental configuration in case of 4 l/s (left) and 5 l/s (right)

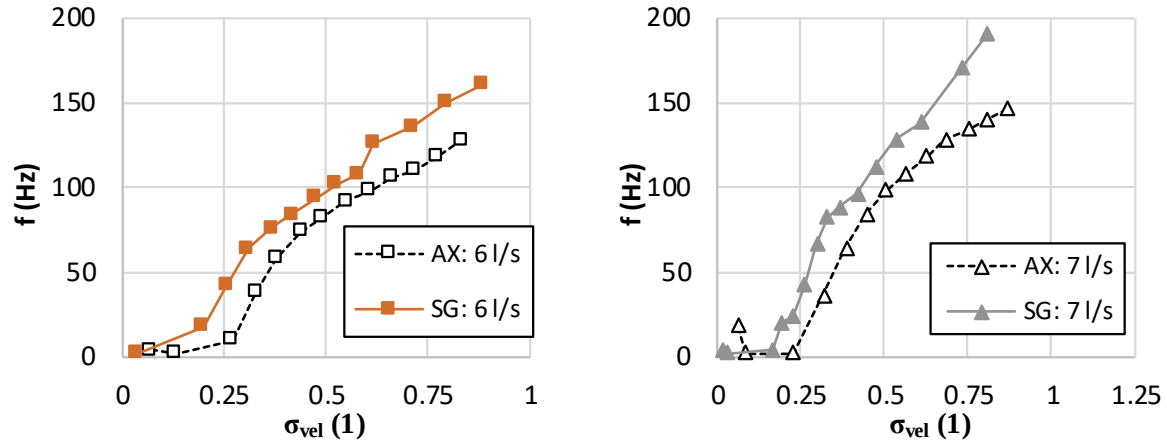

Figure 65 Comparison of dominant frequencies based on the experimental configuration in case of 6 l/s (left) and 7 l/s (right)

The amplitudes of the dominant frequencies obtained by the analysis of the most significant dynamic POD modes (i.e. 1st modes) are depicted for the discharges of 4 and 6 l/s in the Figure 66. The magnitudes are considerably higher in case of the axial inflow, which corresponds to the nature of the captured cavitating structures (i.e. vortex rings). The amplitudes reach their maximum in the region 3 (fully developed stage). Amplitudes corresponding to the higher cavitation numbers are excluded from the charts similarly to the analysis of dominant frequencies. Comparing the charts of the different discharges in the Figure 66, the difference is significant mainly in case of the 4 l/s.

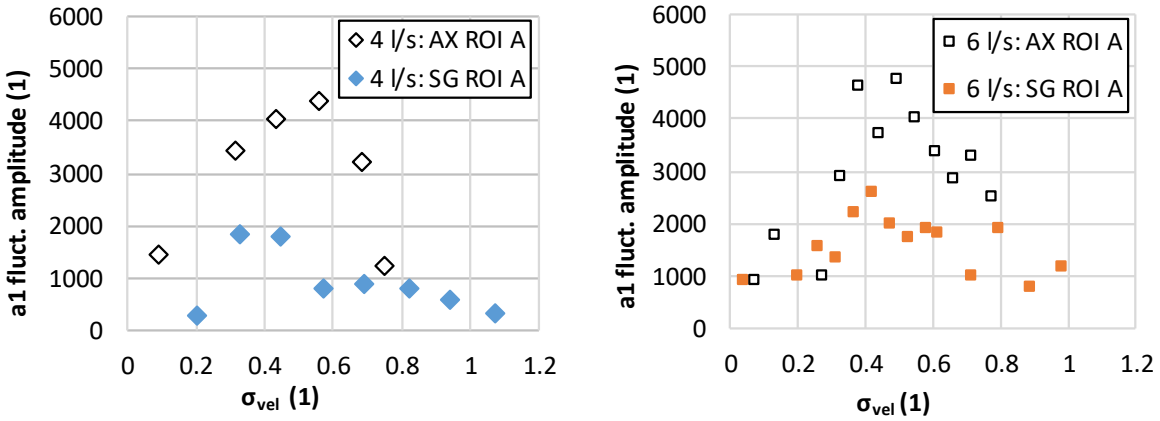

Figure 66 Amplitudes of the dominant frequencies obtained by the POD analysis

Distribution of the POD modes significance can also represents the rich source of the information describing the investigated flow properties as well as the properties of the selected region of interest. During the process of the record decomposition the eigenvectors λ obtained by solving the eigen problem of the correlation matrix $\boldsymbol{C}(t_k', t_k)$ are sorted based on the corresponding eigenvalues $\boldsymbol{e}$. Since the magnitude of eigenvalue $\boldsymbol{e}$ corresponds to the significance of particular POD mode, it is possible to discuss properties of the captured cavitating flow patterns based on the analysis of eigenvalues $\boldsymbol{e}$ magnitudes, respectively significance distribution over the obtained POD modes.

As it has been mentioned at the beginning of the chapter and shown in the Figure 55 and Figure 56 depicting the first several spatial modes $\boldsymbol{\phi}$, the statics had not been subtracted from the records prior the POD analysis. Thus the 0th modes obtained by the POD correspond to the time-averaged structures of the captured cavitating patterns. The relative significance of 0th modes calculated as fraction of the eigenvalue of the 0th mode to the sum of all eigenvalues are depicted in the Figure 67.

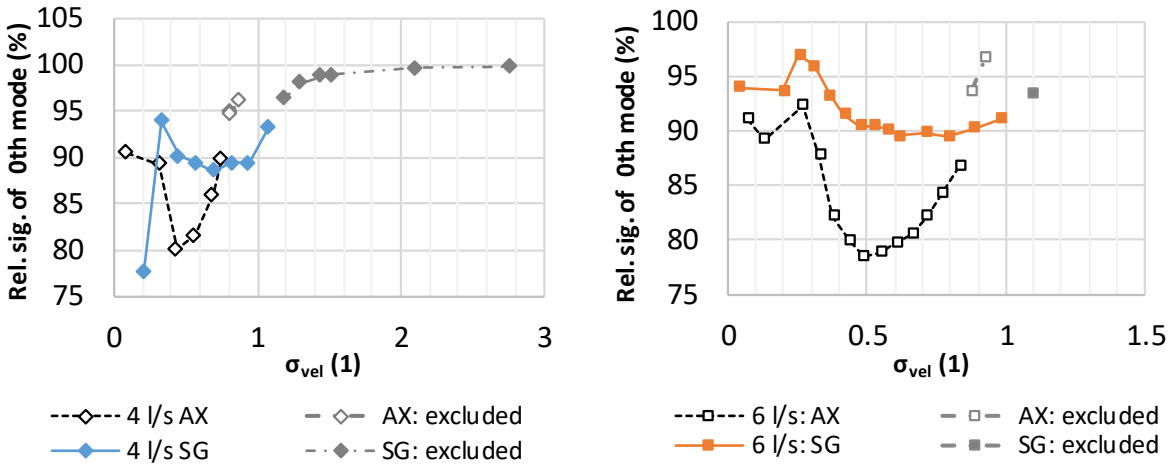

Figure 67 The relative significance of 0th modes in case of 4 l/s (left) and 6 l/s (right)

It is clearly depicted that the 0th modes are dominant regardless the experimental configuration or flow rate. Their relative significance does not fall below the 78 %. The charts contain also the operating points excluded from the analysis of the dominant frequencies. These points exhibit the considerably higher relative significance of the static modes similarly to the supercavitation. This observation is in good agreement with the nature of the captured cavitating patterns. While the main source of the captured fluctuations is represented by the small instabilities of the interface region during supercavitation, the separations or pulsations of the cavitating structures are less significant and much more random during the initial stage of cavitation compared to the fully developed regime. In other words, during the initial stage of cavitation as well as during the supercavitation, the significance of the coherent dynamic structures is considerably lower as it will be shown.

The relative significance of 0th mode is larger in case of the SG presence compared to the axial inflow. The cavitating structures were considerably more stable in case of the cavitation affected by the induced swirl (in term of axial pulsations), which is in contrast to the separation and subsequent motion of the cavitating vortex rings typical for the axial inflow.

The relative significance of the most significant POD modes (1st modes) capturing the dynamic character of captured flow patterns are depicted in the Figure 68.

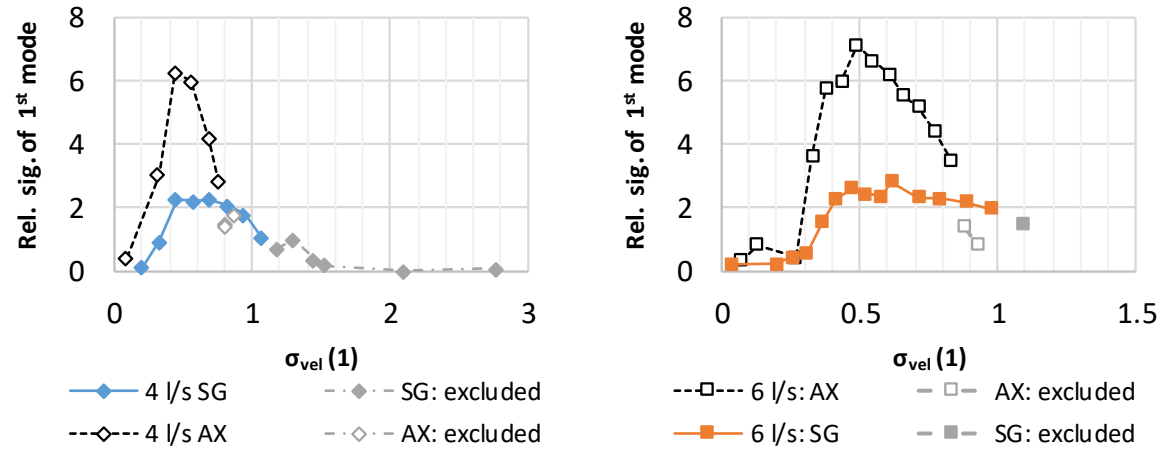

Figure 68 The relative significance of 1st modes in case of 4 l/s (left) and 6 l/s (right)

Comparing the values of the relative significance of the 1st POD modes (see Figure 68) with the analysis of the 0th mode (see Figure 67), it can be stated that the courses of the obtained resulst are different. Nonetheless, following assumptions are still in good agreement with the discussion of the 0th modes relative significance. The 1st modes are more significant in case of the axial inflow regardless the

flowrate, while the situation was completely opposite in case of the analysis of static structures. The dynamic structures were the most coherent during the fully developed regimes of cavitation. During these regimes, the relative significance of the 1st POD modes reaches values up to 6-7 % in case of the axial inflow, whereas maximum values corresponding to the swirl generator presence move around 2 - 2.5 % for both flow rates which are depicted in the charts.

The absence of the periodical fluctuations of the large cavitating structures during the supercavitation and initial regime of cavitation lead to the obvious drop of 1st POD mode relative significance.

It was shown that the significance of the static structure is dominant and greatly exceeds the significance of the 1st POD modes in the whole spectrum of investigated operating points. Nevertheless, distribution of the significance of the higher modes containing the information about the captured dynamic of the cavitating structures can be also discussed in order to provide additional information about the investigated cavitating structures. Figure 69 depicts the cumulative sum of the dynamic POD modes significance of the selected operating points considering the discharge of 6 l/s. Investigated experimental configurations are shown separately in two charts. Comparing these charts several similarities as well as differences based on the experimental configuration can be found.

First of all, the curves corresponding to the supercavitation are clearly distinguishable from the fully developed and initial stage of cavitation regardless the experimental configuration. Transition regime is significantly closer to the supercavitation in case of the axial inflow (see Figure 69, chart on the left, σ_{vel} 0.27). Seeing the similar regime considering the swirl generator presence, it can be stated that the curve of the cumulative significance is still clearly distinguishable from the fully developed and initial stages of cavitation. However, the difference between this regime and supercavitation is considerably more significant compared to the axial inflow (see Figure 69, chart on the right, σ_{vel} 0.27).

Courses of the cumulative sums of the dynamic POD modes significances are very similar comparing each other in case of the swirl generator presence. The differences between these regimes are considerably more pronounced in case of the axial inflow. These observations are in good agreement with the captured cavitating structures. While the gradual growth of the conical cavitating vortex was observed in case of the SG presence, the changes of the cavitating patterns were significantly more complex in case of the axial inflow as it has been described in chapter devoted to the analysis of the captured cavitating patterns and cavitation cycles. Relatively interesting observation is the fact that the initial stage of cavitation is considerably more stochastic in case of the axial inflow (σ_{vel} 0.93) compared to the similar regime (σ_{vel} 0.98) considering the influence of the induced swirl. In the other words, the considerably larger part of the cumulative significance is contained within the higher POD modes in case of the axial inflow considering this regime.

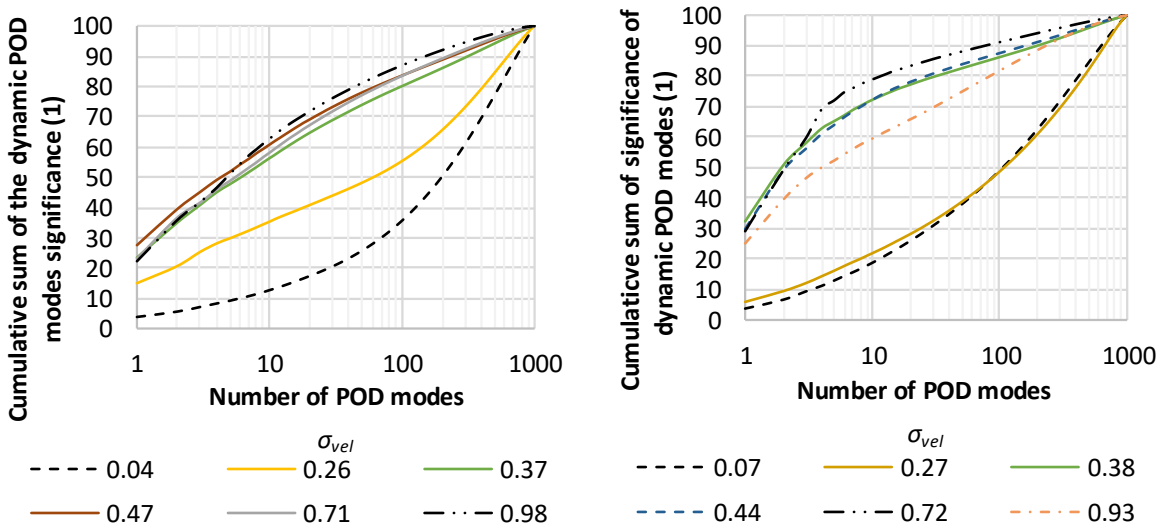

Figure 69 Cumulative sum of the dynamic POD modes significance. 6 l/s - SG (left), AX (right)

Distribution of the significance over the POD modes capturing the investigated flow dynamics (i.e. 0th mode was excluded) can be described using the charts depicting the amount of the POD modes required to reach 80 % and 99 % (for example) of the cumulative sum of significances of these modes. Charts depicting 6 l/s discharge are provided in the Figure 70.

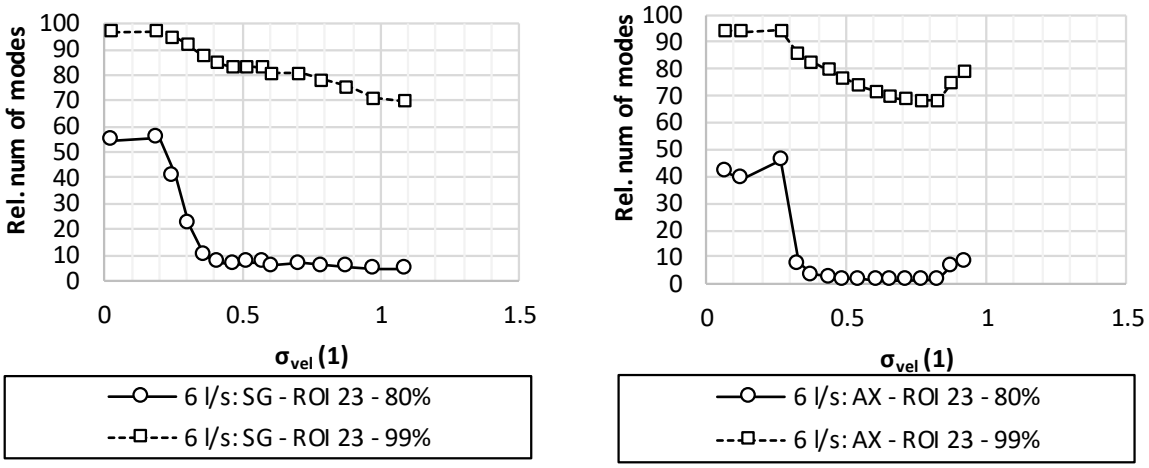

Figure 70 Relative amount of the POD modes required to reach 80 % and 99 % of the significance modes sum

Compared to the previously discussed results, it is obvious that amount of the dynamic POD modes required to reach 99 % and 80 % of the cumulative sum of POD modes significance (excluding 0th modes) is higher in case of the SG presence. This is caused by the fact that relatively large part of the cumulative significance corresponding to the captured dynamics is spread over the large amount of the higher modes.

The amount of the modes required to reach 99 % of the significance is considerably larger compared to the 80 % of significance regardless the experimental configuration. In other words, it would be necessary to use large part of the obtained POD modes to capture the small instabilities. On the other hand, it would be also possible to exploit only a minor portion of the POD modes for the reconstruction and the most important cavitating structures properly. The results of the backward reconstruction of the images using the different amount of the POD modes will be carried out at the end of the chapter.

Considering the 80 % of cumulative significance as required value, only a minor part of the POD modes is needed regardless to experimental configuration. Specifically, less than 3 % of the obtained POD modes would be required in case of the axial inflow and 6% in case of the flow affected by the swirl.

The backward reconstruction of the selected operating point has been done for both investigated configurations. Pseudocoloring using the jet color scheme was utilized in order to highlight cavitating structures (see Figure 71).

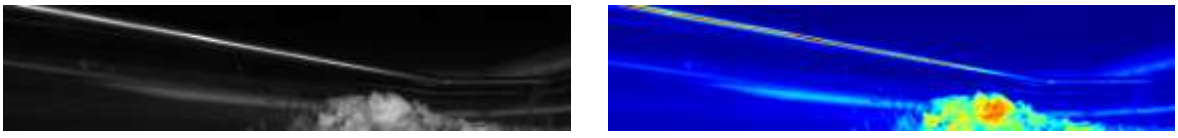

Figure 71 Result of the image pseudocoloring

The following comparison will be done using this approach in order to highlight differences caused by the different amount of the POD modes utilized for the image reconstruction. The amount of the POD modes required to reach the 80 % and 90 % of the cumulative significance in case of the selected operating points is listed in the following table.

	SG σ_{vel} = 0.884		AX σ_{vel} = 0.831	
Rel. Significance:	99 %	80%	99%	80%
Num. of Modes:	753	54	684	18

Table 3 Number of modes required for reconstruction of the original image

It can be seen that the amount of the POD modes which are required to reach 99 % of the total sum of the significance of the modes is considerably higher compared to the 80 %. The comparison of the reconstructed images considering presence of swirl generator is shown in the Figure 72.

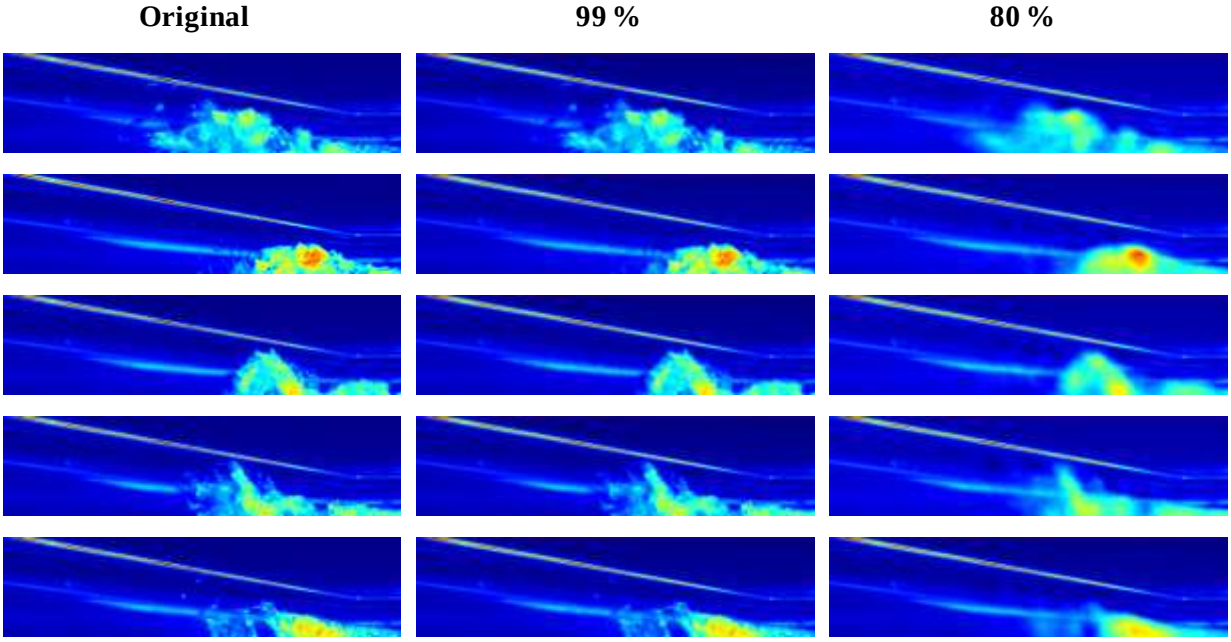

Figure 72 Example of the images reconstructed using the different amount of POD modes in case of the SG presence – 6 l/s, σ_{vel} = 0.88

The cavitating structures obtained using the higher amount of the POD modes are nearly as complex as the originally captured images. More interesting is the observation that the cavitating structures reconstructed using the significantly lower amount of modes (required to reach 80 %) are capturing the main shape of the captured cavitation properly. The information about the highly stochastic instabilities of the interface region is nearly completely lost as well as the smaller cavitating structures are not captured at all. On the other hand, the main cavitating structures can be clearly identified and compared with the originally captured flow patterns with good degree of agreement (these observations are depicted in the Figure 73 in more detail). This can be utilized for the long-term backups of the large amount of the H-S records. For example, in case of the depicted record, only 6 % of the POD modes were required to reach 80 % of significance. Thus, nearly 94 % of disk space can be spared, while the main properties of the captured cavitating structures can be potentially still studied in the future in case that the original data would be lost.

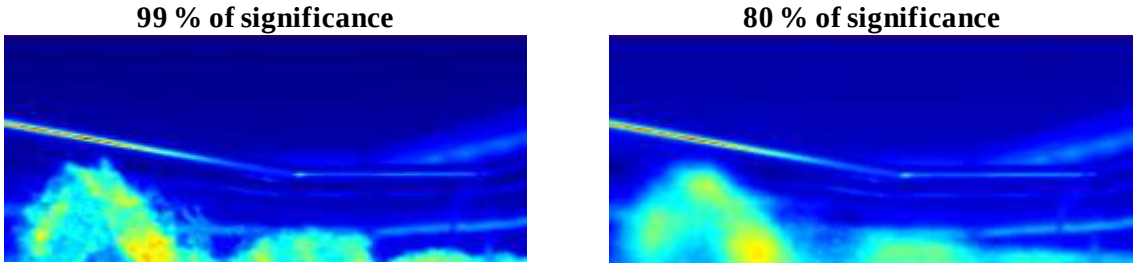

Figure 73 Detail of the helical vortex reconstructed using the different amount of POD modes in case of the SG presence – 6 l/s, σ_{vel} = 0.88

The situation is similar in case of the axial inflow as is shown in the Figure 74. Due to the different nature of the cavitating dynamics, only 3 % of POD modes were required. to reach 80 % of total significance. The separation, as well as the subsequent motion of the vortex ring within the diffuser is clearly captured in case of 80 % reconstruction. On the other hand, the smaller cavitating vortices, which can be found as remains of the collapsed vortex ring of the previous cavitation cycle cannot be identified in this case as it can be seen in the first three rows of the Figure 74.

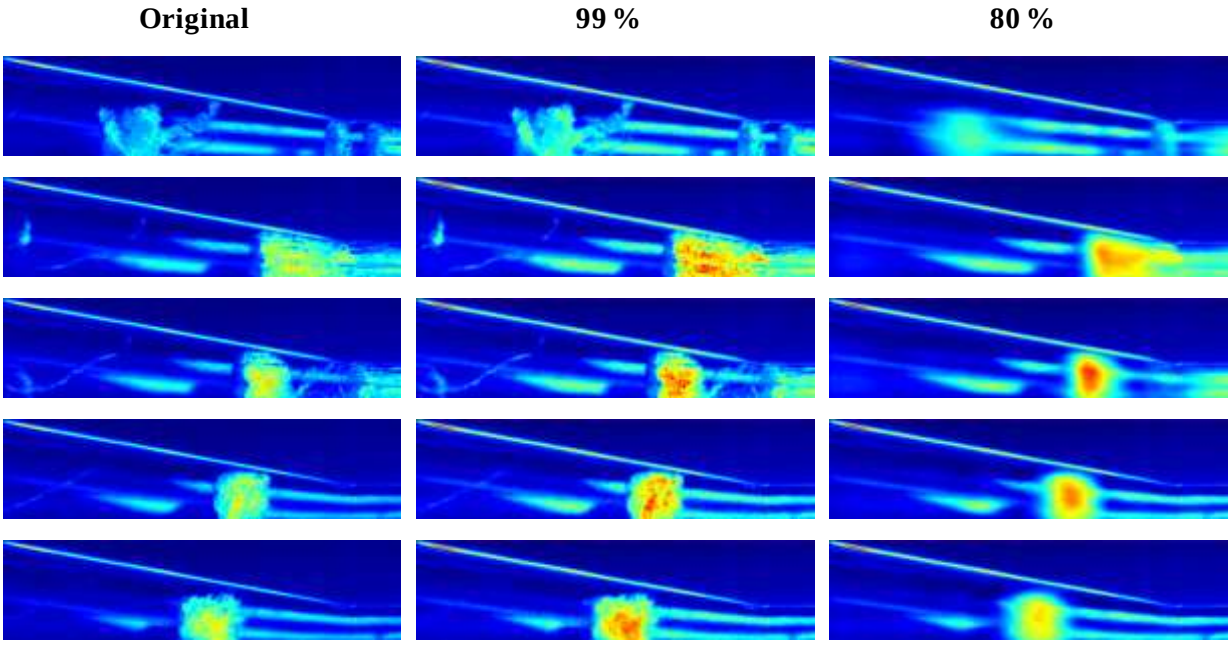

Figure 74 Example of the images reconstructed using the different amount of POD modes in case of the SG presence – 6 l/s, σ_{vel} = 0.83

Partial conclusions

The dynamics of the cavitating flow has been investigated using the POD analysis of the captured HS video records. The following preliminary conclusions can be stated:

1. The results of the dynamic analysis obtained by the POD were verified using the result of the pixel intensity DFT analysis with good degree of agreement. Therefore, it can be stated that the frequencies of the cavitation pulsations identified exploiting the POD are correct.
2. Decrease of the identified frequencies is faster in the region 3 (fully developed cavitation 2), regardless the presence of the swirl generator.
3. Dominant frequencies of the cavitating structures fluctuations are higher in case of the swirl generator presence. While the difference is relatively minor or even negligible in case of the low discharges (4 and 5 l/s), it became considerably more significant with the increasing discharge.

4. The character of the cavitating patterns corresponding to the different regimes of the cavitation and experimental configurations has been discussed using the analysis of the several parameters. The relative significance of the 0^{th} mode corresponding to the static structures (i.e. similar to the time averaged images of the captured records) proved that the fluctuations of the captured structures were considerably more significant in case of the axial inflow in general. This observation was complemented by the analysis of the relative significance of the 1^{st} POD modes corresponding to the most important (coherent) dynamic structures. Values of these parameters were considerably larger in the wide range of σ_{vel} in case of the axial inflow. In other words, the fluctuations of the most significant cavitating structures were more pronounced in case of the axial inflow, while the cavitating structures were considerably more stable when SG had been exploited.
5. Distribution of the relative significance over the dynamic POD modes (i.e. excluding the 0^{th} modes) has been investigated. Using the cumulative sum of this parameter, it was possible to assume that the overall change of the cavitation pattern is more gradual in case of the swirl generator presence. On the other hand, the supercavitation regime was clearly distinguishable investigating this parameter, regardless the experimental configuration.
6. The amount of the POD modes needed to capture the 80% and 99% of the POD modes significance has been discussed at the very end of the chapter. It was shown that the amount of the modes capturing the less important fluctuations is enormous in wide range of operating regimes corresponding to the fully developed and initial stages of cavitation considering both of the investigated configurations. On the other hand, only a minor part of the POD modes is required to reach 80% of the overall significance. Approximately 3 % of the POD modes were needed to reach this value in case of the axial inflow. The slightly higher amount (6 %) was needed to reach the same value in case of the swirl generator presence. Thus, it can be stated that the fluctuations of the cavitating structures are more significant in case of the axial inflow, while the cavitation pattems corresponding to the swirl generator presence were more stable. The images of the selected operating points corresponding to both investigated configurations were reconstructed using the amount of the POD modes corresponding to the 80 % and 99 % of the dynamic significance. It was shown, that the most important cavitating structures were captured using the small amount of the POD modes. This can be relatively useful for the storing of the large amount of the long HS records. As it was stated, using the most important POD modes it would be possible to reduce the size of the stored data of HS records by the more than 90 % in case of both investigated experimental configurations

Experimental analysis of the cavitating flow characteristics

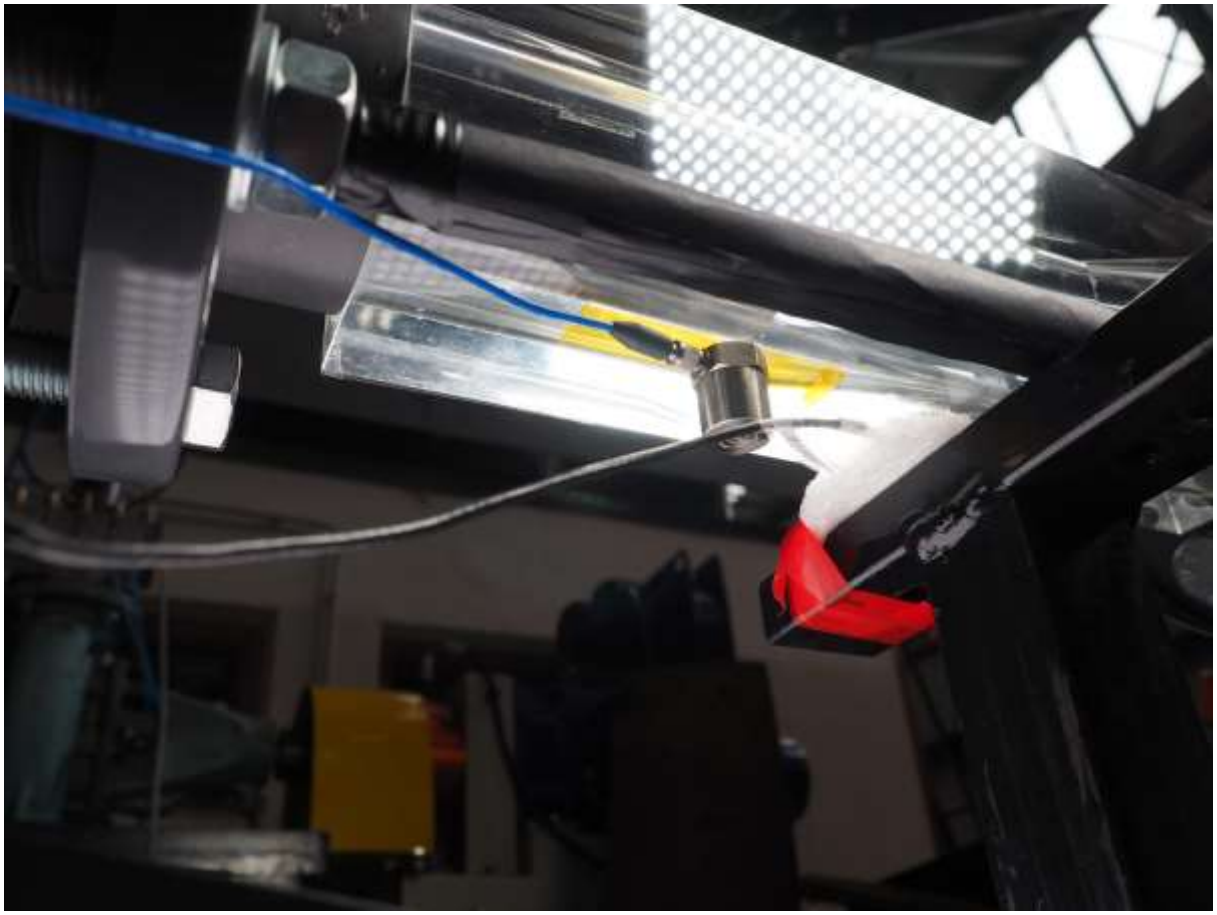

Content of the following chapter:
Time-averaged characteristics as well as the dynamics of the cavitating flow will be discussed in wide range of operating regimes using the analysis of:

1. Hydraulic losses
2. Pipe-wall acceleration
3. Acoustic pressure
4. Acoustic emission
5. Pressure pulsations

4. Experimental analysis of the cavitating flow characteristics

Considerable amount of data was acquired using the various types of transducers during the experimental measurement. The analysis of these records will be provided in this chapter. The chapter is divided into the two sections. The time-averaged signals (i.e. static characteristics of the cavitating flow) will be discussed in the first part of this chapter. The content of the second section of this chapter will be devoted to the analysis of the dynamics of obtained data. Frequency spectra as well as other properties of the signals will be provided, and signals of different transducers will be discussed and correlated. Also, the influence of the exploited definition of cavitation number will be discussed.

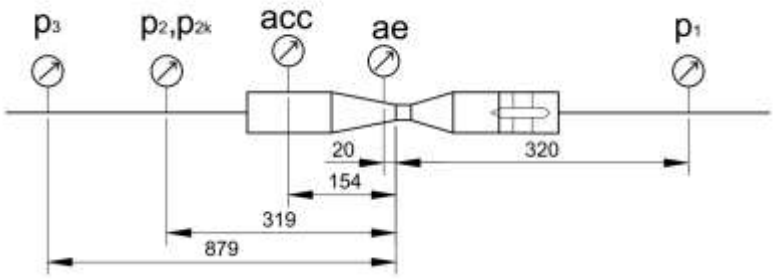

Figure 75 Placing of the transducers during the experimental measurement

Hydraulic losses will be discussed in the whole range of cavitating regimes and investigated configurations to describe the different energetic demands of the investigated configurations at first.

The hydraulic loss coefficient has been calculated using the equation (72), where the relative position of the pressure transducers to the leading edge of the throat of the nozzle is depicted in the Figure 75. Values of ξ are depicted as functions of different definitions of cavitation number in order to provide better insight into the investigated flow properties in the Figure 76.

$$\xi = \frac{p_1 - p_3}{0.5\,\rho v_{th}^2} \tag{72}$$

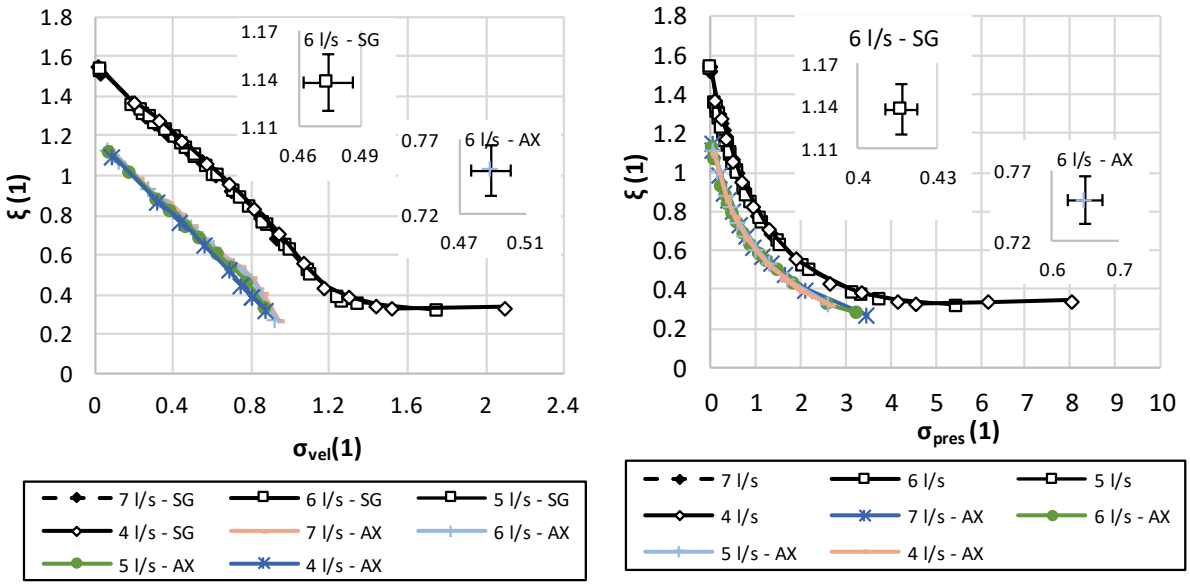

Figure 76 Comparison of the hydraulic loss coefficients shown versus differently defined cavitation numbers (as are defined by eq. (8) and (9))

It is clearly depicted that the hydraulic loss coefficients are significantly larger in case of the swirl generator presence, regardless the exploited definition of cavitation number. This is caused due to the additional minor loss of the SG as well as due to the modified flow field downstream the swirl generator. It can be stated that the difference between the courses corresponding to the different experimental configurations is considerably more significant in case of σ_{vel} exploitation. This is caused by the calculation of the dimensionless parameters, where the relatively important part of the flow kinetic energy devoted to the swirling motion is neglected in case of the SG presence. This discrepancy will be studied and discussed using the numerical analysis in the chapter 5.
The definition of σ_{vel} had been exploited in many contributions published by the author of the thesis [57] (for example) and Rudolf [8] investigating the same or similar geometries of the nozzle. Thus, the definition of σ_{vel} will be preferred in the following text. The most important discrepancies will be described using the comparison with the results utilizing σ_{pres}, while the correction will be carried out using the numerical analysis in the in the chapter 5.

As it can be seen, the transition between the non-cavitating regime and initial stage of the cavitation can be clearly distinguished in case of the induced swirl presence in case of σ_{vel} utilization (see top left chart in the Figure 77). This transition is significantly more gradual considering the other definition of cavitation number. On the other hand, the slight decrease of the hydraulic losses connected with the inception of cavitation can be found in both depicted charts. For instance, the evaluated loss coefficient considering the discharge of 4 l/s corresponding to the non-cavitating conditions (σ_{vel} 2.103) of investigated flow is 0.338 while the hydraulic loss coefficient of the initial cavitation (σ_{vel} 1.521) 0.328 is lower by 3 % approximately.

Further increase of the ξ values is nearly linear down to the lowest values of the investigated σ_{vel} regardless the investigated experimental configuration or flow rate. It is not possible to clearly distinguish the cavitation regimes using the courses of ξ. Comparisons of the hydraulic loss coefficients based on the experimental configuration are shown in the Figure 77 for 4 l/s and 6 ls/.

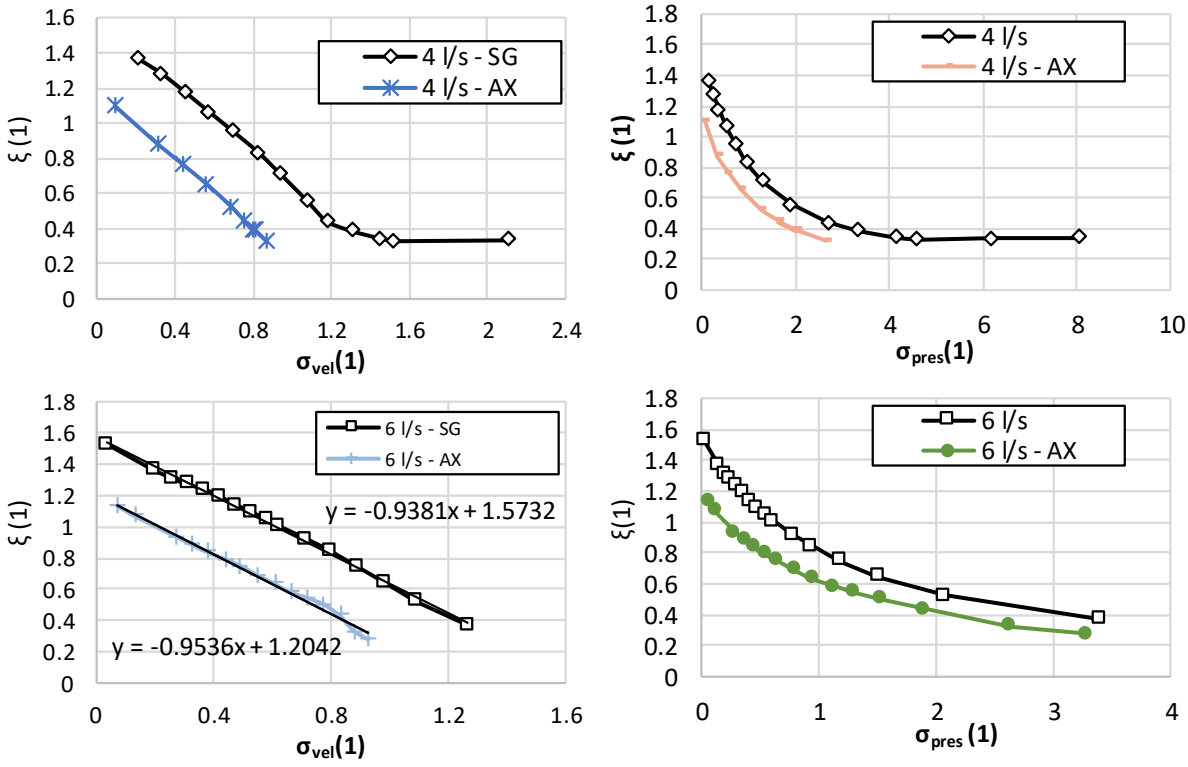

Figure 77 Comparison of hydraulic loss coefficients based on the experimental configuration

Partial conclusions

The results of the hydraulic loss coefficients ξ analysis were depicted versus different definitions of cavitation numbers.

I. Significant qualitative discrepancy based on the definition of the exploited cavitation number was found and described. The exploitation of the v_{bulk} is problematic in case of the flow affected by the induced swirl. This will be discussed and analysed using the CFD simulations.

II. It is possible to identify transition between the non-cavitating and initial stage of cavitation due to the slight decrease of the hydraulic loss coefficient. On the other hand, it is not possible to distinguish different stages of cavitation based on the change of the ξ behaviour.

III. The slope of the hydraulic losses increase with the decreasing values of cavitation number σ_{vel} is nearly the same regardless the experimental configuration. It is shown using the linear approximation of the courses of ξ corresponding to the discharge of 6 l/s. As it is shown, the difference between the values of the slopes is 1.6 %.

4.1. Time-averaged characteristics of the cavitating flow

This section will be focused to the analysis of the time-averaged magnitudes of the fluctuations of acquired signals in order to discuss and characterize the flow properties based on the different experimental configurations and regimes of the cavitation. For this purpose, the signals of pipe-wall acceleration, acoustic emission and noise will be investigated. The results will be depicted for the whole range of investigated operati. Deeper analysis will be carried out for discharges of 4 l/s and 6 l/s. The following results are discussed mainly using the σ_{vel} definition of cavitation number.

4.1.1. Pipe-wall acceleration

As it was mentioned the accelerometer Aura SV129022 exploited for the investigation of the pipe-wall acceleration was mounted to the surface of the transparent nozzle using the acrylic adhesive and thin tape, which protected the surface of nozzle. The transducer was mounted close to the end of the diffuser to capture the vibrations induced by the motion of cavitating structures. Accelerometer was glued to the bottom surface of the nozzle protected by the Kapton tape. Thus, it was still possible to capture the HS-records from the side of the nozzle. The plots of the time-averaged values of magnitude of the pipe wall acceleration fluctuations a are depicted in the following charts for both investigated experimental configurations.

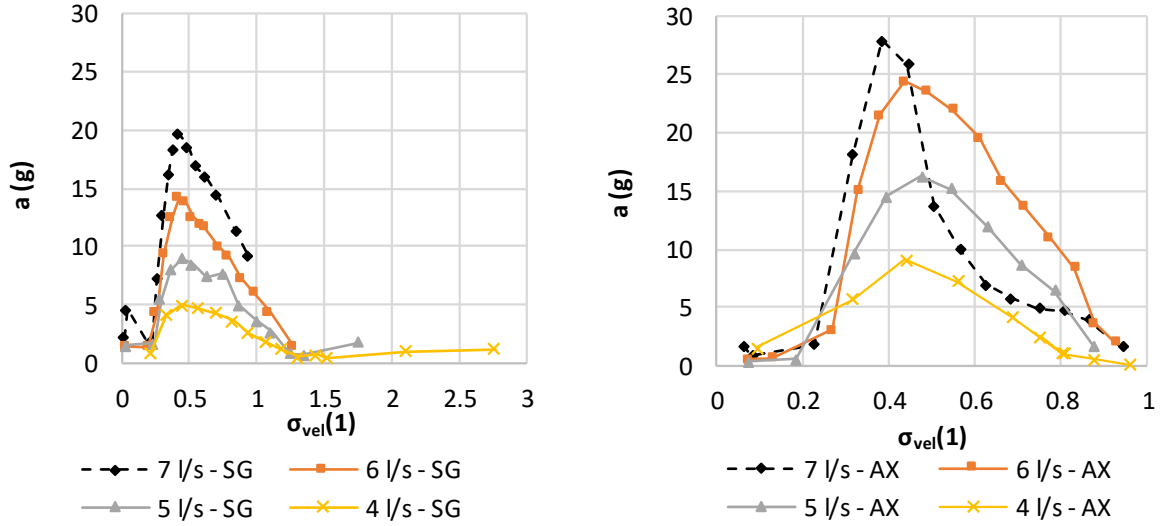

Figure 78Mean values of the pipe-wall acceleration captured in case of SG presence (left) and axial inflow (right)

The course of the mean values of the magnitude of the pipe wall acceleration fluctuations (dynamic component of the acquired signal) a corresponding to 6 l/s was exploited for the definition of the regions of typical cavitation patterns as it has been described. This quantity is referred as acceleration (or pipe-

wall acceleration) in the text and described conclusions are valid in the whole range of investigated flow rates. The observed values of pipe wall acceleration are the higher; the higher is the investigated discharge as it can be seen in the Figure 78. The acceleration is more intensive in case of the axial inflow. With the occurrence of the cavitation in the region 1 the *a* started to increase. The gradual increase of the *a* with the decreasing value of the investigated cavitation number can be found in the region 2. The gradual, but steep decrease of the observed vibrations was observed in the region 3 (characteristic by the presence of the massive cavitating structures). It can be assumed, that this drop of the pipe wall acceleration is caused by the significant presence of the gaseous phase within the flow of the water. In other words, the compliance of the mixture is significantly reduced by the presence of the massive gaseous volume within the flow. The vibrations corresponding to the region 4 (i.e. to the transition between the fully developed stage of cavitation and supercavitation) are relatively small due to the stability of the flow disturbed only by the occasional collapses of the cavitating structures. This is even more significant in case of the supercavitation regime (region 5).

While the obtained courses of the pipe wall acceleration are in good qualitative agreement regardless the investigated discharge in general, slightly different tendency can be observed in case of the axial inflow and the discharge of 7 l/s. This difference is particularly significant between the values of σ_{vel} 0.44 and 0.87. It can be assumed that this has been caused due to the oversaturation of the accelerometer by input signal during this particular measurement and therefore the results of this analysis should be interpreted cautiously.

Comparing the charts corresponding to both investigated configurations, the vibrations were considerably more severe in case of the axial inflow, which caused by the nature of the observed cavitating structures as it has been described in the chapter devoted to the analysis of the captured HS video records. Direct comparison of the investigated configurations is provided in the Figure 79 depicting the the 4 and 6 l/s flow rates. Courses of the mean value of the pipe wall acceleration fluctuations are depicted versus both types of the cavitation number.

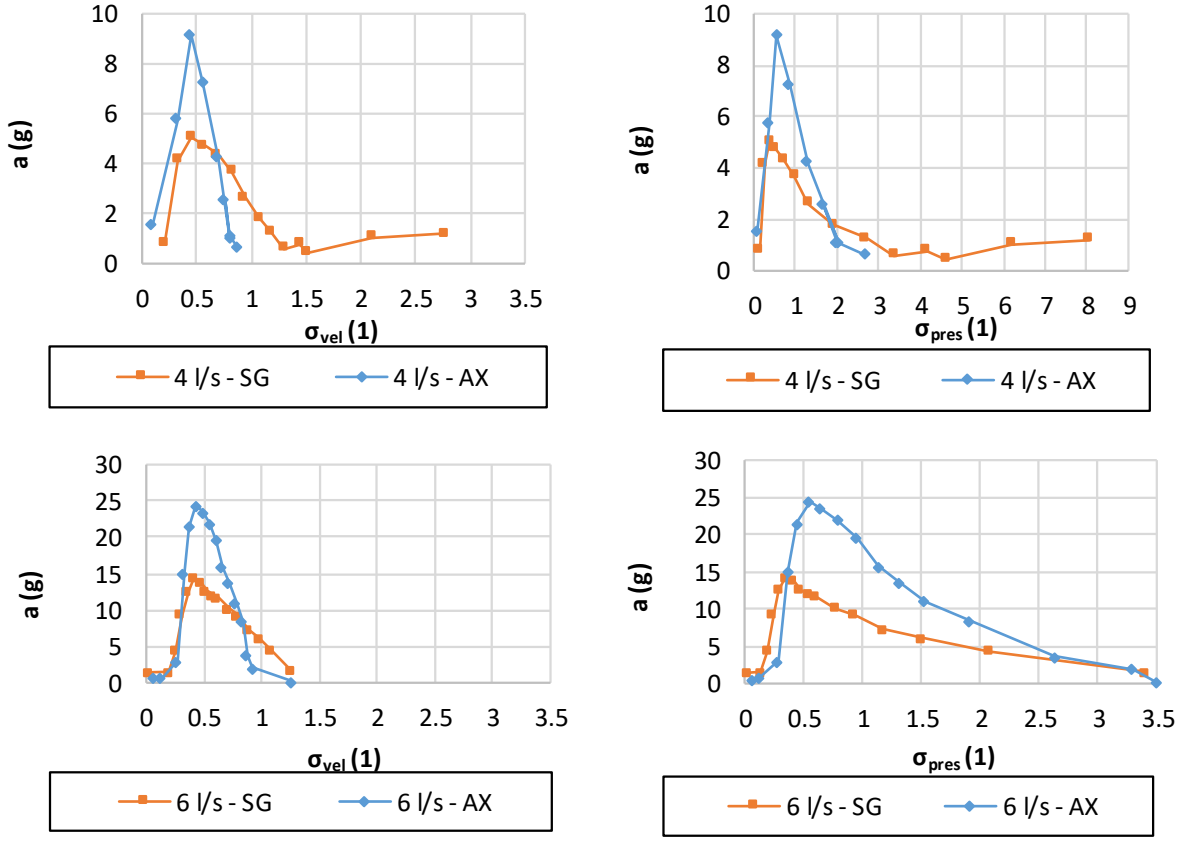

Figure 79 Comparison of pipe-wall acceleration based on the experimental configuration

First of all, it can be stated that the maximum observed values of a corresponding to the axial inflow were significantly higher. This discrepancy reaches 81.11% in case of 4 l/s discharge, while in case of the 6 l/s is lower, but still significant (71.01 %). Comparing the charts exploiting different definitions of cavitating number the important discrepancy between the positions of the maximum values of the vibrations can be found. While in case of the σ_{vel}, the position of these peeks is in good agreement regardless the investigated experimental configuration, the significant shift can be found in case of the σ_{pres} exploitation. This shift reaches approximately 49% of σ_{pres} value based on the actual flow rate, whereas the maximum value of vibrations corresponds to the lower value of σ_{pres} in case of SG presence. This particular discrepancy will be discussed using the results of CFD analysis. On the other hand, the other observations are valid and in good qualitative agreement using both of the exploited definitions of cavitation number.

Seeing the courses of observed pipe wall acceleration, it can be stated that vibrations induced by the cavitating flow were more severe in case of the axial inflow in general. The only exception is the initial stage of cavitation (region 1) and part of the region 2 corresponding to the fully developed cavitation. This observation is in good agreement with the described cavitating structures. While in case of the lower values of cavitation numbers, the structures corresponding to the swirl generator presence were considerably more compact, in case of the initial stage of cavitation the relatively stable cavitating boundary layer was observed in case of initial stage of cavitation. On the other hand, the fluctuations of the cavitating structures were better distinguishable in case of the region 1 considering the presence of the swirl generator. Interesting is the comparison of the initial part of the region 2, where the vibrations induced by the relatively small, but fully developed vortex ring are smaller than the vibrations corresponding to the cavitating structures affected by the induced swirl down to the σ_{vel} value of 0.83 in case of 6 l/s and 0.69 in case of the 4 l/s.

Attention should be devoted to the first and second region which were captured in detail during the measurement of 4 l/s flow rate and presence of the swirl generator (see Figure 80). The mean value of the pipe wall acceleration is slightly higher in case of the highest values of cavitation number (σ_{vel} 2.77 and 2.10) corresponding to the thin cavitating vortex filament with helical vortex breakdown downstream the throat of the nozzle. With the decreasing values of cavitation number (σ_{vel} 1.52 and 1.30), the cavitating vortex became considerably thicker to the less developed regime of cavitation and the value of a starts to decrease relatively significantly. The helical vortex breakdown is far less significant in case of this cavitation pattern in general and it was hardly observable in some moment of the recorded HS video (see the photo 3 in Figure 80) . Detected mean value of the pipe-wall acceleration remained lower compared to the highest investigated values of cavitation number until the complete transition of the straight cavitating vortex to the form of conical cavitating vortex which is accompanied with the periodical axial collapses of this structure. This regime was reached with the σ_{vel} of 1.18.

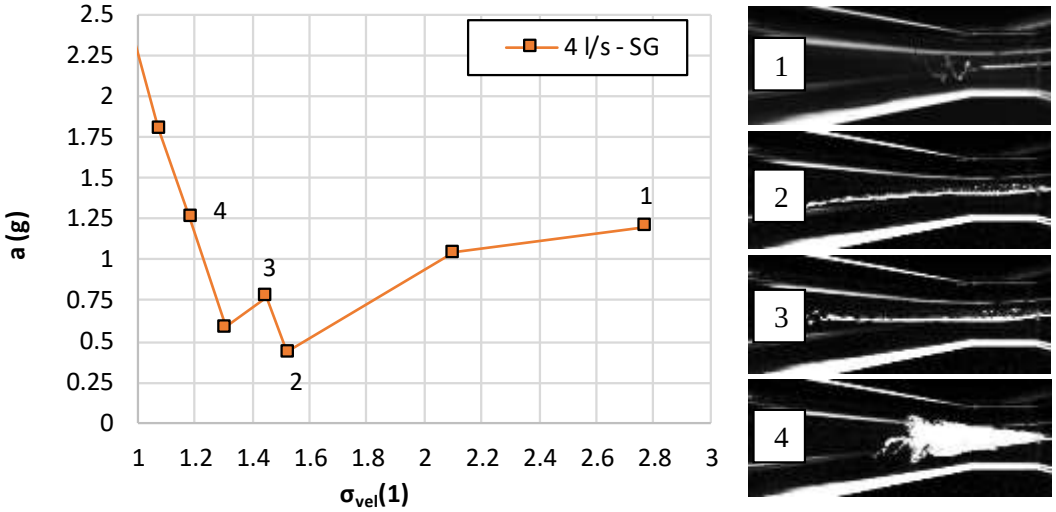

Figure 80 Pipe-wall acceleration in case of the initial stage of cavitation

Partial conclusions

The analysis of the time-averaged values of the pipe-wall acceleration have been carried out and discussed. As it has been shown the obtained data provide interesting observations, therefore it is possible to do several preliminary conclusions:

I. First of all, it is possible to distinguish several regions corresponding to the different cavitation regimes using the analysed vibrations, regardless the investigated experimental configuration.
II. Time-averaged magnitude of fluctuations of pipe wall acceleration (will be referred as acceleration) is higher in the considerable part of investigated cavitation regimes in case of the axial inflow. The maximum values considering 6 l/s discharge are following: Axial inflow 24.42 g, Swirl generator 15.03 g. The relative difference is 71.01 %, thus it can be stated that the vibrations corresponding to the axial inflow can be considerably more severe during the transition from region 2 to region 4. The relative difference corresponding to the lower discharge of 4 l/s is 81.11 %.
III. Different positions of the maximum values based on the exploited definition of cavitation number has been described. Positions of the maximum magnitudes of acceleration corresponding to the different experimental configurations were constant (the difference was negligible compared to the scatter of the investigated operating points) in case of the σ_{vel}. On the other hand, the values of the cavitation number corresponding to the maximum vibrations were significantly lower in case of the swirl generator presence when σ_{pres} was used for the analysis. It can be assumed that this qualitative discrepancy is caused by the v_{bulk} exploitation for the computation of σ_{vel}, where the significant swirl was neglected in case of SG presence. This observation will be discussed using the numerical analysis.
IV. The values of the acceleration corresponding to the cavitating flow influenced by the upstream mounted swirl generator are higher compared to the axial inflow in the minor part of the investigated cavitation regimes (mainly region 1 – initial phase of cavitation). The cavitating structures corresponding to the axial inflow are relatively stable in case of the axial inflow as it has been shown in chapter 2.3.1. When the swirl is introduced by the swirl generator it is possible to detect helical form of vortex breakdown downstream the thin cavitating vortex or precessing vortex similar to the cavitating vortex, which can be observed downstream the runner of Francis turbine under the full-load operation (in case of the region 1).

V. The particular effort has been devoted to the description of the initial stage of cavitation in case of 4 l/s discharge influenced by SG presence. Transition between the thin cavitating vortex filament with clearly distinguishable helical vortex breakdown and the long axisymmetric cavitating vortex accompanied by a decrease of the intensity of vibrations was captured. It can be assumed that the decrease of the measured time-averaged value is caused by the distinction of the helical vortex breakdown and simultaneously by the occurrence of the more massive and stable cavitating structure, which can play a role in vibrations dampening. The further increase of the vibrations can be observed with the transition of the cavitating pattern to the form of periodically collapsing conical cavitating vortex with the helical vortex at its end.
VI. The accelerometer has been oversaturated during the investigation of 7 l/s discharge considering the axial inflow. The solution would be the change of the transducer position. On the other hand, it shows the difference between the investigated experimental configuration due to the fact the data obtained for the same discharge were valid when the swirl generator has been exploited.

4.1.2. Acoustic pressure

The analysis of the time-averaged acoustic pressure p_{ac} was carried out in same manner as the above described analysis of the time-averaged values of the pipe-wall acceleration fluctuations. The acoustic pressure has been measured using the microphone PCB 378B02 which has been placed 70 cm from the throat of the nozzle to capture noise induced by the cavitating flow.
It should be mentioned that the ambient conditions were not ideal. The test section was not acoustically isolated, which was crucial flaw during the investigation of several operation points corresponding to the initial stages of cavitation as well as to the supercavitation. As it has been mentioned, the cavitating structures are relatively stable during these regimes, therefore the ambient noise (i.e. noise induced by the pump, noise of various activities ongoing in the laboratory etc.) became dominant. It was particularly significant in case of the 4 l/s discharge considering the presence of the SG. Since the result obtained for this configuration will be described but omitted from the overall analysis.

The charts depicting the overall results are provided in the Figure 81. The magnitude of acoustic pressure fluctuations induced by the cavitation affected by the swirl is several times lower compared to the axial inflow. This is in good agreement with previously discussed results as well as the subjective feeling of experimental measurement (i.e. it was far more acoustically comfortable to spend longer time close to the experimental rig during the measurement, when the swirl generator was exploited).

Compared to the previously discussed results of pipe-wall acceleration analysis, it can be stated that the depicted courses of the acoustic pressure versus cavitation number σ_{vel} are in relatively good qualitative agreement with the acceleration in case of the axial inflow. In other words, the gradual increase of the acoustic pressure can be found in the region 1 and 2 (i.e. in the region of initial cavitation as well as in the region of fully developed cavitation typical by periodical separation of cavitating vortex rings). Gradual increase continues up to the certain moment. Above that, compared to the pipe-wall acceleration analysis, the maximum values of acoustic pressure are shifted into the region 3 (i.e. region of massive cavitating clouds). It is in good agreement with the personal observation, where it was possible to hear typical noise similar to sound of whip prior the beginning of transition between the fully developed cavitation and supercavitation.

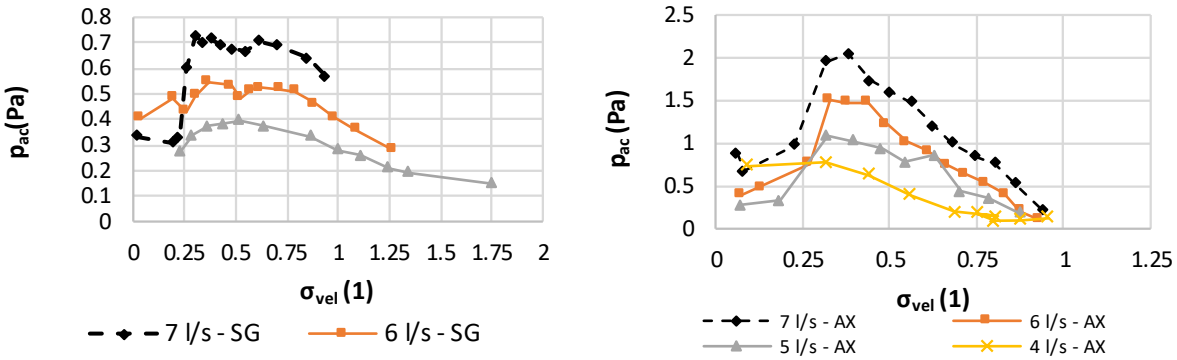

Figure 81 Values of mean acoustic pressure depicted as a function of σ_{vel}

The situation is completely different in case of the SG presence. Compared to the axial inflow and corresponding analysis of the pipe-wall acceleration we can see that the initial increase if the acoustic pressure is relatively steep and the obtained values of the magnitude of the acoustic pressure fluctuations became relatively stable in the region of fully developed cavitation. This is particularly visible in case of the 6 l/s and 7 l/s discharges. As it has been described, the cavitating structures share the same nature within this range of cavitation numbers when the additional swirl is introduced by the generator. The only major difference is size of the typical conical cavitating vortices which are the more massive the lower is cavitation number. The time-averaged values of the acoustic pressure pulsations became low during the transition between fully developed cavitation and supercavitation regardless the investigated experimental configuration. Direct comparison of the analysis of acoustic pressure fluctuations with the above described results of the *a* analysis considering discharge of 6 l/s are depicted in the Figure 82.

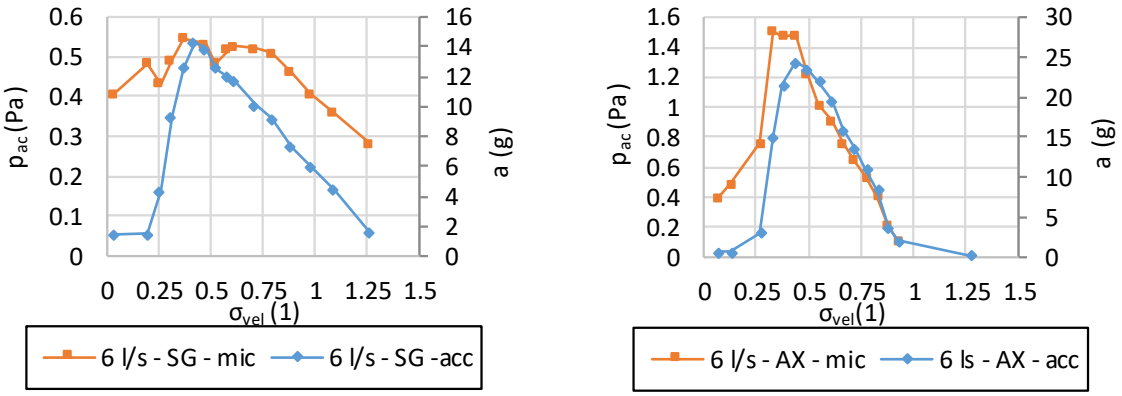

Figure 82 Mean values of acoustic noise in comparison with the mean values of the pipe-wall acceleration

Direct comparison of the acoustic pressures induced by the cavitating flow based on the experimental configuration as well as the chart of the same values depicted as functions of the σ_{pres} are depicted in the Figure 83.

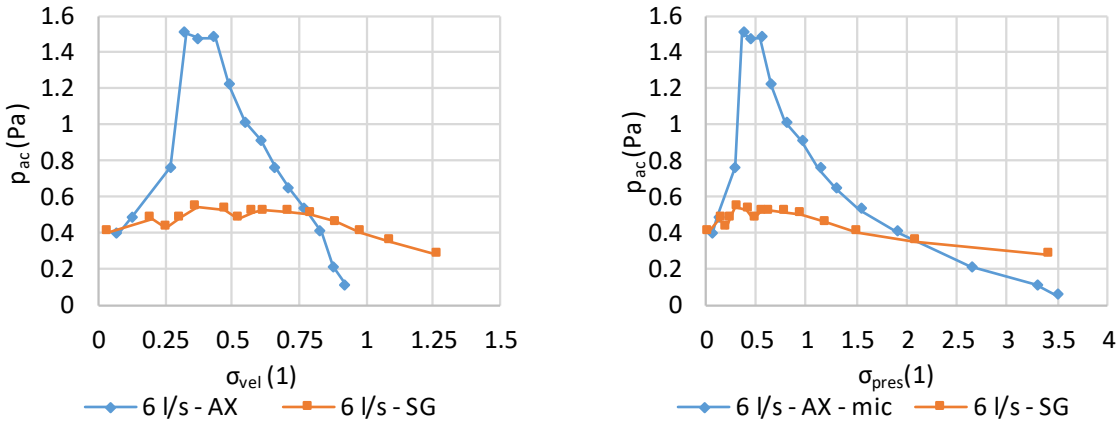

Figure 83 Acoustic pressure induced by cavitation – comparison of different experimental configurations depicted as versus σ_{vel} (left) and σ_{pres} (right)

Similarly, to the analysis of the pipe-wall acceleration, the fluctuations of the acoustic pressure are several times higher in case of the axial inflow in the region of the fully developed cavitation. Interesting observation can be found in case of the higher values of cavitation number close to the initial regime of cavitation. The mean value of the acoustic pressure fluctuations is larger in case of the SG presence similarly to the pipe-wall acceleration analysis in this region. Comparing the position of the intersection of the acoustic pressure courses with the intersections of the mean values of the pipe-wall acceleration fluctuations based on different experimental configurations, it can be seen that the position of the intersection is slightly shifted to the region of more developed cavitation in case of the acoustic noise analysis. This is in in good agreement with the shift of the position corresponding to the maximum mean value of the acoustic pressure fluctuations compared to the mean pipe-wall acceleration; which is depicted in the Figure 82.

The results of the 4 l/s discharge with the upstream mounted swirl generator were excluded from this analysis. This was caused by the fact, that the results were highly influenced by the ambient conditions thanks to the low intensity of the noise induced by the cavitation together with the absence of the ambient noise insulation.

The acoustic pressure can be converted to sound level *Lp* using the using the following equation:

$$L_P = 20\ ln\left(\frac{p_{ac}}{p_0}\right) \tag{73}$$

Where p_{ac} is devoted to the acoustic pressure and *p0* represents reference sound pressure 20 µPa. The max maximum sound level 100.2 dB corresponds to fully developed regime (σ_{vel} 0.38) in case of the 7 l/s flow rate. The maximum sound level obtained in case of the swirl generator presence was 91.2 dB (7 l/s, σ_{vel} 0.30).

Partial conclusions

I. Following observations can be described by the comparison of the obtained results with the analysis of *a*. The results of the mean acoustic pressure fluctuations values show slight shift of the operating points corresponding to the maximum values. The similar shift can be observed in case of the regimes corresponding to the states when the acoustic noise fluctuations of the cavitating flow influenced by SG are more significant compared to the axial inflow. Due to the fact, that both of these shifts tend towards smaller values of cavitation number, it can be assumed that changing of the cavitating flow nature manifests in to the change of vibrations slightly earlier than into the change of the noise characteristic induced by the cavitating flow.

II. The mean values of acoustic pressure fluctuations are considerably lower in case of the cavitating flow influenced by the swirl generator. From the qualitative point of view, the acoustic pressure fluctuations are considerably more stable in case of the SG presence, compared to the axial inflow where the region gradual acoustic pressure fluctuations increase is considerably wider.

4.1.3. Pressure records analysis

The pressures records analysis which will be carried out in this section will be slightly more complex compared to the analysis of the acoustic pressure records and pipe-wall acceleration records.

Beside the analysis of the time-averaged values of magnitude of pressure pulsations (p_{fluct}) recorded by the Kistler 211 B4 transducer downstream the throat of the nozzle which will be done in the same manner as the previous section of this chapter, the analysis of the time-averaged values of the pressure recorded using the transducers p_1, p_2 and p_3 (BD – DMP 331) together with pressure drops p_1-p_2, p_1-p_3 and ratios of the p_2 and p_3 to provide additional information of the cavitating flow properties as well as to justify the choice of the p_3 records for the characterization of the investigated cavitating flows (i.e. for the evaluation of the properties such as hydraulic loss coefficients and cavitation numbers).

The time-averaged values of the pressure fluctuations of the various investigated discharges are depicted in the following chart in the Figure 84.

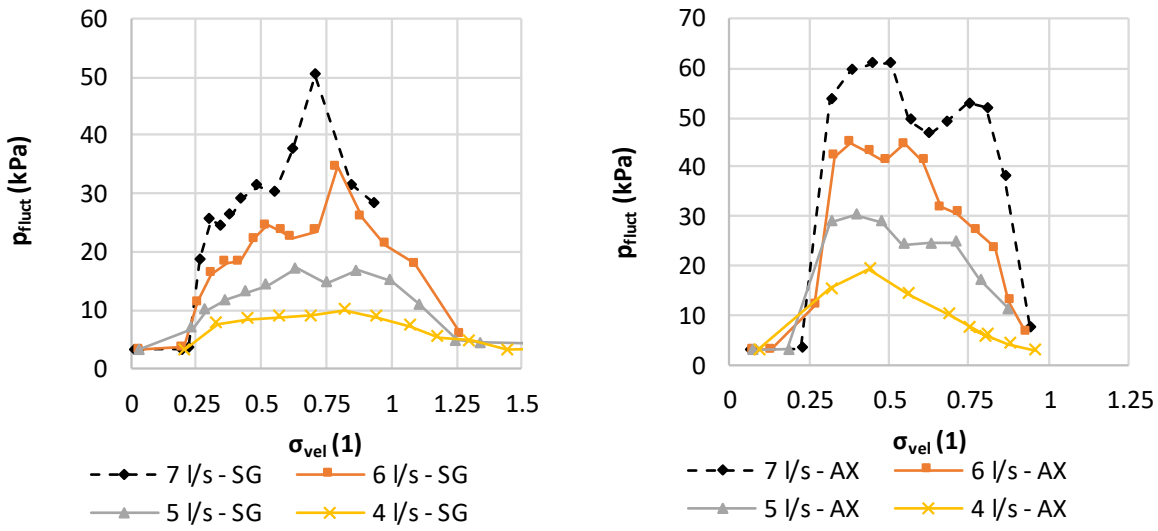

Figure 84 Time averaged values of the pressure values in case of the SG presence (left) and axial inflow (right)

The courses of the time-averaged values of the pressure fluctuations are different compared to the above described properties, regardless the investigated configuration. The occurrence of the coherent cavitating structures is connected with the rapid increase of the mean p_{fluct}. The maximum values of p_{fluct} correspond to the region 2 (i.e. region of fully developed cavitation). Gradual decrease of the p_{fluct} follows in case of the SG presence. On the other hand, in case of the axial inflow another region of the p_{fluct} growth can be found close to region 3.

In contrast to the previously discussed properties of the cavitating flow, the difference between the maximum values corresponding to the different experimental configurations is not so significant. Nevertheless, the maximum values corresponding to the axial inflow are still notably higher. This is particularly visible in case of the higher discharges (6 l/s, 7 l/s).

Direct comparisons of the mean p_{fluct} courses corresponding to the flow rates of 6 l/s and 4 l/s are depicted versus σ_{vel} as well as σ_{pres} in the Figure 85 and Figure 86 respectively.

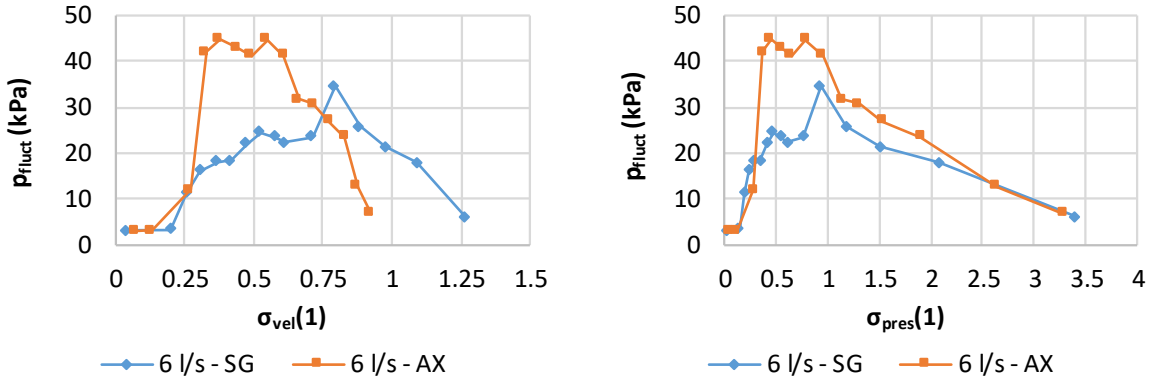

Figure 85 Time averaged values of the pressure fluctuations based on the experimental configuration in case of 6 l/s flow-rate depicted as a function of σ_{vel} (left) and σ_{pres} (right)

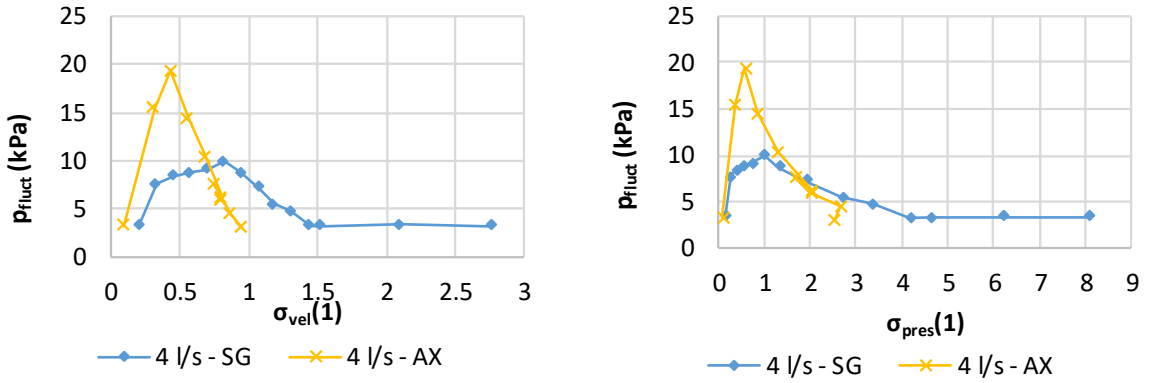

Figure 86 Time averaged values of the pressure fluctuations based on the experimental configuration in case of 4 l/s flow-rate depicted as a function of σ_{vel} (left) and σ_{pres} (right)

Comparing the charts exploiting different definitions of cavitation number, relatively significant discrepancy within the region of less developed cavitation can be identified. While in case of the σ_{vel} the magnitude of p_{fluct} corresponding to the axial inflow is significantly lower compared to the SG presence, the difference is not so significant in case of the σ_{pres}. This discrepancy will be discussed using the numerical analysis, due to the fact that considerable swirl is excluded from the computation of σ_{vel} in case of the SG presence.

As it has been mentioned the records of the pressure transducer p_3 have been chosen as source of the reference pressure for the computations of characteristic parameters of the cavitating flow such as hydraulic loss coefficients and cavitation numbers. It can be explained using the charts of the pressure records. For example, by the comparison of the ratio *p2/p3* corresponding to the different discharges depicted in the Figure 87 versus $\sigma_{vel,}$ the reason is relatively obvious. The value of ratio *p2/p3* is close to the 1 in case of the initial stage of the cavitation since the major loss between the transducer is low. In other word the choice of the transducer would not influence the obtained results in this case.

On the other hand, the significant drop of the pressure ratio value can be identified before the transition to supercavitation. This is particularly visible in case of the SG presence. In other words, the values of the cavitation number and coefficient collapse to the zero before reaching of the stable supercavitation. For that reason, it would be highly problematic or even impossible to distinguish supercavitation regime and transition between the fully developed cavitation and supercavitation based on the evaluated cavitation numbers using the pressure records of p2 transducer. The observed drop of the pressure ratio is caused by the fact that the cavitating structures reached the position of p2 transducer prior the transition to the stable supercavitation. Relatively interesting is also the comparison of the ratio prior the above described drop of its value. The value of the ratio is nearly constant for the whole range

of the investigated cavitation numbers in case of the axial inflow. The situation is slightly different in case of SG presence, where mild increase of the pressure ratio value can be found. This increase is more rapid close to the observed ratio drop. It can be assumed that this increase is caused by the significant redistribution of the flow field affected by the presence of the induced swirl. Above that, as it has been described in the chapter devoted to the analysis of the cavitation patterns, the cavitating vortex is significantly more compact compared to the axial inflow, which can be characterized by the distinguishable separation of the large cavitating structures. Thus, the stable presence of the cavitation can influence the time-averaged flow field close to the transducer more significantly in case of the induced swirl presence.

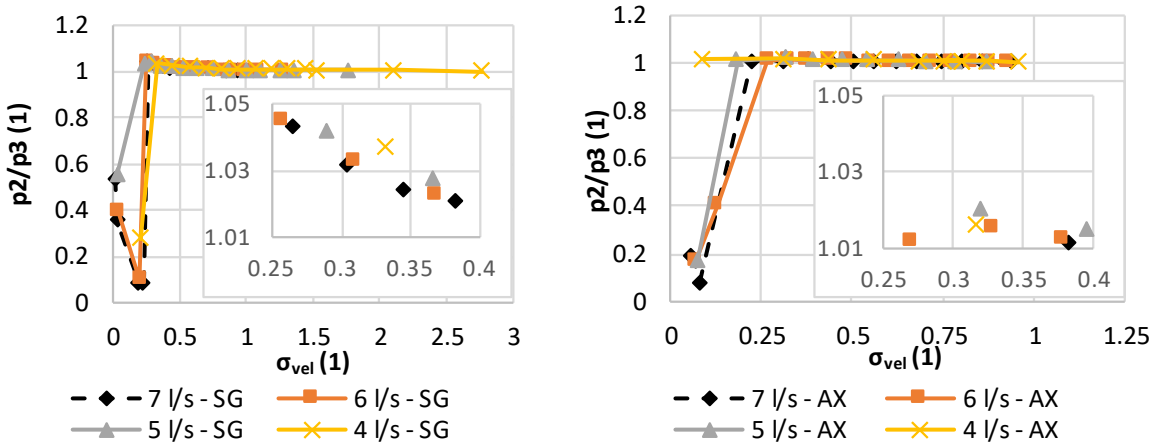

Figure 87 p2/p3 *ratio corresponding to the different discharges depicted as a function of* σ_{vel} *in case of SG presence (left) and axial inflow (right)*

As an additional information the charts of the time-averaged records of p_1, p_2 and pressure drop between these two transducers are depicted in the following figures.

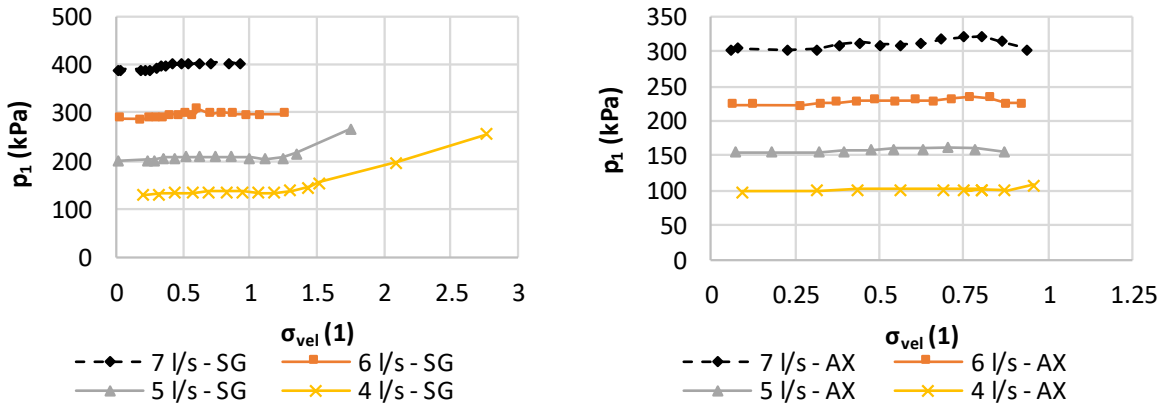

Figure 88 Static pressure measured by the pressure transducer p_1 *during the experimental campaign. SG (left) and AX (right)*

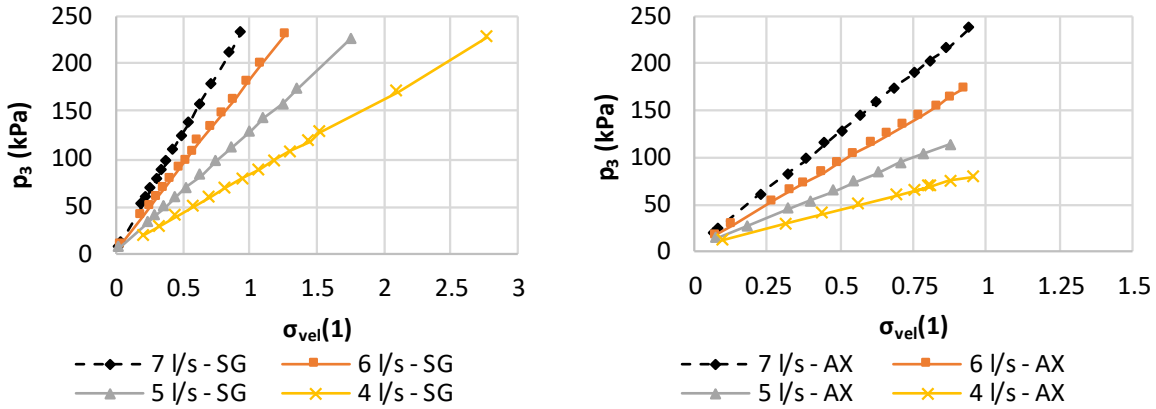

Figure 89 Static pressure measured by the pressure transducer p_3 during the experimental campaign. SG (left) and AX (right)

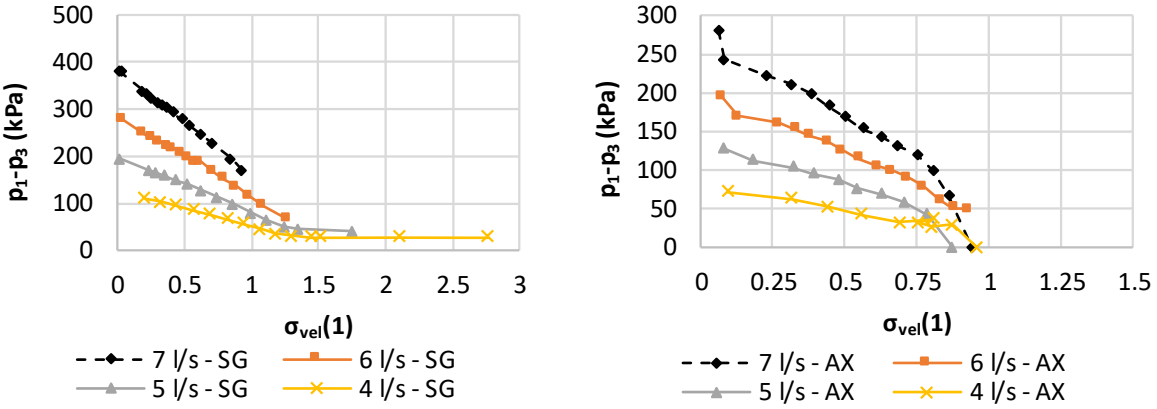

Figure 90 Pressure drop corresponding to the wide range of experimentally investigated operating points. SG (left) and AX (right)

Partial conclusions

I. Based on the charts depicted in the Figure 84 it can be stated that the considerable presence of cavitation within the flow is connected with the significant increase of the time-averaged p_{fluct} value regardless the investigated configuration. On the other hand, the maximum values of time-averaged p_{fluct} correspond to the different regimes of cavitation based on the investigated configuration as it can be seen in the Figure 85 and Figure 86.

II. The values of the time-averaged p_{fluct} are considerably larger in case of the axial inflow, which is in good agreement with the above described properties of the investigated cavitation regimes as well as with the nature of the cavitating patterns corresponding to the different experimental configurations.

III. Significant qualitative discrepancy of the obtained results based on the exploited cavitation number definition has been described. This will be further discussed using the CFD analysis of the cavitating flow.

IV. The mean value of the p_{fluct} is low under the supercavitation regime which is characteristic with the high stability of the cavitating structures regardless the experimental configuration.

V. The exploitation of the p3 transducer for the cavitating flow properties characterization has been explained using the charts of the p_2/p_3 time-averaged values. As it has been shown, it would not be possible to distinguish the supercavitation and transition to the supercavitation using the records of p_2 transducer.

VI. Redistribution of the flow caused by the presence of the swirl was described using the time-averaged p_2/p_3 ratios. As it was shown in the detail of the charts in the Figure 87. Different behaviour of the ratio was described based on the experimental configuration (redistribution of the flow in case of the SG presence)

4.2. Dynamics of the cavitation

Despite the fact that the results of the time-averaged properties discussed in the previous chapter provide rich source of information about the nature of the cavitating flow as well as about the influence of the swirl induced by the upstream mounted swirl generator, the main reason for the investigation was to analyse the cavitation dynamics. For this purpose, the variance *var* (common designation of σ^2 is not applied to prevent confusion with the cavitation number) of the fluctuations will be analysed briefly to provide insight into the statistical properties of the recorded signals corresponding to the different experimental configurations and for the different stage of the cavitation development. The variation *var* has been calculated using the built-in *numpy.var* function (eq. (74)) during the post-processing of experimental data. The variance represents spread of the signal distribution. In other words, the analysed signal is the more fluctuative, the higher is value of variance.

$$var = \frac{\sum (x - \bar{x})^2}{N} \tag{74}$$

Where x represents the analysed signal, $\bar{x}$ is the mean value of this signal and N represents number of the exploited samples.

Above that, the dominant frequencies and power spectrum densities of various investigated properties will be discussed and correlated with the analysis of the highs speed records.

Alongside the properties which were discussed using the time-averaged values of the records (i.e. pipe-wall acceleration, acoustic pressure and static pressure) the results of the acoustic emission will be discussed from the dynamic point of view.

4.2.1. Pipe-wall acceleration

As it was described, the pipe-wall acceleration has been measured using the accelerometer Aura SV129 glued to the bottom wall of the transparent section (Venturi tube). This should be taken into account during the interpretation of the results along with the fact that the vibrations induced by the pump were exciting the vibrations of the cavitation rig.

Seeing the charts of the pipe-wall acceleration variance corresponding to the different cavitation regimes (see Figure 91), investigated flow rates and experimental configurations, good agreement with the conclusion of time-averaged analysis can be found. The oversaturation of the acceleration transducers is observable in case of axial inflow considering the discharge of 7 l/s.

As it can be seen the increasing intensity of the cavitation within the flow is accompanied by the increasing value of the pipe-wall acceleration variance up to the regime of fully developed cavitation (region 3), where the variance of acceleration begins to decrease down to the significantly lower values corresponding to supercavitation. Supercavitation itsel is characteristic by the high stability as it has been described. For example, the maximum value of the pipe-wall acceleration variance is 3703.29 g^2 in case of 6 l/s and axial inflow is corresponding to the σ_{vel} of 0.49, in case of the supercavitation the a_{var} value dropped to 0.5901 g^2 (σ_{vel} 0.071) which is 0.0159 % of the maximum observed value. The situation was similar in case of the SG presence. Value of a_{var} corresponding to the lowest value of investigated σ_{vel} (0.0352) in case of 6 l/s reached 3.31 g^2, which is 0.321 % of the maximum observed value (σ_{vel} of 0.474, a_{var} 1031.709g^2).

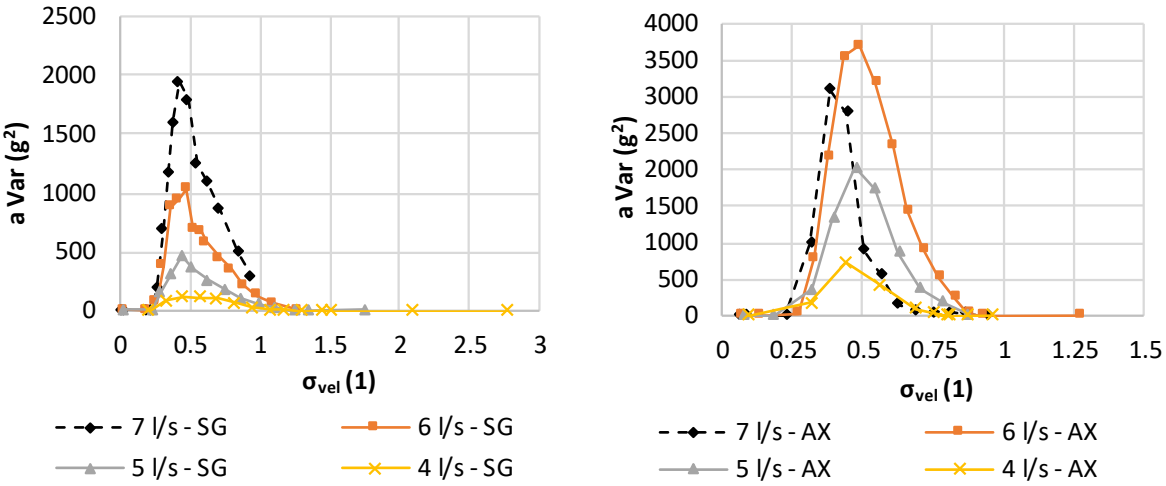

Figure 91 Variance of the pipe-wall acceleration measure during the investigation - SG (left), AX (right)

Relatively interesting is the comparison of the variance corresponding to supercavitation of different experimental configurations (considering 6 l/s). The values are low regardless the experimental configuration. Nevertheless, the magnitude of acceleration variance is significantly higher in case of SG presence compared to the same discharge and cavitation regime corresponding to the axial inflow. The reason of this observation can be devoted to the different phase redistribution across the cross section. While in case of the axial inflow the cavitation volume surrounding the axi-symmetric liquid jet can dampen vibrations, the walls of the nozzle are wetted by the liquid flow in case of the cavitation affected by the induced swirl. Similar observation can be described in case of other investigated discharges.
Since the sampling frequency of the pipe-wall acceleration measurement was the same as in case of the pressure transducers, the analysis of the obtained records in frequency spectra was excluded from the text of the thesis. Nevertheless, as it has been mentioned and depicted in the Figure 51 it was possible to identify the frequencies corresponding to the typical frequencies of the axial pulsations identified using the analysis of the HS video records and the analysis of the pressure pulsations. The more exhaustive analysis will be done in case of the acoustic emission and pressure fluctuations.

4.2.2. Acoustic pressure

Comparing the charts of acoustic pressure variation corresponding to the different experimental configurations (see Figure 93), it is obvious that the acoustic pressure fluctuations were considerably less severe in case of the swirl generator presence. This in good agreement with the above described nature of the different cavitation flow patterns.

In case of the axial inflow, the gradual increase of the investigated signals variations with the decreasing values of σ_{vel} can be found down to the transition between the fully developed stage of cavitating flow and supercavitation. The situation is similar in case of the cavitating flow influenced by the induced swirl. Nevertheless, it should be mentioned that several values depicted in the chart corresponding to this experimental configuration seem to be affected by the ambient noise (i.e. noise induced by the pump, vibrations of the test rig, sounds of the ongoing works in the laboratory etc.). These operating points, which occurred in case of 6 l/s and 5 l/s, are marked using the red crosses.

The values of the acoustic pressure variance corresponding to 6 l/s and supercavitation regime are lower in case of the SG presence. This difference (AX 0.15 Pa^2 vs. SG 0.05 Pa^2) is in contrast with the analysis of pipe-wall acceleration.

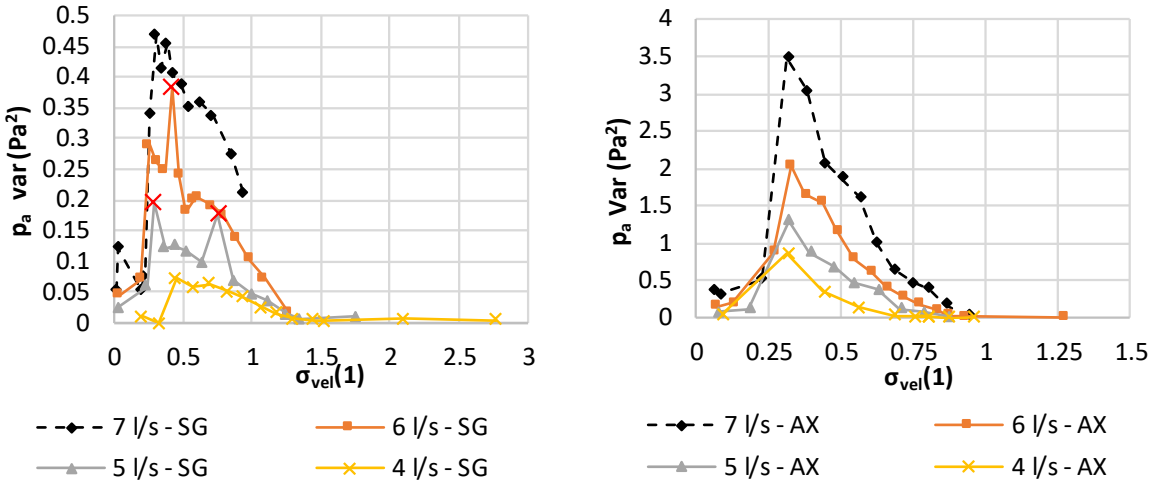

Figure 92 Variance of the acoustic signal measured by the microphone. SG (left), AX (right)

Partial conclusions

I. The analyses of the of the pipe-wall acceleration and acoustic noise variance were provided. Regardless the overall qualitative agreement, different results corresponding to supercavitation were described. The variance of the pipe-wall acceleration was higher in case of the SG presence while in case of the acoustic pressure more severe fluctuations corresponds to the axial inflow. This discrepancy was devoted to the gaseous phase distribution with respect to the location of the acceleration transducer. This assumption was confirmed by the analysis of the acoustic emission where induced fluctuations were more severe in case of SG presence similarly to the pipe-wall acceleration analysis. Nevertheless, it should be mentioned that the difference is relatively low in this particular regime with respect to the stability of the cavitating structures typical for both of these experimental configurations.

II. The values of the *a* variance were relatively low in case of the 7 l/s flow rate and axial inflow due to the oversaturation of transducer (Figure 91 – right). Nevertheless, as it has been shown by the analysis of the acoustic pressure, the fluctuative character of the instabilities induced by the cavitation was the most severe in case of this experimental configuration (7 l/s, AX).

4.2.3. Acoustic emission

The measurement of the acoustic emission has been partially influenced by oversaturation of the UT1000 transducer which was pressed to the bottom wall of the transparent section. This is particularly significant in charts of the acoustic emission variation corresponding to the discharge of 7 l/s in case of the SG presence and discharges of 6 l/s and 7 l/s in case of the axial inflow (see Figure 93). On the other hand, it is still possible to state, that the fluctuations of the analysed signals were considerably less severe in case of the SG presence based on the comparison of results depicted in both of the charts provided in Figure 93.

Seeing the courses of the of the acoustic emission variance of the 4, 5, and 6 l/s discharges in case of the SG presence, the relatively significant difference between the results corresponding to the higher discharges (5, 6 l/s) and the lowest investigated discharge can be observed (Figure 93, left). As it can be seen the *Ae* values start to gradually increase with the increasing amount of gaseous phase regardless the investigated discharge. This increase is the steeper, the higher is the investigated discharge.

The aforementioned difference can be found in the region of fully developed cavitation. While in case of the 4 l/s discharge, the *Ae* variation slightly increases down to σ_{vel} value of 0.696, the less pronounced local maximum of *Ae* variations values close to the σ_{vel} of 0.87 can be found in case of 5 and 6 l/s. These peaks are followed by the slight decrease of the *Ae* variation's values followed by the more pronounced peaks of the *Ae* variations prior the transition regime between the fully developed stage of cavitation and supercavitation. These peaks are followed by the relatively abrupt decrease of

the *Ae* variation values in case of 5 and 6 l/s discharges, while the decline corresponding to the 4 l/s discharge is considerably more gradual without any significant local maximum of the *Ae* variation value prior the transition to supercavitation.

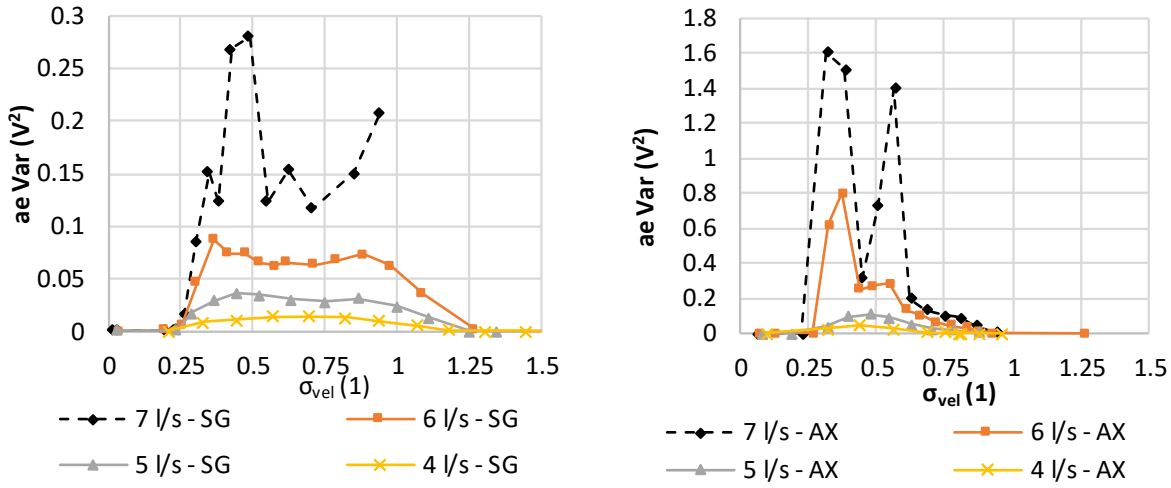

Figure 93 Variance of the magnitude of the acoustic emission fluctuations. SG (left), AX (right)

Since the signals of acoustic emission corresponding to discharges of 6 and 7 l/s were highly affected by the oversaturation in case of the axial inflow, the 5 and 4 l/s flowrates are exploited for the direct comparison of different investigated configurations (see Figure 94).

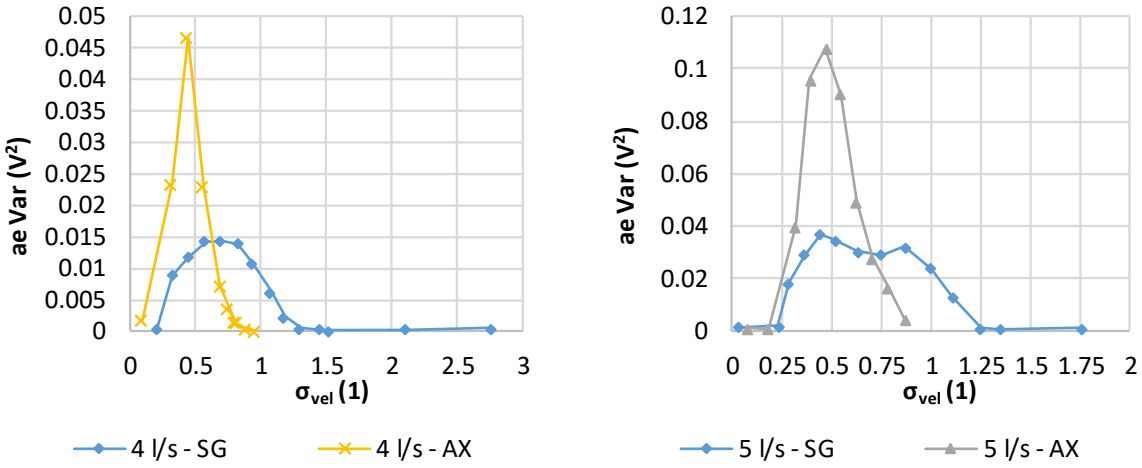

Figure 94 Comparison of the acoustic emission variance for SG and AX configurations.

As it has been mentioned, the maximum observed values of *Ae* variance are considerably larger in case of the axial inflow. Nonetheless, the *Ae* variance values are higher in case of the SG presence in the region of higher σ_{vel}. It can be assumed that this observation is caused by the nature of the cavitating structures corresponding to the different experimental configurations. In case of the SG presence, the cavitating vortices are well developed and significant axial pulsations as well as the precession of the cavitating structures within the diffuser can be observed. The nature of the cavitating structures is considerably more stochastic in case of the axial inflow in this region.

The transition between the cavitation free regime and initial regime of cavitation was captured by the acoustic emission signal for 2.3 l/s as it is depicted in the Figure 95. While the initial part of the *AE* signal corresponding to the flow without the cavitation is relatively steady, the signal after the abrupt occurrence of the thin cavitating vortex filament in the later part of the signal is significantly noisier.

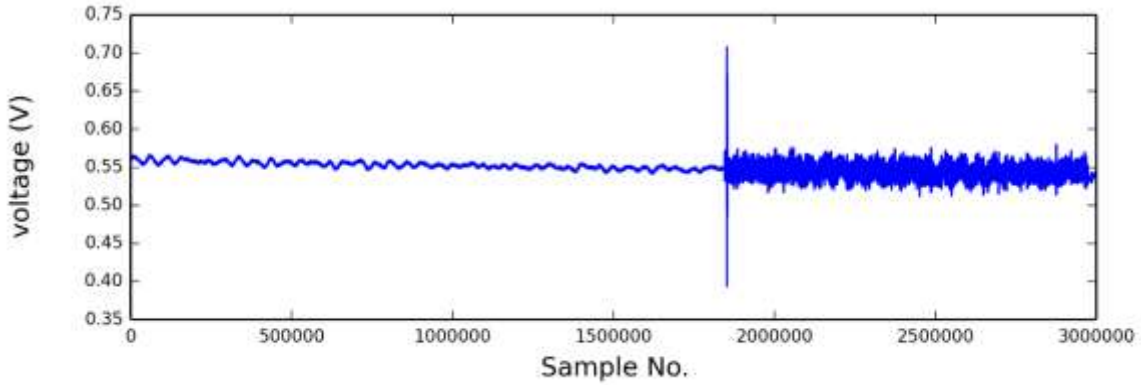

Figure 95 2.3 l/s SG, σ = 4.1: AE signal during the inception of cavitation

In contrast to the analysis of the pressure records which will be focused mainly on the relatively low frequencies corresponding to the fluctuations of the large cavitating structures, the *AE* analysis is devoted mainly to the investigation of the higher frequencies in order of units to tens of kHz. It can be assumed that these frequencies are covering the instabilities corresponding to the nature of the creation, motion and further collapses of the individual bubbles.

Prior the main analysis, the low frequencies of the *AE* fluctuations will be discussed. As it has been mentioned, the *AE* transducer was pushed against the bottom surface of the Venturi nozzle using the rigid spacer, which was anchored to the ground. The surface between the transducer and the wall of the transparent section was covered by the gel. In other words, the wall of the Venturi tube was sliding on the surface of transducer. Thus, the eigenfrequencies of the test bench were captured clearly as it is depicted in the following figures. The *AE* frequency spectra corresponding to the supercavitation regime are depicted in the Figure 96. The peaks close to 7 Hz and 10 Hz can be found in case of both experimental configurations. These frequencies are close to the eigenfrequencies of the test bench obtained by the bump test in case of the horizontal shock. In contrast to the results of the bump test which were based on the analysis of the pipe-wall acceleration, the lower frequency of 7 Hz is more significant. In case of the fully developed stage of cavitation, the clearly distinguishable peaks of the *AE* can be observed close to 19 Hz. This value is close to the test bench eigenfrequency obtained by the analysis of the test bench modal analysis using the vertical shock. These observations suggest that the motion of the transparent section induced by the fluctuations of the cavitating flow was predominantly horizontal in case of the supercavitation. On the other hand, the vertical motion of the section became more significant with the transition of the cavitating flow to the more unstable regimes.

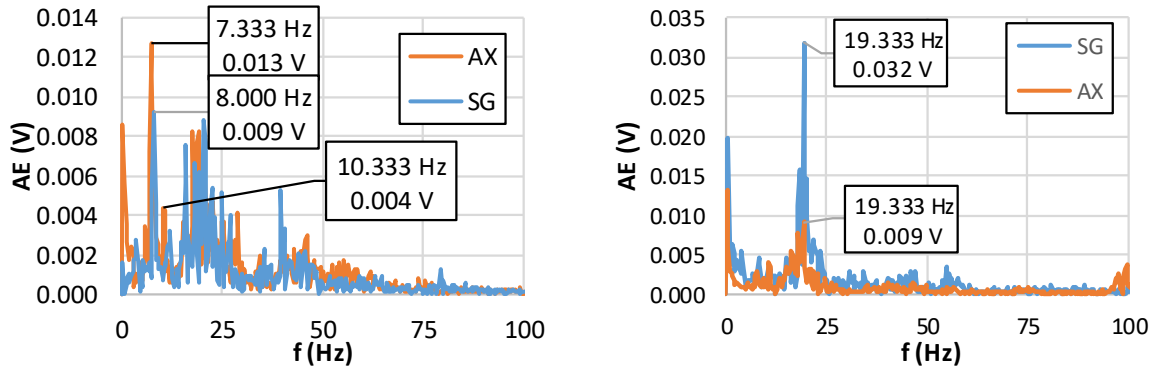

Figure 96 Frequency spectra depicting low frequency pulsations captured using the AE transducer in case of the supercavitation (left) and fully developed cavitation (right)

Using the analysis of the *AE* records it was also partially possible to identify the frequencies of the *AE* fluctuations corresponding to the frequencies of the large cavitating structures pulsations obtained by the HS video analysis. Nevertheless, it shall be emphasized that these frequencies of the acoustic

emission were not dominant nor significant with respect to the frequency spectra obtained by the analysis of the records as it will be shown. Peaks corresponding to these frequencies were not distinguishable in each of the investigated operating points. This is similar to the results of pipe-wall acceleration analysis. In the other words, the *AE* analysis was not suitable for the determination of the frequencies corresponding to the fluctuations of the large cavitating structures, regardless the fact that under the certain conditions it was possible to distinguish these frequencies within the frequency spectra. The correlation of the pressure frequency spectra with the frequency spectra of acoustic emission is depicted in the Figure 97 (SG, Q = 5 l/s, σ_{vel} = 0.52). The range of the depicted frequencies is restricted to vicinity of the frequency of the axial pulsations determined using the analysis of the pressure fluctuations. As it can be seen, the similar frequency of the *AE* fluctuations is also clearly distinguishable. Nevertheless, it shall be emphasized that this agreement is rather exceptional.

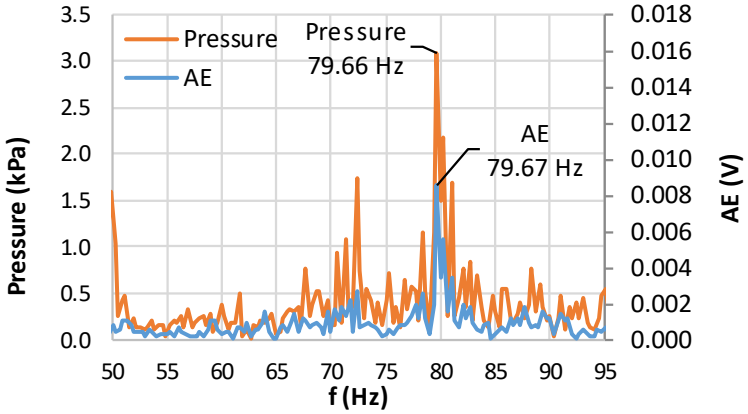

Figure 97 Comparison of the low frequency spectra corresponding to the pressure fluctuations with the analysis of acoustic emission. (SG, Q= 5 l/s, σ_{vel} = 0.52)

The last part of this chapter will be devoted to the analysis of high frequency instabilities captured by the AE transducer. Since the transducer was over saturated in case of the higher discharges, the flow rate of 5 l/s will be utilized for the analysis. Nevertheless, these results will be complemented by the analysis of different discharges whenever it will be convenient.

The frequency spectra will be discussed using the selected operating points corresponding to the wide range of investigated cavitation regimes.

It should be noted that some of the presented results could be problematic due to the fact that the discussed frequencies are outside the recommended operating range of this transducer (0.1-1 MHz). Thus, the characteristic of the transducer was provided by M. Čala (Figure 98) in order prevent misleading conclusions.

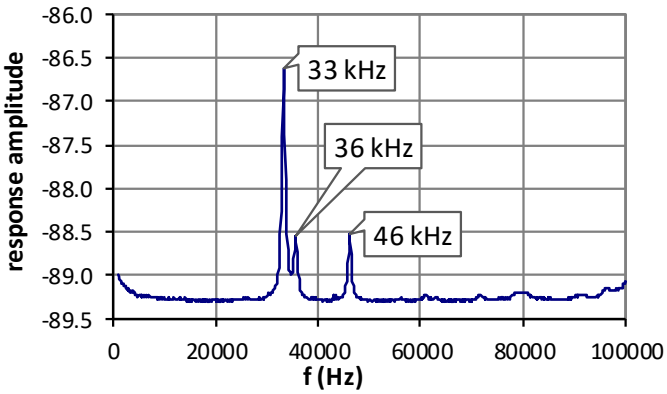

Figure 98 Frequency response of the UT1000 transducer

Region 1 – initial stage of cavitation

The initial regime of cavitation corresponding to the flow rate of 5 l/s will be extended by the results obtained by the analysis of the lower discharge of 2.3 l/s. The measurement of this flow rate was devoted particularly to the analysis of the initial regimes of cavitation. Therefore, it is possible to compare acoustic emission induced during the initial cavitation with the cavitation-free regime. Comparing the frequency spectra depicted in the Figure 99, it is obvious that the amplitudes corresponding to the lower value of the cavitation number are considerably higher compared to the higher value of the σ_{vel}. The reason for this observation is the fact that the higher value of σ_{vel} corresponds to the regime with no cavitation, while in case of the lower value of the σ_{vel} the thin but stable cavitation vortex filament occurred within the throat of the nozzle. Thus, it can be assumed that the presence of this small but distinguishable cavitating structure is well captured by the *AE* record. The frequency spectra capturing acoustic emission induced by the cavitation contains significant noise between 5 kHz and 20 kHz. As the most significant peak within this frequency band, the frequency of 8368 Hz is marked in the figure. The less significant, frequency 37 kHz correspond well to the significant peak captured in the frequency response of the exploited transducer. Thus, it can be assumed that this particular part of the frequency spectra is not induced by the presence of cavitation. These frequencies will be marked in the following charts, nevertheless their presence will not be discussed anymore.

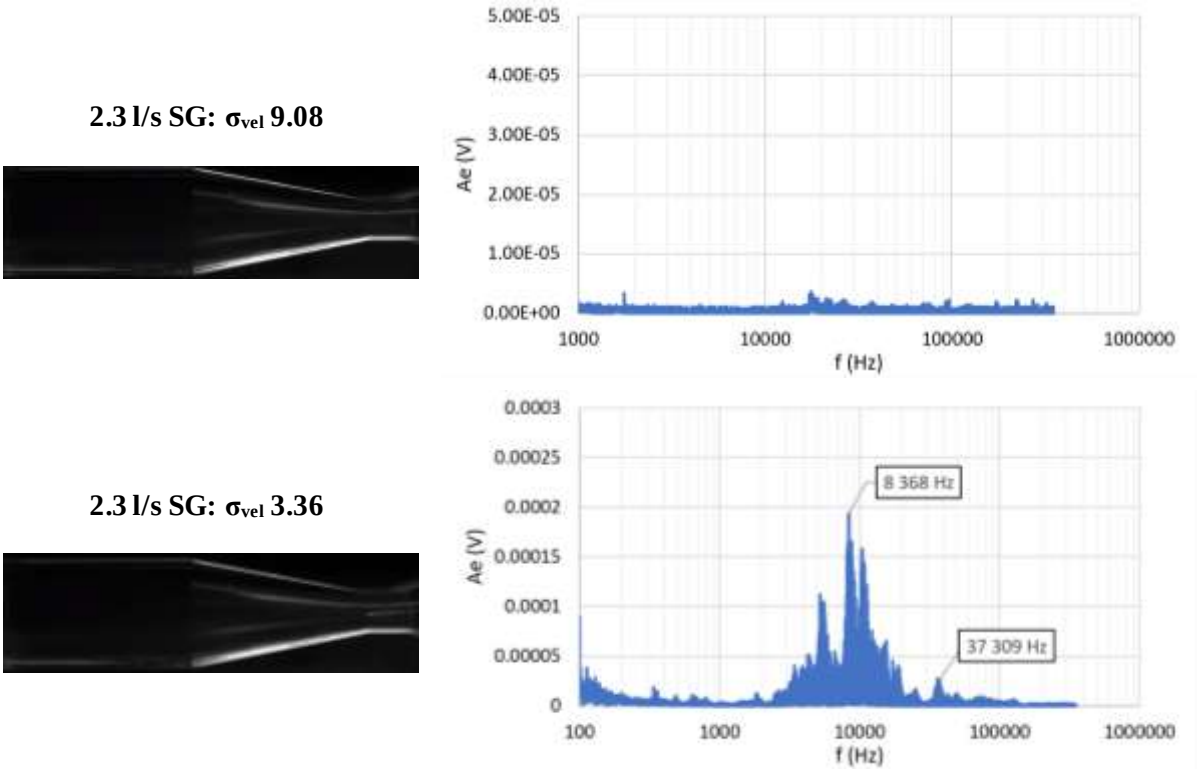

Figure 99 Spectral analysis of the acoustic emission in case of the initial regime of cavitation. (3 l/s, SG)

The *AE* frequency spectra of the initial cavitation in case of the 5 l/s are depicted in the Figure 100. The maximum amplitudes are higher compared to 2.3 l/s. As it can be seen, the semilogarithmic visualization of the spectral analysis was utilized to depict the wide range of frequencies in reasonable scale. The wideband noise close to the problematic frequency of 37 kHz is followed by the minor increase of the amplitudes close to the frequency of 129 kHz.

Regardless the minor differences, it can be stated that the abovementioned observations are valid for both investigated experimental configurations. On the other hand, amplitudes are lower in case of the axial inflow. This is in good agreement with the values of the mean pipe-wall acceleration in the 1st region.

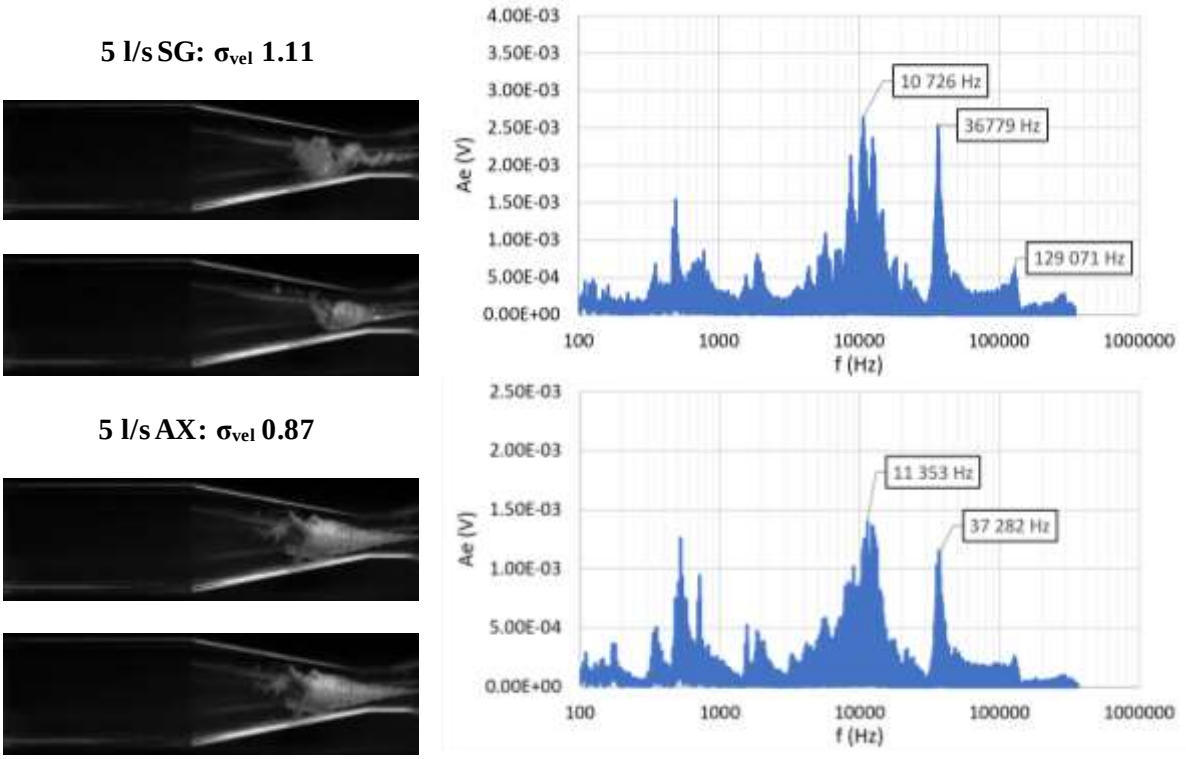

Figure 100 Spectral analysis of the acoustic emission in case of the initial regime of cavitation. (5 l/s, SG – top, AX - bottom)

Region 2

The results of AE analysis corresponding to the region 2 are similar to the initial cavitation as it can be seen in the Figure 101. No significant differences were observed in the region of the high frequencies (5 kHz and more) based on the experimental configuration,

Seeing the lower frequencies, it can be found that the amplitude corresponding to axial inflow became higher compared to the cavitating flow influenced by the induced swirl. The values of the maximum amplitudes within the region between 5 kHz and 20 kHz are still larger in case of the SG presence.

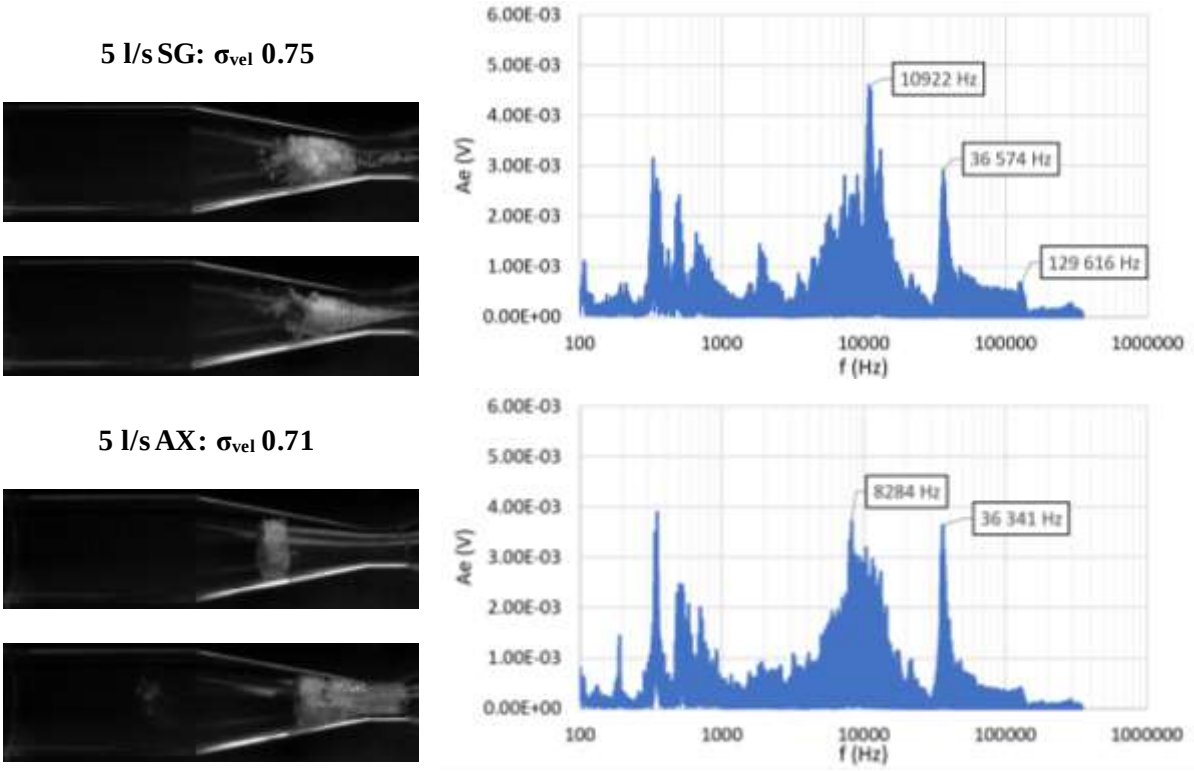

Figure 101 Spectral analysis of the acoustic emission in case of the 2nd region of cavitation. (5 l/s, SG – top, AX - bottom)

Region 3

In case of 3rd region the results will be complemented by the analysis of 6 l/s and 4 l/s in order to describe the influence of the flow rate magnitude on acoustic emission induced by the cavitation. Nonetheless, the discrepancies resulting from the experimental configuration will be described at first using 5 l/s discharge.

Since the differences based on the experimental configuration are in good agreement with the less developed stages of cavitation, the following description will be brief. As it can be seen in the Figure 102, the considerable amount of *AE* fluctuations was captured in the frequency band of 5-20 kHz. In contrast to the previous regions, the amplitudes correspond to the *AE* fluctuations are higher in case of the axial inflow in the whole range of depicted frequencies. Thus, it can be assumed that the *AE* emission induced within this part of frequency spectra is higher in case of the separation of the large cavitating clouds compared to the pulsations of the cavitating conical vortex in case of the SG presence. This is different compared to the 2nd region, where the captured *AE* emissions were lower in case of the cavitating vortex rings (axial inflow) compared to the SG presence.

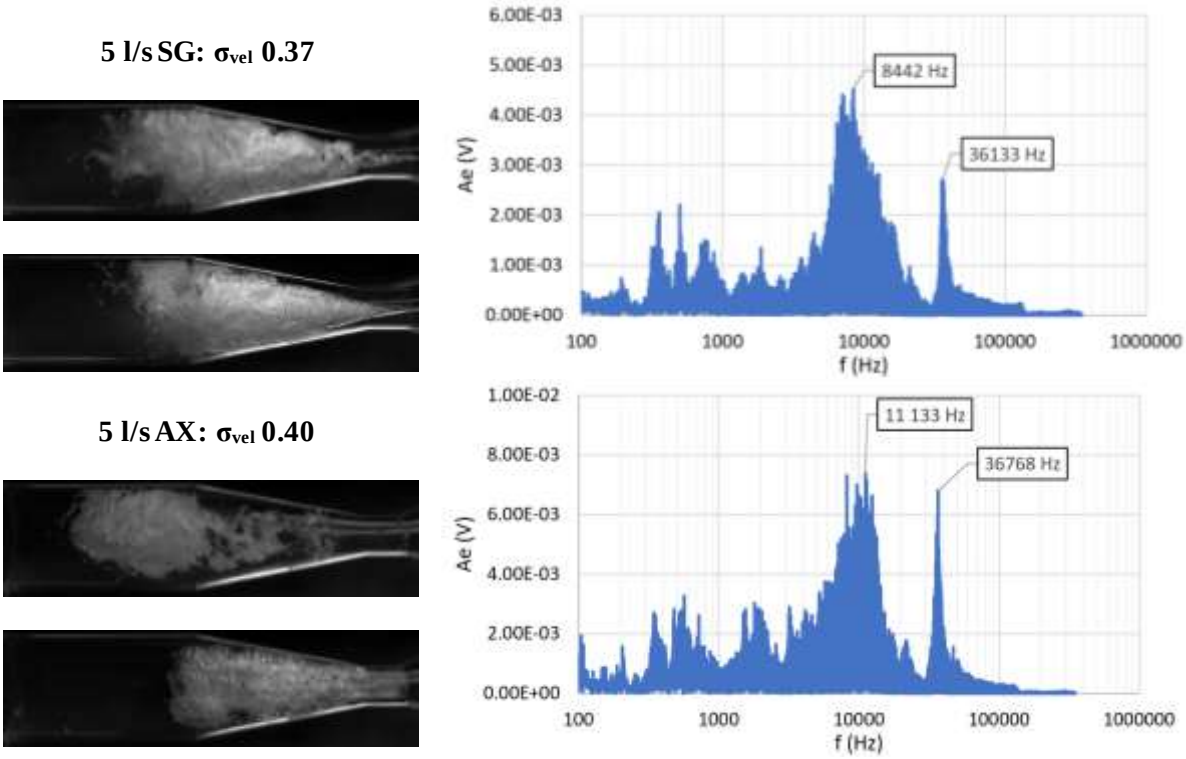

Figure 102 Spectral analysis of the acoustic emission in case of the 3rd region of cavitation. (5 l/s, SG – top, AX - bottom)

The frequency spectra corresponding to flow rates of 4 l/s and 6 l/s affected by the presence of swirl generator are provided in the Figure 104. Following observations can be described in comparison with the frequency spectra which was obtained by the analysis of 5 l/s flow rate (considering the similar value of σ_{vel} of analysed operating points). While the typical frequency bands are similar as in case of the 5 l/s, the actual values of amplitudes are proportional to the analysed flow. The chart showing the maximum amplitudes within the abovementioned frequency band (5-20kHz) is provided in the Figure 103 and as it can be seem they are increasing with the increasing flow rate.

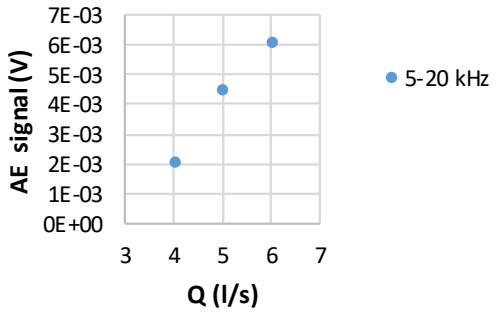

Figure 103 Chart depicting values of maximum amplitudes based corresponding to the different flow rates.

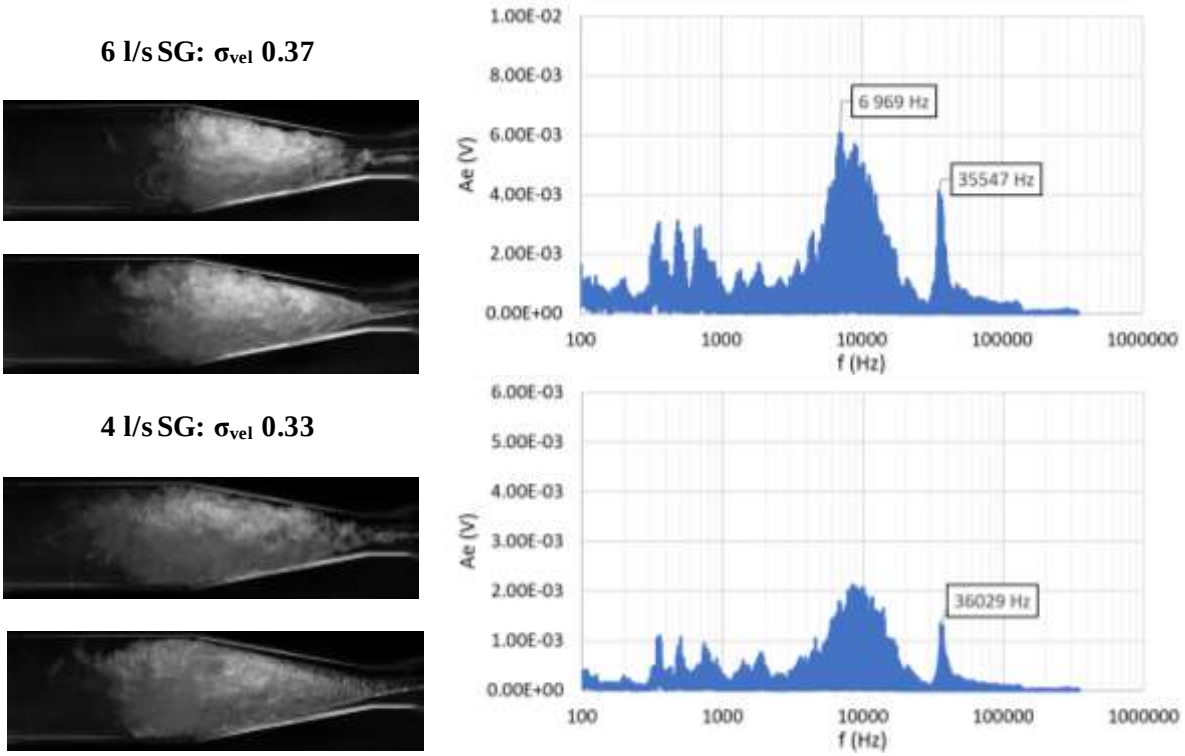

Figure 104 Spectral analysis of the acoustic emission in case of the 3rd region of cavitation. (5 l/s – top, 4 l/s bottom)

Region 5

Since the nature of the cavitating structure was alternating in case of the region 4, it was problematic to make some representative conclusions based on the obtained results. Thus, the 4th region was excluded from the analysis.

As it has been described the nature of the supercavitation is completely different based on the experimental configuration. Nevertheless, the fact that the noise, pressure pulsations and vibrations are significantly lower in this regime of cavitation is typical for both of the investigated experimental configurations. The same conclusion can be stated in case of the acoustic emission. Regardless the experimental configuration, the maximum amplitudes are significantly lower compared to the previous results. On the other hand, this is the first and the last similarity between the results of the supercavitation analysis based on the experimental configurations. Frequency spectra is relatively similar to the previous operating points in case of the SG presence as it can be seen in the first row of the Figure 105. The situation is completely different in case of the axial inflow. It can be seen that the low frequencies within the frequency spectra captured some significant fluctuations (see Figure 105, 2nd row). However, the signal contained no significant fluctuations with the frequency higher than 4 kHz. This might be the consequence of the fact, that in case of the supercavitation regime of axial inflow the liquid jet was surrounded by the water vapor. Thus, the walls of the Venturi tube close to the *AE* transducer were not fully wetted by the liquid water (thin film of the liquid was captured on the walls) and therefore the gaseous phase surrounding of the liquid jet dampened the higher frequencies.

5 l/s SG: σ_{vel} 0.019

5 l/s AX: σ_{vel} 0.076

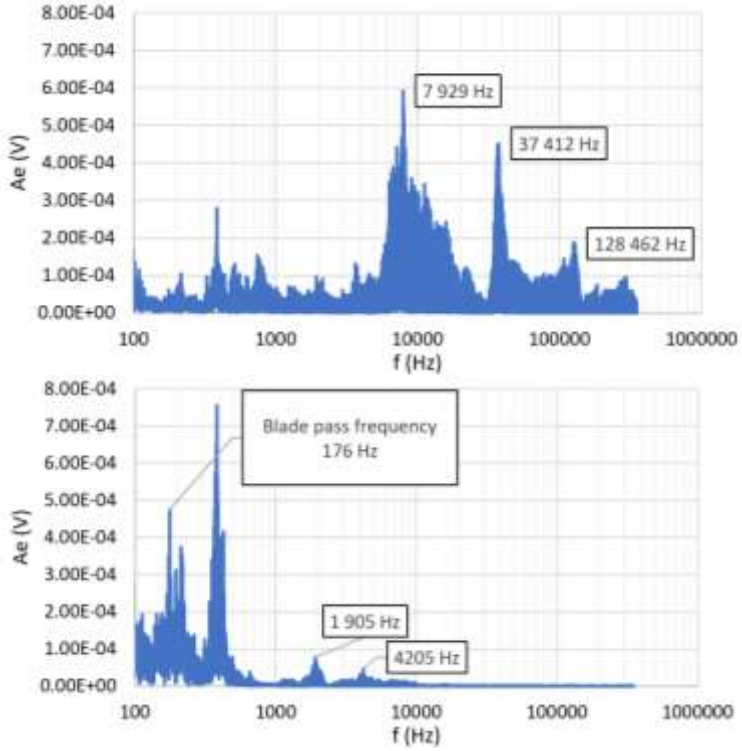

Figure 105 Spectral analysis of the acoustic emission in case of the supercavitation. (5 l/s, SG – tom, AX - bottom)

Partial conclusions

I. The course of the variance is different compared to the analysis of the variance corresponding to the pipe-wall acceleration and acoustic pressure.
II. Measurement of the AE was significantly affected by the oversaturation of the signal in case of the higher flow-rater (6 and 7 l/s). The problem was worst in case of the axial inflow as is depicted in the Figure 93.
III. The variance of the *AE* fluctuations is considerably higher in case of the axial inflow. In other words, the fluctuations of the acoustic emission are more severe in case of the axial inflow. The severity of fluctuations also increases with the increasing flow rate.
IV. The inception of the thin cavitating vortex within the throat of the nozzle was captured as it is shown Figure 95.
V. Frequency spectra of acoustic emission were investigated based on the experimental configuration and regime of cavitating flow. The nature of the obtained signals differed significantly based on these parameters. Nevertheless, the wideband noise ranging from 5 kHz to 20 kHz has been captured. It shall be emphasized that these frequencies lie bellow the recommended operating range of transducer. Thus, the main conclusion is that the investigation should be repeated using the suitable transducer to provide more reliable results.
VI. Despite the fact that the overall intensity of the fluctuations is higher in case of the axial inflow. The opposite results corresponding to the less developed stages of cavitation were described.
VII. AE transducer captured the eigenfrequency of the test bench.

4.2.4. Static pressure

The dynamics of the pressure fluctuations has been studied using the pressure records acquired by the Kistler 211 B4 transducer. Conclusions similar to the analysis of the acoustic emission can be stated. On the other hand, some of the observed pressure fluctuations properties differ significantly from the acoustic emission as it will be described. 3

It should be noted that the results corresponding to the higher flow rates are not affected by the oversaturation of transducer as in case of the *Ae* analysis.

Two local peaks of the pressure variance can be found in case of the SG in case of the 6 l/s and 7 l/s and partially in case of the 5 l/s. The local increases in case of the 4 l/s are far less distinguishable (see Figure 106, chart on the left). As it can be seen in the chart, the sudden increase of the variance of the static pressure fluctuations can be found prior the transition to the supercavitation, other dominant peaks are located in the region of higher σ_{vel}.

The gradual increase of the pressure fluctuations can be found with the decreasing value of σ_{vel} considering the axial inflow (see Figure 106, chart on the right). The results corresponding to the 7 l/s are slightly different. Significant region of the variance of pressure fluctuations can be found close to the abrupt increase of this value connected with the occurrence of the coherent and distinguishable vortex rings (σ_{vel} 0.81) as is depicted in the chart in the Figure 106 (left side). Comparing the results of the pressure analysis with the corresponding results of the *Ae* variance in case of the 5 and 4 l/s, it can be stated that the increase of the pressure variance continued deeper to the region of lower values of σ_{vel}.

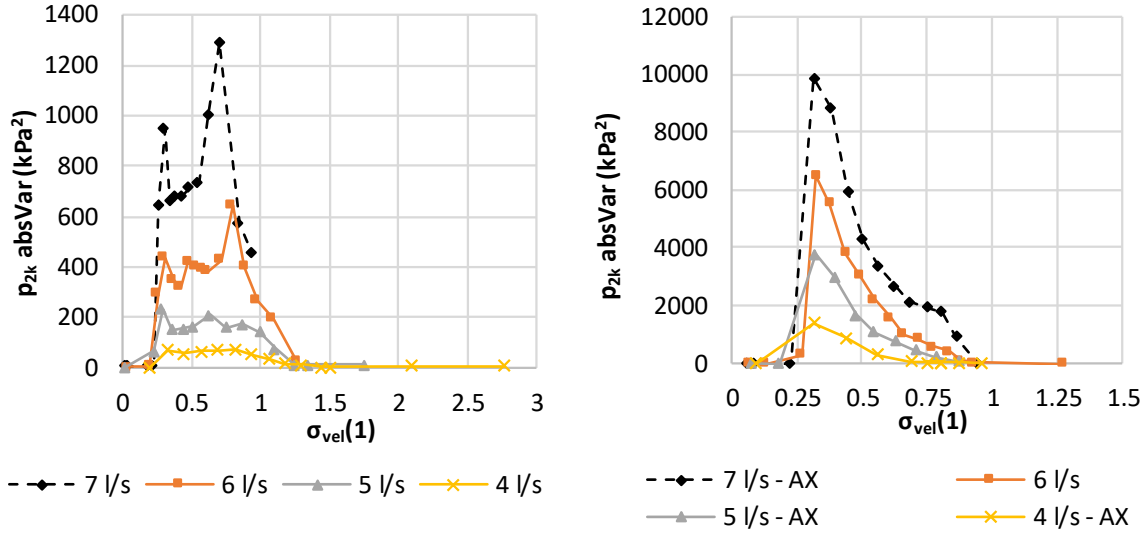

Figure 106 Variance of the pressure fluctuations magnitude captured by the Kistler pressure transducer

Comparing the results of the p_{fluct} variance with the analysis of the acoustic pressure it can be observed that the courses of these quantities are in relatively good qualitative agreement in case of the axial inflow (Figure 107 – right, in case of 6 l/s). On the other hand, seeing the comparison corresponding to the flow affected by the induced swirl (Figure 107 – left, in case of 6 l/s), significant discrepancy can be found. Thus, it can be assumed, that the main source of the pressure pulsations is also the source of dominant acoustic pressure fluctuations in case of the axial inflow. Presence of the induced swirl was stabilizing the large cavitating structures, but it also created considerably more complex flow field, with large amount of less significant flow structures, which acted as the source of pressure fluctuations. These structures on the other hand did not play any significant role in the noise emission with respect microphone resolution. Furthermore, the same observation can be done comparing the results of the pipe-wall acceleration with the p_{fluct} analysis. Nevertheless, seeing the results of the acoustic emission variance, it can be stated that the influence of the less significant instabilities connected with the presence of induced swirl were captured properly as it has been described.

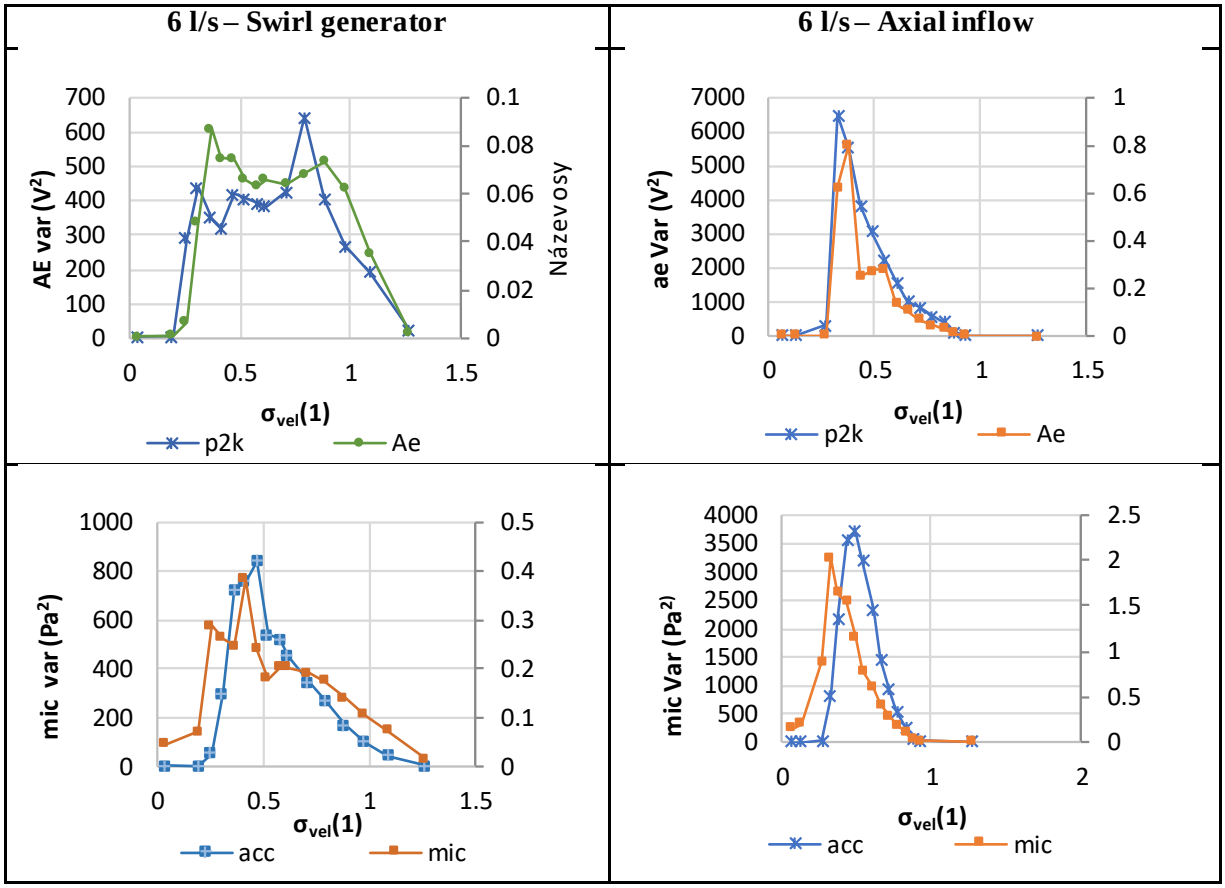

Figure 107 Comparison of the various signal variance

It can be also stated the magnitude of the pipe-wall acceleration variance starts to decrease earlier (i.e. in case of the larger σ_{vel} values) compared to the other investigated signals.

The records of the pressure fluctuations were postprocessed using the spectral analysis to identify the characteristic frequencies of the pulsations induced by the cavitating flow. It should be mentioned that the problem with the electricity interference has occurred during the experimental measurement. Thus, it has been necessary reflect this fact during the analysis of the results, especially in case of the initial regime of cavitation. Examples of the frequency spectra, which were obtained by the analysis are depicted in the Figure 108.

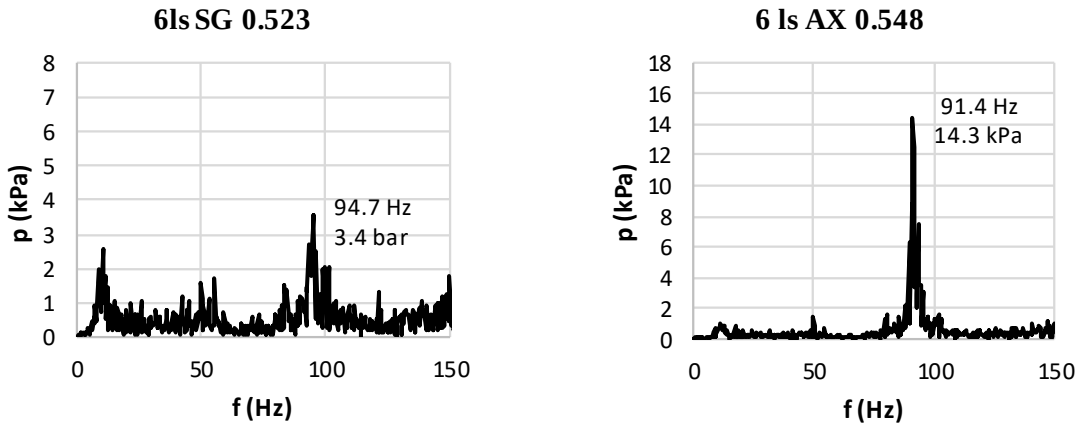

Figure 108 Example of the pressure frequency spectra. SG (left), AX (right)

The HS records analyses were corelated with the spectral analysis of the pressure fluctuations corresponding to the flow rate of 6 l/s in the chapter 3. It was possible to identify the frequencies

corresponding to the axial pulsations with a good degree of agreement. As it can be seen in the Figure 109 depicting dominant frequencies corresponding to the various flowrates and both investigated experimental configurations as functions of σ_{vel}, the overall observations corresponding to the analysis of the pressure pulsations are the same as in case of the HS video analyses using the FFT of the pixel intensity fluctuations and POD of the selected region of the interest. The identified frequencies were the larger, the larger was value of the cavitation number up to the moment where the induced pulsations became too weak to be identified using the p_k probe downstream the Venturi nozzle. Since the course of the frequency values has been already discussed in the chapter devoted to the HS records analysis, it would be sufficient to state, that the values of the axial pulsations were increasing with the increasing flow-rate. Also, the values of the frequencies were larger in case of the SG presence.

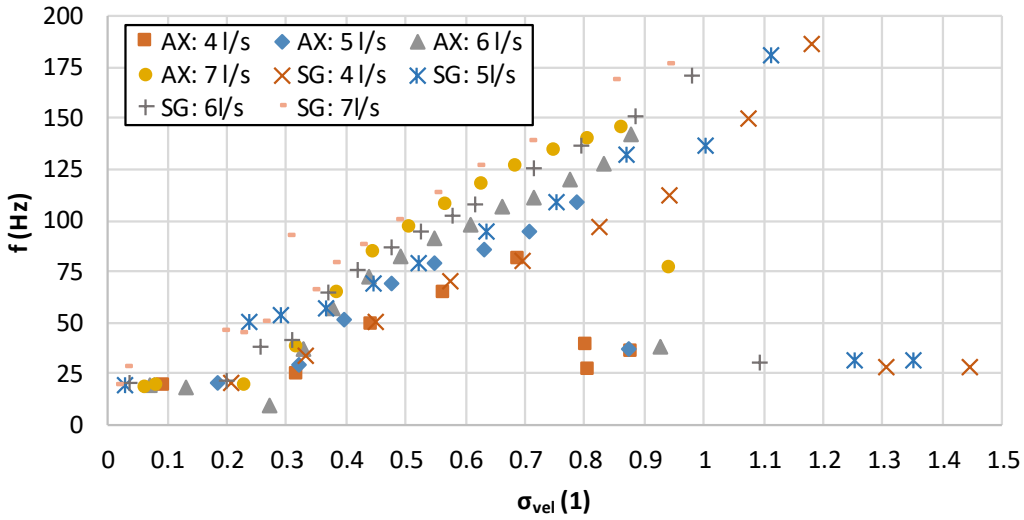

Figure 109 Dominant frequencies of the axial pulsations depicted as a function of σ_{vel}

The values corresponding to the different investigated flow-rates became uniform in case of the Strouhal number utilization (equation (75)), as it can be seen in the Figure 110. On the other hand, the values of the Strouhal number are slightly higher in case of the SG presence.

$$Sh = \frac{f \cdot d_{th}}{v_{bulk}} \tag{75}$$

Where f represents observed dominant frequency of the cavitation fluctuations and velocity v_{bulk} and representative length d_{th} (diameter of the throat) are related to the throat of the nozzle.

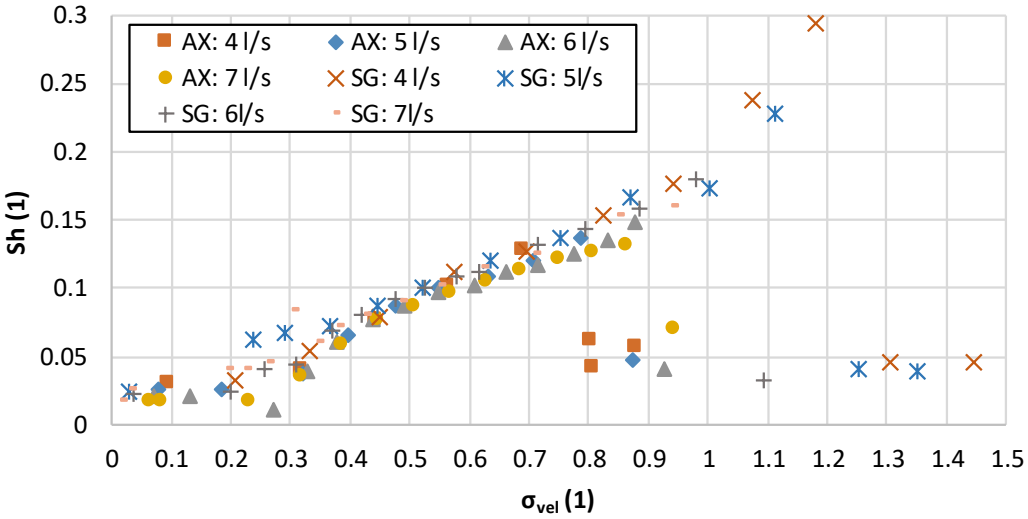

Figure 110 Strouhal numbers corresponding to the axial pulsations depicted as a function of σ_{vel}

Discrepancy of the Strouhal number values corresponding to the different configurations of experiment is considerably more obvious in case of the σ_{pres} utilization (Figure 111). This discrepancy is caused by the fact that the v_{bulk} utilized in case of the σ_{vel} does not reflect the tangential and radial components of velocity which are considerably more significant in case of the SG presence.

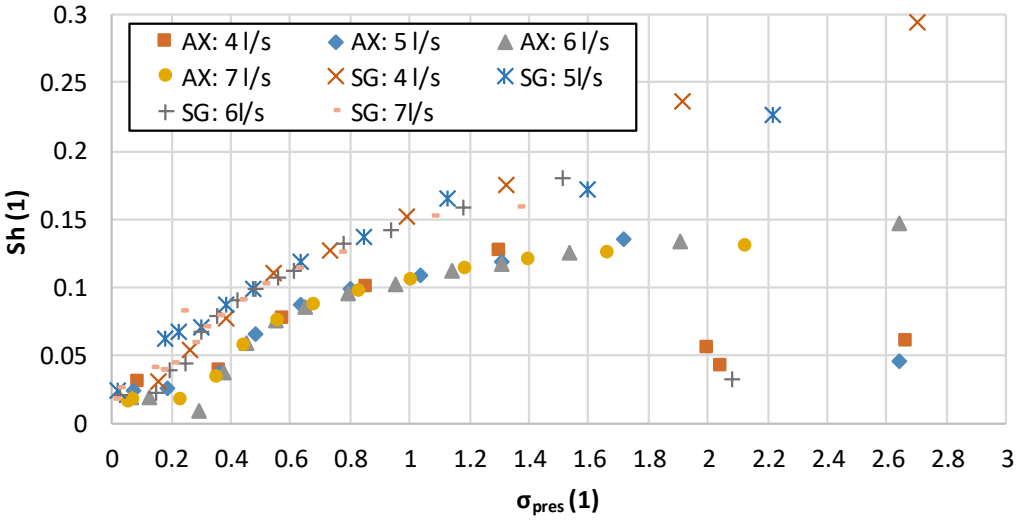

Figure 111 Strouhal numbers corresponding to the axial pulsations depicted as a function of σ_{pres}

Partial conclusions

I. The variance of the pressure fluctuations was investigated. In general, it can be stated that the pressure fluctuations are more severe (fluctuative) in case of the axial inflow as it is clearly depicted in the Figure 106.

II. Significant peaks of the pressure fluctuations can be found close to the transition between the initial regime of cavitation to the fully developed stage and in case to the transition of the fully developed stage to the supercavitation in case of the SG presence. This is

particularly visible in case of the 6 l/s and 7 l/s and partially in case of the 5 l/s. The increase of the variance is increasing gradually in case of the axial inflow.

III. The results of signals variance corresponding to the different properties of the cavitating flow are compared in the Figure 107. Significant discrepancies and similarities were described. Relatively interesting is the fact that in case of the SG presence the results of AE and p2k analysis share the same nature with the two distinguishable peaks close the transitions between the regimes while the results corresponding to the pipe-wall acceleration and acoustic pressure are different. These results correspond relatively well to the results of the axial inflow investigation, where gradual increase of the variance (regardless the investigated signal) was observed with the decreasing value of cavitation of number. The values dropped rapidly close to the transition to the supercavitation regime.

IV. The spectral analysis of the pressure signals was carried out and the frequencies of the axial pulsations were depicted as a function of σ_{vel}. The value of the frequency was decreasing with the decreasing value of the cavitation number.

V. Frequency was the higher, the higher was investigated discharge. The pressure pulsations induced in case of the SG presence have higher frequency than in case of the axial inflow. These observations are in good agreement with the analysis of HS records.

VI. Strouhal numbers were calculated using the obtained frequencies to provide more general form of the results. The values of *Sh* were depicted as functions of σ_{vel} and $\sigma_{pres.}$ As it is clearly depicted by the comparison of Figure 110 and Figure 111 the utilized definition has a crucial impact on the comparison of the results corresponding to the different configurations. While in case of the σ_{vel} is the difference between the experimental configurations relatively small (but still visible), in case of the $\sigma_{pres.}$ is the difference far more pronounced. The *Sh* values corresponding to the SG presence are considerably higher compared to the axial inflow. This discrepancy is caused by the neglection of the swirl and radial component of velocity in case of the σ_{vel} evaluation. This problem will be described using the numerical analysis if the hydraulic losses and their comparison with the experimental results.

Numerical analysis of the cavitating flow

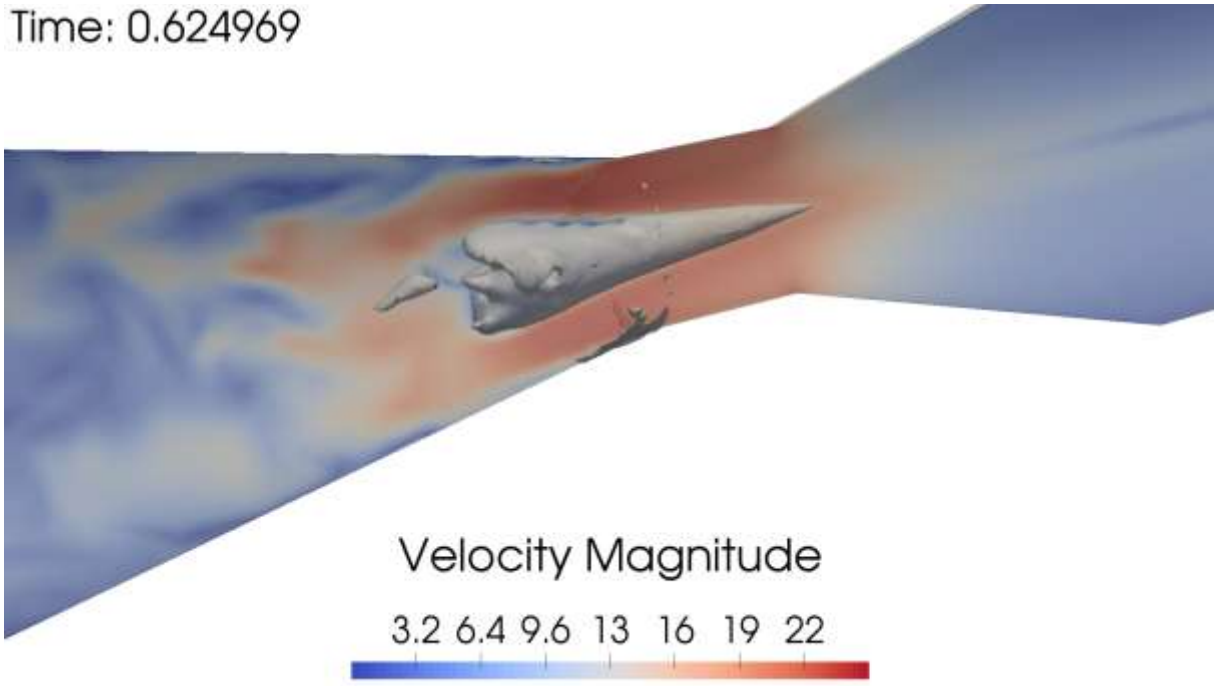

Content of the following chapter:
Results of the unsteady multiphase CFD simulations carried out using the OpenFoam will be exploited for the discussion of:

1. Hydraulic losses
2. Optimization of the comp
3. Cavitation dynamics

5. Numerical analysis of the cavitating flow

The following chapter is devoted to the description of the numerical investigation of the cavitating flow within the Venturi tube with and without the upstream mounted swirl generator. The computations were carried out using the OpenFoam v1606+ and the individual parts of the process will be described in the following sections. It shall be also mentioned that the actual settings of the investigated cases were based on the preliminary investigation of the cavitating flow within the Venturi nozzle considering the axial inflow. This investigation has been published by Kozák et al. [51] where the correlation of the numerical data with experimental results obtained by Gríger [46] was provided.

Experiments considering Venturi nozzle without the upstream swirl generator were investigated using the pressure records, high-speed video and numerical analysis. The cavitation was observed in wide range of regimes from the cavitation inception to the supercavitation. It was concluded that the vortex rings are the most significant source of the pressure fluctuations, thus the FFT analysis of the high-speed video provided reasonable results compared to the FFT analysis of the pressure records.

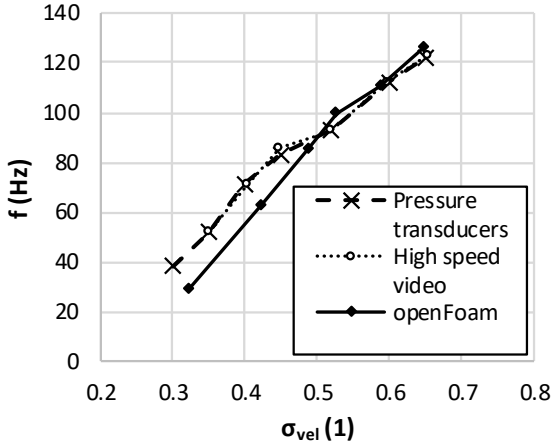

Figure 112 Comparison of the dominant frequencies corresponding to the different methods of investigation, Q = 7 l/s, axial inflow (AX) [51]

The numerical investigation of the problem was carried out using opensource CFD code OpenFoam using InterPhaseChange solver and Kunz model of mass transfer. The CFD computations were focused mainly on the regime of partial cavitation and transition to the fully developed cavitation. Dominant frequencies (i.e. frequency of vortex ring separation) were in good agreement with reality in case of higher values of the cavitation number. Discrepancy between numerical and experimental results was more significant in case of transition from the partial to the fully-developed regime of cavitation, which is depicted in the Figure 112. On the other hand, it was stated that the locations of the cavitation structure separation and extinction were predicted quite well in the whole spectrum of the numerically investigated cavitation regimes as is depicted in the Figure 113.

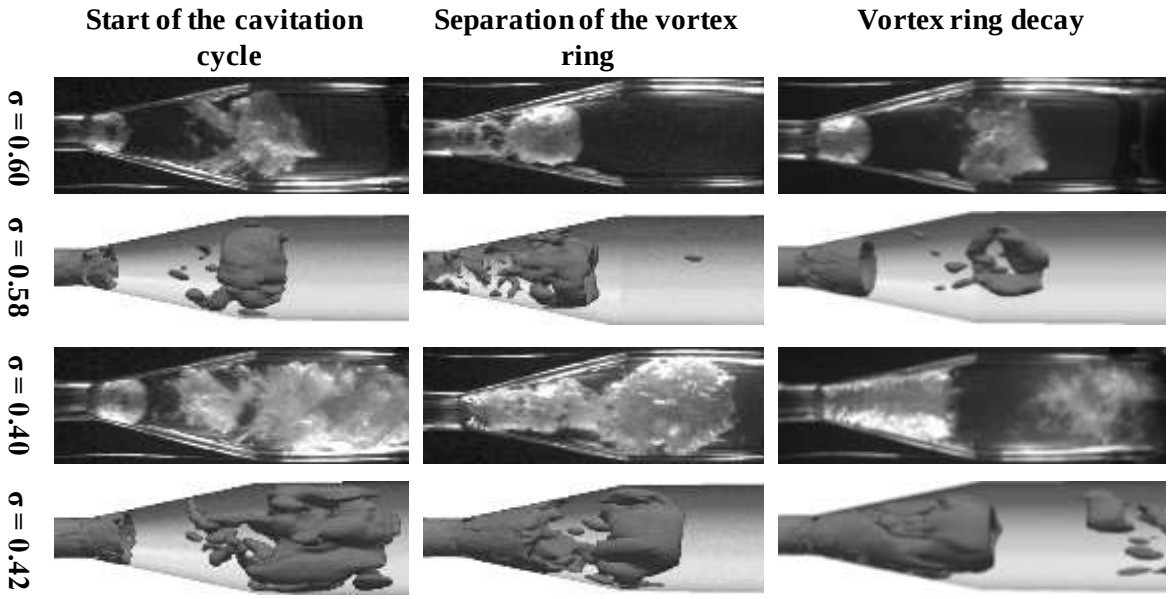

Figure 113 Comparison of the cavitation cycle stages captured during the Gríger's experiments [46] with numerical analysis carried out by Kozák [51], (Q = 7l/s)

Moreover, the coherent cavitating jet surrounded by the saturated vapor was well predicted, which is depicted in the Figure 114. The main difference between the reality and computation has been attributed to the inadequate length of the computational domain. Liquid jet surrounded by the gaseous phase was stable, and it collapsed in the elbow downstream the nozzle during the experiment, while the jet obtained by numerical simulations collapsed frequently.

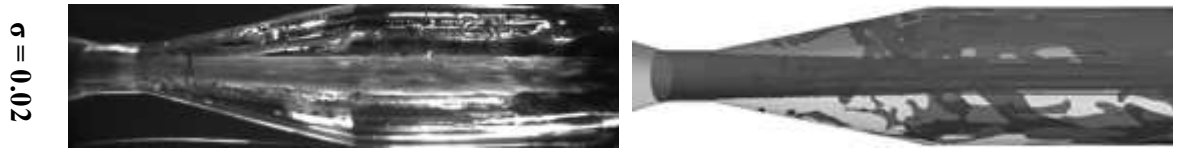

Figure 114 Comparison of the numerically predicted supercavitation jet with experiment

Since it was stated that the numerical results obtained during this investigation were in good agreement with the experimental data, the similar approach was exploited during the presented research. The main difference is represented by the computational grid, which was created using the Gambit as purely hexahedral. This approach was not applicable for the geometry considering presence of the SG. Therefore, the predominantly hexahedral grids were utilized during following investigation.

5.1. Pre-processing: Preparation of the geometry

Since the geometries of the investigated cases are highly similar, and the only difference is the presence of the swirl generator in case of the simulations of cavitation affected by the induced swirl, only the preparation of this more complex geometry will be described.

Input geometry has been created using the commercial CAD software, based on the geometry of the experimental equipment. Inlet and outlet part of the geometry have been extended for the CFD simulation.

The whole geometry has been divided into several parts to provide a simple possibility of the further mesh refinement These separated geometrical entities has been exported as a stl files. The stl file format has been chosen due to its compatibility with many meshing utilities such as blockMesh, snappyHexMesh and especially cfMesh. Separated stl files has been merged into the final file, which was checked to prevent occurrence of defects such as gaps between edges of the connected surfaces.

The list of the geometrical entities of the decomposed computational domain is shown in the following Table 4 as well as in the Figure 115.

Name of the geometrical entity	Description of the geometrical entity
inlet	Inlet of the domain
swirlGenWalls*	Walls surrounding the swirl generator
walls	Walls of the pipes including Venturi tube
outlet	Outlet of the domain
leadingEdge*	Leading edges of the swirl generator vanes
trailingEdge*	Trailing edges of the swirl generator vanes
vanes*	Vanes without leading and trailing edges
swirlGenHub*	Hub of the swirl generator

Table 4 List of the decomposed geometrical entities, which were used for the further mesh generation. (geometrical entity excluded in case of pure axial flow simulations, as well as in case of the simulations excluding the SG to reduce the grid size)*

Same approach was applied in case of the geometry exluding the swirl generator. The overall dimensions of the computational domain were preserved, while the decomposition of the pipeline walls was simplified thanks to the absence of the swirl generator.

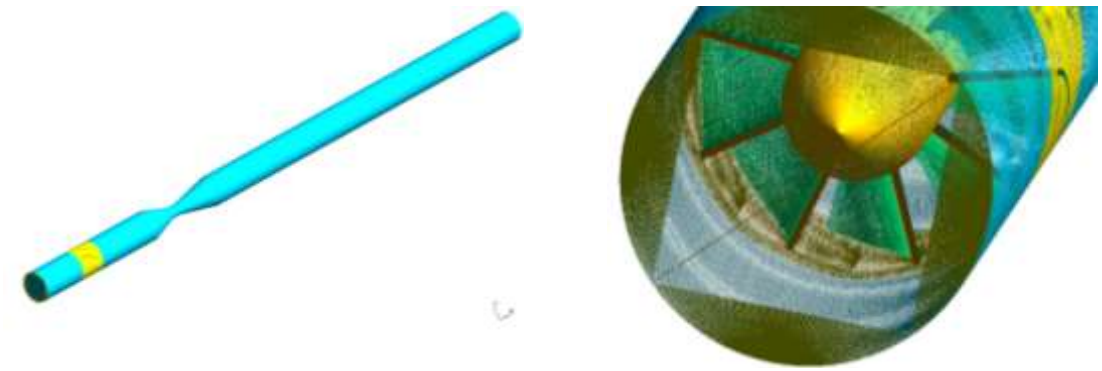

Figure 115 Computational domain overall view (left), decomposition of the walls near the SG and insight to the computational domain depicting decomposition of the SG (right)

5.2. Pre-processing: computational grids

Computational grids for the CFD analysis have been created using the cfMesh software, with the only exception considering purely hexahedral mesh generated using the Gambit as it will be described in the following text. CfMesh was chosen for its capabilities as well as for the fact that it is provided under the GPL license. This software is capable to create several types of computational grids based on the types of cells.

This meshing software is capable to create predominantly hexahedral using cartesianMesh workflow. This type of computational mesh was chosen based on the previous experiences as well as the general fact that hexahedral type of cells provides reasonable ratio between the quality of results and computational demands which are tightly bounded to the amount of the cells within the computational mesh.

Particularly important is the fact the cfMesh includes wide range of the mesh refinement tools. In addition to the boundary layers near the walls of the pipeline including the Venturi tube, the mesh has been refined near the vanes of the swirl generator its hub and in the region downstream the spike of the generator. The region downstream the spike of generator was refined also to capture swirl structure. Boundary layer near the vanes of the swirl generator has been excluded and replaced by the mesh refinement to prevent occurrence of low-quality elements.

Generation of the computational grid (CG) is driven by the meshing dictionary *meshDict*, which had to be placed in the *constants* directory of the OpenFoam case. The overall properties of the generated computational mesh are prescribed in the dictionary, including the maximum cells size, regions of refinements, boundary layers and types of the boundary conditions.

The whole computational domain is depicted in the Figure 116, where the geometry is divided into to the subsets of surfaces based on the boundary conditions, which will be described at the end of this chapter.

Figure 116 Computational domain in case of SG presence

As it has been mentioned, during the numerical investigation several computational grids were exploited. The grids can be divided into the three groups. The first group of the computational grids containing the CG1 and CG2 was created for the simulations of the cavitating flow influenced by the presence of the induced swirl. The whole experimental section including the swirl generator was considered in this case. The second group contains the CG3 which was exploited for the investigation of the cavitating flow dynamics. The swirl generator has been excluded and replaced by the pre-calculated profiles of velocity, turbulent kinetic energy and dissipation rate. This approach led to the significant reduction of the size of the grid and resulting computational time demands. On the other hand, this approach represents obvious trade-off, which lead to the certain problems as it will be described in the following chapters. The last group contains the CG4 which was utilized for the analysis of axial inflow excluding the swirl generator. The computational domain of the CG4 has the same dimensions (length) as the CG1 and CG 2. The grid has been generated using the same setting as in case of CG1. The only difference, beside the absence of the swirl generator, was exclusion of the refined region close to the axis within the throat of the nozzle. This led to significant reduction of the CG4 size compared to the size of CG 1. The list of the exploited computational grids is shown in the Table 5. The information of the overall amount of the cells as well as the relative representation of the hexahedral cells within the grids are provided. As it has been mentioned, the utilized computational grids were generated using the cartesianMesh algorithm included in the CfMesh meshing software. Comparing the relative representation of the hexahedral cells within the CG1 and CG2 (containing the body of the swirl generator) with the CG4 or CG3 (excluding the body of generator) it is obvious that the presence complex surfaces of the generator lead to the considerable increase of the non-hexahedral cells within the domain. On the other hand, the relative representation of the hexahedral cells never dropped below 96 % as it is also shown in the table.

Grid	Description	Cells	Hex. cells
CG 1	SG/CD - refined	2513319	96.4 %
CG 2	SG/CD - coarse	1857978	96.2 %
CG 3	Sliced - refined	1287400	99.5 %
CG 4	Axial inflow	1348604	99.8 %

Table 5 List of the computational grids utilized for the CFD analysis

5.2.1. Quality of the computational grids

The fundamental precondition of the successful CFD simulation is sufficient quality of the utilized computational grid. The most important parameters of the grids are represented by so-called non-orthogonality and skewness of the cells of computational grids together with the aspect ratio. It should be mentioned that the definitions of these parameters usually slightly differ based on the considered CFD software. Definition of these parameters in the OpenFoam is as follows.

The value of the grid non-orthogonality is represented by the magnitude of angle between the face normal vector and the vector connecting the centers of the adjacent cells (Figure 117). The value of non-orthogonality plays crucial role as contributor to error due to the way that gradients are calculated at faces of the cells. It is possible to increase value of **nNonOrthogonalCorrectors** within the fvSolution dictionary. Nevertheless, the maximum value of the non-orthogonality should be less than 75 (preferably less than 70). High value of the non-orthogonality undesirably affects the convergence of the numerical simulation.

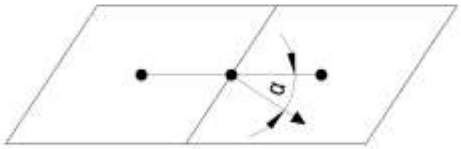

Figure 117 Non-orthogonality in OpenFoam – graphical representation

The value of skewness is given by the distance between the location of the face center and the vector connecting the centers of the adjacent cells as it is depicted in the Figure 118. The skewness introduces numerical diffusion, which takes effect during the computation of fluxes between the adjacent cells. This is particularly important in case of the tetrahedral computational girds, where **skewness corrected** scheme should be introduced.

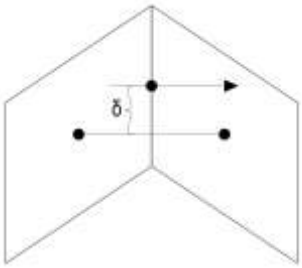

Figure 118 Skewness in OpenFoam - graphical representation

The aspect ratio is defined as the ratio between the cell width and cell length. From the definition of this parameter implies that the cells with the highest values of the aspect are usually part of the boundary layers at the same time it should be noted that large aspect ratio is acceptable within the regions without the strong transverse gradient (i.e. boundary layers).

The utilized computational grids were checked using the checkMesh utility prior the beginning of the CFD simulations. Table 6 is listing the obtained values of the maximum non-orthogonality, skewness and aspect ratios corresponding to the individual computational grids as the most important parameters of the mesh quality.

Grid	max non-orthogonality	avg. non-orthogonality	skewness.	aspect ratio
CG 1	68.7	5.9	2.7	104.1
CG 2	68.6	6.3	3.5	100.7
CG 3	65.8	4.6	1.0	105.1
CG 4	67.0	4.3	1.2	112.3

Table 6 List of the main quality parameters of the computational grids exploited during the numerical investigation

As it is depicted the maximum values of non-orthogonality never exceeded the 70. Thus, all the exploited grids fulfilled the requirements of the quality and therefore it was possible to assume that all of them are suitable for the numerical investigation.

5.2.2. Computational grids – refinements

Computational grids have been divided to three main groups and their sizes and parameters of quality have been described. Nevertheless, it is necessary to show and compare the refined regions as well as the overall nature of the grids to complete the description of the preparation of the grids. This will be suitable with respect to the further discussion of the obtained results.

The **boundaryLayer** utility was exploited for all walls contained within the computational domain with the exception of the near wall regions close to the surfaces of the generator vanes. This utility splits the cells close the wall in to the defined amount of the cells with the specified thickness of the first layer, the thickness growth ratio and the number of layers within the boundary layer. The details of the boundary layers in case of the CG1 (the same setting has been exploited in case of the CG3 and CG4) with the boundary layer of CG2 are provided in the Figure 119.

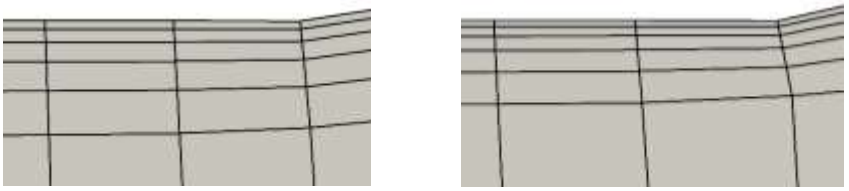

Figure 119 Comparison of the boundary layers CG 1 (left) and CG 2 right

In case that the **boundaryLayer** utility of the cfMesh was exploited in this region it was not possible to reach suitable values of the non-ortohogonality close to the trailing edges of the vanes as well as in the corners between vanes and shroud (wall of the pipe) of the swirl generator. The lowest maximum values of the non-orthogonality which were obtained using the **boundaryLayer** utility in these regions did not fall below the value of 78. While it was possible to obtain the results, which were in the relatively good qualitative agreement with the experimentally observed cavitating structures, the instability of the computations was unacceptable. Therefore, so-called **localRefinement** utilitity has been exploited to refine the computational grids close the vanes of the swirl generator. This approach led to the significant improvement of the non-orthogonality and skewness (see Table 6). On the other hand, this type of refinement represents a specific trade-off since the overall amount of the elements within the refined region is significantly higher compared to the boundary layer. The refinement is well depicted in the figures Figure 120 and Figure 121 which are comparing the surface meshes of the swirl generator in case of the CG1 and CG2. The trailing as well as the leading edges of the vanes were refined even more to capture the geometry of the generator properly.

Figure 120 Surface mesh of the swirl generator - CG1

Figure 121 Surface mesh of the swirl generator - CG2

The inter blade regions of the computational grids CG1 and CG2 are compared in the Figure 122. As it is relatively clearly visible, the cells are slightly smaller in case of the CG1 where reduced value of the maxCellSize has been exploited compared to the CG2.

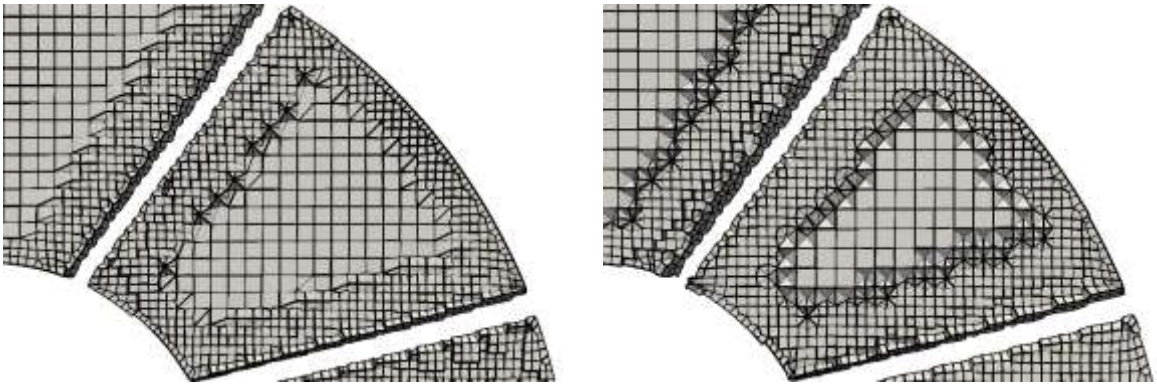

Figure 122 Comparison of the computational grids CG1 (left) and CG2 (right) in the inter-blades regions

Beside the reduced maximum size of the cells, the main difference between the CG1 and CG2 is refinement of the computational grid close to the axis downstream the spike of the swirl generator. This refinement has been done using **objectRefinement** utility. The main reason was to capture this region in more detail since some of the cavitating flow properties were not captured using the CG2 properly (the calculations utilizing the CG2 grid were carried out before the CG1). Nevertheless, the refinement

of this region leads to the significant increase of the computational grid size and consequent increase of the computational demands. The same refinement has been considered in case of the CG 3. The comparison of the computational grids CG1 and CG2 in the throat of the nozzle is depicted in the following figures.

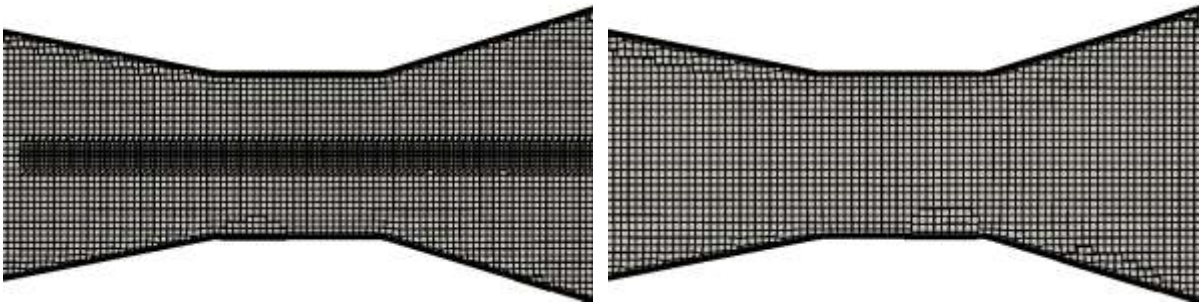

Figure 123 Longitudinal slice of the computational grids CG1 (left) and CG2 (right)

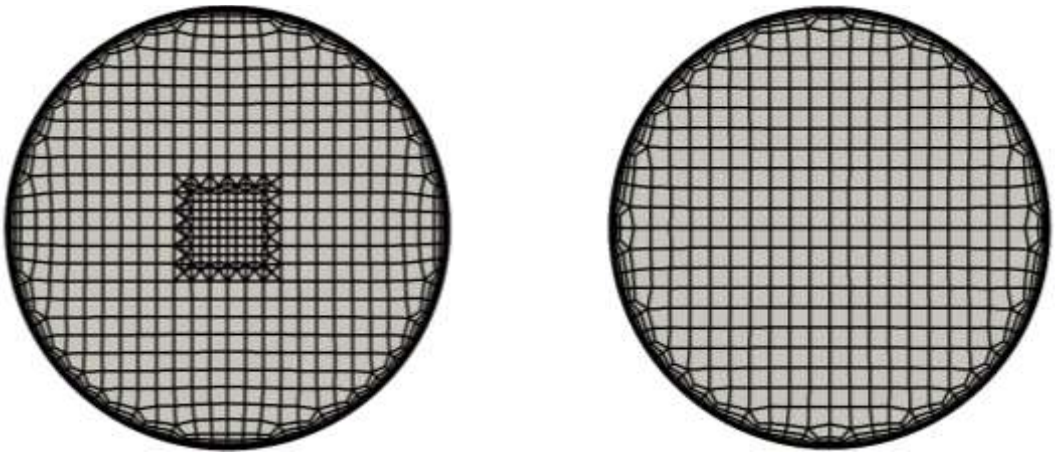

Figure 124 Comparison of the computational grids cross section within the throat of the nozzle. CG 1 (left), CG2 (right)

Since the CG 3 shares the same setting with the CG1 it is unnecessary to repeat the same images.

The last part of this section is devoted to the description the outlet of the computational domain. The density of the outlet part of the computational grid was decreased in order to reduce overall size of the of the girds by the increase of the size of the cells within this region. This increase was done in several steps to reduce the problems connected with the sudden increase of the cells size. The results of this approach are depicted in the Figure 125.

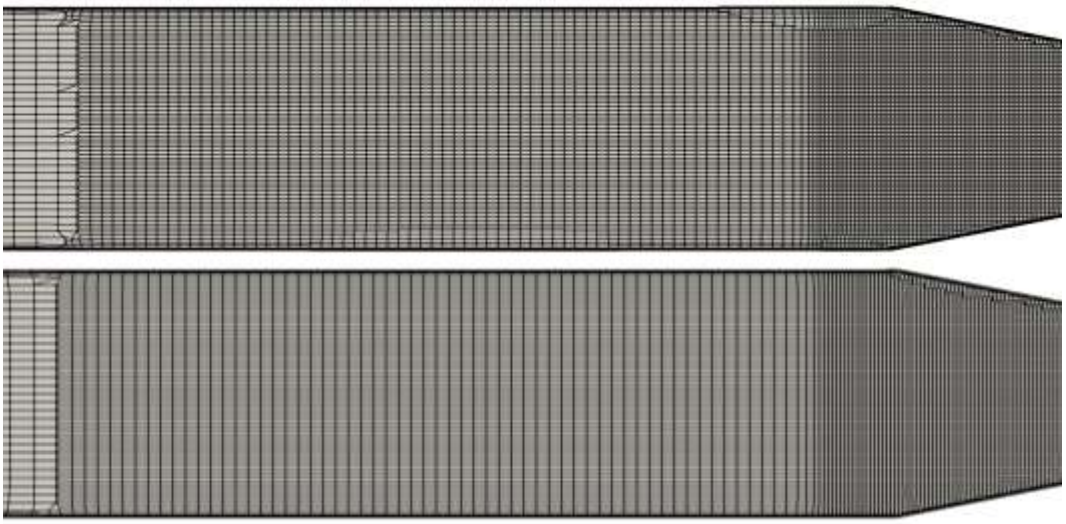

Figure 125 Comparison of the cells size transition downstream the diffuser of the nozzle. CG1 (top), CG2 bottom. The grids CG3 and CG 4 shared the same setting with the CG1

5.3. Pre-processing: boundary conditions, physical properties setting, and constants required for the numerical analysis

Boundary conditions represent crucial part of the CFD simulation. Thus, the conditions must be chosen and set properly to correspond the real-life flows which are investigated numerically. This section will be devoted to the description of the boundary conditions utilized for the numerical analysis. Overall, it can be stated that the boundary conditions were set to mimic the selected investigated operating points as accurate as it was possible (with certain simplifications which were considered as a reasonable trade-off between the accuracy and the computational time as it will be described). The individual computations share many properties, due to the similar nature of the investigated experimental configurations. Therefore the exploited boundary conditions will be described at once, with the references to the exceptions which resulted from the nature of the investigated case or from the approach chosen from the numerical analysis investigation. The general overview of the chosen boundary conditions is given in the Table 10, which is divided into the specific fields which are required for the computations carried out using the interPhaseChangeFoam solver. Since the simulations exploiting the computational grids CG 1 and CG 2 were the most complex, the complete list of the boundary conditions is provided. In case of the second group and the computations of the axial inflow, only the modifications are mentioned in the following part of this section.

Group 1 – CG1, CG2				
patch name	**inlet**	**outlet**	**walls**	**swirl generator***
U	fixedValue	inletOutlet	noSlip	noSlip
p_rgh	zeroGradient	fixedValue	zeroGradient	zeroGradient
alpha.water	fixedValue	zeroGradient	zeroGradient	zeroGradient
k	tIKEI**	inletOutlet	kqRWallFunction	kqRWallFunction
epsilon	tIMLDRI***	inletOutlet	epsiloWallFunction	epsiloWallFunction
nut	calculated	calculated	nutWallFunction	nutWallFunction

*Table 7 Complete list of the boundary conditions utilized in case of the simulations considering the complete geometry including the swirl generator. *group of patches including vanes, trailing edges, leading edges hub and shroud, **turbuletIntensityKineticEnergyInlet, ***turbuletIntensitMixingLengthDissipationRateInlet*

In case of the second group of the numerical simulations excluding the presence of the swirl generator, the inlet boundary condition of U, k and epsilon were modified. The presence of the SG has been

mimicked using the results of the simulations considering the complete geometry. Time-averaged profiles of the velocity (x,y and z components), turbulent kinetic energy and turbulent dissipation rate were computed 0.5 mm downstream the end of the SG using the ParaView. These profiles were exported and utilized as the inlet boundary conditions of these quantities for the numerical analysis of the dynamics of cavitating flow. For this purpose, the timeVaryingMappedFixedValue was utilized as the inlet boundary condition, while the required profiles were stored in the boundaryDataFolder nested in the constant folder of the computed cases. The abovementioned profiles will be described in the chapter 5.9.

The completely same set of the boundary conditions as in case of the first group of the simulations has been utilized for the axial inflow investigation (excluding the patches of swirl generator).

The fixed values of the inlet velocities and outlet pressures were set according to the time-averaged data obtained by the analysis of the experimental measurement. Nevertheless, in case of the velocity the certain simplification has been considered to reduce the computational time required for convergence of the calculated cases. For the numerical analysis, the discharge of 6 l/s was chosen for both of the investigated experimental configurations. While the specific outlet pressure was set according to the experimental data in each simulation, the constant value of velocity was considered regardless the investigated operating point. This value was obtained as the average discharge of the corresponding set of measurement. As it has been noted in the chapter devoted to the experimental measurement description, the actual discharge was set manually after the stabilization of the pressure within the pressure vessel. Therefore, the actual values of the discharges were slightly different for the specific investigated operating points. Nevertheless, the discharge uncertainty caused by this approach was minor as it is depicted in the Figure 126. Thus, it can be assumed that the resulting mistake should be negligible. On the other hand, this approach significantly reduced time of the simulations, which represented crucial problem during the investigation. It is also worth to note that the potential discrepancy between the experimental discharge and discharge considered for the numerical analysis was taken into account during the process of the numerical results evaluation (i.e. computation of the cavitation number, Strouhal number etc.). As it is depicted in the following charts (Figure 126), the discharge oscillated mildly regardless the experimentally investigated discharge. Nevertheless, it is clearly depicted that the uncertainty (i.e. the range between the highest and lowest measured discharge in this case) was considerably higher in case of the swirl generator presence. In other words, it was more difficult to set the specific discharge when the flow was affected by the induced swirl. On the other hand, even in case of the swirl generator presence the error introduced by the mean velocity utilization as the inlet boundary condition never exceeded 1.3 % in case of the 6 l/s flow rate, which was chosen for the numerical investigation.

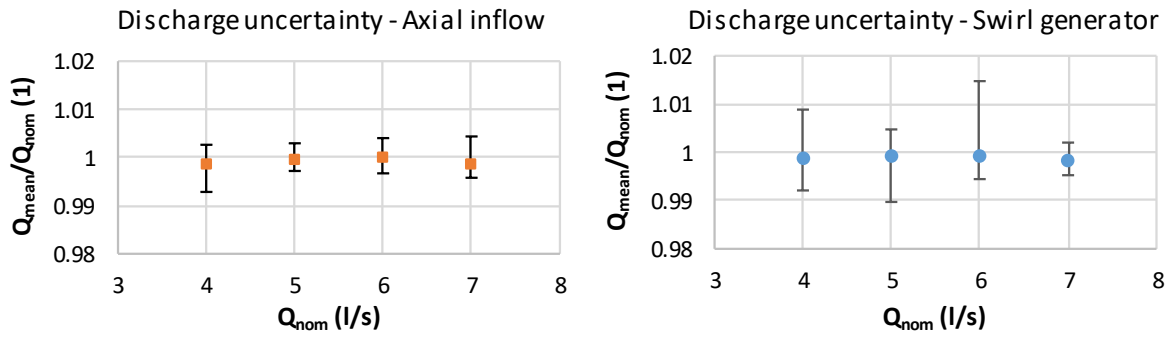

Figure 126 Uncertainty of the discharge during the experimental measurement

The outlet pressure has been set according to the mean values obtained by the analysis of the p_3 transducer records.

Similarly, to the setting of the inlet velocity, the properties of the water and saturated vapor were calculated using the mean values of the water temperature. The Table 8 contains the values of the properties exploited during the numerical simulations.

		Swirl generator	Axial inflow
p_{vap}	Pa	3557.18	4280.276
σ_{surf}	$kg\,s^{-2}$	0.07164	0.0719
ρ_{liq}	$kg\,m^{-3}$	996.52533	995.60328
ν_{liq}	$m^2\,s^{-1}$	$8.55 \cdot 10^{-7}$	$7.98 \cdot 10^{-7}$
ρ_{vap}	$kg\,m^{-3}$	0.02565	0.030919
ν_{vap}	$m^2\,s^{-1}$	$376.3 \cdot 10^{-6}$	$319 \cdot 10^{-6}$

Table 8 Physical properties of the water and saturated vapor required for the CFD case setting

To complete description numerical analysis setting, the constants required by the chosen mass transfer model must be provided. Kunz mass transfer model was chosen based on the preliminary simulations and good results of the cavitating flow investigation within the Venturi tube considering the axial inflow, which were published by Kozak et al. [51]. This model requires (except the abovementioned properties of liquid and saturated vapor) certain sets of coefficients as it has been described in the chapter devoted to the cavitation modelling using the CFD. The list of the utilized coefficients is provided in the following table.

	Swirl generator	Axial inflow
U_{inf}	2.6573329	2.658556
t_{inf}	0.201706	0.201613
C_c	900	1000
C_v	12000	10000

Table 9 Constants and coefficients required by Kunz model of mass transfer utilized for the numerical investigation

Where the t_{inf} has been calculated according to [16] as fraction of inlet velocity (U_{inf}) and the inlet diameter of the computational domain. The values of the C_c and C_v coefficients were set based on the previous author's experience with this setting utilized during the investigation of the cavitating flow within the Venturi tube considering axial inflow. [51] These values were slightly modified in case of the SG presence based on the preliminary results as it is shown in the table. It should be mentioned that the setting of the C_c and C_v coefficients acting as source terms of condensation and evaporation is purely empirical.

5.4. Pre-processing: numerical schemes and solvers settings

The numerical schemes exploited during the investigation as well as the setting of the solvers were nearly identical during the whole CFD investigation of the cavitating flow. Thus, the overall description will be provided in the following section, while the specific modifications required by the certain simulations will be emphasized. Schemes as well as the solvers settings exploited during the investigation were chosen based on the previous numerical investigation of the cavitating flow [51], and partially based on single-phase investigation of the swirling flows published by Štefan [45]. The final setting of the numerical schemes represents certain compromise between the accuracy and stability of the simulations.

The sets of the numerical schemes required by the chosen solver are specified in fvSchemes dictionary, which must be stored in the system folder of the CFD case. These schemes are divided to groups by their nature. Since the simulations were carried out as transient, the temporal discretization had to be specified as ddtScheme. In case of the simulation considering the whole geometry including the SG (i.e. group 1), the backward scheme has been chosen. Nevertheless, the Euler temporal discretization scheme was exploited in case of the simulations considering the axial inflow based on the previous experience with this type of cavitating flow simulation [51]. The Euler temporal discretization scheme has been also utilized in case of the simulations exploiting the sliced computational domain to ensure the stability of the computation. Nevertheless, based on the preliminary experience it shall be

noted that the difference between the Euler and backward ddtScheme is negligible considering very short length of time steps.

The other setting of the numerical schemes utilized during the numerical investigation was same all of the carried simulations. This part of fvSchemes dictionary is listed in the following table.

gradSchemes	
default	Gauss linear
grad(U)	cellLimited Gauss linear 1
divSchemes	
div(phi,U)	Gauss linearUpwind grad(U)
div(phi,k)	Gauss linearUpwind grad(k)
div(phi,epsilon)	Gauss upwind
div(phi,alpha)	Gauss vanLeer
div(phi,R)	Gauss interfaceCompression
div(R)	Gauss linear
div(phi,nuTilda)	Gauss linear
div(rhoPhi,U)	Gauss linearUpwind grad(U)
div((muEff*dev(T(grad(U)))))	Gauss linear
div(((rho*nuEff)*dev2(T(grad(U)))))	Gauss linear
laplacianSchemes	
default	Gauss linear limited corrected 0.33
interpolationSchemes	
default	linear
snGradSchemes	
default	limited corrected 0.5

Table 10 List of the exploited discretization schemes during the numerical analysis of the cavitating flow (default – all of the unspecified)

The equations solvers, tolerances and algorithms of the investigated OpenFoam case are defined within the fvSolution dictionary. The comprehensive description of the utilized setting would require considerable space and above that the setting was slightly modified several times during the investigation to increase stability of the simulations when it was necessary. Nevertheless, the typical setting exploited during the investigation is attached to the thesis to provide this information.

Overall, the PBiCG solver was exploited for the alpha water, U, k, and epsilon fields, while the p_rgh field has been solved using the GAMG solver. It should be also noted that the relative tolerance (rel_Tol) has been set to 0 except for the p_rgh field where this value was set to 0.1. The tolerances utilized in the solvers setting was varying between the 1e-7 and 1e-8.

Due to the transient nature of the investigated problems the PIMPLE algorithm was exploited for the coupling of the momentum and mass conservation equation. The relaxation factors were set to the 0.2 in the considerable part of the carried-out simulations. The nCorrectors value, which defines how many times the algorithm solves the pressure equation and momentum corrector in each step was set to 2. The nOuterCorrectors value has been set to 20 which is maximum allowed number of loops over the entire set of equations during the timestep. However, number of these loops significantly decreased during the simulations and usually stabilized at 2. In other words, the 2 loops were sufficient to reach the tolerances prescribed in the residualControl subdictionary of PIMPLE.

The simulations were carried out as transient, while the temporal discretization scheme has been described in the paragraph devoted to the fvSchemes, the length of the time-steps has not been mentioned yet. During the simulations considering the whole geometry, the variable length of time step based on the maximum value of the Courant number was used. This is allowed by the adjustTimeStep setting within the control dictionary of the investigated cases. The value maxCo and maxAlphaCo were set to 0.2. It was possible to use higher values (i.e. longer time-steps), but the decrease of the simulation

stability was unacceptable. This setting resulted in time-steps length of approximately $6\ 10^{-7}$ s.

In case of the CG 3 (considering sliced computational domains and precalculated profiles of inlet velocity, k and ε) and simulations of the axial inflow (CG 4), the constant time-step of $1.5\ 10^{-6}$ s has been set. This modification has been done to provide more appropriate results for the further analysis of cavitation dynamics. The time-step length was chosen based on the previous simulations considering the adjustable time-step setting, while the stability of the simulations remained satisfactory (the value of Courant number never exceeded 0.32).

5.5. Pre-processing – probes

Saving of the whole set of the computed data is usually not possible with the required time resolution since the significant disk space requirements is unbearable. Thus, so-called probes were defined in controlDictionaries of the simulations. These utilities allowed to store only the required data in certain points (probes) in order to mimic transducers exploited during the experimental investigation.

Using the OpenFoam probes the values of the pressure, were stored in the selected points with the period of 5E-5 s. The most important probes were located according to the pressure transducers exploited during the experimental measurement. Thus, it was possible to correlate the CFD results with the experimental data (i.e. pressure pulsations, hydraulic losses). The additional probes were exploited for the more detailed analysis of the cavitating flow properties. The list of the probes locations, which were defined during the whole CFD investigation is provided in the Table 11. It should be noted that some of the listed probes were out of the sliced computational domains (i.e. the probes upstream the swirl generator considering the location of p1 pressure transducer).

#	Location	Description
1	(0 0 -0.063)	p1 – upstream the SG
2	(0 0.025 -0.063)	p1 – upstream the SG
3	(0.025 0 -0.063)	p1 – upstream the SG
4	(0 0 0.577)	p2, p2k – downstream the straight part of the transparent section
5	(0 0.025 0.577)	p2, p2k – downstream the straight part of the transparent section
6	(0.025 0 0.577)	p2, p2k – downstream the straight part of the transparent section
7	(0 0 0.950)	p3* – downstream the straight part of the transparent section
8	(0 0.025 0.950)	p3* – downstream the straight part of the transparent section
9	(0.025 0 0.950)	p3* – downstream the straight part of the transparent section
10	(0 0 0.188)	Straight part of the transparent section upstream the throat
11	(0 0.009 0.188)	Straight part of the transparent section upstream the throat
12	(0.009 0 0.188)	Straight part of the transparent section upstream the throat
13	(0 0.01 0.270)	Diffuser downstream the throat of the nozzle
14	(0.01 0 0.270)	Diffuser downstream the throat of the nozzle
15	(0 0.014 0.290)	Diffuser downstream the throat of the nozzle
16	(0.014 0 0.290)	Diffuser downstream the throat of the nozzle
17	(0 0.02 0.320)	Diffuser downstream the throat of the nozzle
18	(0.02 0 0.320)	Diffuser downstream the throat of the nozzle

Table 11 List of the point probes utilized during the numerical investigation of the cavitating flow (the position of these probes was shifted slightly compared to the position of the p3 transducer to reduce length of the computational domain)*

5.6. Hydraulic loss analysis – influence of the computational grid density

The hydraulic loss coefficient was evaluated using the OpenFoam probes 2 and 8 records to correlate the numerical and experimental data. Since the computational domain has been sliced in case of the 2nd group of simulations, the correlation of ξ was possible only in case of the 1st and 3rd group of simulations, which were considering the whole geometry (including the SG in case of the 1st group). The obtained

results will be discussed for the individual experimental configurations separately to ensure clarity of description of the results and the utilized methodology of the hydraulic loss coefficient evaluation.

5.6.1. Hydraulic losses influenced by the presence of the SG

As it has been mentioned at the beginning of the section devoted to the analysis of the experimental data, the exploitation of the bulk velocity could be problematic in case of the SG presence. The bulk velocity corresponded well with the actual velocity of the flow within the throat of the nozzle in case of the axial inflow. On the other hand, the neglection of the radial and mainly the tangential velocity components can lead to the misinterpretation of the obtained results in case of the SG presence. Thus, the effect of the correction of ξ and σ_{vel} values of using the CFD results will be described in this section. Furthermore, the effect of the computational grid density will be discussed using computational grids with slightly different densities of the cells as well as including different regions of refinement. The computational grids CG 1 and CG 2 were exploited for this purpose. The comparison of the obtained results with the experimental data is shown in the Figure 127. Bulk velocity was utilized for the calculation of the ξ and σ_{vel} to follow the same methodology as in case of the experimental data analysis.

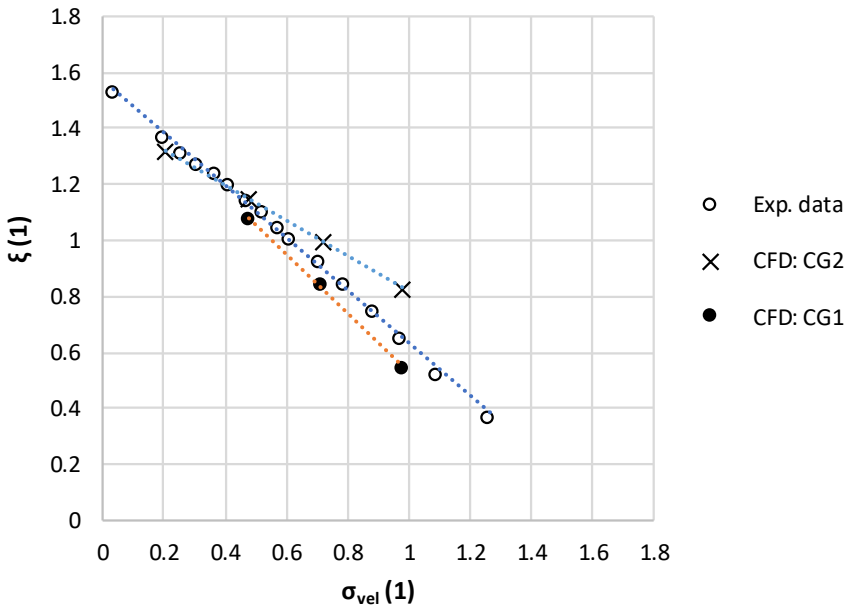

Figure 127 Correlation of the experimental results with the numerical analysis of the hydraulic loss coefficient utilizing different computational grids in case of the swirl generator presence

The experimentally obtained course of the hydraulic loss coefficient is nearly linear within the investigated range of the cavitation regimes as it can be seen in the chart. This linearity has been captured regardless the exploited computational grid. It should be mentioned that the simulations utilizing the CG 2 were carried out prior the simulations considering the refined mesh. Based on the obtained results it was possible to state, that the value of the ξ was in good agreement with the experimental data in case of the low cavitation numbers (i.e. in case of the large cavitating structures), but the difference between the numerical and experimental results are significantly worse in case of the initial regimes of the cavitation as it is clearly depicted in the Figure 127. Therefore, the CG 1 has been refined and the special care was devoted to the region close to the axis downstream the spike of the swirl generator. These modifications led to the significant improvement of the slope of hydraulic loss curve as it is depicted in the chart. Therefore, it can be assumed that the refined grid provides considerably more accurate prediction of the hydraulic losses. The main disadvantage of the refinement was represented by increase of the computational time demands, which made nearly impossible to make proper investigation of the cavitation dynamics as it will be described. Refined computational grid has been chosen for the further analysis of the numerical results.

To correct the experimental data, the kinetic energy correction factor has been calculated using the equation (76) based on the time-averaged values obtained by the CFD computations exploiting the refined grid (CG1). The evaluation of the α_{corr} computations has been done at the inlet of the throat of Venturi tube, due to the stability of the of the flow. The obtained values of the α_{corr} are shown in the following table.

$$\alpha_{corr} = \frac{\iint v_{ax} \cdot v_{mag}{}^{2} \, dS}{v_{bulk}{}^{3} \, S} \tag{76}$$

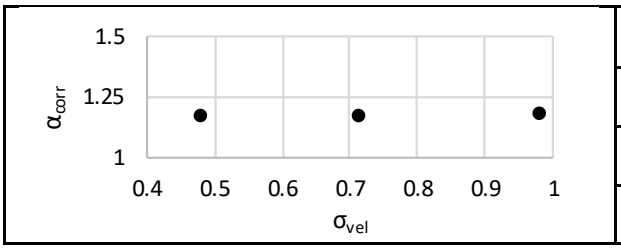

σ_{vel}	α_{corr}
0.48	1.710
0.71	1.720
0.98	1.777

Figure 128 Kinetic energy correction factor - values obtained by the numerical analysis considering refined grid CG1

As it can be seen, the value of the α_{corr} is stable, regardless the investigated operating point. Thus, the experimental results were corrected using the mean value of the α_{corr} (1.1732). The comparison of the corrected experimental results with the numerical analysis (considering the velocity magnitude as the reference value for the computation of the σ_{vel} and ξ are depicted in the Figure 129.

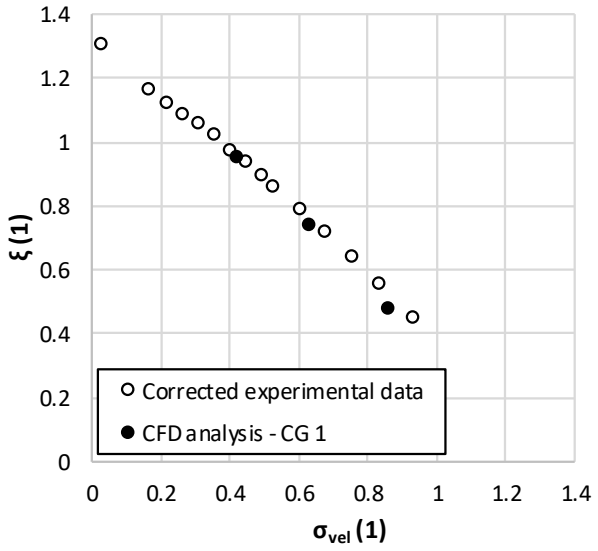

Figure 129 Comparison of the corrected experimental results with the CFD analysis of hydraulic loss coefficient in case of the swirl generator presence.

The results of the hydraulic losses analysis were also evaluated in case of the axial inflow considering using the grid CG 4 and flow rate of 6 l/s. The general tendency of the increasing ξ with the decreasing value of σ_{vel} was predicted accurately. On the other hand, the actual value of the hydraulic loss coefficient is slightly overpredicted compared to the experimental results as it is depicted in the Figure 130. Since the numerical analysis has been focused mainly on the cavitation influenced by the induced swirl, this

discrepancy was found acceptable and the further effort was devoted to the analysis of the cavitation dynamics as it will be described in the following sections of this chapter.

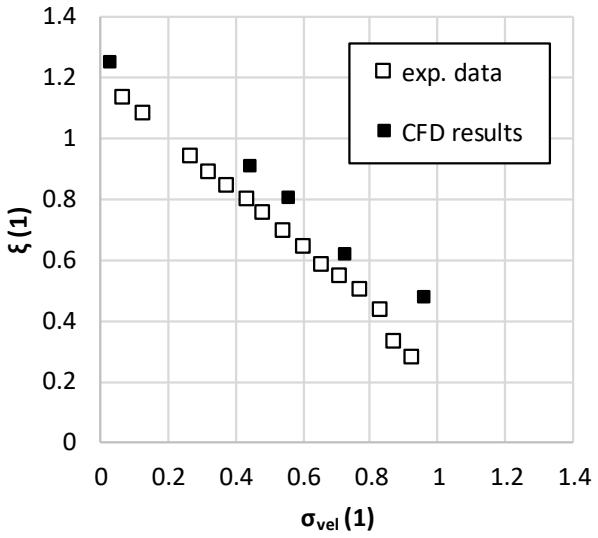

Figure 130 Comparison of the hydraulic loss coefficient obtained by the CFD with the experimental results in case of axial inflow

However, it is interesting that the results for both investigated experimental configurations are slightly different from the qualitative point of view regardless the fact that the utilized computational grids were generated using the same setting. While general tendency of the ξ depending on the σ_{vel} was captured in both of the investigated configurations, the actual values were slightly underpredicted in case of the swirling flow investigation in contrast to the axial inflow investigation, which provided slightly overpredicted values of the hydraulic loss coefficient.

5.7. Cavitating structures captured using the CFD – dynamics of cavitating flow influenced by the induced swirl

While the hydraulic losses predicted by the CFD analysis were compared with the experimental results in the previous section of this chapter, the main purpose of the following text will be to describe the cavitating structures predicted by the numerical analysis, compare these results with the experimental data and consequently to analyse cavitation dynamics. Dominant frequencies as well as the variation of the velocity and pressure fields during the cycle of cavitation development will be discussed in case of the SG presence as well as in case of the axial inflow.

As it has been mentioned, the numerical analysis exploiting the complete test section geometry (CG 1) was unbearably time-consuming for the investigation of cavitation dynamics. Nonetheless, the qualitative comparison of the predicted cavitation structures was discussed in [58].

Although the results of the numerical analysis utilizing the CG1 were in reasonably good agreement with the experimental observations from the hydraulic loss coefficient point of view, two major differences of the flow fields downstream the swirl generator shall be noted. Thin cavitating vortex filament was observed downstream the spike of SG during the experiments as it is depicted in the Figure 131. The vortex filament has not been captured numerically using the abovementioned settings and computational grids. On the other hand, the significant pressure drop in the region of the nozzle axis can be seen in the Figure 131 and above, that the contour of the averaged vapour void fraction (0.75) extends into the diffuser upstream the throat of the nozzle. The second qualitative discrepancy between the numerical and experimental flow downstream the swirl generator is represented by the periodical pulsations of the cavitating boundary layer within the diffuser downstream the throat of the nozzle observed in case of the CFD analysis as is depicted in the same figure. The cavitation in this region was

relatively seldom in case of the experiments. Significant cavitation of boundary layer was observed only during the supercavitation regime in in case of experiments.

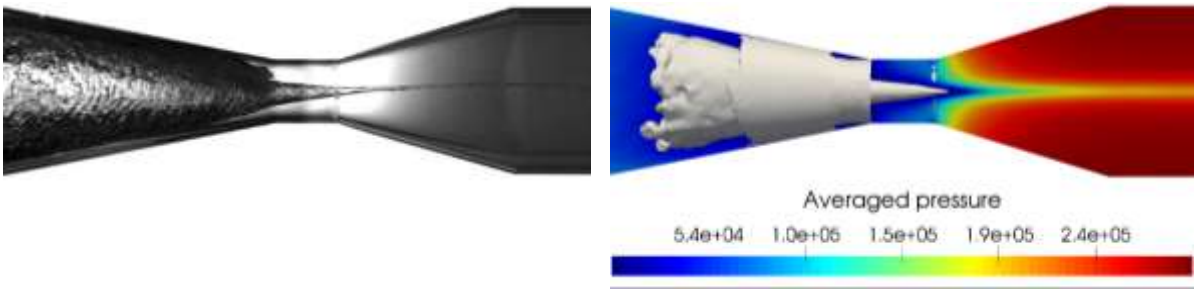

Figure 131 Main flaws of the numerical analysis of the cavitating flow considering the full geometry of the test section (CG1) – overpredicted cavitation of the boundary layer and absence of the cavitating vortex filament downstream the spike of SG. (75% of the vapor)

The absence of the cavitating vortex filament in case of CFD simulations could be partially devoted to the rough surface of the real swirl generator, where the small imperfections of the spike play an important role in the process of the cavitation inception. On the other hand, the overestimated cavitation of the boundary layer points to slightly different redistribution of the flow downstream the nozzle throat in case of CFD analysis.

Regardless the abovementioned flaws of numerical computations, the obtained results are in good agreement with the experimental observations. Downstream the coherent conical cavitating structure, the relatively short, but significant, helical vortex can be found in case of H-S image corresponding to the cavitation number of 0.98 (Figure 132). It was possible to capture this phenomenon using the refined computational grid CG1.

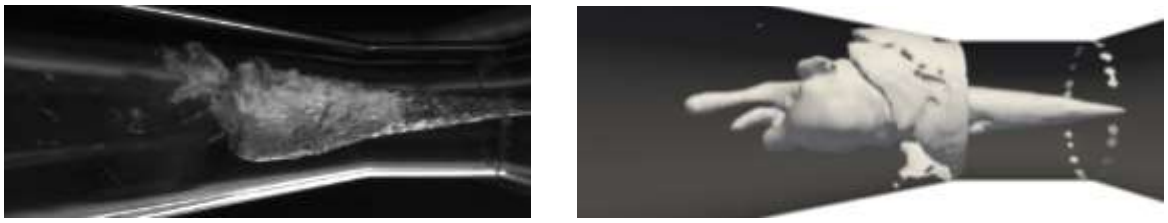

Figure 132 Cavitating vortex captured using the CFD

The helical vortex breakdown in the throat of the nozzle observed during the experimental measurement was also captured using the CFD (Figure 133). Contour of 0.25 of vapour void fraction was exploited for the cavitation visualization again.

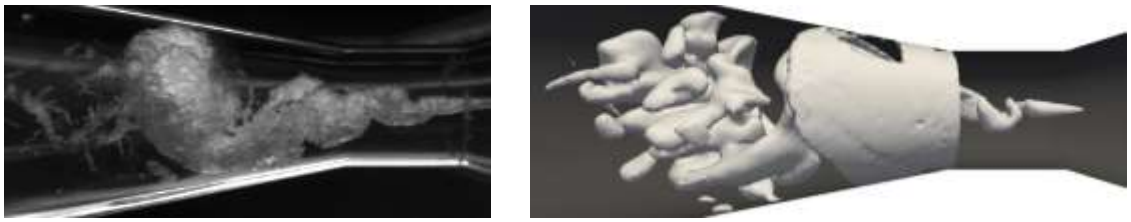

Figure 133 Helical vortex breakdown captured using the CFD

The comparison of the axial velocity and vapour void fraction fields with the images captured using the HS camera is provided in the following set of images (Figure 134). The images correspond to the maximum length of the cavitation structures, prior the beginning of its collapse. First of all, it should be emphasized that the HS images represent 3D instantaneous spatial distribution of the cavitation within the flow and the images of 2D longitudinal cross-section was chosen for the numerical results visualization. As it is clearly depicted, the amount of the gaseous phase is the higher, the lower is

cavitation number. Above that, the predicted length of the cavitating structures prior the beginning of their collapse is in good agreement with the experimental observation. Several conclusions can be stated, comparing the vapor void fraction and field of axial velocity.
The region of the significant backflow can be found within the core of the cavitating vortex, which has been also observed on the HS records. As it is clearly depicted in the set of figures, the significant amount of liquid water can be found within the core of cavitating vortex in case of the cavitation numbers of 0.71 and 0.48. While the HS records do not provide information of the phase distribution across the cross-section of the nozzle, it was possible to observe that the liquid water was sucked in to the cavitating vortex in the cavitation closure region (Figure 135).

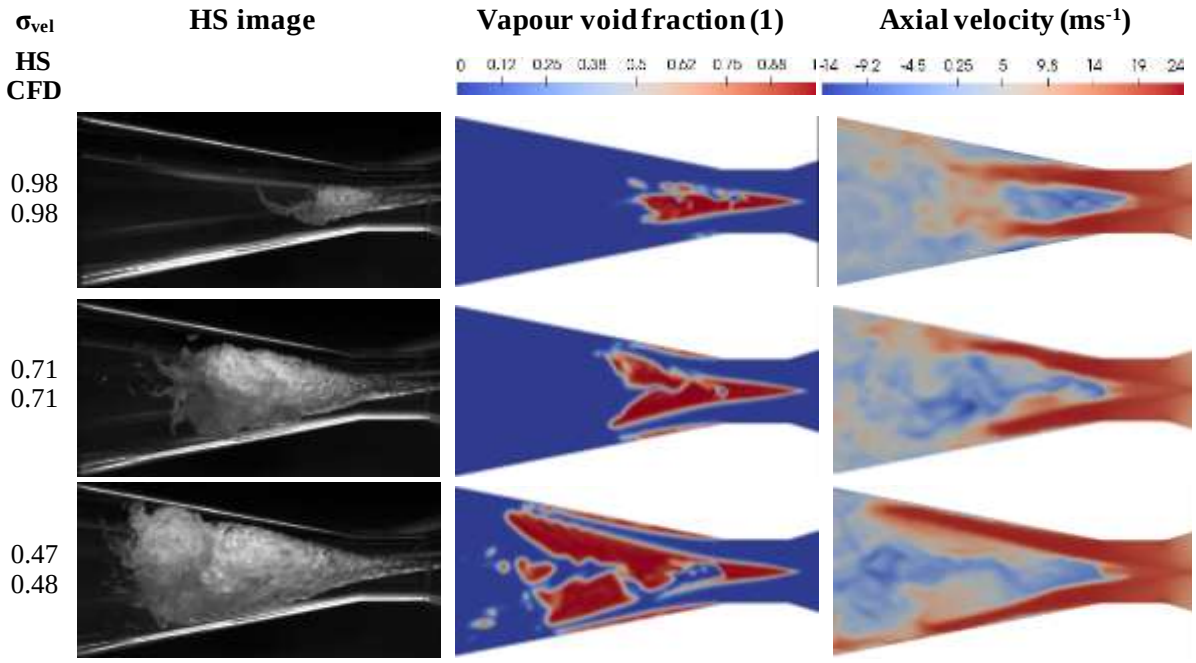

Figure 134 The images captured using HS camera in comparison with the numerical results obtained using the refined mesh of complete test section (CG 1)

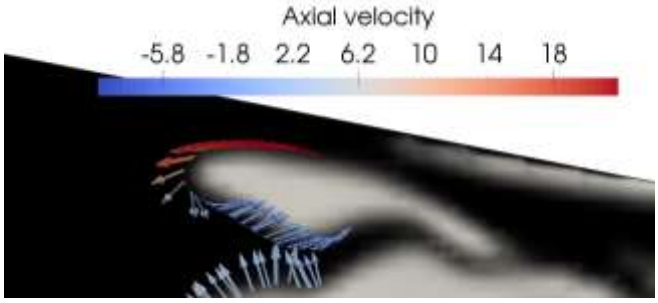

Figure 135 Detail of the cavitation closure region with velocity vectors colored by the axial velocity magnitude

As it has been shown the results of the numerical analysis considering the geometry including SG were in good agreement with the experimental data from the hydraulic loss coefficient as well as from the overall character of the predicted cavitating structures points of view. The main problem of this approach was unbearable computational time required for the proper analysis of the cavitating structure dynamics. Therefore, the computational domain has been sliced downstream the SG and the obtained time-averaged profiles of the velocity U, turbulent kinetic energy k and turbulent dissipation rate ε were utilized as the inlet boundary condition. This approach led to the significant reduction of the

computational grid size. Above that, the time step length was increased, due to the fact that the small cells surrounding vanes of the SG were excluded from the computational domain. Based on the comparison of simulations of the corresponding operating points considering computation of 1000 timesteps, it can be stated that this approach has been approximately 6.5 times faster. The contours of the exploited inlet boundary conditions are depicted in the Figure 136.

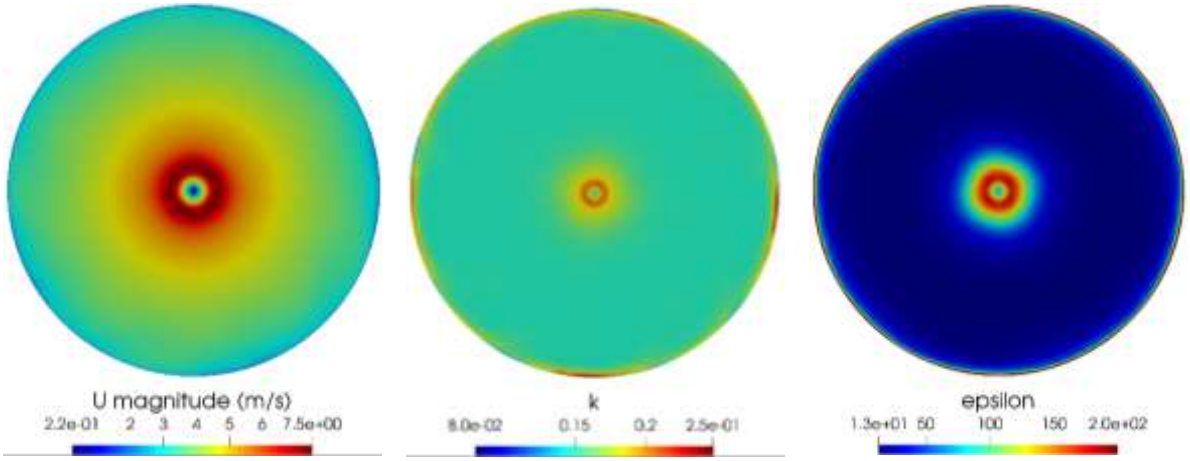

Figure 136 Profiles of the inlet boundary conditions exploited during the simulations considering sliced computational domain

Prior the analysis of dynamics, time-averaged contours of the axial velocity field, pressure field and distribution of the vapor void fraction in the whole range of investigated operating points are provided in the following set of images (see Figure 137).

Predicted presence of the gaseous phase in the Venturi tube was the more significant, the lower was investigated cavitation number. Presence of the pulsating cavitating structures within the diffuser related to the creation of the backflow region close to the axis of the test section was captured. This is clearly visible in the fields of the axial velocity. The reversed flow region vanished in case of the supercavitation as well as in case of the initial stage of cavitation within the Venturi tube. Therefore, it can be assumed that the onset of the reversed-flow region plays crucial role in pulsations of the cavitating structures similar to the part-load operation of the hydraulic turbines.

Predicted increase of the gaseous phase amount within the Venturi nozzle is gradual up to the σ_{vel} 0.435. Nevertheless, with the decreasing outlet pressure (and consequently cavitation number), the abrupt increase of the gaseous phase presence within the depicted slices can be found. This is in good agreement with the course of the pipe wall acceleration as it has been described.

Cavitation cycles predicted by the numerical analysis as well as the detailed description of the obtained results will be provided for the selected operating points in the following subsections.

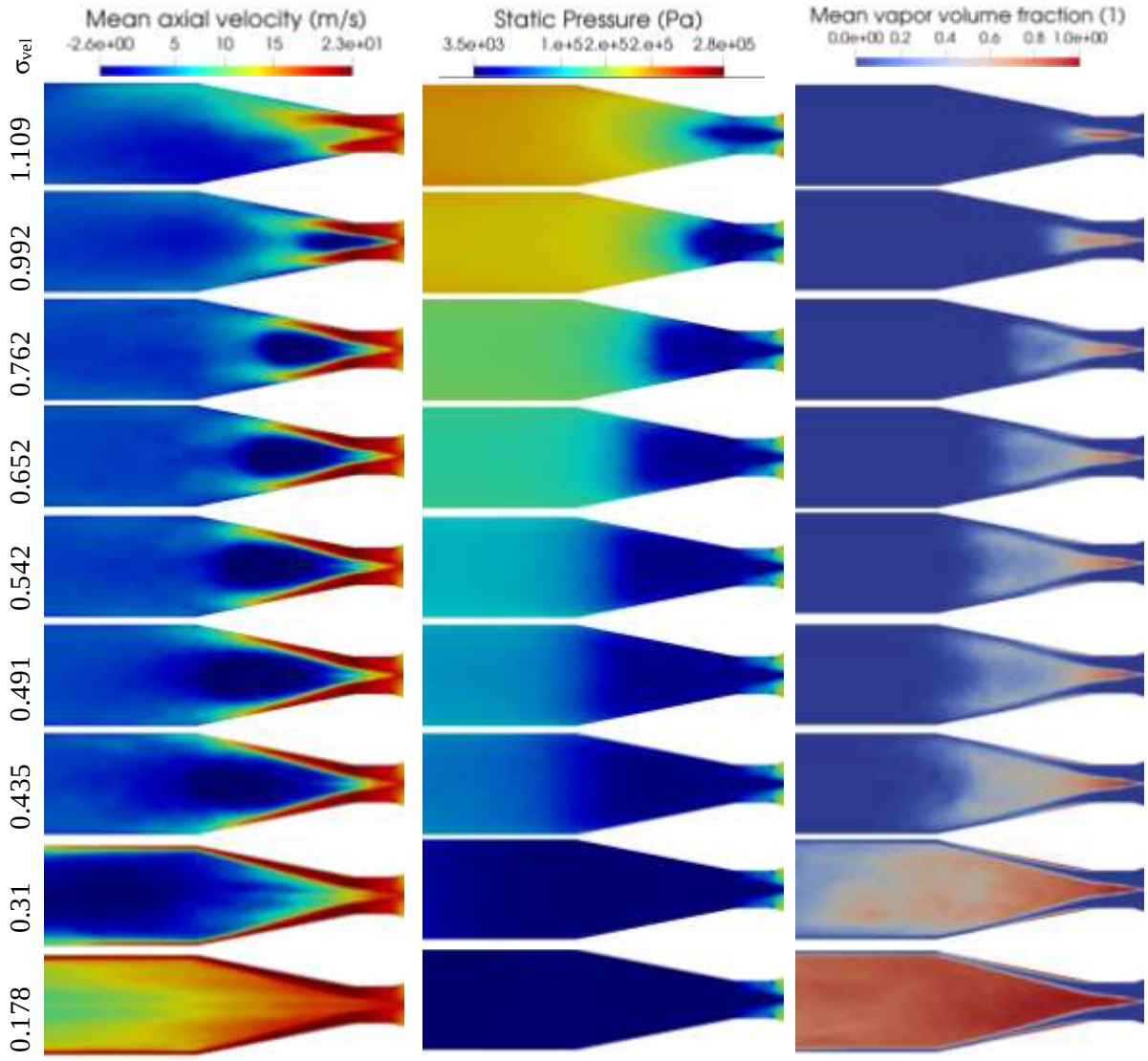

Figure 137 Set of images depicting time-averaged fields of axial velocity, static pressure and vapor void fraction obtained by the numerical analysis considering SG presence

5.7.1. Initial stage of cavitation, region 1, σ_{vel} 1.09, outlet pressure 200 kPa

The occurrence of the conical cavitating vortex in case of the SG presence is preceded by the presence of the straight cavitating vortex as it has been described in the chapter 2.3.1. This regime of cavitation was investigated numerically. As it can be seen in the Figure 138, the straight vortex filled by the gaseous phase occurred within the throat of the nozzle. The gradual growth of the cavitating vortex downstream the diffuser as well as the consequent partial collapse of the structure was observed using the CFD. The flow field downstream the throat was highly disturbed. The large region of the recirculation can be found within the diffuser as it can be seen in the images depicting fields of axial velocity.

Interesting is the fact that the transitions of the straight cavitating vortex to the form of the small conical cavitating vortex was captured during the investigation as it is shown the in penultimate row of the Figure 138. Occurrence of this type of cavitating structure within the flow is accompanied with the vortex breakdown at the tip of the structure. This was observed during the experimental as well as during the numerical investigation of the phenomenon.

In the chart depicting the records of the static pressure as a function of time (see Figure 139), the significant qualitative difference can be stated based on the position of the pressure probe. The pressure signals within this chart correspond to the 5th, 10th and 13th probe as is indicated by the color of the

corresponding rows in the Table 11. The same color will be exploited also in the following charts depicting the records of static pressure obtained by CFD. Description of these three probes is as follows:

- p1: pressure probe upstream the throat of the nozzle, located on the axis of the Venturi tube
- p2: pressure probe downstream the throat of the nozzle, close to the trailing edge of the throat
- pk: pressure probe close to the wall, same position as p_2 (BD sensors) and p_{2k} (Kistler) pressure transducers exploited during the experimental campaign

While the pressure shocks corresponding to the partial collapse of the thin cavitating vortex (position 1 in the chart) can be found regardless the position of the pressure probe. Higher frequencies of the pressure fluctuations corresponding to the cavitating vortex rotation are captured clearly in case of the p2 close the trailing edge of the throat. This pressure pulsation propagated partially to the pressure probe pk. The transition of the straight cavitating vortex to the conical vortex can be also identified in the pressure record without any problem from the qualitative point of view.

The pressure field corresponding to the longest straight cavitating vortex (position 2 in the chart) captured during the cycle is depicted of the second row of the set of the images. As it can be seen the nature of the captured vortex is similar to the straight cavitating vortex which can be found downstream Francis turbine during the operation under the overload conditions. The region of the low pressure close to the axis of the nozzle is considerably larger compared to the beginning of the cycle right after the partial collapse of the cavitating vortex.

The 3rd position highlighted in the chart (see Figure 139) of the static pressure corresponds to the presence of the nearly conical cavitating vortex depicted in Figure 138. The instantaneous pressure field shows significant qualitative change compared to the pressure field corresponding to the straight vortex (see Figure 140). The region of the low pressure is visibly shorter but thicker within the throat of the nozzle. Increased diameter of the cavitating structure leads to the significant redistribution of the flow within the throat and the pressure drop on the edges is more apparent in case of the conical structure, which is in good agreement with the nature of the fields of axial velocity depicted in the set of images.

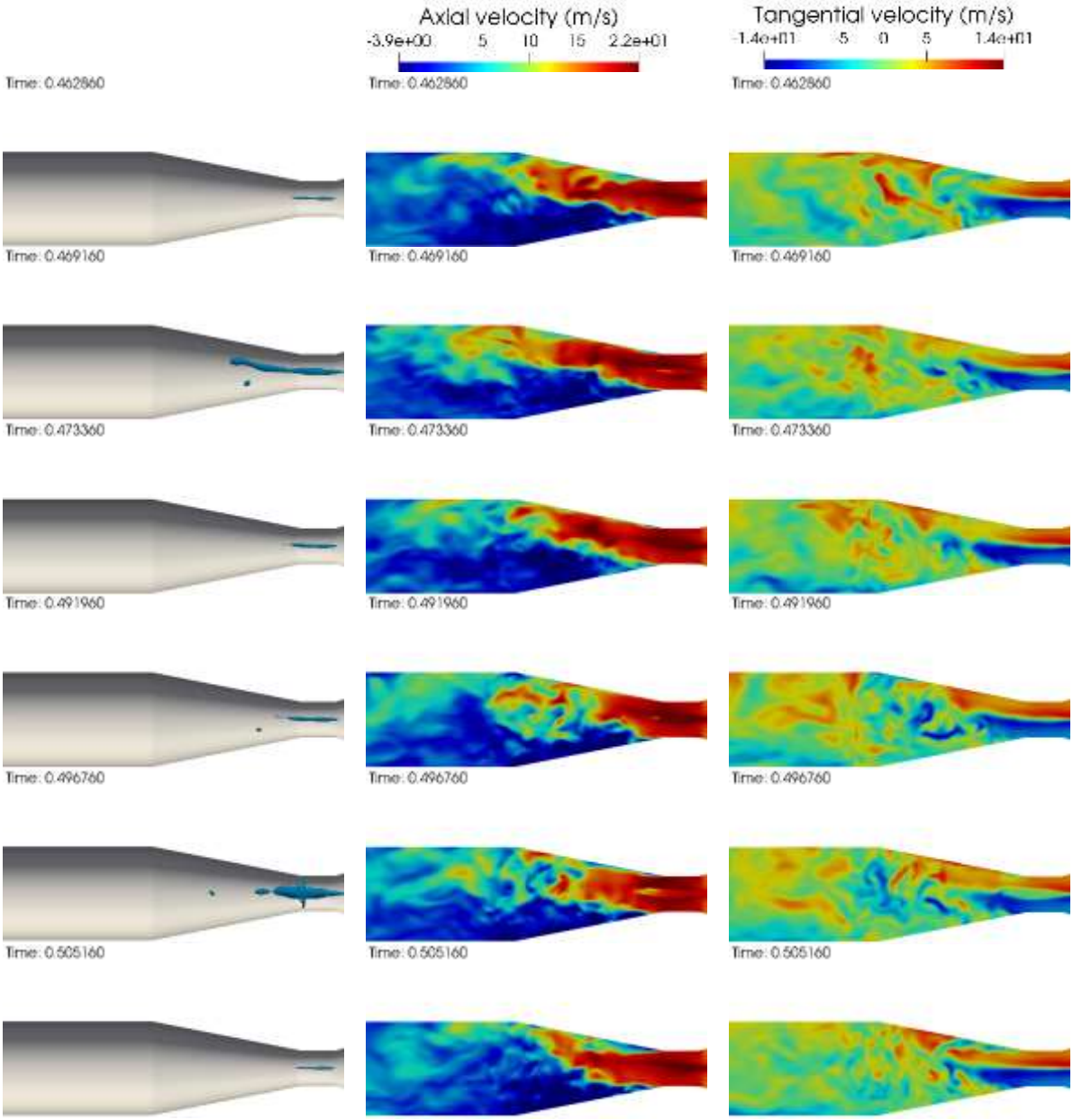

Figure 138 Set of instantaneous images depicting cavitation cycle, SG, initial stage – σ_{vel} 1.09, right column – 75% vapor, middle column - axial velocity, right column tangential velocity.

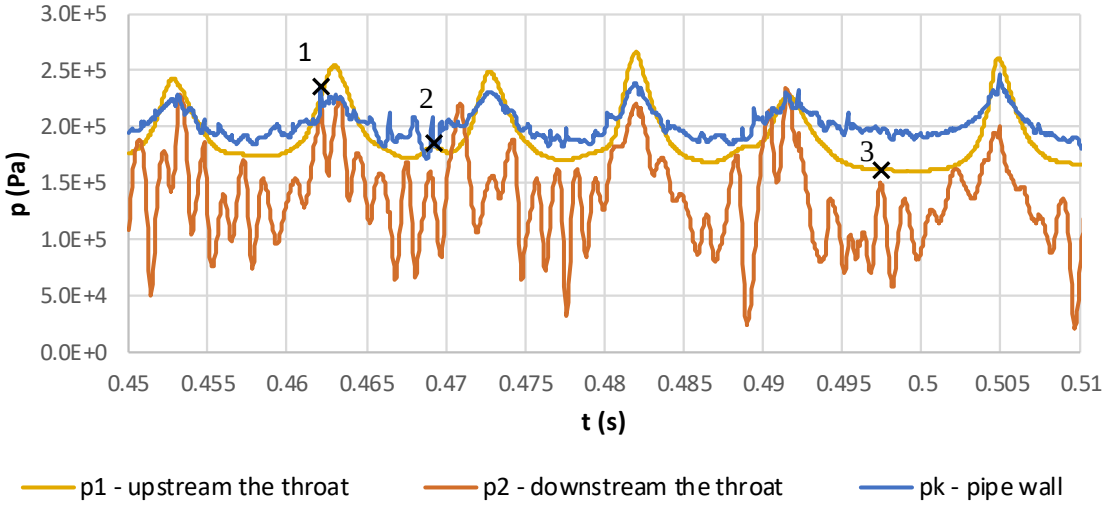

Figure 139 Numerically predicted course of the static pressure captured in three different positions in case of the initial stage of cavitation (σ_{vel} 1.09) and SG presence.

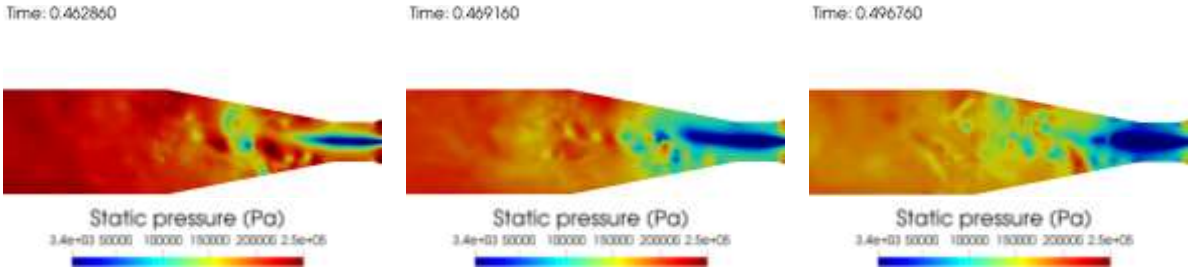

Figure 140 Maps of the pressure field during the cavitation cycle, initial stage (σ_{vel} 1.09) and SG presence. Position 1 – left, Position 2 – middle, Position 3 - right

5.7.2. Fully developed cavitation, σ_{vel} 0.76, outlet pressure 140 kPa

Presence and pulsations of the conical cavitating vortex as the typical structure of the more developed stages of cavitation has different nature from the qualitative as well as from the quantitative point of view. Nevertheless, some of the main properties of the cycle are similar to the initial stage of the cavitation.

The typical cycle ,as is shown it the Figure 143, begins right after the complete collapse of the cavitation within the throat of the nozzle. Comparing the velocity field corresponding to this regime with the velocity field of the initial stage of the cavitation, important difference can be found in case of the flow redistribution. As it has been described in case of the time-averaged fields, the region of the highest velocity moved from the region close to the axis of the nozzle towards to the walls of the nozzle. Prior the re-creation of the cavitating structure within the throat, the large region of the backward flow can be found within the throat of the nozzle. As it has been described in the chapter devoted to the description of the cavitation cycles using the H-S video records, this back flow region plays a crucial role during the collapse of the cavitating vortex. Helical vortex breakdown is clearly depicted using the field of tangential velocity.

Similarly as in case of the initial stage of the cavitation, the collapse prior the beginning of the cycle is caused by the significant pressure shock as it is depicted in the chart in the Figure 141. This shock was captured by the probes upstream and downstream the throat, while it was not captured using the probe pk (position 1 in the chart). The pressure shock within this region was slightly delayed (position 2 in the chart).

The following pressure shock can be found in case of the pk probe in the middle of the cavitation cycle as a beginning of the collapse of the cavitation structure within the diffuser of the nozzle

(position 3 in the chart). Pressure records are complemented by the images of the pressure fields provided in the Figure 142.

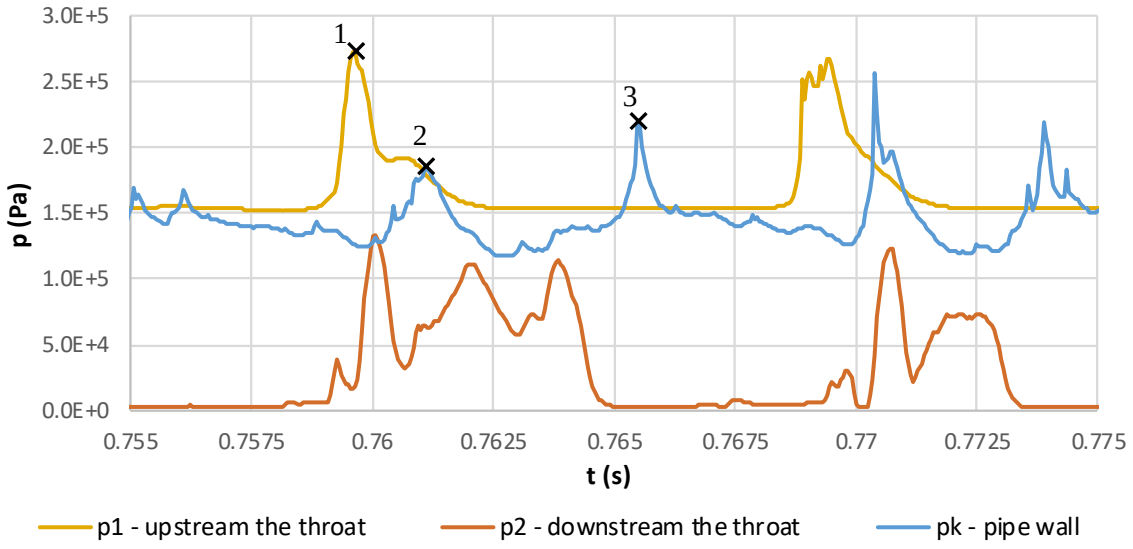

Figure 141 Numerically predicted course of the static pressure captured in the three different positions in case of the initial stage of cavitation (σ_{vel} 0.76) and SG presence.

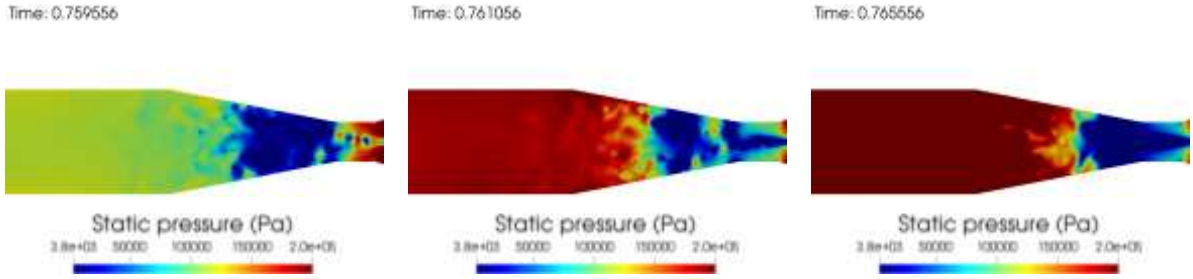

Figure 142 Maps of the pressure field during the cavitation cycle, initial stage of cavitation (σ_{vel} 0.76) and SG presence.

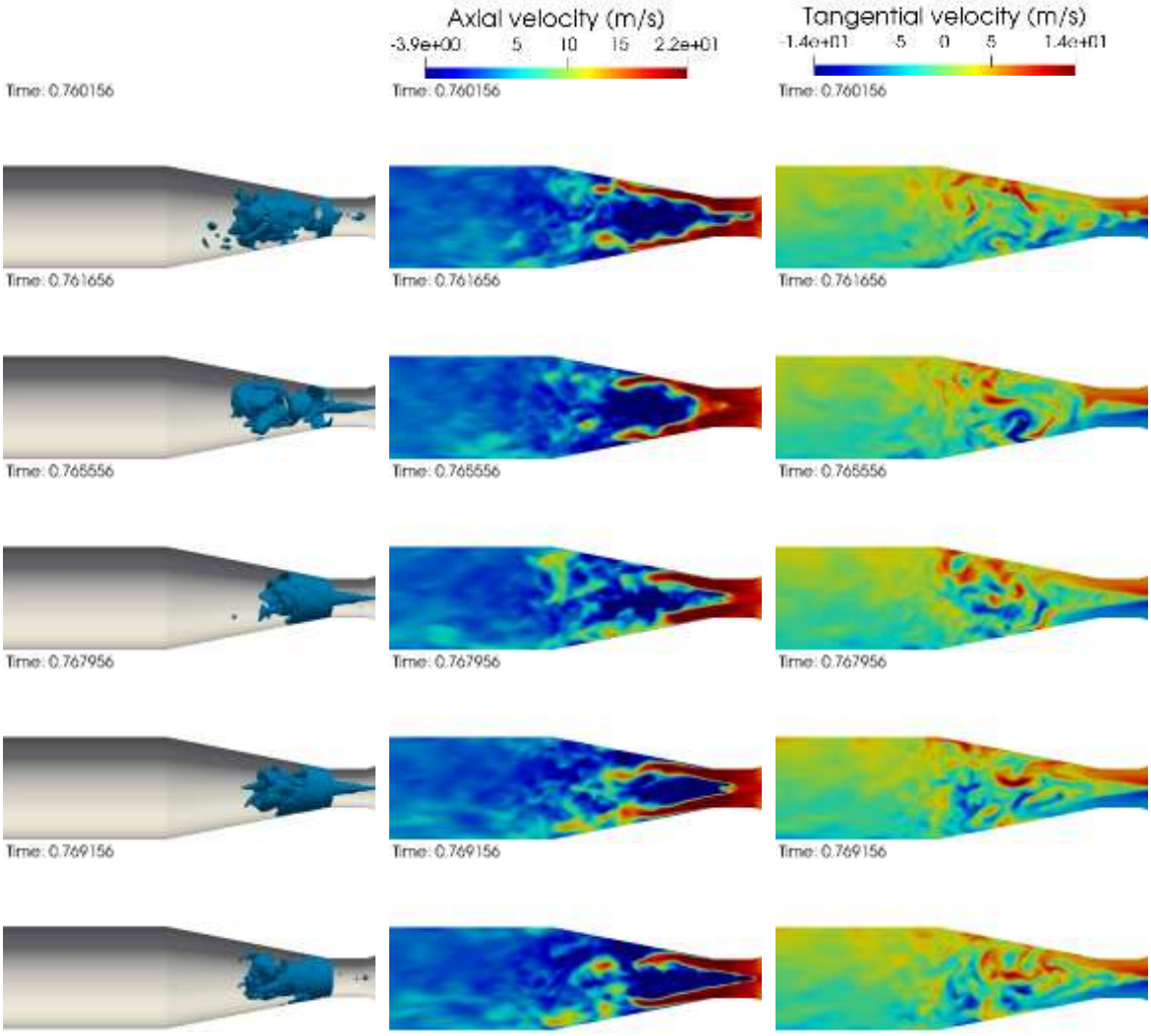

Figure 143 Set of images depicting cavitation cycle, initial stage – σ_{vel} 0.76, right column – 75% vapor, middle column - axial velocity, right column tangential velocity.

5.7.3. Fully developed cavitation, σ_{vel} 0.43, outlet pressure 80 kPa

The conical cavitating vortex became more significant with the further decreasing value of the cavitating number, as it has been described using the H-S records and as it is depicted in the Figure 144. As it can be seen in the chart depicting the values of the static pressure during the time (Figure 145), the most important properties of the pressure fluctuations are similar compared to the previous operating point as well as the general development of the cavitating structure during the cycle. Thus, the in-depth description of the obtained results is not necessary. On the other hand, it would be useful to describe the influence of the decreasing cavitation number value using the obtained pressure records. It is obvious that the length of the cavitation cycle period is considerably lower. This agrees with the analysis of the experimental data including the analysis of the pressure pulsations and H-S video records. The quantitative results of the cavitation dynamics predicted by the numerical methods will be provided at the end of this chapter. The courses of the static pressure records depicted in the Figure 145 are similar to the previously discussed operating point.

Comparing the records corresponding to the pressure probe p2 with the previously described operating point it can be seen that the re-creation of the stable cavitating structure after its collapse lasted approximately same time (0.004s). On the other hand, propagation of the pressure shock clearly captured by the p1 and p2 probes is less important in case of the pressure probe pk compared to the previous operating point, where this pressure shock was captured even in the straight pipe downstream the

diffuser of the nozzle. The representative pressure fields during the cycle are depicted below the chart of static pressures in the Figure 146.

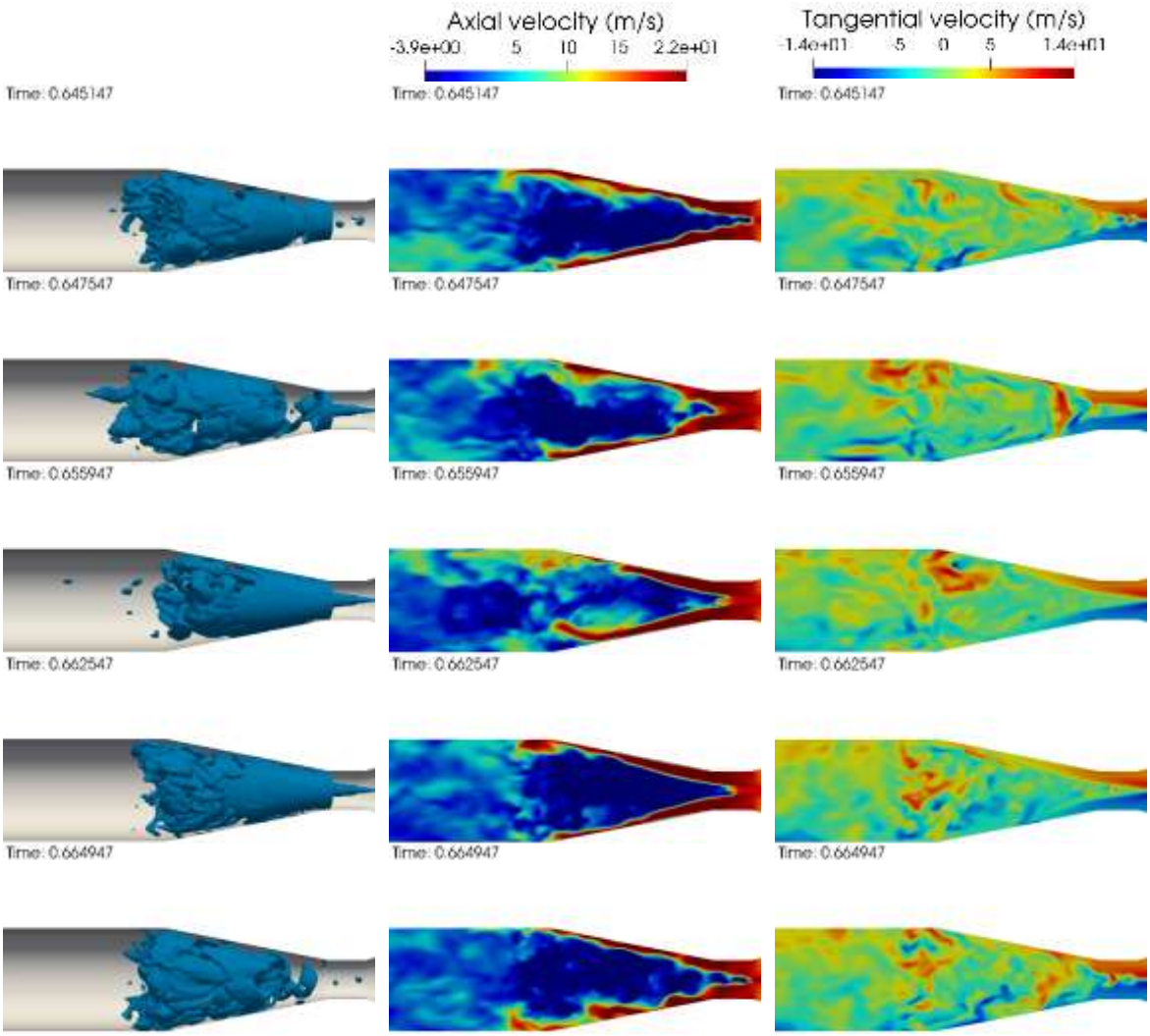

Figure 144 Set of images depicting cavitation cycle, fully developed stage – σ_{vel} 0.43, right column – 75% vapor, middle column - axial velocity, right column tangential velocity.

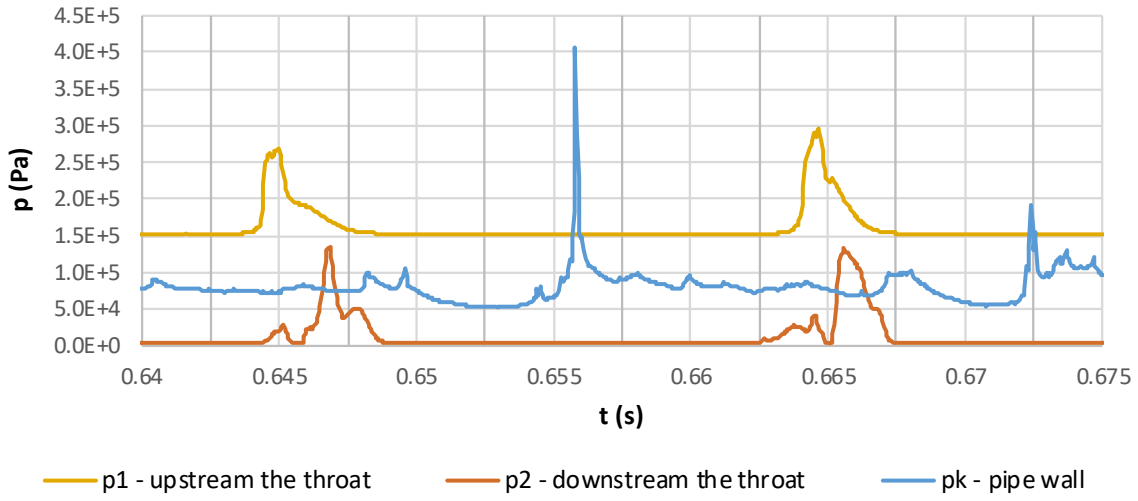

Figure 145 Numerically predicted course of the static pressure captured in the three different positions, fully developed cavitation (σ_{vel} 0.43) and SG presence.

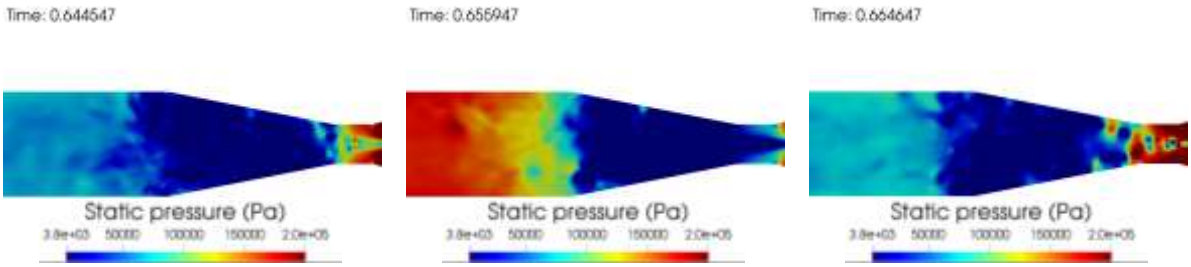

Figure 146 Maps of the pressure field during the cavitation cycle, fully developed cavitation (σ_{vel} 0.43) and SG presence.

5.7.4. Supercavitation, σ_{vel} 0.178, outlet pressure 40 kPa

Supercavitation in case of the SG presence has been captured using the CFD with the partial success. It shall be noted that the cavitation number of the corresponding experimentally recorded operating point was slightly higher (σ_{vel} *0.205*) and no collapse was observed during the experiment even though this value is close to the transition regime.

While the cavitating structure itself was captured properly, the occasional decay occurred in case of the CFD analysis. This might be caused by the relatively short computational domain and potential subsequent pressure reflection from the outlet boundary. It shall be also noted that the value of the cavitation number was underestimated in this particular simulation considering the prescribed value of the outlet pressure (90 kPa).

The attempt to numerically predict the supercavitation considering even lower outlet pressure was also done without success due to the instability of the calculation. This simulation has been excluded from the further investigation due to the unbearable time-demands.

The cavitating vortex remained quasi-stable during the major part of the simulated flow time. As the most interesting part of the simulation, the captured collapse and consequent re-creation of the large cavitating vortex within the nozzle is depicted in the Figure 147. This type of the cavitation cycle is typical for the transition regime. It is clearly depicted that during the collapse of the cavitating structure, the large region of reversed flow can be found in core of the flow, while thin layer of fast flowing liquid close to the walls of the diffuser as well as the straight pipe persist stable during the whole cycle. The complete collapse of the cavitating vortex within the throat of the nozzle and the helical vortex breakdown were clearly captured as it is depicted in the set of images. After the consequent growth of

the new cavitating vortex, the structure remained stable until the end of the simulation as it is depicted in the last two rows of images.
The record of the numerically captured static pressures during the collapse of the cavitating structure is depicted in the Figure 148. While the re-creation of the cavitating vortex is fast close to the throat of the nozzle (regardless if upstream or downstream), the stabilization of the cavitating vortex within the pipe downstream the diffuser lasted considerably longer after the crash of numerical simulation.
Pressure fields complementing the chart of the static pressures are depicted in the Figure 149.

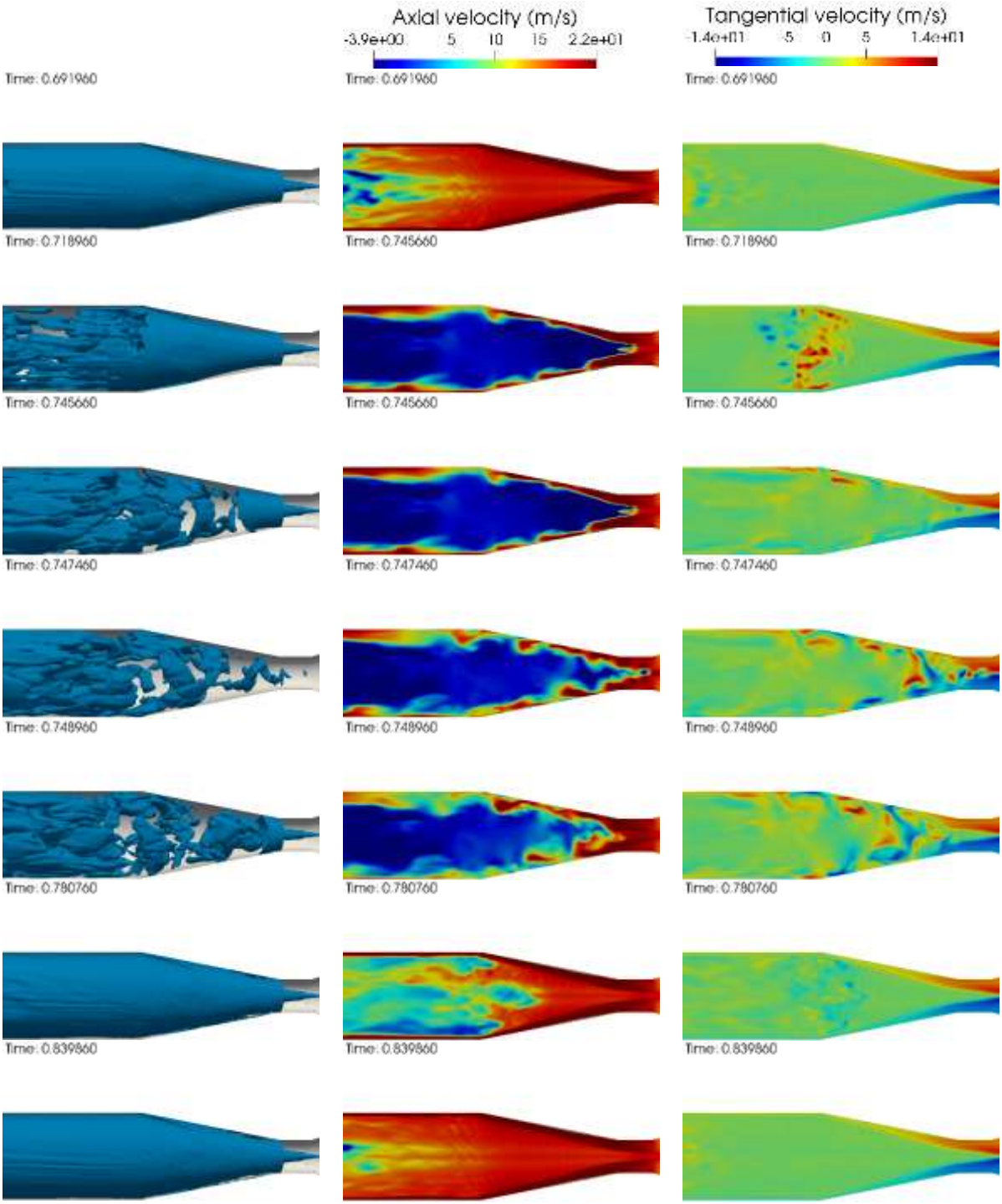

Figure 147 Set of images depicting cavitation cycle, transition between the fully developed stage and supercavitation – σ_{vel} 0.178, right column – 75% vapor, middle column - axial velocity, right column tangential velocity.

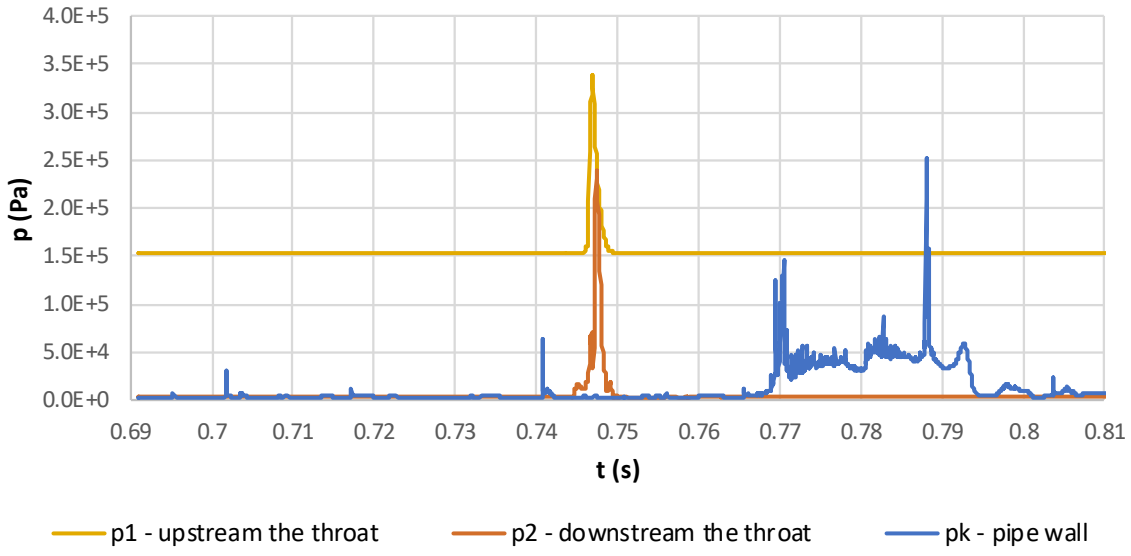

Figure 148 Numerically predicted course of the static pressure captured in the three different positions, transition between the fully developed stage and supercavitation (σ_{vel} 0178) and SG presence.

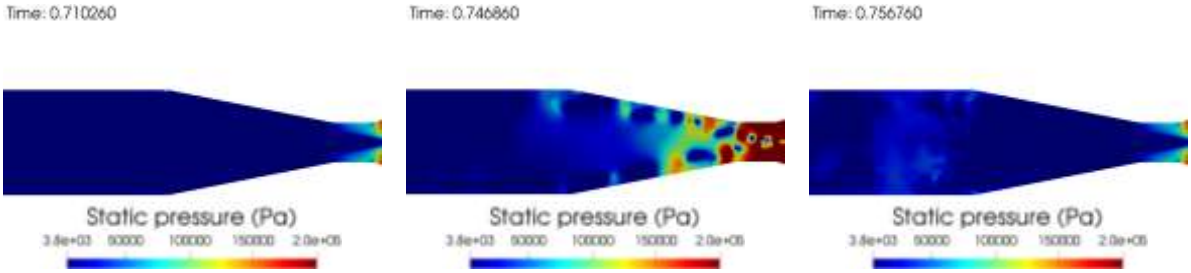

Figure 149 Maps of the pressure field during the cavitation cycle, transition between the fully developed stage and supercavitation (σ_{vel} 0.178) and SG presence.

5.8. Cavitating structures captured using the CFD – dynamics of cavitating flow in case of the axial inflow

It shall be emphasized that the main effort has been devoted to the numerical investigation of the cavitation induced by the swirl before the description of the results corresponding to axial inflow. Therefore, the overall amount of the investigated operating points is significantly lower compared to the previous section of this chapter.

Nevertheless, the additional results of the multiphase simulations corresponding to the axial inflow in this geometry were published by author in [51] and partially they are provided in the Figure 113. These results are not published as a part of this thesis, since the simulations were carried out considering the discharge of 7 l/s based on the experimental data which were obtained by Gríger et al. [46] and partially published by Rudolf et al.[8].

The fields of the axial velocity, static pressure and vapor void fraction are depicted in the set of images in the Figure 150.

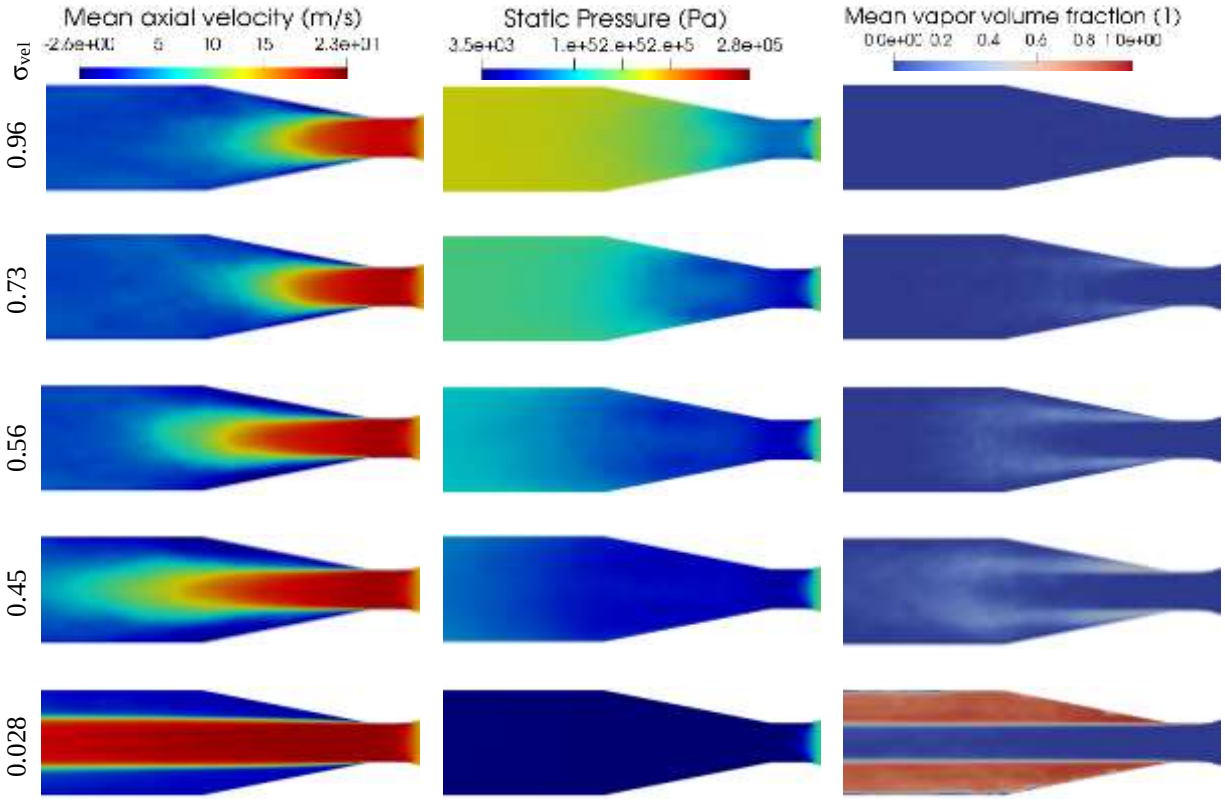

Figure 150 Set of images depicting time-averaged fields of axial velocity, static pressure and vapor void fraction obtained by the numerical analysis considering axial inflow

When the fields of the vapor void fraction α_{vap} corresponding to the axial inflow are compared to the fields of α_{vap} affected by the presence of the SG, the obvious qualitative discrepancy can be found. The maximum values of the α_{vap} are significantly higher in case of the SG presence, which is in good agreement with the experimental results described in the chapters devoted to the analysis of the HS records. The cavitating structures were more stable in case of the SG presence, while the considerably more significant fluctuations of the gaseous phase volume were observed in case of the axial inflow in the whole range of the investigated regimes (except the supercavitation, which was stable regardless the experimental configuration). The fluctuations of the cavitating structures led to more severe pipe-wall acceleration fluctuations induced in case of the axial inflow. This can supported using the standard deviation of the static pressure as it is depicted in the Figure 151.

Figure 151 Static pressure standard deviation on case of the SG presence (left - 100kPa) and axial inflow (right – 104 kPa)

5.8.1. Initial stage of cavitation, σ_{vel} 0.96, outlet pressure 175 kPa

The initial stage of the cavitation which was investigated during this simulation (Figure 154) is characteristic by the occurrence of the cavitating boundary layer within the throat of the nozzle. As it can be seen in the set of images depicting the cavitation cycle using the α_{vap}, the cavitation is limited mainly to the throat of the nozzle, while the pulsations captured by the analysis were very fast.

As it can be seen the cycle starts at the leading edge of the throat and starts its growth downstream. The separation of the boundary layer at the trailing edge of the throat occurs slightly after the beginning of the cycle. Since the investigated cavitation number was high, these two cavitating regions did not merge during the cavitation cycle, which is typical for the slightly more developed stages of cavitation. Nevertheless, it shall be mentioned that the amount of gaseous phase was underestimated compared to the experiment in case of this simulation.

The static pressure captured using the three pressure probes is depicted in the Figure 152. It can be stated that the pressure pulsations captured during this simulation were same from the qualitative point of view, regardless the position of the pressure probe. In other words, the pressure shock captured using the pressure probe upstream the throat of the nozzle was captured also by the pressure probe located within the straight pipe downstream the diffuser of the nozzle. As it will be shown in the following sections, this behaviour vanished with the increasing amount of the gaseous phase within the flow.

The pronounced pressure shocks depicted in the chart are accompanied with the complete collapse of the cavitation in the nozzle. Corresponding fields of the static pressure is depicted in the Figure 153.

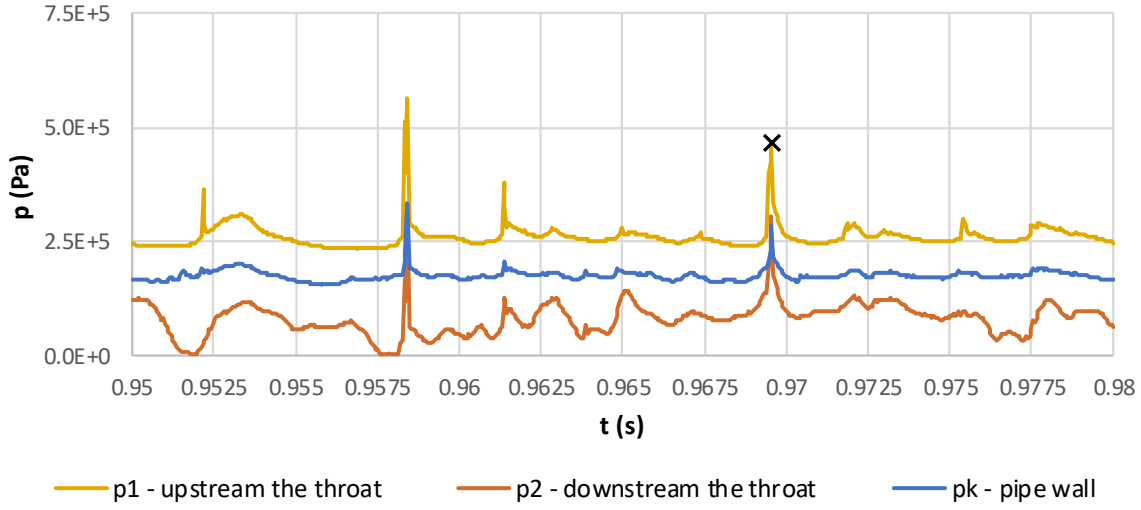

Figure 152 Numerically predicted course of the static pressure captured in the three different positions, initial stage of cavitation (σ_{vel} 0.96), axial inflow.

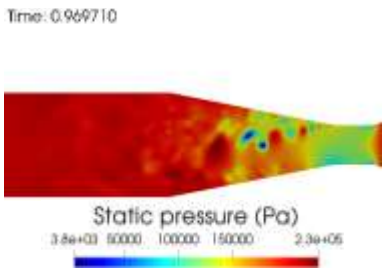

Figure 153 Map of the pressure field during the cavitation cycle, initial stage of cavitation (σ_{vel} 0.96).

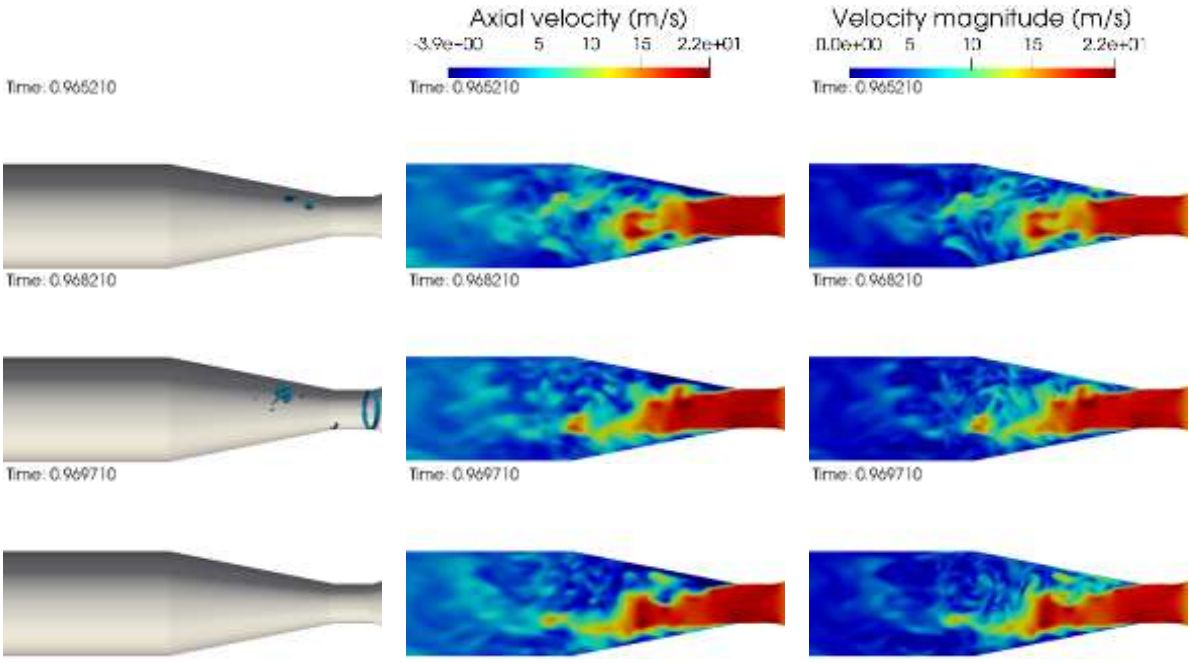

Figure 154 Set of images depicting cavitation cycle, initial stage – σ_{vel} 0.96, right column – 75% vapor, middle column - axial velocity, right column velocity magnitude, axial inflow.

5.8.2. Fully developed cavitation, σ_{vel} 0.73, outlet pressure 134 kPa

Relatively significant increase of the amplitudes of pressure pulsations can be in case of the more developed stage of cavitation found (see Figure 155 and Figure 156). This regime is typical by the periodical shedding of distinguishable cavitating vortex rings which are entrained by the flow to the region higher pressure downstream the nozzle where the rings collapsing inducing the pressure shocks.

The cavitation cycle sown in the Figure 157 starts by the development of the cavitating boundary layer within the throat of the nozzle right after the collapse of the previous cycle. As it can be seen, the collapse has been captured mainly by the probes p1 and p2 (close to the throat of the nozzle). On the other hand, minor increase of the static pressure can be found also in the record acquired by the probe pk. It is worth to mentioned, that this increase was not detected in case of the more developed stages of cavitation as it will be described in the next chapter. Corresponding pressure field is provided in the Figure 156.

Growth of the cavitating boundary layer is accompanied by the gradual pressure decrease up to the moment, when the cavitating vortex ring collapses within the straight pipe downstream the diffuser of the nozzle. This collapse induces distinguishable pressure shock captured by the pressure probe pk. Nevertheless, the newly created cavitating structure within the diffuser is significant enough, thus the pressure shock has not been captured by the probes close to the throat of the nozzle.

The end of the cycle is characteristic by collapse of the cavitating boundary layer within the throat as it has been mentioned. The pressure pulsations are considerably more significant upstream the throat of the nozzle, compared to the pulsations captured using the probe pk.

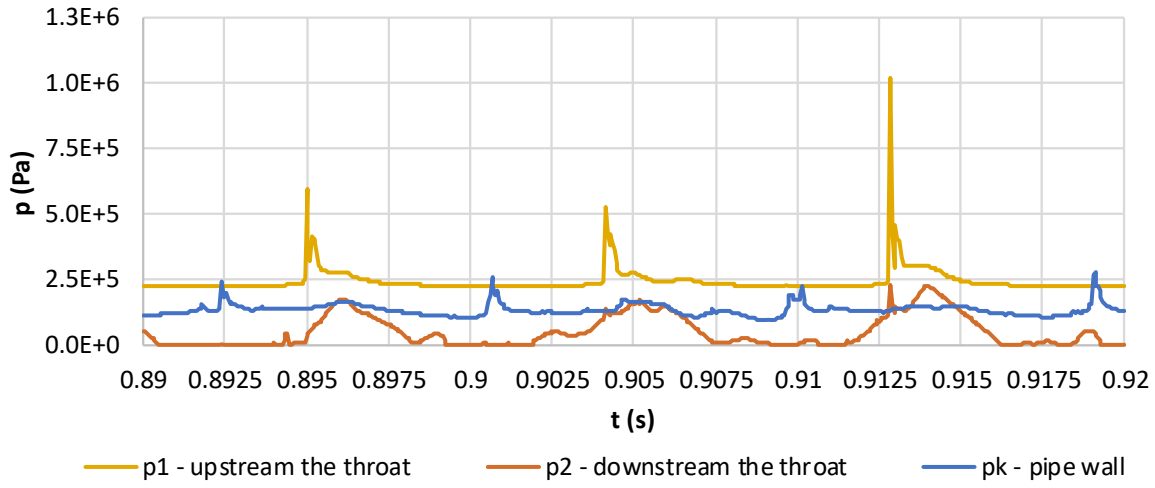

Figure 155 Numerically predicted course of the static pressure captured in the three different positions, initial stage of cavitation (σ_{vel} 0.73), axial inflow.

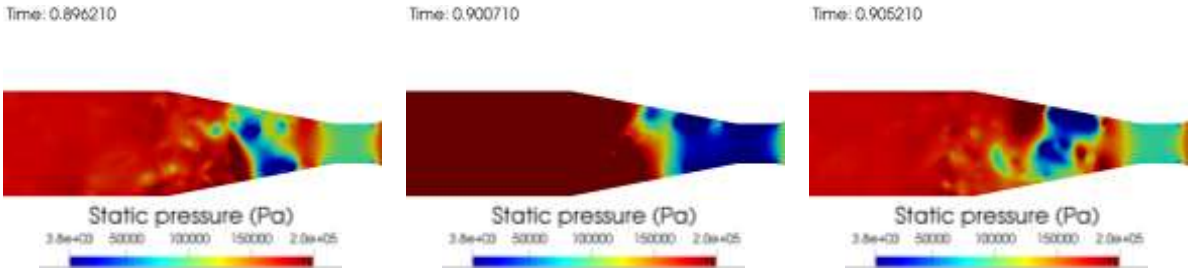

Figure 156 Map of the pressure field during the cavitation cycle, initial stage of cavitation (σ_{vel} 0.73).

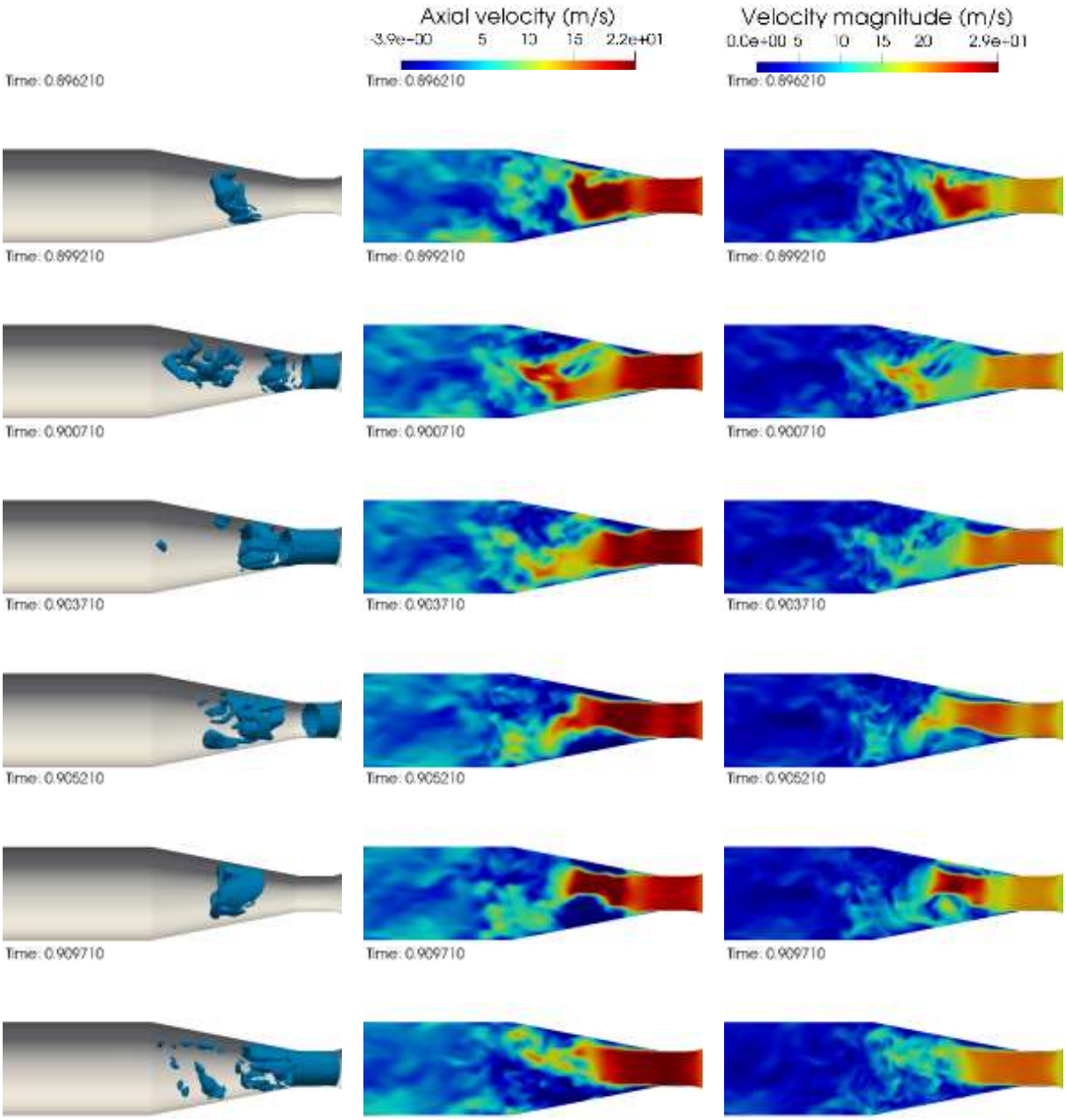

Figure 157 Set of images depicting cavitation cycle, initial stage – σ_{vel} = 0.96, right column - 75% vapor, middle column - axial velocity, right column - velocity magnitude, axial inflow.

5.8.3. Fully developed cavitation, σ_{vel} 0.45, outlet pressure 84 kPa

Fully developed cavitation characteristic by the periodical separation of the large cavitating clouds was also predicted correctly by the numerical analysis. Seeing the chart of the static pressure during the time depicted in the Figure 158 and comparing magnitudes of the pressure with the images of the constant vapor volume fraction during the cycle (Figure 160), it can be seen the values of the static pressure are relatively steady prior the beginning of the cycle. The collapse of the cavitation within the throat of the nozzle is accompanied by the sudden pressure shock which was captured upstream and downstream the nozzle, on the other hand its propagation downstream to the straight section was not significant as it is depicted in the values of the static pressure captured using the probe corresponding to the pressure transducer utilized during the experimental campaign. This sudden increase occurred right after the separation of the cloud as it depicted in the Figure 159.

The pressure shock captured by the p_k probe corresponding to the pressure transducer exploited during the experimental campaign corresponds to the collapse of the cavitating cloud which occurred

during the previous cavitation cycle. Pressure shock is limited mainly to the straight part of the nozzle, while it has not been captured by the probes upstream the newly created cavitation cloud.

The following separation of the cavitating cloud and consequent decay of the cavitation within the throat of the nozzle corresponding to the end of the cycle is related to the pressure shock in this part of the computational domain as it has been described above.

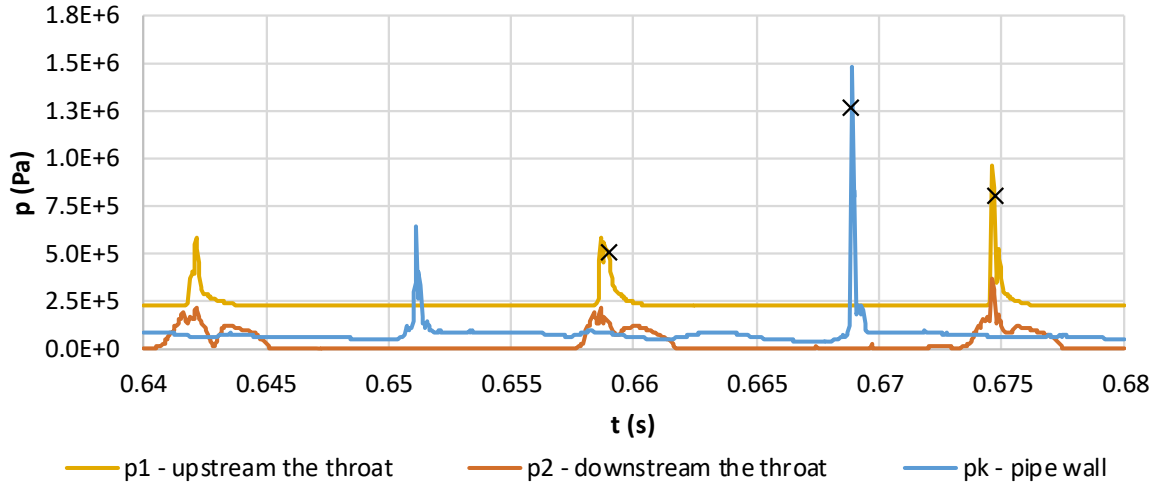

Figure 158 Numerically predicted course of the static pressure captured in the three different positions, fully developed stage of cavitation (σ_{vel} 0.45), axial inflow.

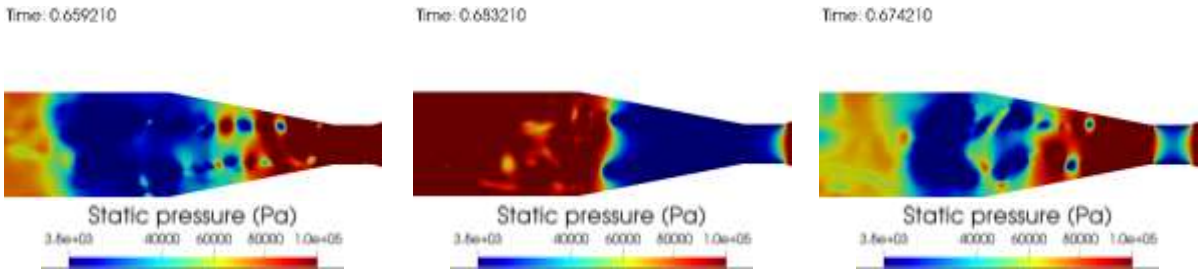

Figure 159 Maps of the pressure field during the cavitation cycle, transition between the fully developed stage and supercavitation (σ_{vel} = 0.45), axial inflow.

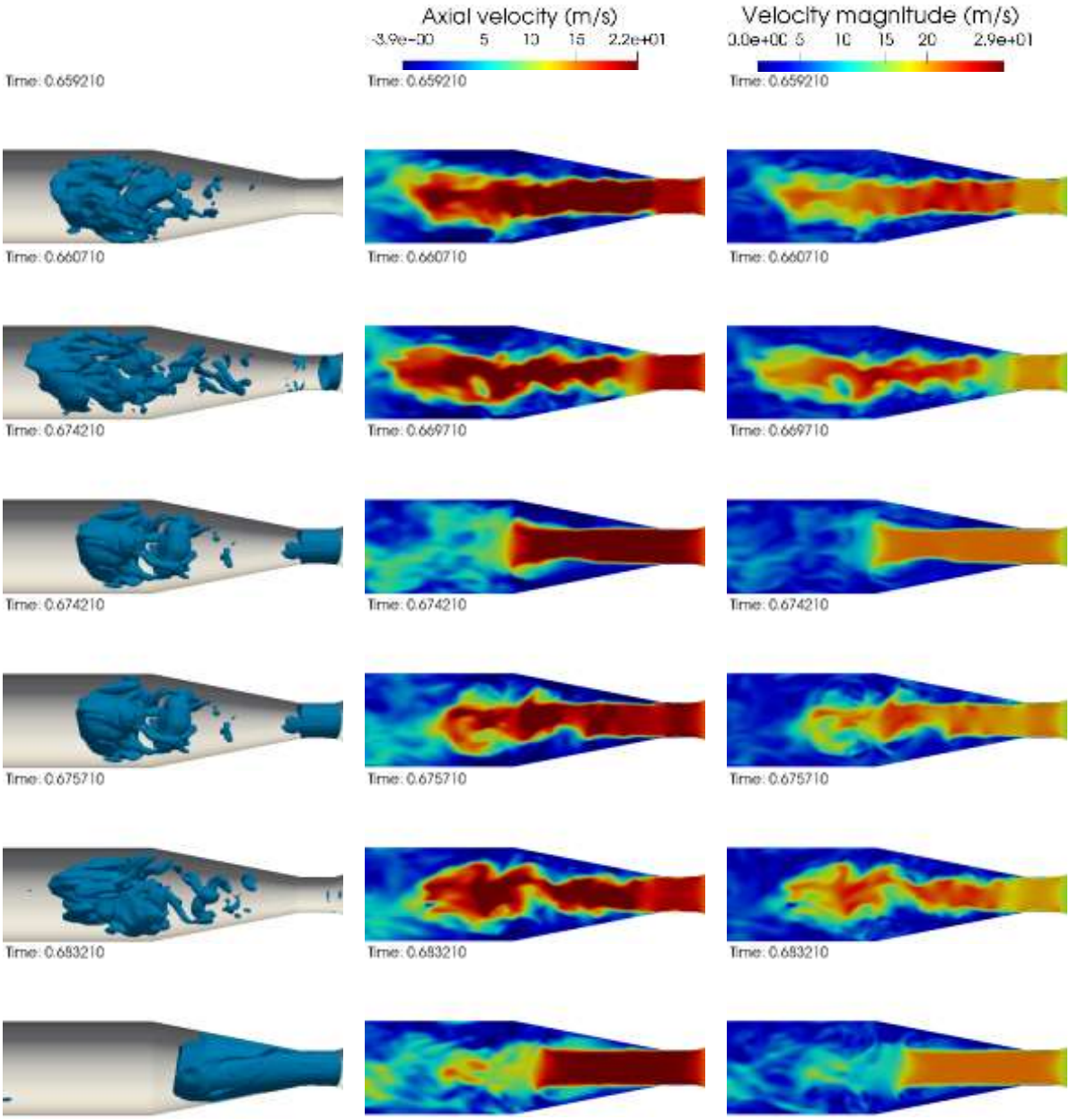

Figure 160 Set of images depicting cavitation cycle, fully developed stage – σ_{vel} = 0.45, right column - 75% vapor, middle column - axial velocity, right column - velocity magnitude, axial inflow.

5.8.4. Supercavitation, σ_{vel} 0.028, outlet pressure 17 kPa

As it is shown in the Figure 161, the typical liquid jet surrounded by the saturated vapor was well-predicted. The value of the static pressure was stable during the simulation as is shown in the Figure 162. The small instabilities of the pressure recorded by the p_k probe within the straight part of the computational domain can be devoted to the motion of the small liquid droplets on the wall of the pipe. Representative field of the static pressure is depicted in the following figure. It is clearly depicted that the actual values are close to the value of the saturated vapor pressure in the whole domain downstream the throat of the nozzle. The lowest values of the static pressure can be found close to the transition between the straight throat of the nozzle and conical diffuser (i.e. in the region of the liquid flow separation from the walls of the nozzle). It can be also seen that the pressure within the liquid jet is slightly higher. This observation can be devoted to effect of surface tension.

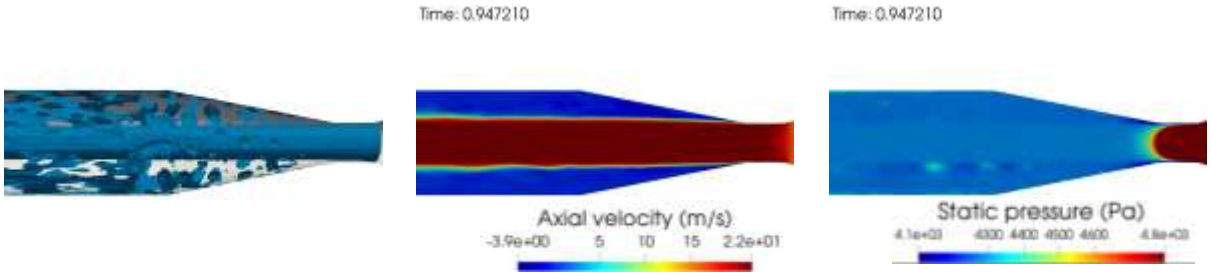

Figure 161 Set of images depicting cavitation cycle, fully developed stage – σ_{vel} 0.028, right column - 75% vapor, middle column - axial velocity, right column - velocity magnitude, axial inflow.

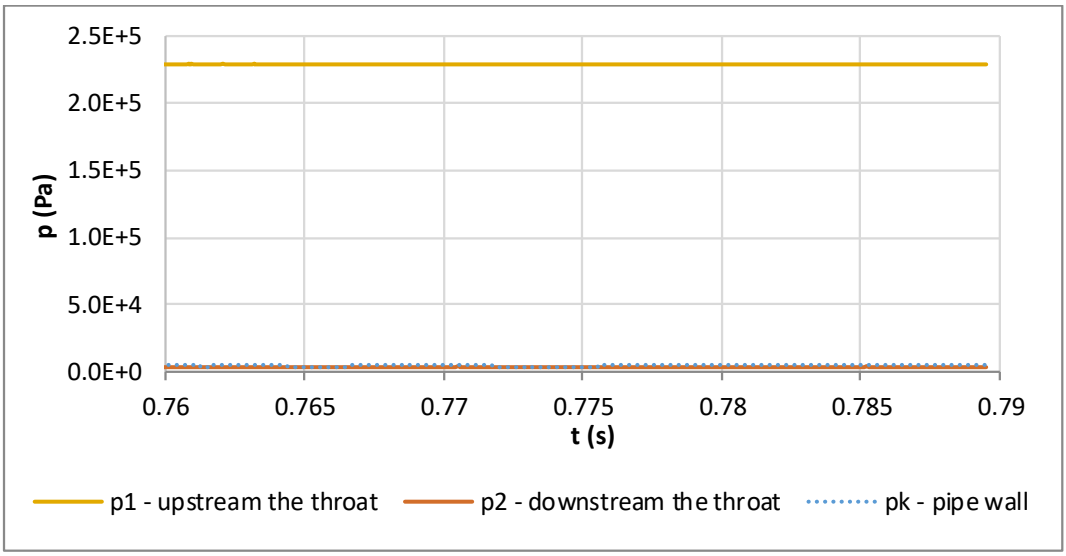

Figure 162 Numerically predicted course of the static pressure captured in the three different positions, supercavitation (σ_{vel} 0.028), axial inflow.

5.9. Numerical analysis of the cavitation dynamics

The pressure signals captured during the numerical simulations were analysed using the Fourier transform to identify dominant frequencies of the investigated cavitating structures. Example of the input signals corresponding to probe 9 and the obtained results are depicted in the Figure 163. This probe was chosen since the pressure records obtained using this probe were the most appropriate for the analysis of the frequencies corresponding to the collapses of the large cavitating structures (taking into account relative short length of the analysed signal and complex nature of the flow downstream the diffuser of the Venturi nozzle). It should be mentioned that the length of the pressure signals investigated using the Fourier transform was 0.2 s and more. Relatively short length of the signals was subsequent to the time demands of these simulations.

It can be stated that the dominant frequency is relatively clearly distinguishable, regardless the investigated experimental configuration. The obtained frequency is slightly higher in case of the SG presence (112.6 Hz) compared to the axial inflow (110.3 Hz), although the cavitation number corresponding to the axial inflow is slightly higher. On the other hand, the amplitude corresponding to the obtained fundamental frequency of the signal of axial inflow analysis is higher. In fact, both of these observations are in good agreement with the discussion of the HS image analysis as well as the analysis of the pressure signals. Beside the dominant frequencies the higher harmonic frequencies can be found regardless the investigated experimental configuration too.

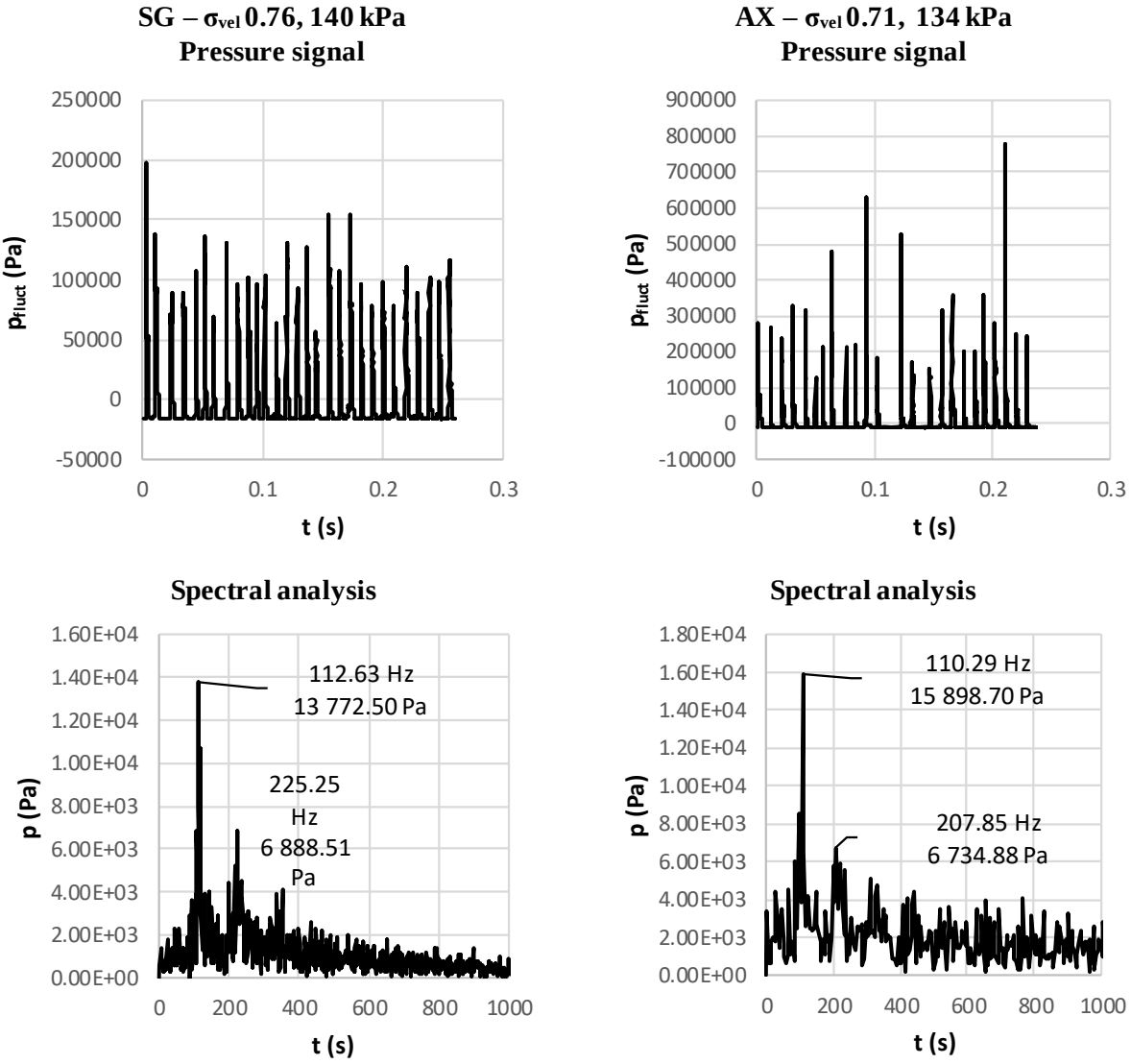

Figure 163 Example of the pressure signals obtained by the numerical investigation of the cavitation flow (top) and spectral analysis of these signals (bottom)

Dominant frequencies and values of the corresponding amplitudes are listed in the Table 12. It was possible to distinguish the frequencies of periodical collapses of the cavitating structures without any significant problems up to the cavitation number of 0.99. Using the pressure signal captured by the probe 12 it was possible to detect frequency of 148.43 Hz, which is in good agreement with the results of the H-S records analysis. The second problem represents the analysis of the fully developed axial inflow (σ_{vel} of 0.44). The dominant frequency of 127 Hz fit relatively well to the first harmonic frequency of the 61.9 Hz as it is depicted in the Figure 164. Therefore, the frequency of 61.9 Hz will be utilized for the correlation of the CFD results with the results of the pressure fluctuations and POD analysis of the HS records.

Exp. Cfg.	σ_{vel}	Dom. F.	Amp.	Commentary
	-1	(Hz)	(Pa)	-
SG	0.18	5.87	3.9	-
SG	0.31	20.65	3412.4	-
SG	0.43	70.72	11608.7	-
SG	0.49	79.38	13680.8	-
SG	0.54	86.13	11881.2	-
SG	0.65	104.48	17150.4	-
SG	0.76	112.63	13772.5	-
SG	0.99	148.43	3673.2	Dom. frequency 50.78, estimated using the probe 12
SG	1.09	111.46	12350.7	-
AX	0.03	4.83	0.2	-
AX	0.44	61.90	16383.2	Highest amplitude corresponds to 127 Hz
AX	0.55	81.00	14714.3	-
AX	0.71	110.29	15898.7	-
AX	0.94	183.22	11356.7	-

Table 12 Dominant frequencies of the pressure pulsations obtained by the CFD analysis

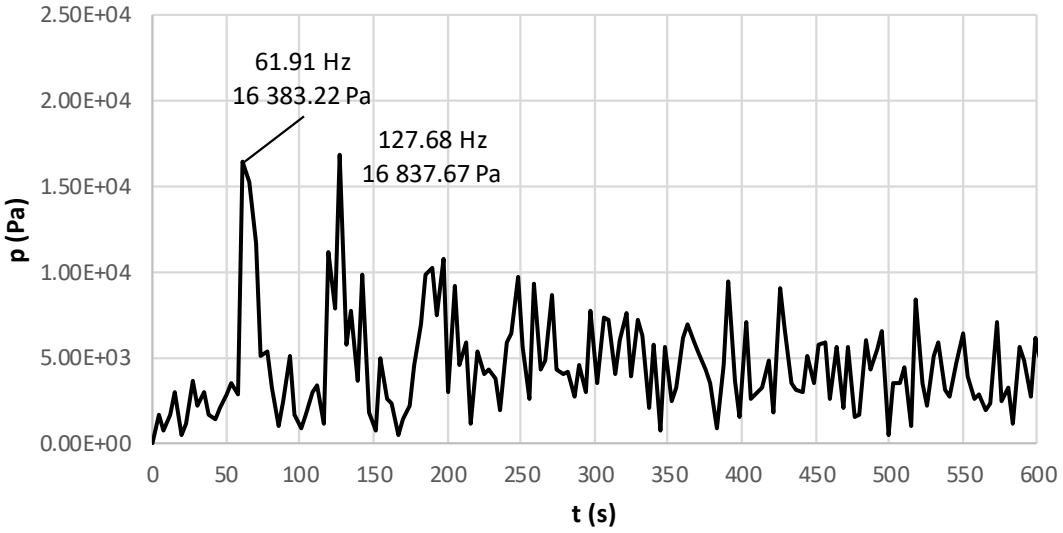

Figure 164 Problematic result of the spectral analysis corresponding to the fully developed cavitation in case of the axial inflow (σ_{vel} 0.44).

Correlation of the results obtained by the numerical analysis with results of the HS video records analysis and results of the pressure pulsations captured during the experimental campaign is depicted in the Figure 165.

As it can be seen the results of the CFD analysis are in good agreement with the analysis of the experimental data in general. On the other hand, it shall be also noted that the frequency predicted by the CFD analysis is considerably smaller compared to the analysis of the experimental data in case of the least developed cavitation regime which was investigated numerically (σ_{vel} = 1.09). On the other hand, it was not possible to clearly distinguish the dominant frequency corresponding to this particular regime using the POD analysis. It can be stated that the accuracy of the numerically obtained results is sufficient and the exploited numerical analysis provide reliable tool for the prediction of the dynamics of the cavitating structures which were observed within Venturi nozzle.

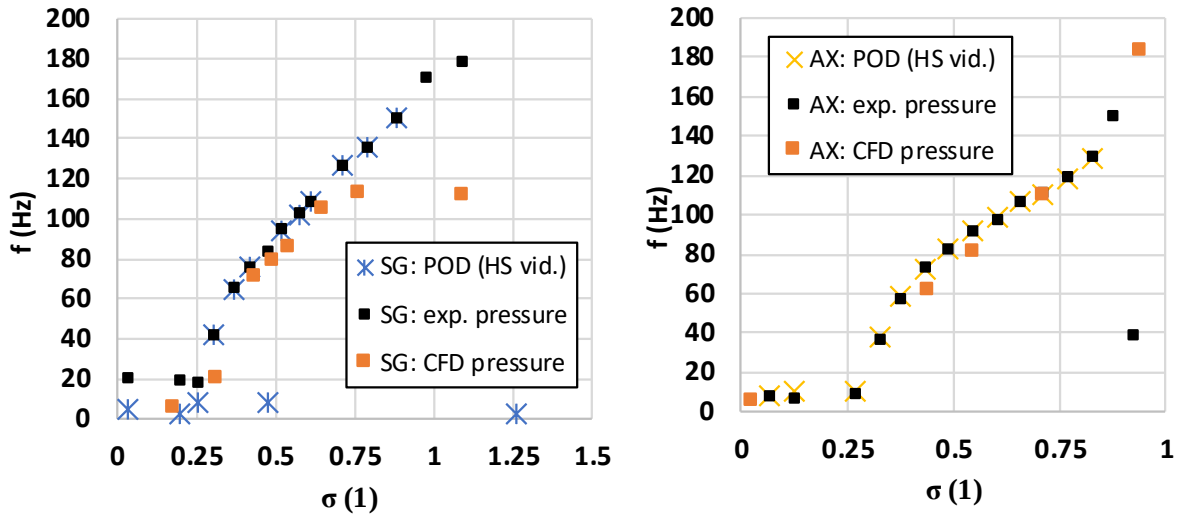

Figure 165 Correlation of the dominant frequencies obtained by the CFD analysis with the results of the pressure fluctuations investigation and analysis of the HS records

Partial conclusions

I. The numerical analysis has been carried out based on the previous experience with the CFD simulations of cavitating flow. It can be stated that the results are in good agreement with the experimental measurement.

II. The full geometries were exploited during the analysis of the hydraulic loss coefficients. The influence of the grid density was studied in case of the SG presence. It was stated that the results are in relatively good agreement with the results the experimental analysis considering both computational grids. Nevertheless, the results were better in case of the finer mesh. Above that, the flow structures obtained using the finer mesh provided better results with respect to the experimental observations.

III. In case of the SG analysis, the kinetic energy correction factor has been exploited in order to correct the experimental data. It was possible to minimize the impact of the radial and tangential velocity components neglection for the calculation of cavitation number and hydraulic loss coefficient.

IV. The overall results show good degree of agreement with the experimental data. Although, the values of the ξ are slightly underpredicted in case of the SG presence. In contrast, these values are slightly overpredicted in case of the axial inflow.

V. The flow structures captured by the numerical analysis corresponded well with the experimental observations. Characteristic flow patterns, such as vortex breakdown were captured by the CFD.

VI. Since the computational demands of the simulations considering the presence of SG were unbearable for the analysis of the cavitation dynamics (considering wide range of investigated regimes), the geometry was sliced downstream the swirl generator. It was possible to 6.5 times reduced the computational times. Thus, it was possible to carry out the analysis of the pressure pulsations captured by the CFD properly.

VII. The flow patterns during the cavitation cycles were captured using the field or various quantities. The course of the pressure during the cycle was discussed using the three different pressure probes considering several operating points for both experimental configurations.

VIII. The spectral analysis of the pressure signals obtained by the CFD was carried out. It can be stated that results are in good agreement with the experimental data regardless all the simplifications which were exploited during the analysis. This statement is valid for both experimental configurations. These results are compared with the experimental data in the Figure 165.

Investigation of cavitating flow using the computed tomography

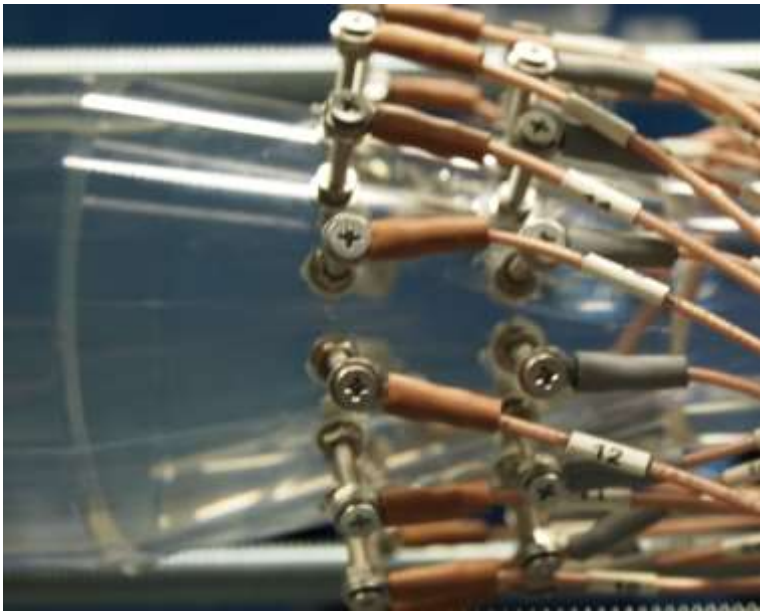

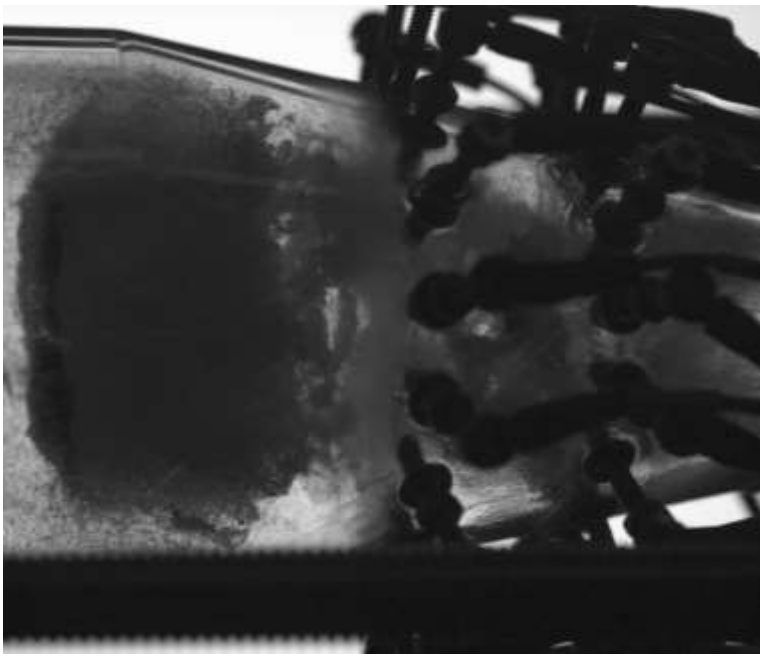

Content of this chapter:

EIT tomography will be exploited for:

1. Discussion of the time-averaged distribution of cavitation.
2. Correlation of the EIT investigation with the results of CFD analysis

6. Investigation of cavitating flow using the computed tomography

The experimental measurement focused on the EIT has been carried out in the experimental facility of Technical University of Liberec. The main purpose of this measurement was to investigate usability of available device for the hydrodynamic cavitation investigation. Distribution of the conductivity across the two cross-sections of the Venturi tube downstream the throat of the nozzle was investigated with the focus on the possible hysteresis occurrence. Furthermore, the additional measurement has been done to complement the previous experimental and numerical results. Venturi tube with the same main dimensions as in case of the experimental measurement was exploited for purpose of the measurement. Two modifications of the nozzle were done due to the technological reasons. The straight part of the nozzle downstream the diffuser was shortened due to the manufacturing possibilities of the supplier. Moreover, the outer shape of the new nozzle was circular due to the easier mounting and sealing of electrodes. The main tomography measurements were carried out in two planes downstream the throat of the nozzle as it is depicted in the Figure 166. The planes P1 and P2 has been located 29.8 mm and 39.7 mm downstream the throat of the nozzle. These positions were chosen based on the previous measurement and the expected range of the achievable cavitation regimes.

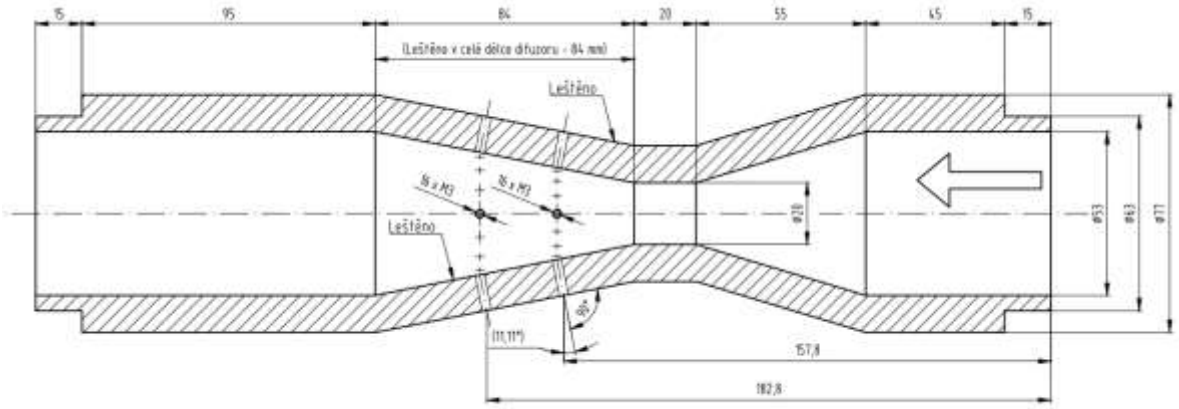

Figure 166 Main dimensions of the Venturi tube utilized for the EIT investigation. Measuring plane P1 is closer to the throat of the nozzle

The close up view on the Venturi tube with the mounted EIT electrodes is provided in the Figure 167. Certain restriction of the measuring planes P1 and P2 locations was represented by the dimensions of the Venturi tube and significant amount of the measuring electrodes (16 in one plane) and their wirings as it is clearly depicted. Thus, it was relatively difficult to capture the cavitation dynamics using the HS camera.

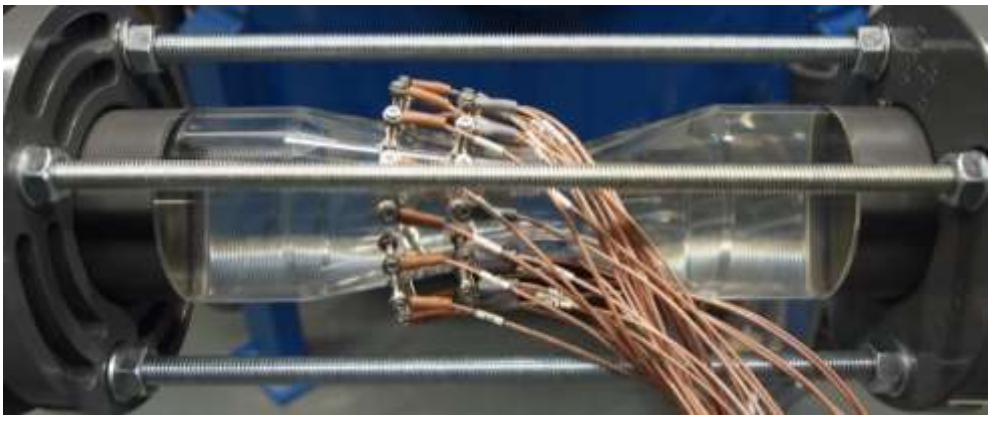

Figure 167 Wiring of the EIT mounted to the Venturi nozzle

The diameters of plastic piping as well as the positions of the pressure transducers were the same as in case of the experimental investigation carried out at Brno University of Technology to assure comparability of the obtained results. On the other hand, the experimental rig was opened to the atmosphere. In other words, it was possible to investigate only the limited range of the cavitation regimes since the cavitation number was function of the actual flow rate only.

Figure 168 Venturi nozzle mounted to the test rig

Experimental measurement was captured using the high-speed camera Phantom v611 with the sampling frequency of 2000 fps and video resolution of 1280 by 800 pixels. For this measurement backlit scene technique has been exploited. The experimental setup including the HS camera and the matrix of LEDs acting as a source of the back light during the measurement is depicted in the Figure 134.

Figure 169 HS camera and ilumination of the scene

The example of the image captured using this setup is provided in the Figure 170. In contrast to the experimental setup described in chapter 2, where the dark background and front lights were exploited, the cavitating regions are dark in this case.

Figure 170 Cavitating vortex ring passing throug the measuirng plane P2

Cavitation stage was adjusted using the flow rate control by the pump speed regulation during the main part of the investigation. The resistivity distribution was measured in several operating points from the non-cavitation regime to the maximum achievable stage of the cavitating flow development and back to the cavitation-free regime. It should be emphasized that the following convention will be exploited in the following text: the measurement from the cavitation-free regimes to the fully developed cavitation will be referred as UP (increasing Q), while the measurement from the fully developed cavitation to the initial regimes of cavitation will be referred as DOWN (decreasing Q). The investigated range of

cavitation regimes was partially restricted by the maximum rotational speed of the pump. However, the crucial restriction was represented by the probes of the EIT, respectively by leakage of these probes which was observed, when the vibrations reached certain intensity. It should be mentioned that the repeated sealing of the electrodes using the cyanoacrylate led to the gradual degradation of the optical properties (transparency) of the nozzle between the measuring planes.

In the second part of the investigation the regime of cavitation was controlled using the throttle valve downstream the Venturi nozzle. This approach has been exploited for the measurement corresponding to 6 l/s discharge with and without the SG. These results will be correlated with the vapor void fraction obtained by the numerical analysis.

The reference value of the water conductivity exploited for the EIT calibration was 1.12 mS/cm. The list of the transducers and other equipment exploited during the experimental measurement provided in the following table.

EIT	CT device	EIT ITS p2+
p_1, p_2, p_3	Pressure transducers	BD331I
Q	Flow meter	FN 2014.1
t	Thermometer	Rawet PTP 55
HS	High speed camera	Phantom v611

Table 13 Utilized experimental equiplment

6.1. EIT investigation of cavitation hysteresis and the influence of the induced swirl to the phase distribution

The phase distribution has been investigated with the particular effort to observe potential hysteresis during the transition between the initial stage of cavitation and fully developed cavitation. This investigation is successive to the previously published results of the cavitation hysteresis investigation during the transition between the fully developed cavitation and supercavitation considering the axial inflow [57].

The investigation has been done for the both experimental configurations (i.e. Axial inflow and inflow affected by the induced swirl). The following charts are depicting the values of the hydraulic loss coefficient versus the cavitation number (see Figure 171).

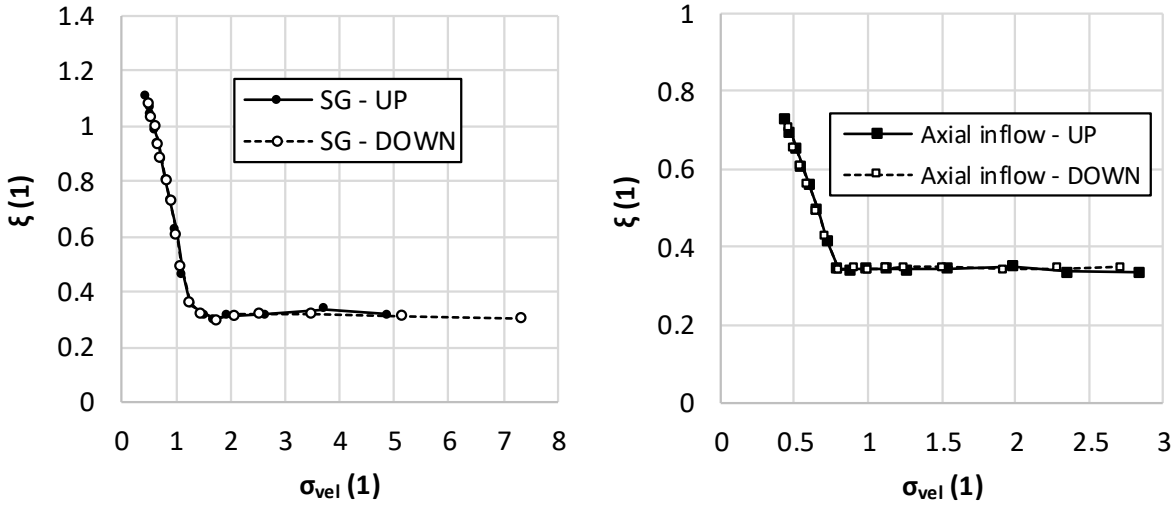

Figure 171 Hydraulic loss coefficient depicted as a function of cavitation number during the measurement of the cavitating flow considering SG presence (left) and axial inflow (rigt).

No observable difference of the evaluated values of ξ based on the discharge change direction can be found regardless the investigated experimental configuration. The transition between the cavitation-free regime and initial stage of cavitation is gradual in case of the SG presence, while in case of the axial inflow the inception of cavitation is rather abrupt. As it can be seen in the Figure 171 depicting the charts of the whole ranges of the investigated operating regimes and in more detailed Figure 172 focused on the transition between the cavitating and non-cavitating regimes. The first occurrence of the cavitation is connected with the minor decrease of ξ value which is followed by the linear increase of the hydraulic loss coefficient. This transition was more complex considering the influence of the induced swirl. The thin straight cavitating filament in the axis of the pipe occurred during the operation in high values of σ_{vel} (3.7). Presence and length of this filament were highly unstable. Nevertheless, this cavitating structure has no significant influence on the value of ξ. As it has been described in the chapter 3, the decreasing value of cavitation number lead to the increasing length of this cavitating filament until the tip of the filament reached the inlet part of the diffuser downstream the throat when the helical vortex breakdown occurred at the end of the filament. This phenomenon was observed close to the σ_{vel} of 2.5 (regardless the direction of discharge gradient). Occurrence of the helical vortex structure was related to the decrease of the ξ down to the σ_{vel} of 1.7. when the straight axisymmetric cavitating vortex similar to the full load vortex of Francis turbines was captured. The further decreasing value of cavitation number lead to linear increase of the hydraulic loss coefficient. The last specific cavitation pattern observed during this experimental measurement occurred when the σ_{vel} of 1.26 has been reached. The axisymmetric vortex transformed to the form of the conical cavitating vortex close to the shear layer between the central stagnant region and region of the liquid flow close to the walls of the Venturi tube. Increase of ξ with the decreasing value of σ_{vel} was considerably faster in the region of the conical cavitating vortex presence.

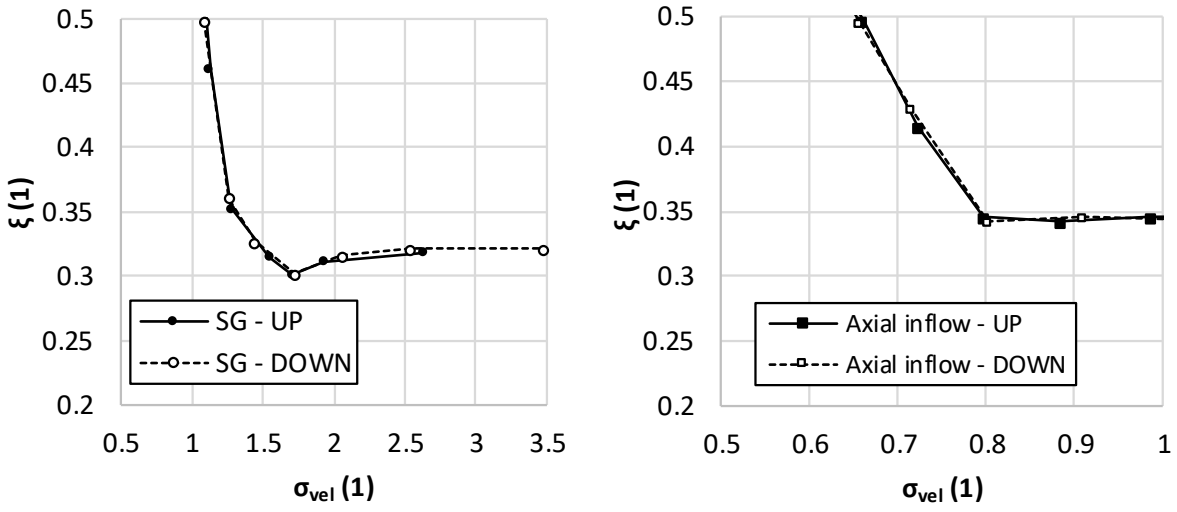

Figure 172 Details of the of the hydraulic loss coefficients during the significant transitions of the flow nature. SG – left, AX – right.

Prior the analysis of the phase distribution, it could be beneficial to discuss the courses of the measured averaged values water resistivity ρ versus the cavitation number captured during the test campaign.

It is possible to state, that the measured ρ is lower in case of DOWN direction regardless the investigated experimental configuration and measuring plane. Nevertheless, this discrepancy is far more pronounced in case of the SG presence. This observation could lead to the assumption that the cavitation amount is lower in case of the transition from the fully developed cavitation to the initial stages of cavitation (UP direction). This would be completely inconsistent with the preliminary expectation of the higher cavitation amount in this direction of the σ_{vel} gradient. Above that this discrepancy has not been

observed in the results of the ξ analysis. These facts suggest that the reason of this discrepancy was not based on the gaseous phase amount within the water, but in the variation of another property of liquid.

Most probable reason of this observation seems to be a gradual increase of the temperature during the experimental measurement (the salinity as well as other properties of the liquid remained stable during the measurement).

Increase of the temperature was faster when the SG was mounted into the system (in a consequence of the higher hydraulic losses), which correspond to the observed more significant ρ discrepancy in case of this experimental configuration. Maximum value of ρ discrepancy did not exceed 0.6 Ωm, while temperature difference at the beginning and at the end of the measurement was 2.03 °C (in case of the SG utilization) as it is depicted in the Figure 173 and Figure 174. Based on the previous experience with the experimental equipment, the change of the liquid resistivity during the operation in the range of the usual temperatures is linear and it does not exceed 1 Ωm per 1 °C of liquid temperature change (based on the water salinity). Since, the observed value of the liquid resistance decrease is comparable and considering the results of the ξ analysis, it is possible to assume that this discrepancy in the measured resistivity can be devoted to the increase of the liquid temperature rather than to hysteresis of the cavitation presence.

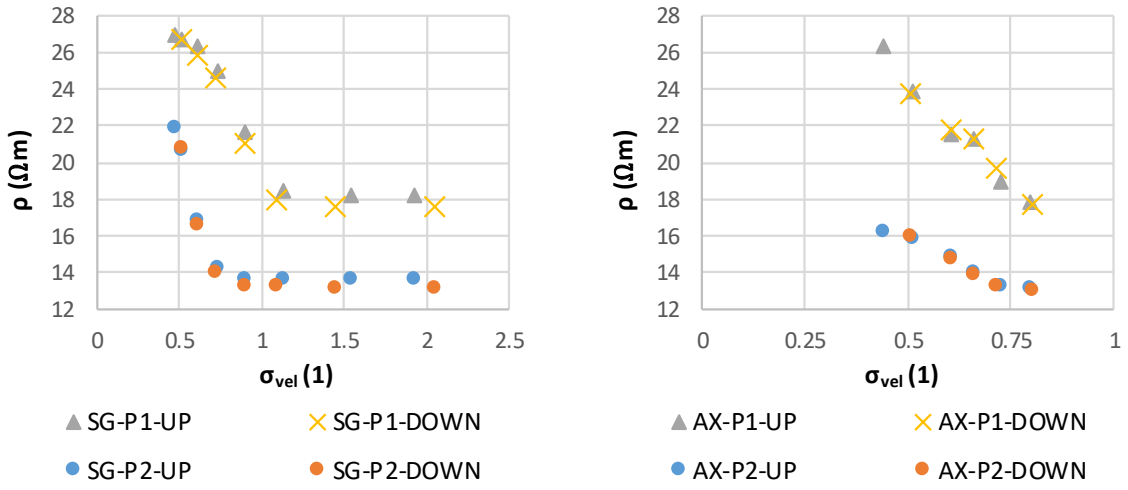

Figure 173 Change of the water resistance during the experimental investigation of the hysteresis presence. SG – left, AX – right.

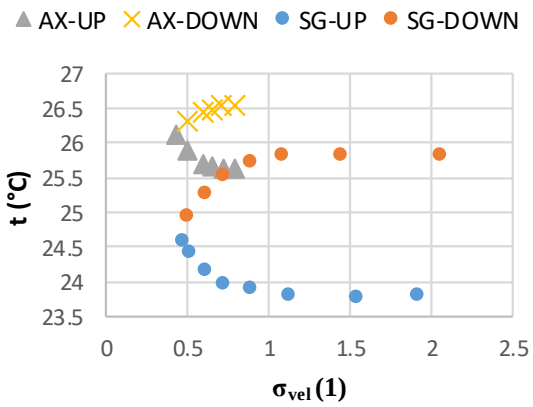

Figure 174 Increase of the water temperature during the experimental measurement

6.2. Analysis of the EIT results

The analysis of the EIT results will be focused on the time-averaged profiles of the conductivity measured across the two measuring planes P1 and P2 downstream the throat of the Venturi tube. The time-averaged fields (images) of conductivity exploited for the analysis were obtained as mean images computed using the approximately 30 s long records of data. Gathering of data for individual snapshots took approximately 20 ms. In other words, it was not possible to investigate cavitation dynamics, due to the higher frequencies of the cavitating structures fluctuations. The resolution was 316 pixels for the measuring plane. On the other hand, this experimental technique is still capable to provide valuable information about the qualitative nature of the different stages of cavitating flow observed during the investigation.

The conductivity maps corresponding to the cavitation free regime are provided in Figure 175. As it can be seen by the range of the corresponding color bars, the measured conductivity is highly uniform across the both investigated measuring planes.

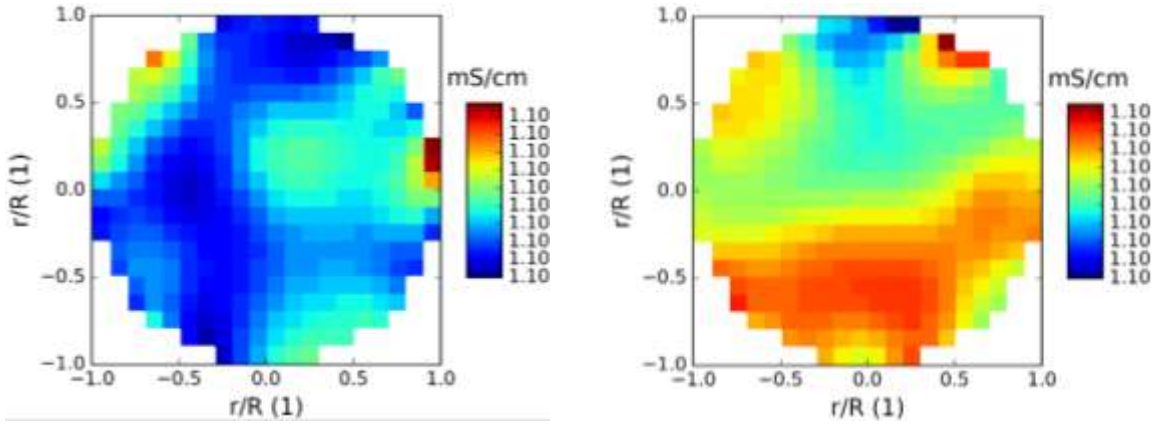

Figure 175 Map of the conductivity captured during the calibration measurement without the swirl generator. P1 – left, P2 – right.

The situation became completely different in case of the cavitation presence. The gaseous volume contained within the liquid flow causes the decrease of the measured conductivity. Nevertheless, the detected change of the conductivity caused by the presence of the second phase within the flow has not been sudden as it will be depicted and discussed in the following text. Therefore, it can be stated in advance, that the available EIT equipment is not appropriate for the direct validation of multiphase CFD simulations. The results corresponding to the individual experimental configurations will be discussed separately for the sake of the text clarity. Conclusions regarding the influence of the additional swirl will be discussed at the end of the chapter.

6.3. EIT investigation of the cavitating flow influenced by the presence of the induced swirl

The profiles of the time-averaged conductivity over the selected diameters of measuring planes are depicted in the Figure 176 considering the UP direction and in the Figure 177 considering the DOWN direction. The error bars shown in the figures are corresponding to the type A uncertainties evaluated based on the conductivity value variation within the individual pixels of the depicted profiles. Since the results are in good agreement for both of investigated directions of the discharge gradients from the qualitative point of view, the overall description of the obtained results will be provided only for one of them (UP – from the cavitation free to fully developed stage of cavitation).

Cavitating helical vortex was barely reaching the measuring plane P1 in case of the initial cavitation (Q = 3 l/s). Thus, the conductivity profile was nearly constant. Above that, the actual values of the conductivity were slightly higher compared to the cavitation-free conditions. This observation can be devoted to the higher velocity of the liquid flow through the magnetic field emitted by electrodes of the EIT probes. The mild deformation of conductivity profile can be found in case of the P1 plane

considering flow rate increased to the 3.5 l/s. As it can be seen, the conductivity profiles remained undisturbed in case of the P2 measuring plane up to the discharge of 4.5 l/s, when the length of cavitating vortex became sufficient to reach the required length. The overall conductivity along the whole length of the depicted profile was decreasing with the increasing discharge (i.e. with the increasing amount of gaseous phase within the flow) in case of the P1. Minimum values of the conductivity are located close to the axis regardless the investigated operating point. This agrees with the general nature and especially with the stability of the cavitating structures close to the throat of the nozzle in this particular range of cavitation numbers. The situation is more complex in case of the second measuring plane P2. The profiles corresponding to the 4.5 l/s and 5 l/s are similar to the profiles measured in the cross section P1. These profiles are corresponding to the operating points during which the relatively small, but still sufficiently significant, amount of cavitation was reaching the P2 plane during the cycle. The profile of 5.5 l/s became flatter compared to the operating points corresponding to the lower discharges. During the investigation of this operating point the maximum length of the cavitating vortex observed during the cycle of cavitation was reaching the P2. Thus, the amount of the gaseous phase flowing through the measuring plane became more significant. The interesting profiles can be found in case of the most developed stages of cavitation corresponding to the discharges of 6 l/s and 6.25 l/s. The local maximum of the conductivity can be found close the axis of the measuring plane in contrast to the previous operating points. This is in good agreement with the experimental (and also numerical) observations. The maximum length of the coherent cavitating vortices was considerably longer, thus the transition of these structures through the measuring plane was captured properly. The local maximum corresponds to the observed creation of liquid (and therefore more conductive) backflow region within the core vortices. Nevertheless, it is clearly depicted that it would be highly problematic to determine the exact position of the cavitating structures presence (i.e. diameter of the cavitating vortices) based on the results of the EIT.

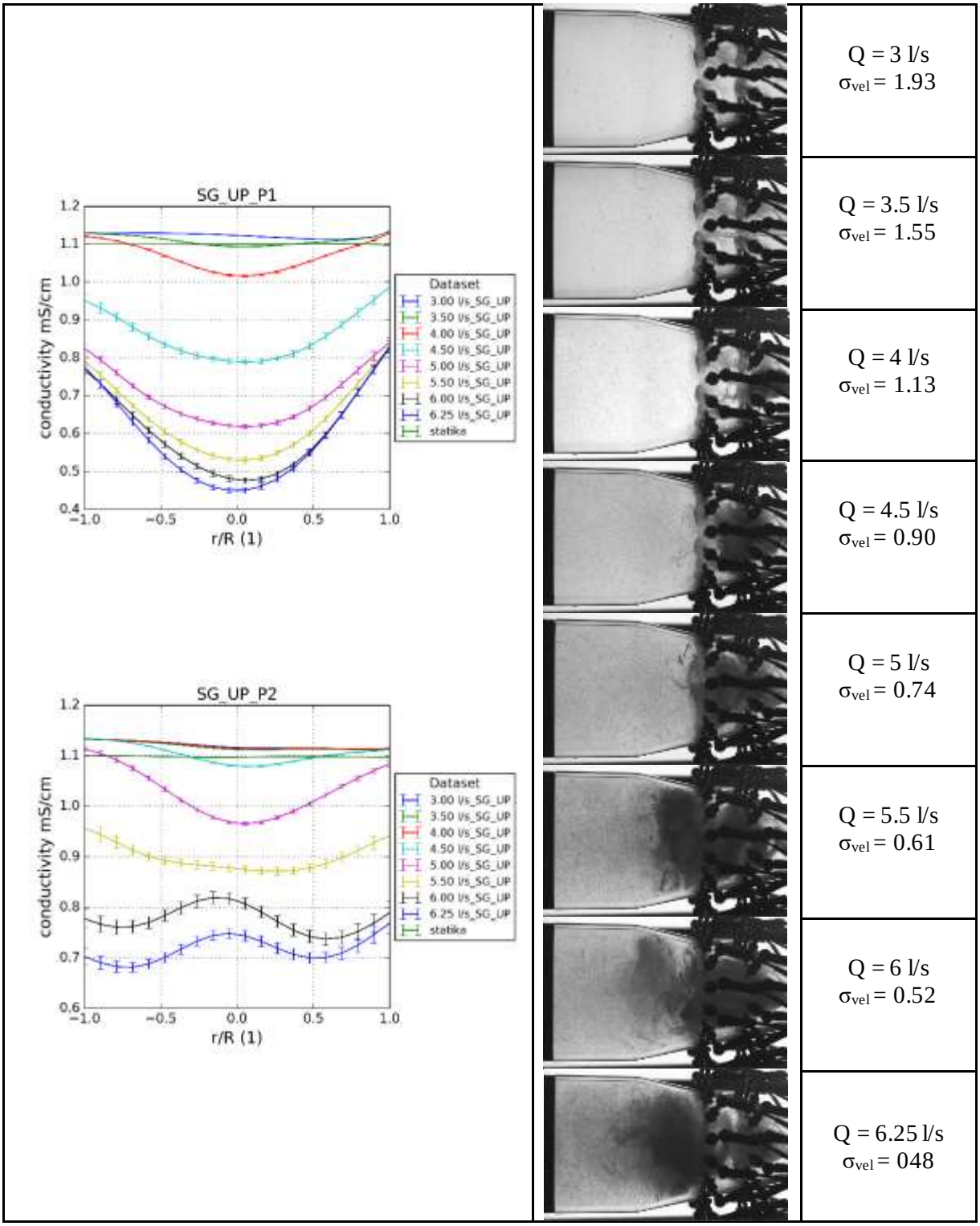

Figure 176 Conductivity profiles measured during the increasing discharge (decreasing cavitation number) with images of the cavitating structures prior their collapse.

The similar conclusions are valid for the opposite direction of the discharge. Conductivity profiles corresponding to these measurements are shown in the Figure 177. Slight shift of the profiles can be found comparing the corresponding operating points from the conductivity point of view.

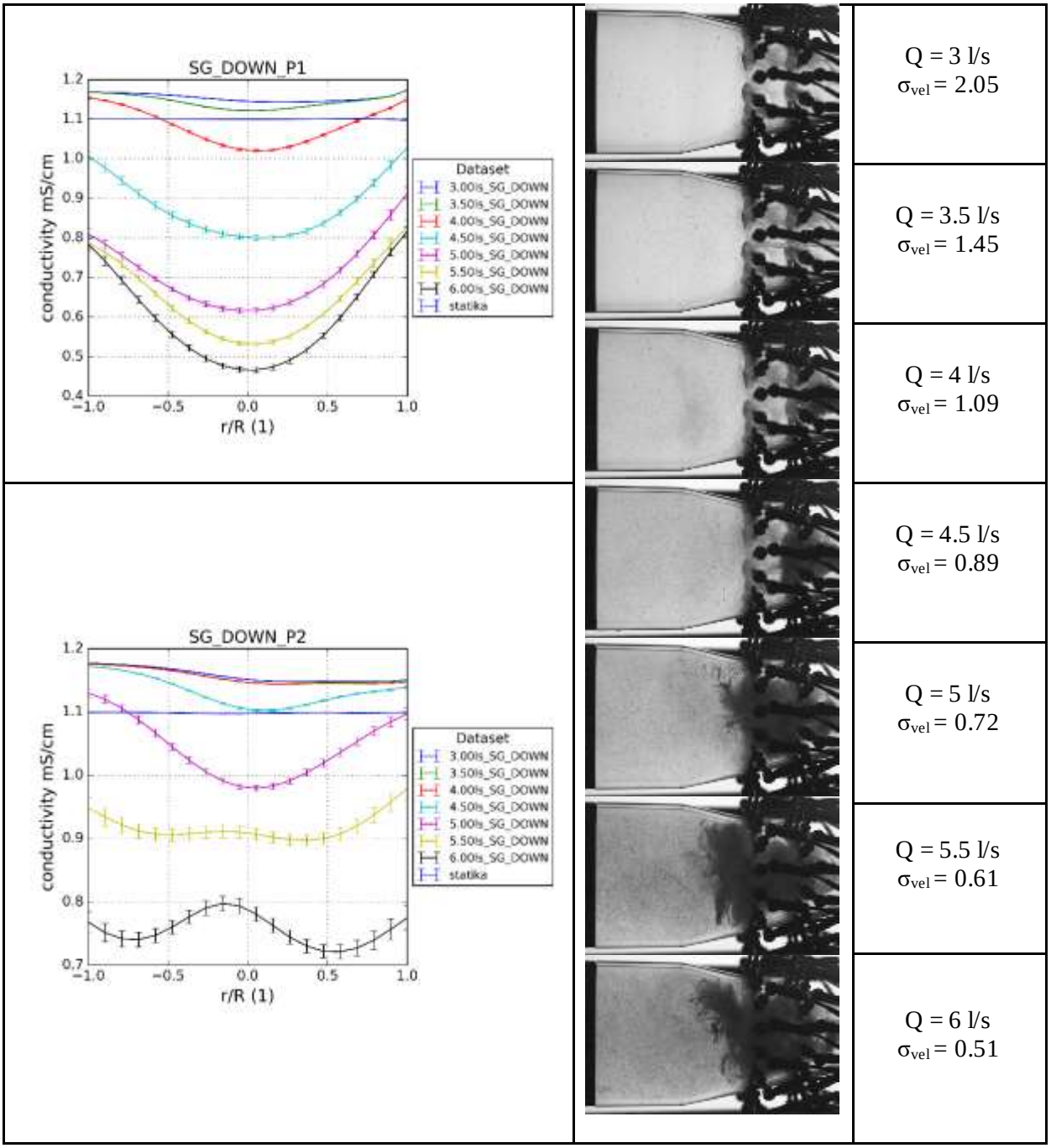

Figure 177 Conductivity profiles measured during the decreasing discharge (increasing cavitation number) with images of the cavitating structures prior their collapse in case of SG presence.

Direct comparison of the selected operating points is provided in the following text to study this discrepancy. It should be repeated, that the temperature of the water was slowly increasing during the experiments as it has been shown at the beginning of this section.

6.4. Q_{nom} = 6 l/s, fully developed cavitation

The most developed stage of cavitation comparable based on the direction of the discharge gradient change corresponds to the nominal discharge of 6 l/s. The operating points are characterized by the σ_{vel} of 0.518 in case UP direction and 0.511 in case of the DOWN direction. Comparing the conductivity maps depicted in the Figure 178, it can be concluded that the presence of gaseous phase seems to be slightly more significant in case of the DOWN direction regardless the considered measuring plane. It should be also considered that the water temperature was higher by 0.55 °C which lead to the increase

of the water conductivity. This fact is in contrast with the shown data. As it is relatively obvious from the maps, the core of the low conductivity close to the axis is wider in case of DOWN direction considering the P1 measuring plane. In case of the conductivity maps devoted to the P2, the central region of higher conductivity (i.e. higher amount of the liquid phase) is larger in case of the UP direction, regardless the general qualitative agreement of the obtained results. These observations suggested that there can be found minor difference between the gaseous phase amount within the flow based on the direction of the discharge change. In other words, the cavitation remains more significant compared to the transition from the initial stages of cavitation during the transition from the more developed stage of cavitation.

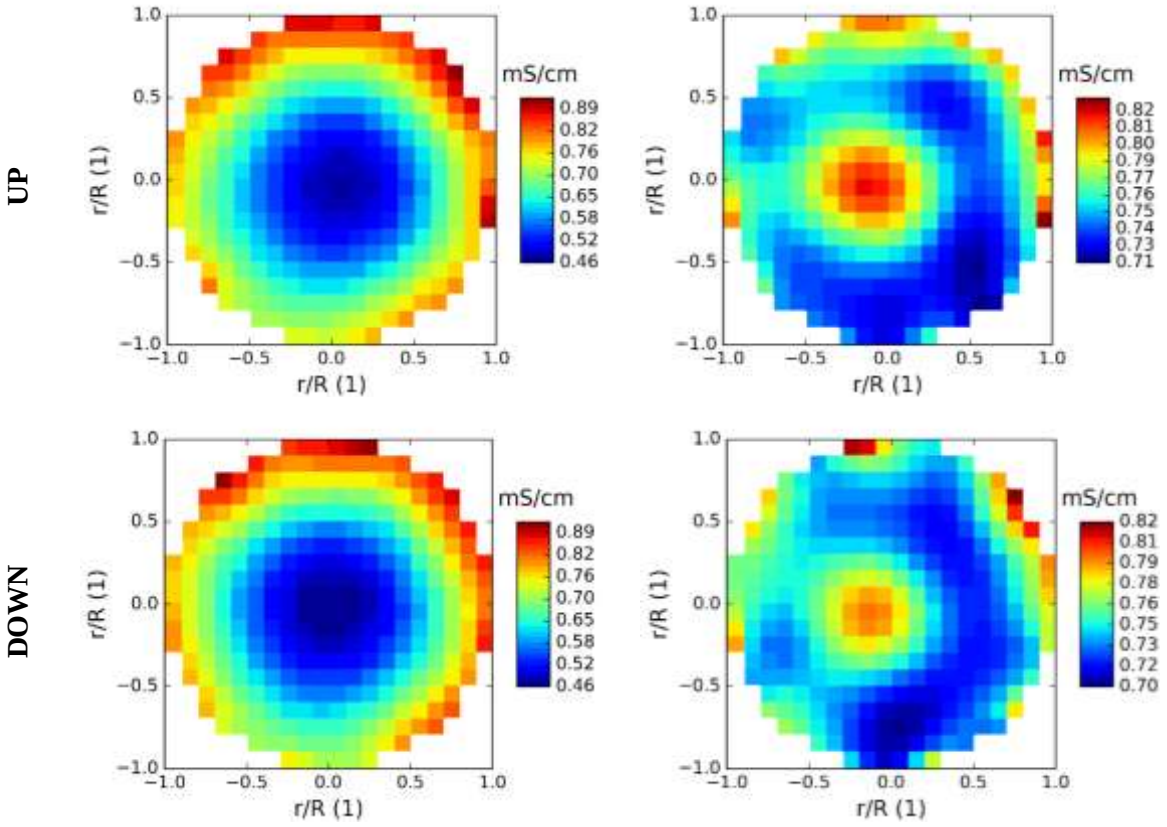

Figure 178 Conductivity maps in planes P1 (left) and P2 (right) corresponding to nominal flow rate of 6 l / s in case of SG presence.

Abovementioned discrepancies can be directly compared using the charts depicting profiles of conductivity along the selected diameter of the measuring planes (Figure 179). As it can be seen the shift is remarkable mainly in case of the P2 measuring plane, which is in good agreement with the fact that the front part of the cavitating vortex close to the throat of the nozzle is significantly more stable and coherent.

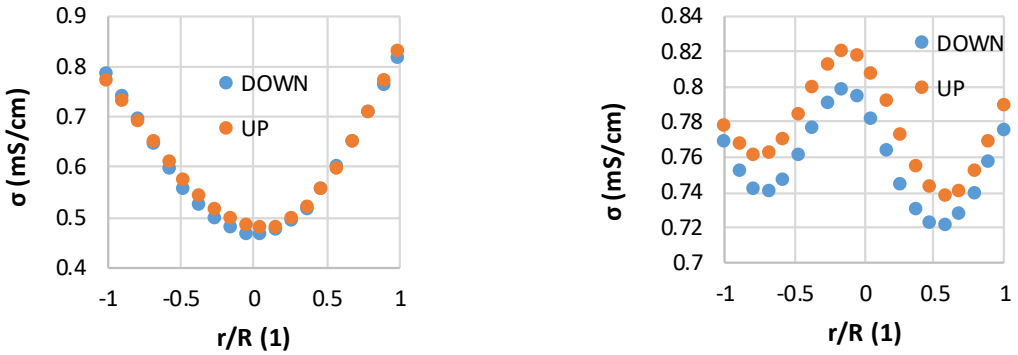

Figure 179 Comparison of the conductivity profiles over the selected diameter of measuring planes P1 (left) and P2 (right) corresponding to the nominal flow rate of 6 l/s and SG presence.

6.5. Q_{nom} = 5.5 l/s, fully developed cavitation

The results corresponding to the Q_{nom} of 5.5 l/s are shown in the same manner, therefore the general description of the methodology is the same as in the previously discussed Q_{nom} of 6 l/s. The evaluated values of σ_{vel} were following: UP direction 0.614, DOWN direction 0.612. The temperature difference between these two operating points has been 1.12°C. The conductivity maps corresponding to the both measuring planes are depicted in the Figure 180.

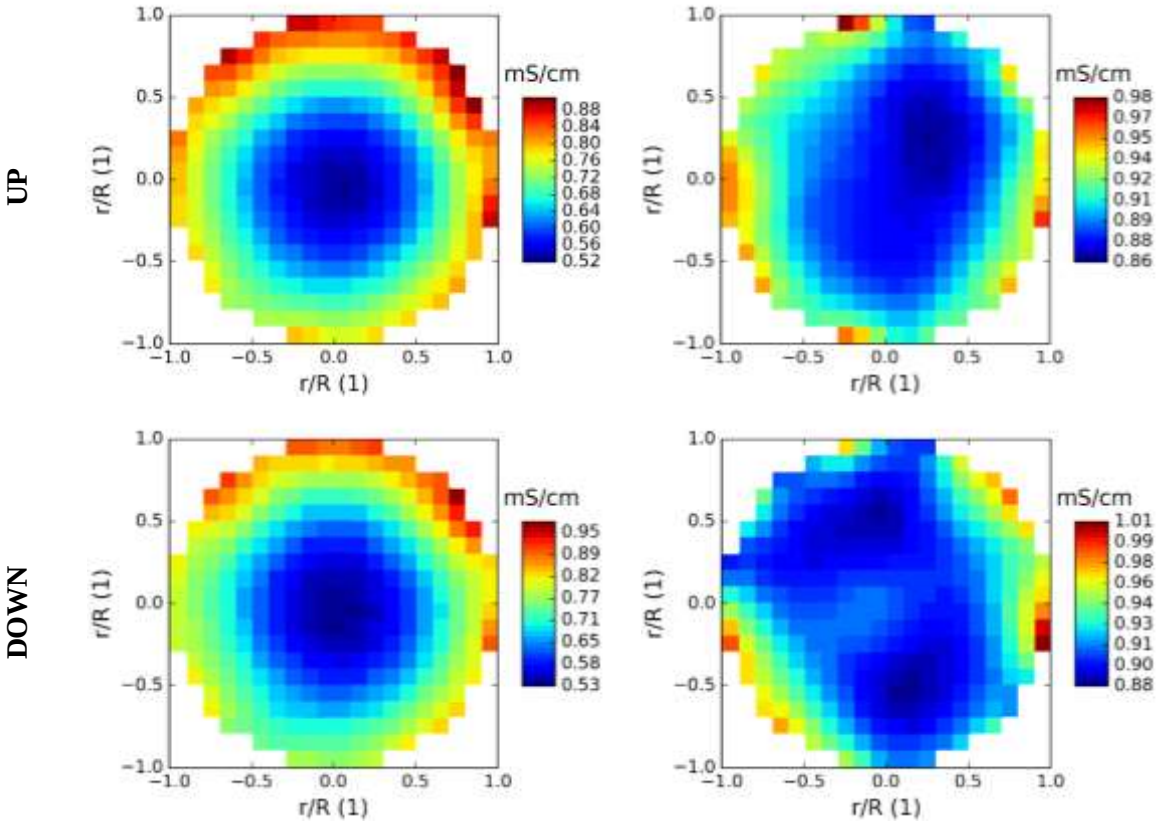

Figure 180 Conductivity maps in planes P1 (left) and P2 (right) corresponding to nominal flow rate of 5.5 l / s in case of SG presence.

Interesting observation can be describe by comparison of the conductivity profiles corresponding to the P2 measuring plane (Figure 181, right). As it can be seen, the actual values are slightly higher in case of the DOWN direction, which is in contrast with the previously discussed operating point. On the other hand, the shape of the profile is considerably more similar to the more developed stage of the cavitation considering the DOWN direction. In other words, the shift of the conductivity values can be devoted to

the increased temperature. Based on the conductivity profile it can be assumed that the cavitation was slightly more developed in case of the transition from the fully developed stage to initial stage of cavitation. On the other hand, it should be admitted than the observed discrepancy is relatively small.

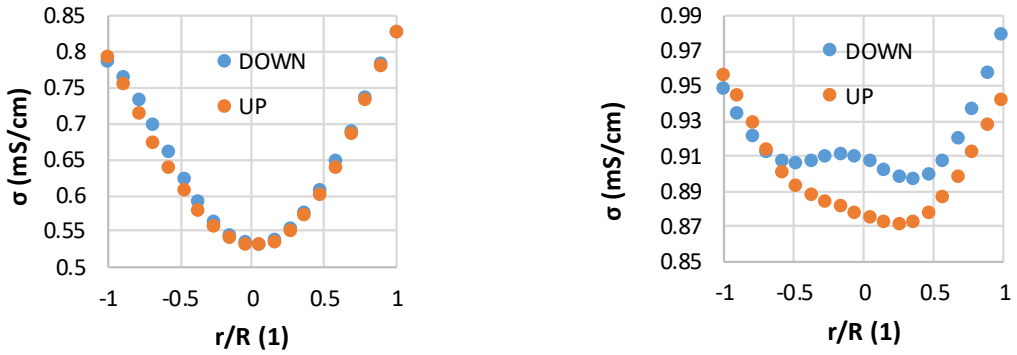

Figure 181 Comparison of the conductivity profiles over the selected dimater of measuring planes P1 (left) and P2 (right) corresponding to the nominal flow rate of 5.5 l/s and SG presence.

6.6. Q_{nom} = 5 l/s, fully developed cavitation

The cavitation numbers corresponding to the lowest discharge of 5 l/s which is discussed in more details were as follows. The values of σ_{vel} evaluated in case of the UP direction was 0.736 and in case of the DOWN direction the evaluated value was 0.725. The increase of temperature between these two operation points was 1.57°C. It should be noted that the 5 l/s discharge has been chosen as the lowest discharge for the detailed discussion due to the fact, that the presence of the gaseous phase was considerably more seldom in the P2 measuring plane considering lower flow-rates. As it can be seen, the qualitative comparison of the conductivity maps corresponding to the different measuring planes is in better agreement compared to the above described regimes of cavitation as it can be seen in the Figure 182. This observation is subsequent to the fact that the decay of the coherent cavitating structure was observed upstream the measuring plane P2, while the residual cavitating vortices were still able to reach the P2 plane in sufficient amount which lead to significant deformation of the conductivity profile close to the axis of the pipeline.

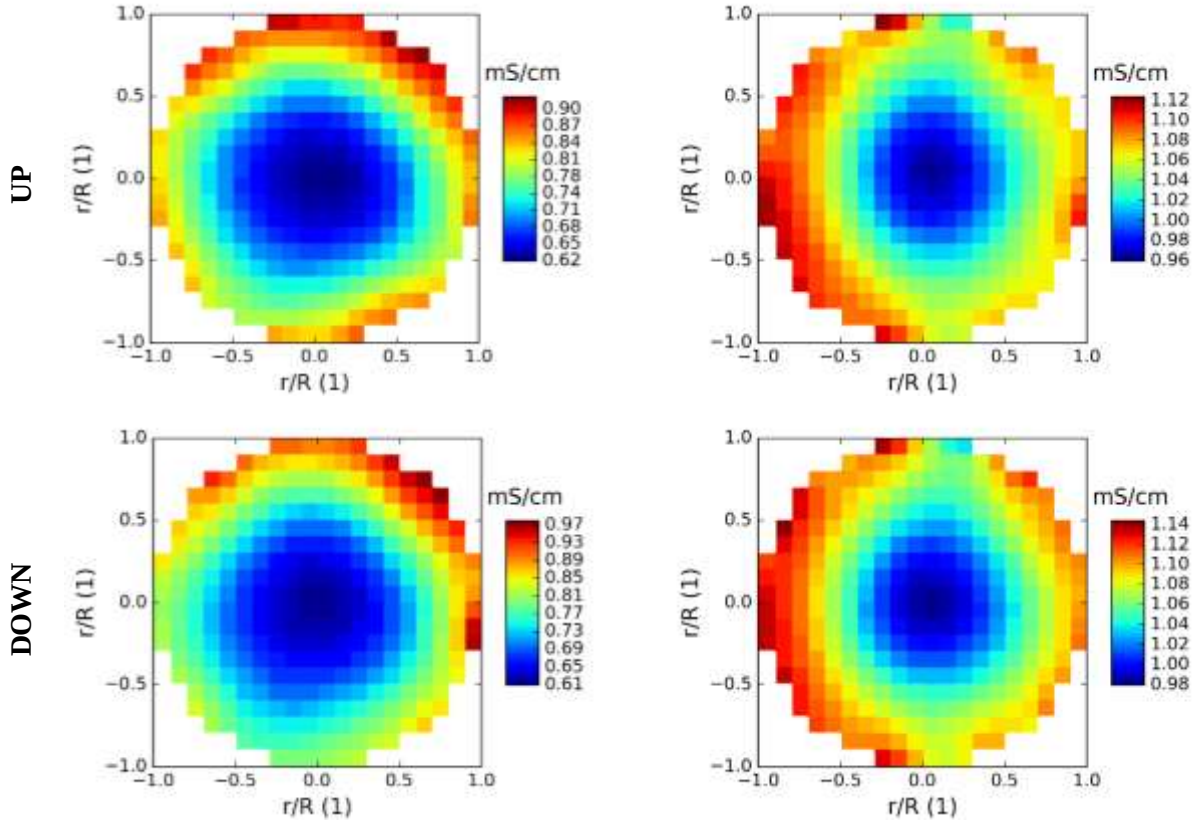

Figure 182 Conductivity maps in planes P1 (left) and P2 (right) corresponding to nominal flow rate of 5 l / s in case of SG presence.

The conductivity profiles are similar regardless the investigated cross sections. The obvious shift of the actual values of conductivity in case of P2 measuring plane can be devoted to the increased temperature. It should be also emphasized that discrepancy between the cavitation numbers is larger compared to the previously discussed more developed stages of cavitation. Nevertheless, since the value of σ_{vel} corresponding to the DOWN direction is lower (i.e. cavitation should be slightly more developed compared to the UP direction) the lower conductivity could be expected, which is in contrast with the actual values of conductivity depicted in the Figure 183. Thus, it can be assumed that the influence of the temperature is more important that the small difference between the evaluated cavitation numbers.

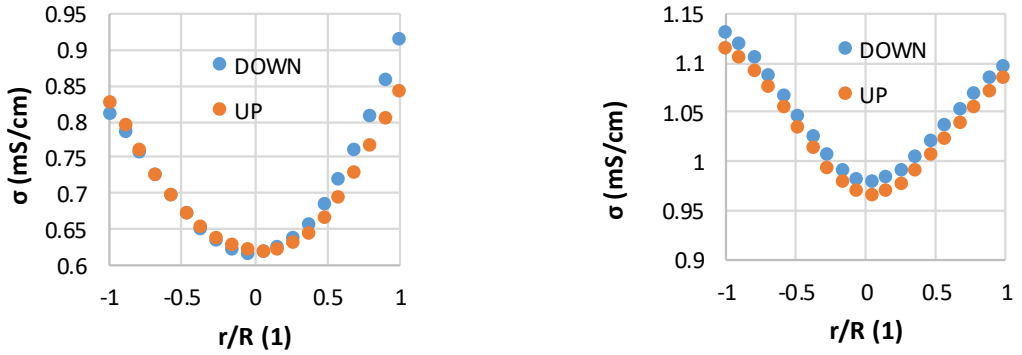

Figure 183 Comparison of the conductivity profiles over the selected dimater of measuring planes P1 (left) and P2 (right) corresponding to the nominal flow rate of 5 l/s and SG presence.

6.7. EIT investigation of the cavitating flow in case of the axial inflow

The results corresponding to the analysis of the axial inflow will be provided in the same manner as in case of the analysis of the cavitation affected by the presence of swirl generator. The periodical separation of the cavitating vortex rings is characteristic for this experimental configuration. In other words, the redistribution of the gaseous phase across the investigated measuring planes is completely different compared to the experiments focused on the induced swirl investigation.

In contrast to the SG presence, the cavitation occurred close to the wall of the Venturi tube, while the liquid flow was concentrated close to the axis. As it can be seen in the overview of the conductivity profiles measured in the P1 (see Figure 184), the measured conductivity tended to decrease with the increasing discharge close to the walls of the nozzle. On the other hand, the significant increase of conductivity with the increasing flow rate can be found close to the axis of the nozzle. The only exception to this proportionality corresponded to the highest investigated discharge (6.5 l/s). Decrease of the maximum conductivity value close to the axis can be devoted to the significant increase of the cavitation volume compared to the lower discharges as it is captured by the images of the cavitating structures.

It is also worth noted, that the values of the conductivity computed close to the axis of the nozzle were increasing above the value of the static conductivity. This can be devoted to the considerable magnitude of the axial velocity together with relatively small amount of the gaseous phase close to the axis of the nozzle. It is also clearly depicted that the type A uncertainty corresponding to the axial inflow is considerably higher compared to the experimental configuration considering the presence of SG. This behaviour is subsequent to the more dynamic process of the observed cycles of cavitation in case of the axial inflow.

The conductivity profiles measured in P2 (i.e. in larger distance from the throat of the nozzle) are in relatively good agreement with the results obtained in case of SG presence from the qualitative point of view. The profiles corresponding to the axial inflow have a similar course as in case of the SG presence, which can be explained by the nature of the observed cavitating structures. In contrast to the P1 measurement, the thicker liquid layer close to the walls of the nozzle was stable enough to increase conductivity value close to the wall of the nozzle, while another region of the increased conductivity can be found close the axis of the nozzle (middle if the vortex ring). This observation can be done in case of the discharges of 5.50 l/s and 6 l/s. In case of the lower or higher discharges the local maxima close to the axis distinguished. This can be devoted to the fact, that the coherent cavitating structure collapsed upstream the P2 cross section in case of the lower discharges. The opposite assumption can be done in case of the highest discharge of 6.50 l/s when the maximum length of the cavitating structures considerably exceeded the position of this measuring plane. In other words, the measuring plane has been filled by the significant amount of the cavitation during the considerable part of the cavitation cycle period.

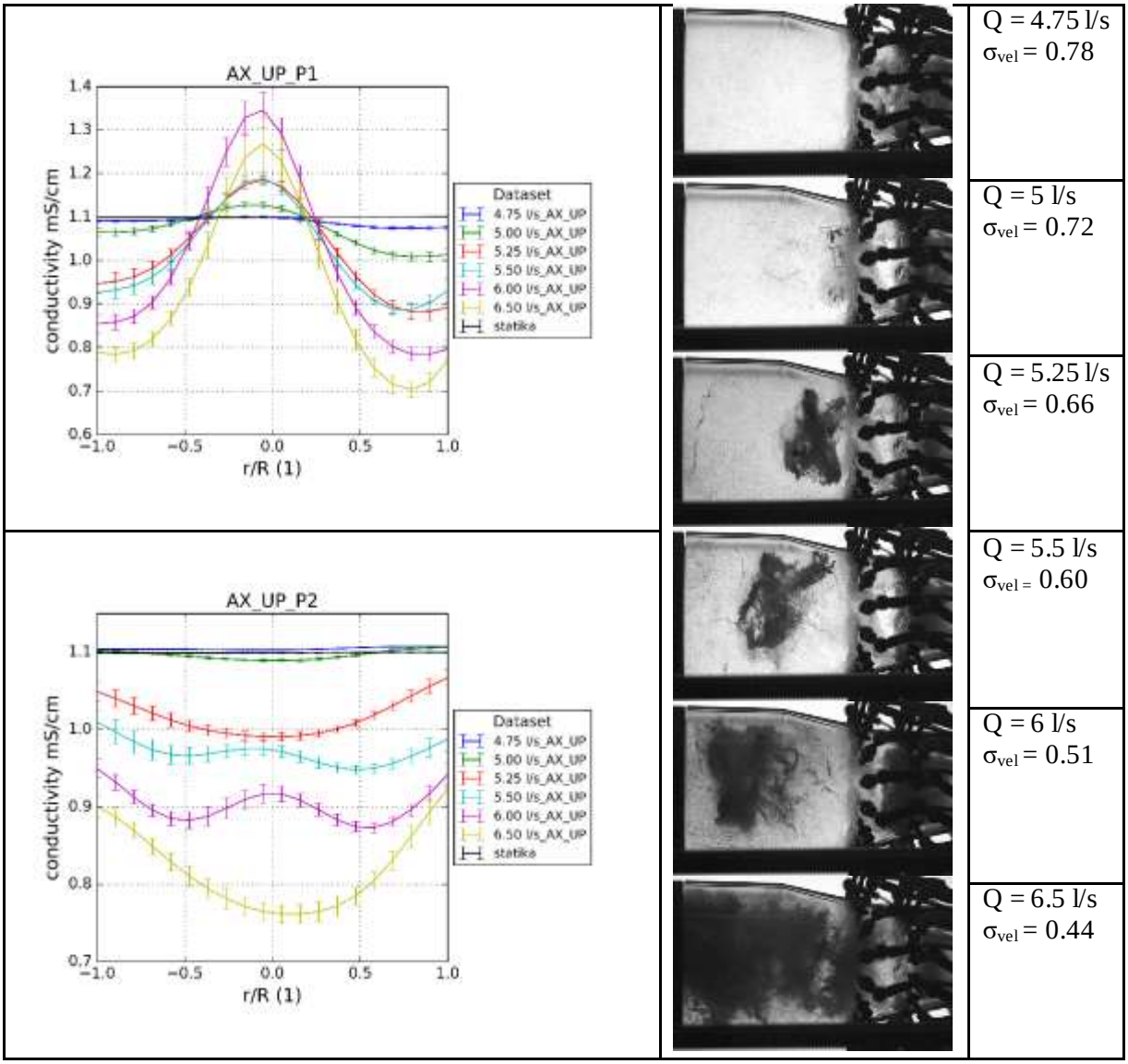

Figure 184 Conductivity profiles measured during the increasing discharge (decreasing cavitation number) with images of the cavitating structures prior their collapse in case of AX presence.

The similar results were acquired in case opposite direction of the discharge gradient change as it can be seen in the Figure 185. It should be noted that the conductivity profiles corresponding to the P2 measuring plane are visibly deformed and shifted to the left side. Other properties and assumptions described for the UP direction of the discharge gradient change are still valid and applicable for this set of measurements. The abovementioned discrepancy will be discussed in the following part of this chapter.

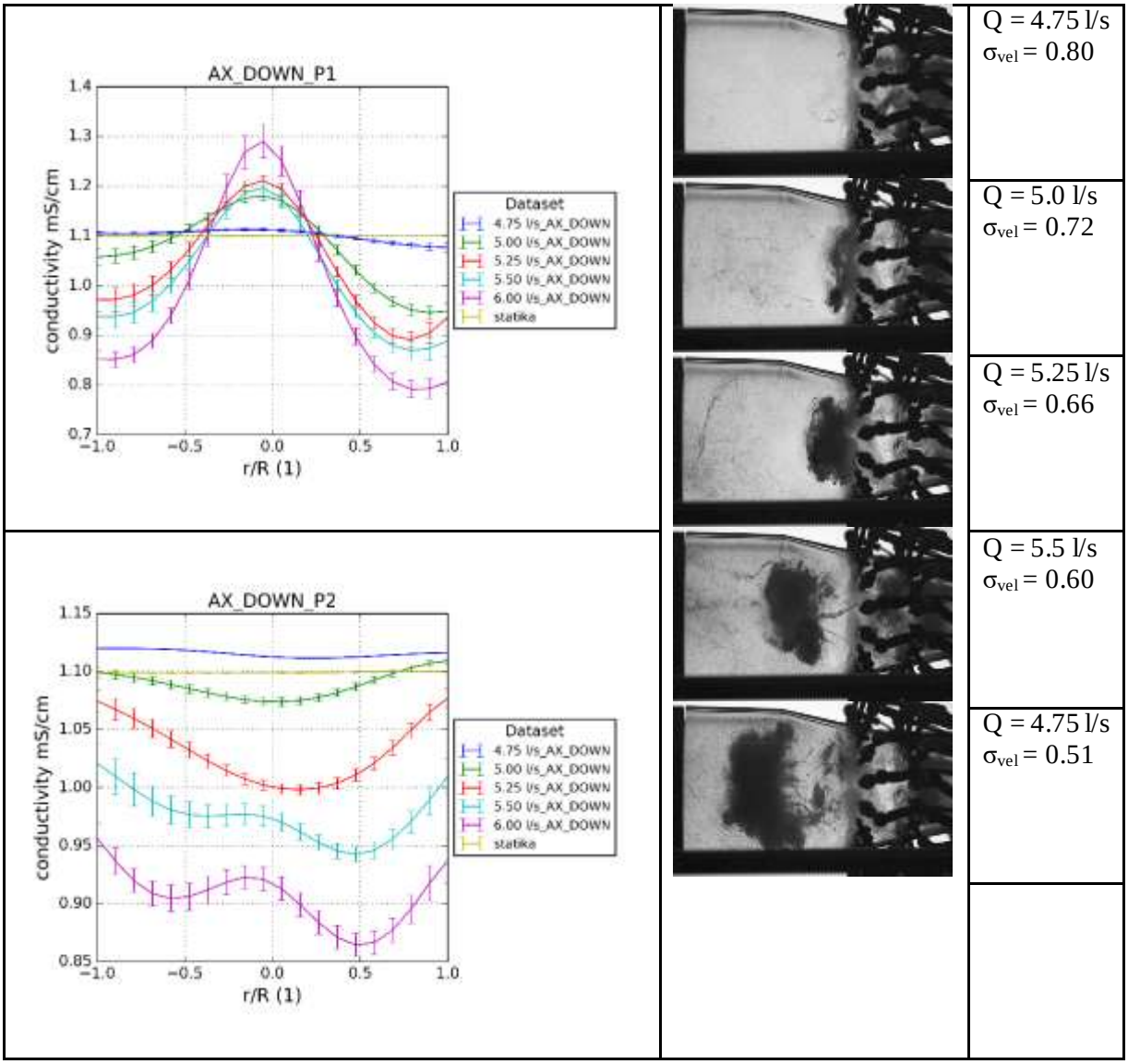

Figure 185 Conductivity profiles measured during the decreasing discharge (increasing cavitation number) with images of the cavitating structures prior their collapse in case of AX presence.

6.8. Q_{nom} = 6 l/s, fully developed cavitation

The most developed stage of cavitation investigated from the cavitation hysteresis point of view corresponds to 6 l/s. Considerable amount of gaseous phase present during the most part of the cavitation cycle within the P1 measuring plane led to the creation of the massive region of lower conductivity close to the wall of nozzle. The liquid core of the vortex rings is clearly captured in both discharge gradient directions close to the axis of the nozzle (see Figure 186). It is worth to noted that the liquid layer was observed between the surface of the nozzle and cavitating structures during the experimental measurement. The values of conductivity close to the wall are slightly higher in the corresponding conductivity maps. Nevertheless, it should be emphasized that this increase is minor, which can be devoted to the restrictions of the EIT as well as to the low resolution of the captured maps.

The liquid flow between the cavitating structures and the walls of the nozzle is well distinguishable by the measuring plane P2. As it can be seen in the Figure 186, the obtained maps of conductivity are more complex compared to the maps which were obtained in the P1 plane. Together with the clearly depicted region of the liquid flow close to the walls of the nozzle, the increase of the conductivity was also captured close to the axis.

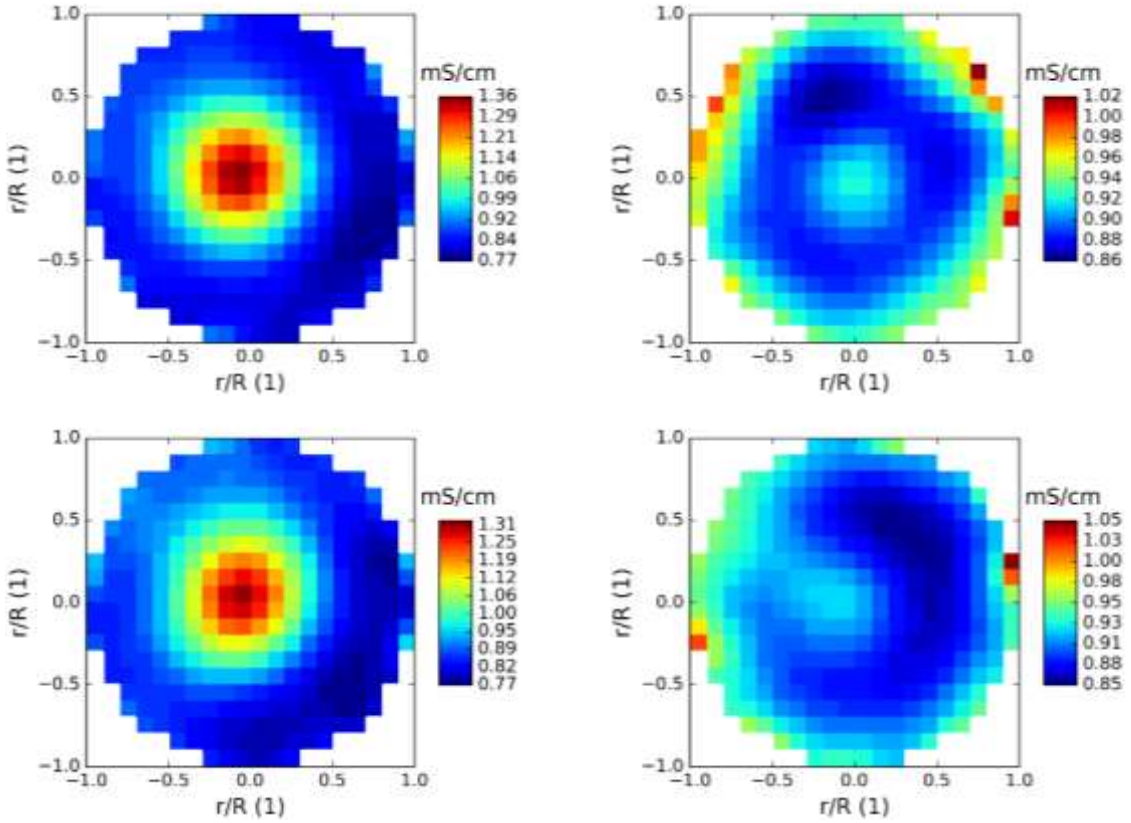

Figure 186 Conductivity maps in planes P1 (left) and P2 (right) corresponding to nominal flow rate of 6 l/s in case axial inflow.

Direct comparison of the conductivity profiles along the selected diameters of the diffuser is shown in the Figure 187. Since type A uncertainty corresponding to the axial inflow is considerably higher in contrast the analysis of the cavitation influenced by the SG, it is possible to state, that the profiles are in good agreement regardless the measuring plane.

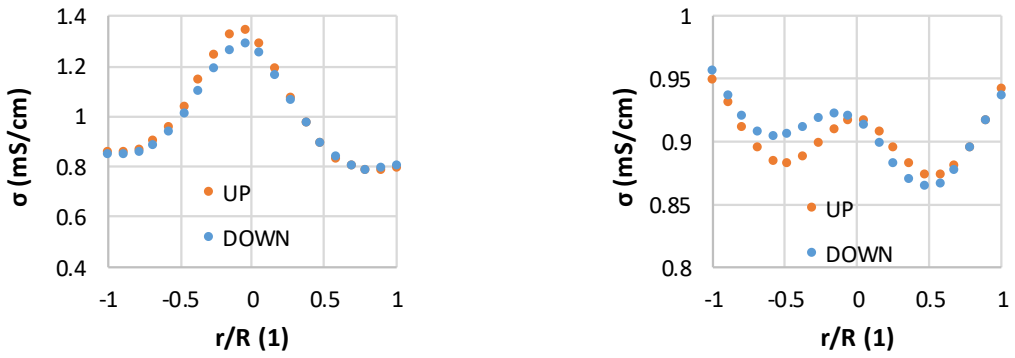

Figure 187 Comparison of the conductivity profiles over the selected dimater of measuring planes P1 (left) and P2 (right) corresponding to the nominal flow rate of 6 l/s and axial inflow.

6.9. Q_{nom} = 5.5 l/s, fully developed cavitation

The results of the 5.5 l/s discharge show the same observations as were described in case of the 6 l/s as it is clearly depicted in the Figure 188 and Figure 189.

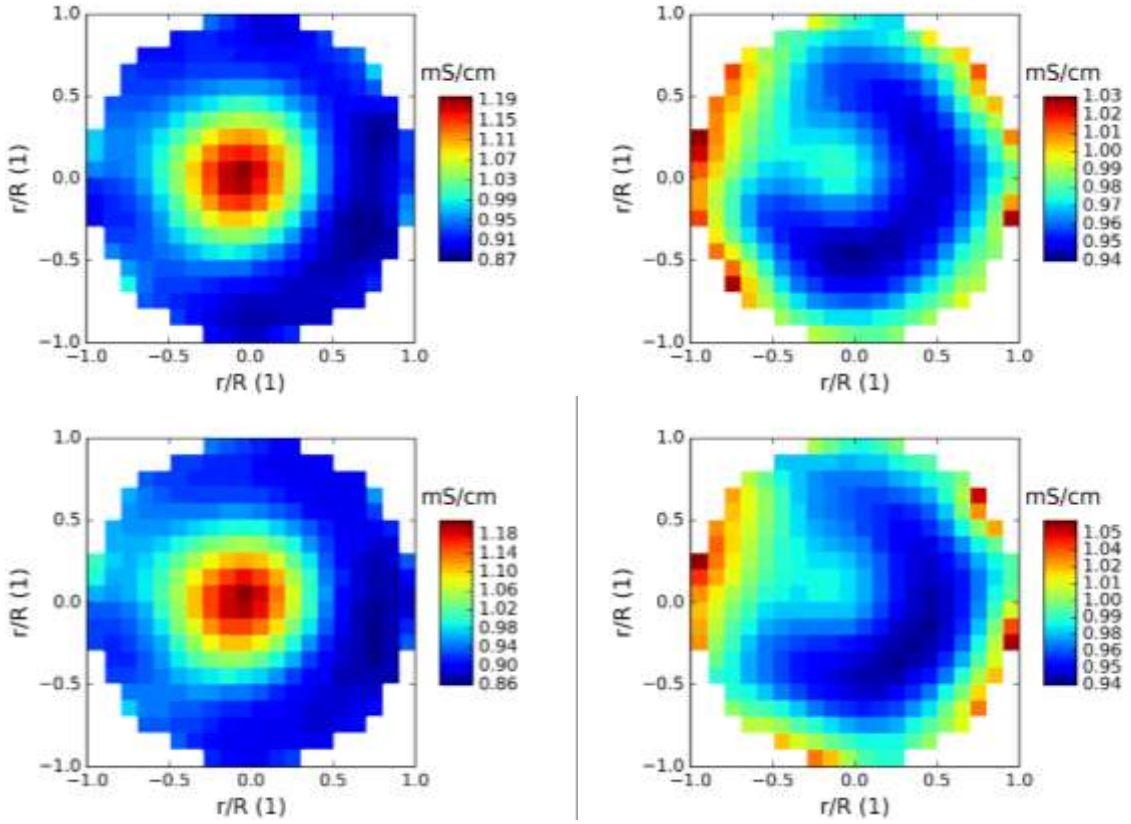

Figure 188 Conductivity maps in planes P1 (left) and P2 (right) corresponding to nominal flow rate of 5.5 l/s in case axial inflow.

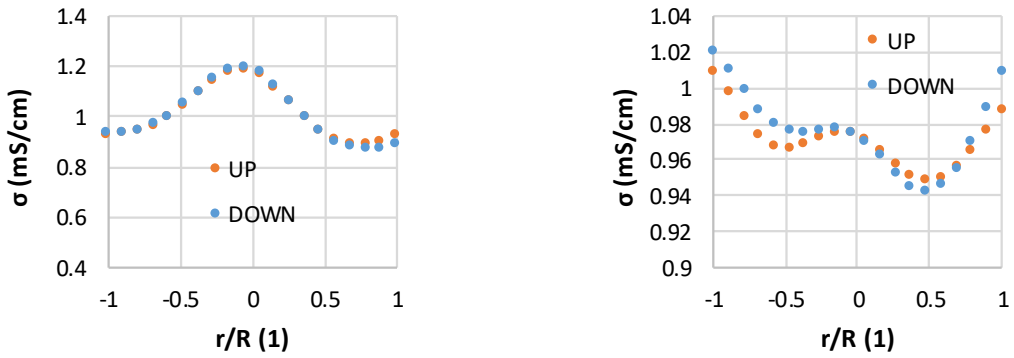

Figure 189 Comparison of the conductivity profiles over the selected dimater of measuring planes P1 (left) and P2 (right) corresponding to the nominal flow rate of 6 l/s and axial inflow.

6.10. 5 l/s, initial stage of cavitation

Slightly different structure of the conductivity maps compared to the operating points described above correspond to the discharge of 6 l/s. The region of the higher conductivity close to the walls of the nozzle can be found in P1 plane which is consequence of the reduced amount of gaseous phase contained within the flow (Figure 190).

The maps of conductivity captured in the P2 measuring plane are completely different compared to the more developed stages of cavitation due to the collapse of the coherent cavitating structures upstream the measuring plane.

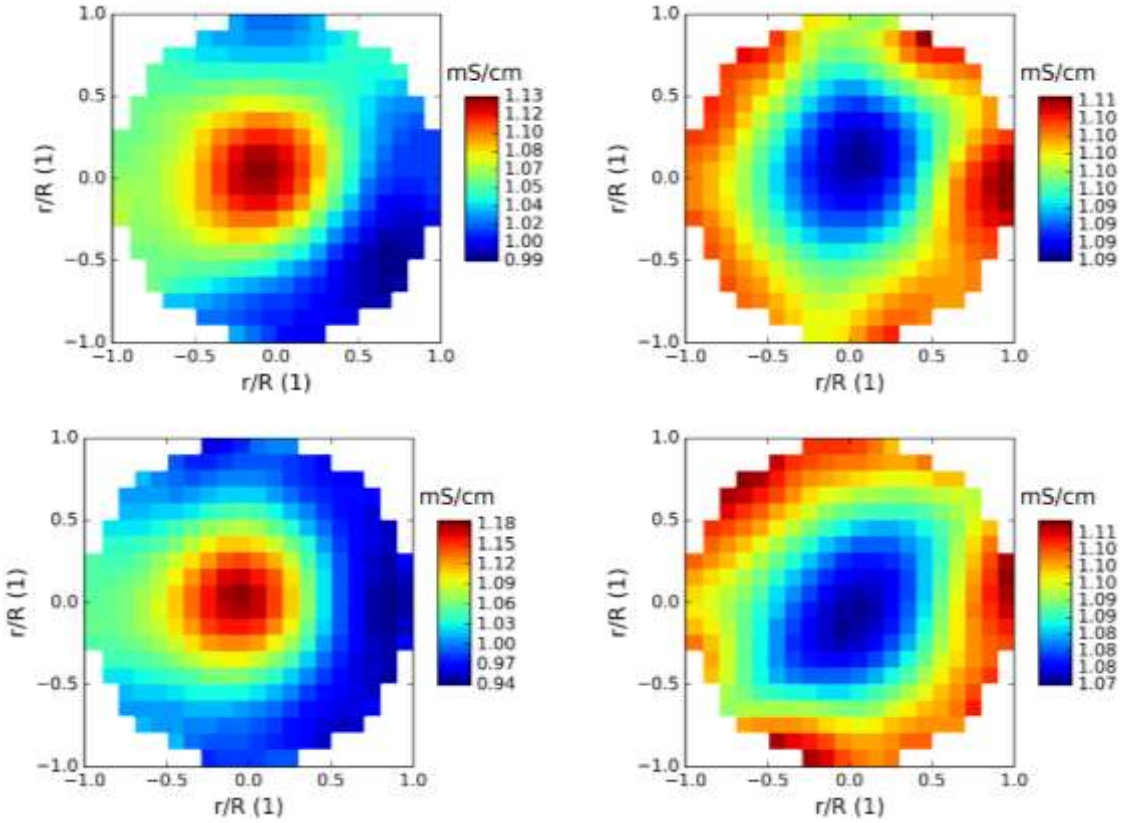

Figure 190 Conductivity maps in planes P1 (left) and P2 (right) corresponding to nominal flow rate of 5 l/s in case axial inflow.

The comparison of the conductivity profiles (Figure 191) shows relatively significant discrepancy in case of the P2 measuring plane. While in case of profiles obtained in the measuring plane P1, the values corresponding to the DOWN direction are slightly higher close to the axis of the nozzle, the situation is completely opposite in case of the P2 measuring plane. This observation imply that the cavitating flow was more developed and coherent in case of the DOWN direction.

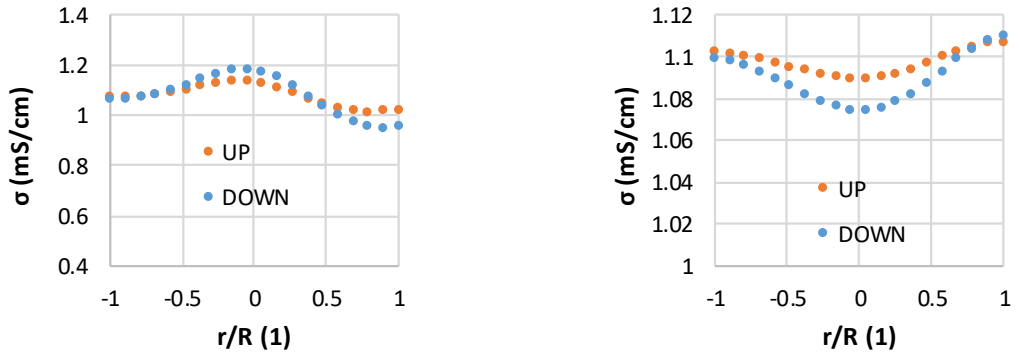

Figure 191 Comparison of the conductivity profiles over the selected dimater of measuring planes P1 (left) and P2 (right) corresponding to the nominal flow rate of 5 l/s and axial inflow.

On the other hand, the conductivity values are lower in case of the UP direction in case of the conductivity profiles measured in P2 for 5.25 l/s and 4.75 l/s flow rates (i.e. operating points close to the discharge of 5 l/s) in the Figure 192.

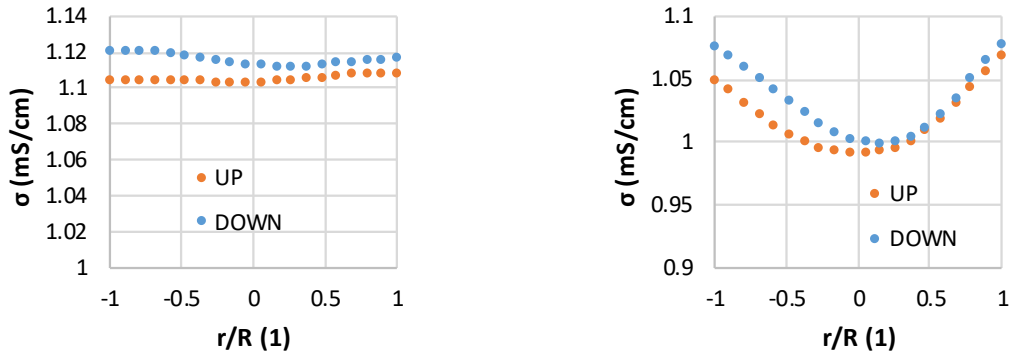

Figure 192 Conductivity profiles corresponding to the nominal flowrates of 4.75 l/s (right) and 5.25 l/s (right) measured in the plane P2.

6.11. Final discussion of the EIT results

As it has been shown, it was possible to clearly distinguish the regimes of cavitation as well as the general nature of the cavitating structures in the measuring planes based on the maps of conductivity. Using these results, it was possible to observe different gaseous phase distribution within the flow based on the investigated configuration. On the other hand, results of the hysteresis analysis based on the conductivity profiles provided only inconclusive results. Thus, the mean values of conductivity over the whole measuring planes were calculated and depicted versus the corresponding values of σ_{vel} to exclude the influence of the conductivity maps asymmetry. As it is shown in the charts in the Figure 193 devoted to the experimental configuration including the SG and Figure 194 depicting charts of the axial inflow analysis, the slightly higher values of conductivity can be found in case of the DOWN direction. This is in good agreement with the results of the resistivity and hydraulic loss analysis and it can be devoted to the increase of the liquid temperature as it has been explained in the resistivity analysis discussion. It should be noted, that slightly different shape of the conductivity maps was obtained for the corresponding operating points based on the direction of the flowrate change. Using the above-mentioned results, it shall be concluded that the hysteresis of the cavitation stage based on the EIT analysis has not be proved. Nevertheless, it is possible that the potential change of the gaseous phase within the flow based on the discharge gradient change direction is minor and therefore undistinguishable due to other factors such as water temperature increase or the low temporal and spatial resolution of the exploited EIT equipment.

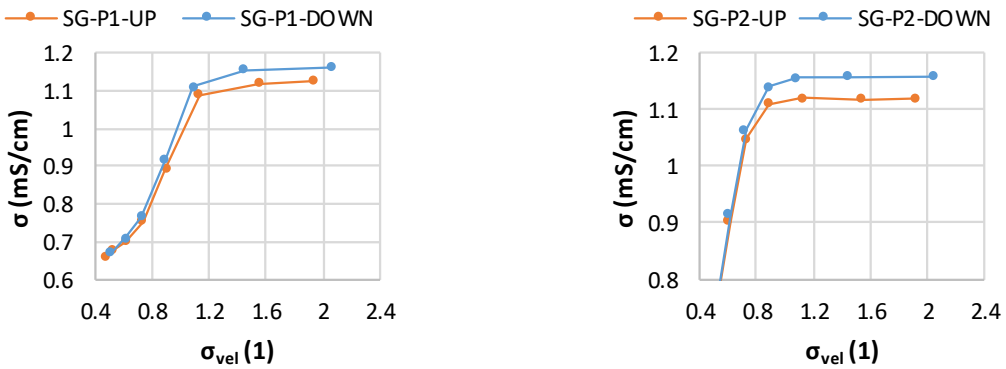

Figure 193 Averaged values of conductivity in case of the SG presence. P1 – left, P2 – right.

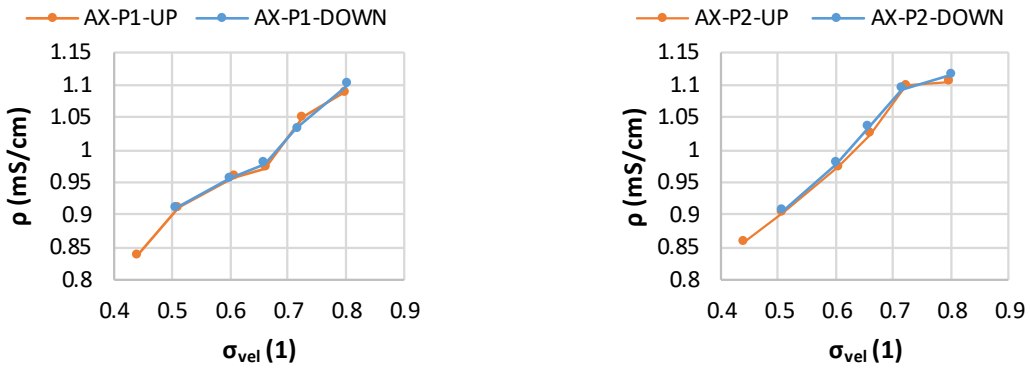

Figure 194 The averaged values of the measured conductivity on case of the axial inflow. P1 – left, P2 – right.

The image of the gradual increase of the gaseous phase amount within the flow can be provided by the direct comparison of the mean conductivities obtained in measuring planes P1 and P2 during the investigation. Seeing the chart devoted to the axial inflow analysis (Figure 195 - right), it can be stated that the results between the values of conductivity is relatively significant only in case of σ_{vel} between the 0.65 and 0.75, which is caused due to the separation and consequent downstream motion of the cavitating vortex rings. The results are completely different in case of the SG presence (Figure 195 - left). As it can be seen the values of ρ remained relatively similar down to the σ_{vel} of 1.13 when the straight axisymmetric cavitating vortex occurred. The discrepancy between the conductivity values corresponding to the individual measuring planes remained significant down to the most developed stage of cavitation which was captured by the EIT. During this regime, the coherent cavitating vortex lengths was significantly larger than the distance of the P2.

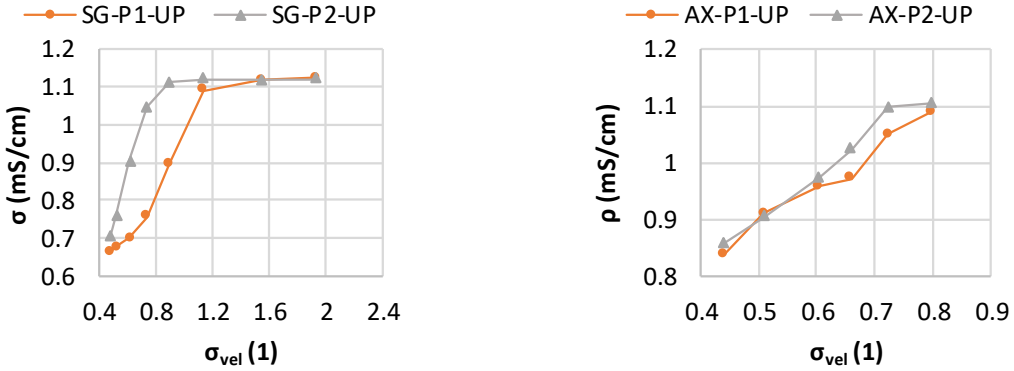

Figure 195 Comparison of the averaged conductivities measured in the plane P1 and P2 in case of SG presence (left) and axial inflow (right)

6.12. Comparison of the numerical results with the EIT analysis

The main purpose of the second part of the EIT investigation was to compare the distribution of the conductivity with the distribution of the vapor volume fraction obtained by the CFD. For the purpose, the previously described numerical results were exploited, while the experimentally investigated cavitation regimes were set up using the butterfly valve mounted upstream the Venturi tube.

Prior the description of the results several facts shall be emphasized. First, the analysis of the above described CFD results was exploited in this section. Therefore, the in-depth description of the numerical setting as well as the description of the computational grids can be found in the chapter devoted to the numerical analysis of the cavitating flow.

The malfunction of the measuring plane P2 has occurred during this part of the experimental investigation as it is clearly depicted in the Figure 196. The conductivity maps corresponding to the P2 measuring plane were highly distorted. This malfunction was probably caused by the severe vibrations and consequent leakage of the EIT electrode. Since it was not possible to repeat the measurement, the results obtained during the hysteresis investigation were exploited to describe the differences between the CFD and EIT results in the P2 measuring plane. Operating points are therefore not completely corresponding using this approach. It shall be kept in mind that the observed qualitative discrepancies between the vapor volume fraction distribution and conductivity can be highly influenced by these discrepancies in case of the P2 measuring plane.

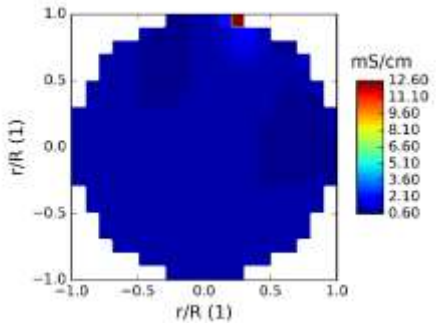

Figure 196 Distribution of the conductivity in the measuring plane P2 distorted due to the malfunction of the EIT measurement.

6.13. Cavitating flow influenced by the presence of the swirl generator – comparison of the CFD and EIT results

The main disadvantage of the exploited EIT measuring equipment is clearly depicted in the following images (Figure 198). The resolution of the EIT is significantly lower compared to the resolution of the CFD analysis. Despite the low resolution of the EIT, it is still possible to state that the results are in qualitative agreement in case of the measuring plane P1.

The volume fraction of the water is low in the centre of the cross section, which is in good agreement with the drop of the conductivity values. The main discrepancy can be found close to the wall of the diffuser. While in case of EIT results the highest values of the conductivity can be found in this region, in case of the CFD results the significant water volume fraction drop is clearly captured. As it has been described, this is one of the most significant discrepancies between the experimental and numerical observations.

With the increasing cavitation number, the cavitation of the boundary layer downstream the throat of the nozzle became less significant as it can be seen by the comparison of the water volume fractions corresponding to the P1 measuring planes and different operating regimes.

Interesting observation can be found in case of the σ_{vel} of 0.76 (CFD). AS it can be seen the cavitation of the boundary layer is less significant as it has been described. On the other hand, the increase of the water volume fraction close to the centre of the measuring plane can be found in case of the CFD result, while the values of conductivity are minimal in this region. This is probably caused by the low resolution together with the low sampling frequency of the EIT equipment.

As it has been described, the direct comparison of these methods in case of the P2 measuring plane has been influenced by the malfunction of the EIT. Nevertheless, the general tendency of the volume phase distribution is similar for both discussed methods. In case the most developed cavitation regime (σ_{vel} 0.54), where the discrepancy between the cavitation number and investigated discharge based on the discussed method is minimal, the good agreement between the water volume fraction and conductivity distributions can be found. The presence of the liquid close to the walls of the nozzle is corresponding to the increased values of the conductivity in this region. Also, the distributions of the water volume fraction and conductivity close to the centre of the measuring plane are in good agreement.

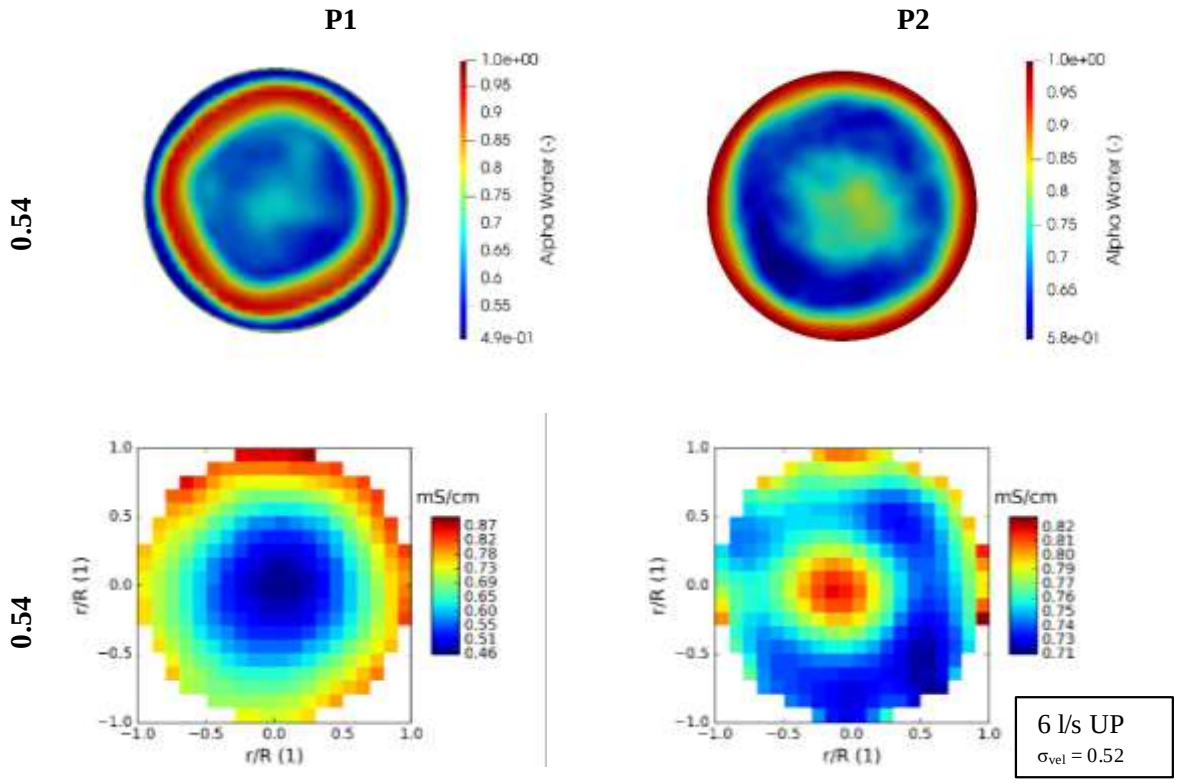

Figure 197 Qualitative comparison of the conductivity maps with the distribution of gaseous phase obtained by the CFD analysis in case of the SG presence – part 1

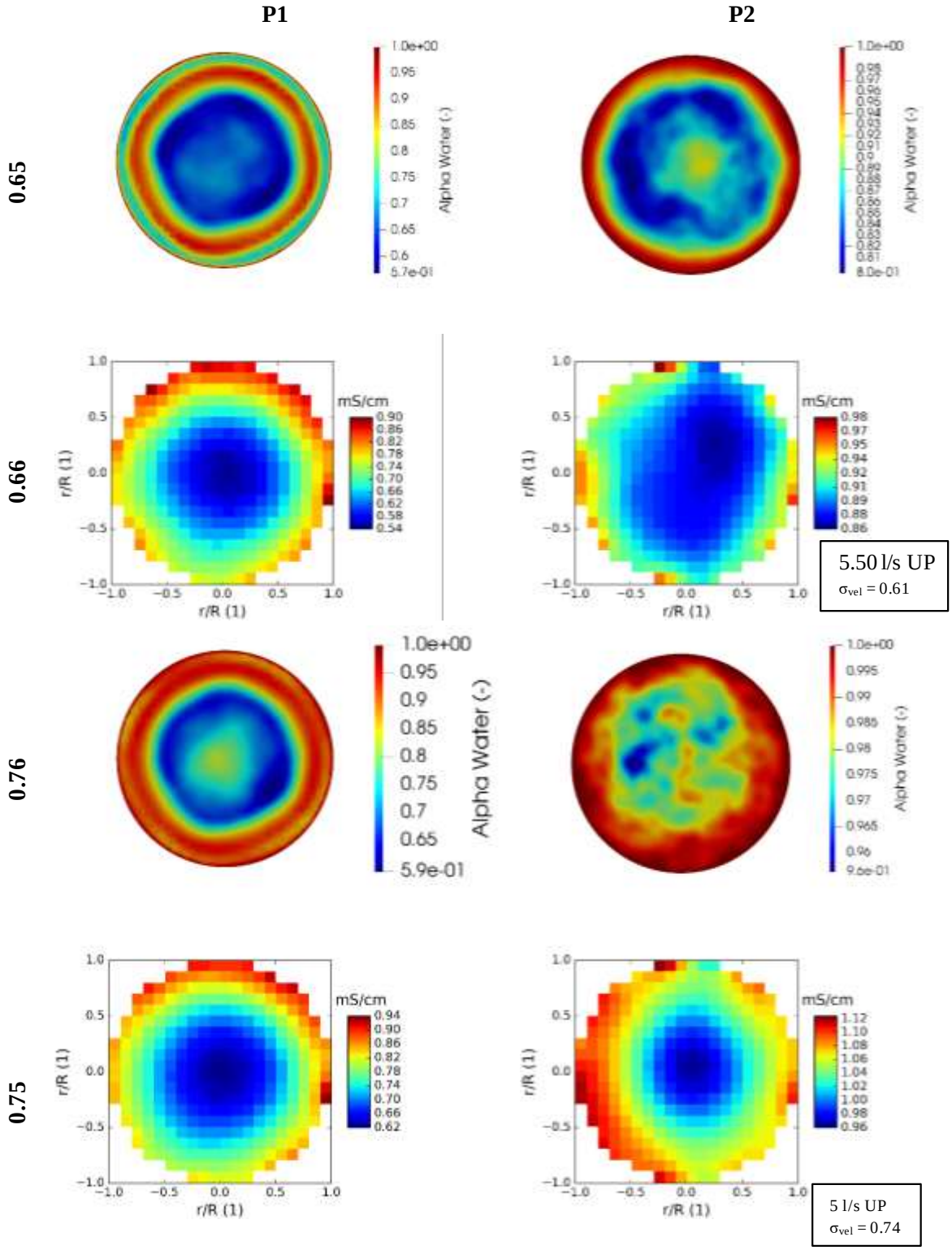

Figure 198 Qualitative comparison of the conductivity maps with the distribution of gaseous phase obtained by the CFD analysis in case of the SG presence – part 2

6.14. Cavitating flow in case of the axial inflow – comparison of the CFD and EIT results

The significant flaw of the EIT equipment resulting from its resolution shall be emphasized once again. As it can be seen in the Figure 199, there is no significant increase of the conductivity close to the walls of the diffuser in case of the EIT analysis. In contrast, the thin but significant layer of the increased water volume fraction close to the walls is clearly visible in case of the CFD results. This is in good agreement with the observed cavitating vortex rings which were surrounded by the liquid water in the region of P1 as it is clearly captured in the HS camera photos depicted in the Figure 176.

The comparison of the results corresponding to the P2 measuring plane is in relatively good qualitative agreement in case of the σ_{vel} of 0.56 where the discrepancy between the flow rate and cavitation number between the EIT and CFD results is not so significant. On the other hand, the results corresponding to the less developed cavitating flow are completely different as it can be seen in the Figure 200.

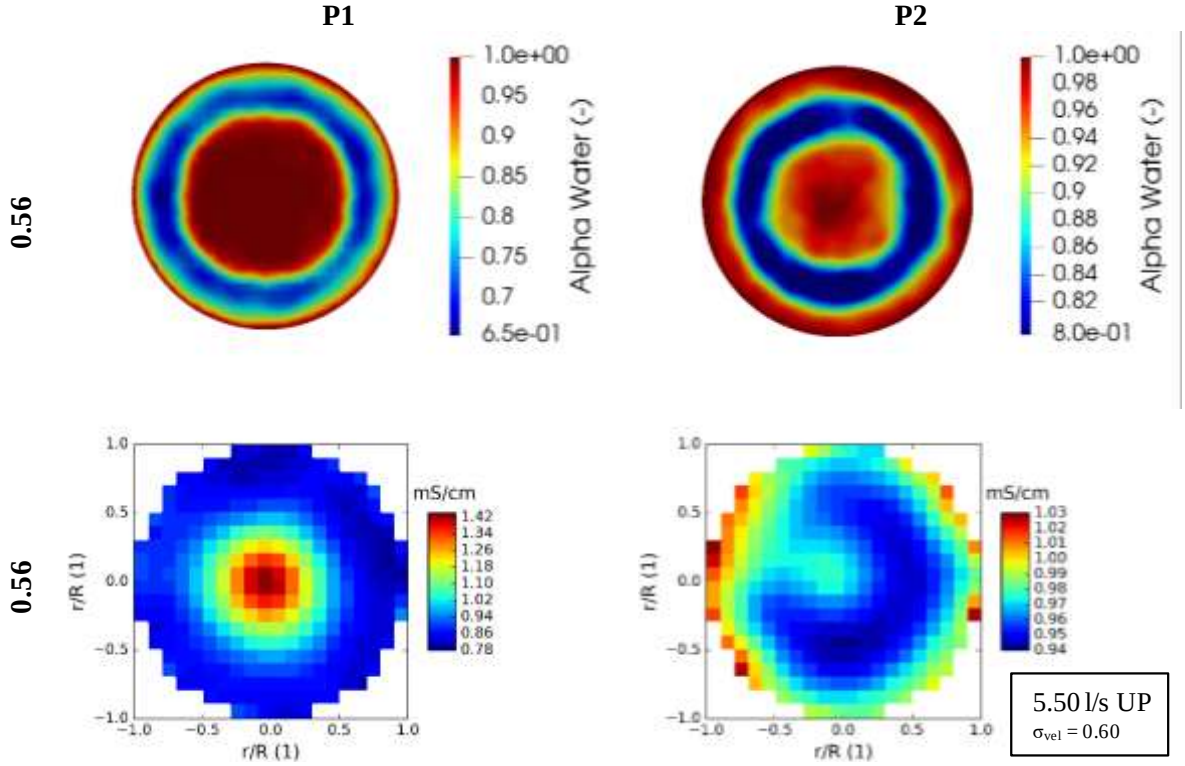

Figure 199 Qualitative comparison of the conductivity maps with the distribution of gaseous phase obtained by the CFD analysis in case of the axial inflow – part 1

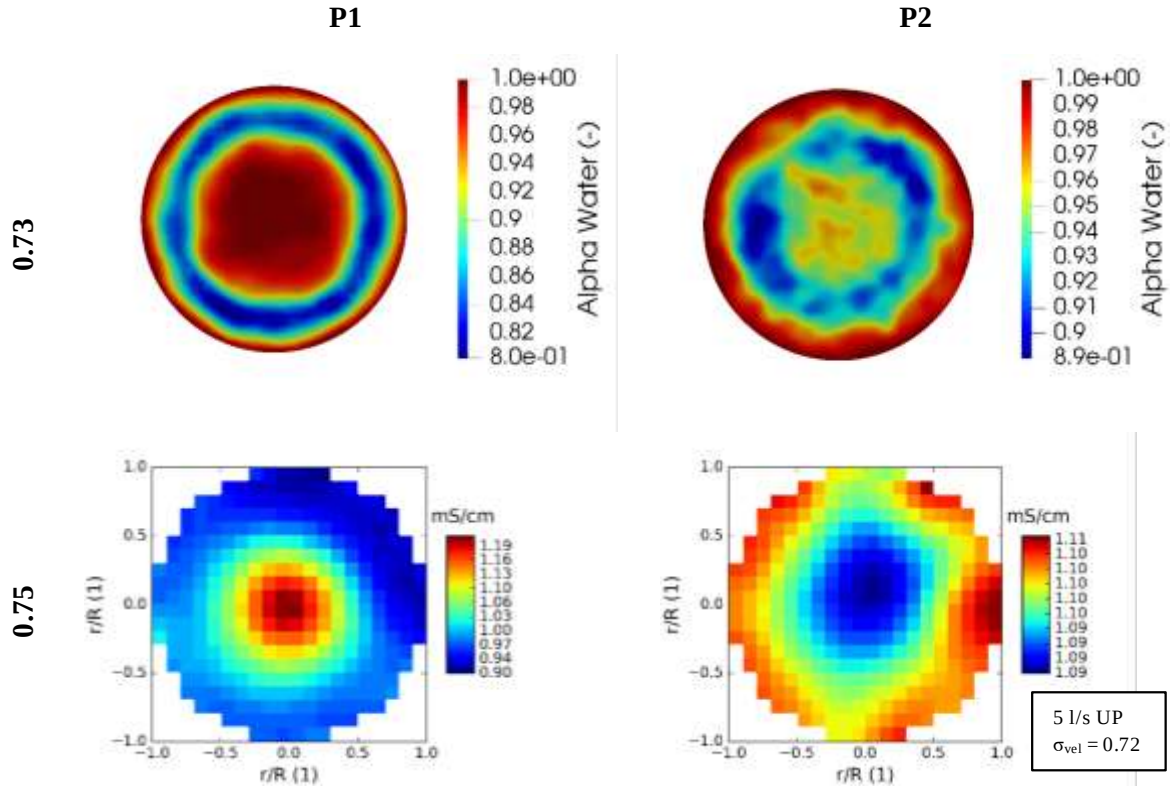

Figure 200 Qualitative comparison of the conductivity maps with the distribution of gaseous phase obtained by the CFD analysis in case of the axial inflow – part 2

6.15. Partial conclusions of the EIT analysis

It is possible to detect the cavitation within the flow as well as to distinguish the general character of the cavitating structures in the liquid flow using the exploited EIT measuring device. This can be done by the analysis of the conductivity distribution over the measuring planes. The main disadvantages of the exploited EIT device are represented by the low sampling frequency and low spatial resolution. Due to the low sampling frequency it was not possible to investigate development of cavitating structures as well as the overall dynamics of the cavitation based on the conductivity variation during the time. Therefore, only the time-averaged maps of conductivity were exploited for the analysis and further comparison of this method with the CFD results. The low spatial resolution can lead to the undetectability of the less spatially significant (but important) flow characteristics. This was shown in case of the axial inflow analysis, where the thin liquid layer surrounding the cavitating vortex rings was not detected in the P1 measuring plane.

Thus, it can be stated that the exploited EIT device is more appropriate for the industrial applications, where the precision on the small spatial and temporal scales does not represent important requirement.

The cavitation hysteresis has been investigated in the first phase of the EIT measurement. The transition from the cavitation-free regime to the fully developed regime of cavitation and vice versa has been investigated in case of the axial inflow as well as in case of the SG presence. Despite the fact that some of the partial results suggested the the hysteresis presence based on the minor differences between the corresponding operating points, it is not enough to confirm the hysteresis based on the computed tomography investigation. The main problem is the low spatial resolution of the EIT device as well as the significant impact of the external influences to the variation of the conductivity values. Mainly the increasing temperature influenced the obtained values of the time-averaged conductivities as it was shown. From this point of view, the results were influenced mainly in case of the SG presence due to the increased hydraulic loss.

The comparison of the EIT results with the numerically obtained phase distribution is highly problematic due to the reasons which were described. Since the change of the measured conductivity is gradual, it is impossible to distinguish the interphase region based on the EIT results. On the other hand, the qualitative agreement of the EIT results with the CFD analysis is good and the general properties of the cavitation distributions were captured using both of these methods in case of the measuring plane P1.

Unfortunately, the malfunction of the measuring plane P2 has occurred during this set of measurements due to the significant vibrations and consequent EIT electrodes leakage.

Conclusions

The main goal of the thesis was to investigate cavitating flow induced by the swirl generator within the Venturi tube and compare its properties with the cavitating flow considering the axial inflow. Various methods including experimental and numerical investigation of the problem (attempt of the EIT application shall be emphasized) were exploited.

The wide range of the experimental data were obtained and some of them were corelated with the unsteady multiphase numerical simulations which were carried out using OpenFoam and its *interPhaseChangeFoam* solver. Using this approach, it was possible to identify typical cavitating structures, their dynamics and other properties based on the different conditions. Thanks to the extent of the investigation, it is possible to use the provided data as a background for further experimental or numerical investigation. Since the results of numerical simulations are in great agreement with the experimental data, it can be also stated that the proposed setting of CFD simulations was successfully validated. Thus, it can be exploited for the further research of cavitation. Prediction of the cavitation dynamics and connected increase of hydraulic loss can be predicted with great degree of confidence. Utilization of the EIT for the experimental analysis of the phase distribution was investigated. Since the spatial and temporal resolution of the exploited equipment (EIT ITS p2+) was low, it was not possible to provide proper validation of CFD results. Nevertheless, it can be stated that, at least from the qualitative point of view, the EIT and CFD results agree relatively well. Detailed description of the obtained results discussed in the thesis is provided in the following text.

The cavitation regimes were divided into 5 regions based on the analysis of the pipe-wall acceleration. Typical flow patterns were described using the HS video records from the initial regime of cavitation to the supercavitation. Similarities and discrepancies resulting from the experimental configuration were described. The interesting flow patterns were observed in case of the initial regime of cavitation and utilization of the swirl generator. The thin cavitating vortex was getting longer with the decreasing value of the cavitation number. It was possible to observe helical vortex breakdown at the tip of the vortex filament. With the further decreasing value of the cavitation number, the vortex filament transformed into axisymmetric vortex similar to the full load vortex typical for the Francis turbines operated under the specific of-design conditions. This type of the cavitating flow transfomed into the form of conical cavitating vortex as it was captured using the high-speed video as well as using the numerical analysis.

In general, it was stated that the cavitating structures are considerably more compact in case of the SG presence, where no significant separation was observed in the whole range of investigated operating regimes.

On the other hand, the separation of the cavitating structures which are entrained by the flow until the collapse in the region of higher pressure was described in case of the axial inflow. These collapses played a crucial role during the cavitation cycle.

The onset of the stagnant (backflow) region within the conical cavitating vortex was observed with the decreasing cavitation number in case of the SG presence. The gradual growth of this region upstream the vortex end significantly affects the instability of this cavitating structure. The vortex partially collapsed when the backflow region reached the throat of the nozzle. The partial collapse accompanied by the observable helical vortex breakdown was rapid and followed by very fast re-creation of the cavitating vortex.

The typical cavitating vortex rings were observed in case of the axial inflow. Size of these rings was the larger, the lower was cavitation number up to the certain moment when the form of the ring transformed to the massive cavitating clouds.

Supercavitation regime represents interesting type of the cavitation. Induced noise, vibrations and pressure pulsations are minimal compared to the fully developed or initial stages of cavitation. This observation is valid regardless investigated configurations. However, this is the first and the last similarity which can be stated. The presence of the induced swirl completely changes the flow field within the nozzle. Thus, the observed flow structures and redistribution of the phases were completely

different. The liquid jet close to the axis was observed in case of the axial inflow. The jet was surrounded by the vapour, while in case of the introduction of the additional swirl by the generator, the stable conical vortex occurred within the nozzle. This vortex was separated from the walls of the nozzle by the thin layer of the liquid water.

The overall nature of the cavitating flow has been described using the analysis of the HS records where maps of the time averaged values of the pixel intensities and values of the corresponding standard deviations (RMS images) were processed in form of 2D maps describing the whole range of the investigated operating regimes of individual flowrates. These charts were exploited to support the abovementioned observations.

The last part of the HS video analysis was devoted to the investigation of the cavitation dynamics. For this purpose, the in-house codes were created using the Python programming language. The first method utilized the spectral analysis of the pixel intensity fluctuations, where the source pixel was chosen automatically from the preselected region of interest. The second approach was based on the proper orthogonal decomposition (POD) of the captured records. The overall results obtained using both methods were in good agreement. However, each approach has some specific advantages and disadvantages. Spectral analysis of the pixel intensity fluctuations is faster and relatively robust considering the semi-automated choice of the source pixel. On the other hand, the POD provides deeper insight into the investigated phenomenon since the captured record is decomposed into finite number of modes which can be investigated separately. Moreover, the POD seems to be even more robust, which is convenient in case of the processing of large number of the video records. Despite these differences, the overall results were in good agreement. It was stated that the frequencies of the cavitating structures pulsations were decreasing with decreasing value of cavitation number. It was also stated that the frequencies are related to the investigated flow rate, whereas value of the frequency was proportional to the value of the investigated flow rate considering the constant value of the cavitation number. The induced swirl also increased the frequency of the pulsations. However, the actual pulsations were not as severe as in case of the axial inflow. This is in agreement with the experimental measurement. It should be also noted that the results of the HS video analysis were correlated with the spectral analysis of pressure fluctuations as well as with the spectral analysis of the pipe-wall acceleration. It was stated that the results were in good agreement with the pressure pulsations analysis. In case of the pipe-wall acceleration the partial agreement was also found. The pulsations corresponding to the pipe-wall acceleration analysis were noisy and dominant frequencies of this particular analysis differed from the analysis of the pressure pulsations. Nevertheless, it was possible to identify the desired frequencies within the pipe-wall acceleration spectra as locally significant peaks. Thus, it was concluded that the results of the HS video analysis can be trusted.

The cavitating flow properties were investigated experimentally using the analysis of pipe-wall acceleration, acoustic pressure, acoustic emission and pressure records. These quantities were significantly affected by the cavitation. Thus, it was possible to identify properties specific for the individual cavitation regimes as well as to correlate results corresponding to flow affected by the induced swirl with the axial inflow. First part of the chapter was devoted to the description of the time-averaged values of fluctuations magnitude using which was carried out using the analyses of the pipe-wall acceleration, acoustic pressure and pressure records. As it was said, the course of the mean values of the magnitude of pipe-wall acceleration fluctuations a was utilized for the description of the five different regions of cavitating flow. The actual values were proportional to the investigated flow rate while the vibrations induced by cavitating flow were more severe in case of the axial inflow in most of cavitation regimes. The first exception was supercavitation, where the vibrations where higher in case of the SG presence. This is possibly caused due to the different redistribution of the phases over the cross section of the nozzle based on the experimental configuration. The second exception is the initial regime of cavitation where the vibrations were more significant in case of the cavitating vortex presence.

Specific drop of the values corresponding to the different cavitating structures in the region of initial cavitation was described using the analysis of 4 l/s flowrate considering presence of the SG.

It can be stated that the vibrations of the test rig induced by the cavitation became more severe with the decreasing value of cavitation number, up to the certain moment when amount of the gaseous phase within the flow became sufficient to dampen these vibrations. This moment defined the transition between the 2nd and 3rd region of cavitating flow. While both regions are typical by the periodical pulsations of the cavitating structures, the observed amount of cavitation is significantly lower in case of the less developed regime. The observed values of the time averaged fluctuations of pipe-wall acceleration dropped rapidly with the further decreasing cavitation number until the transition to the supercavitation and supercavitation itself.

The analysis of the acoustic pressure captured using the microphone was carried out in the same manner. Fluctuations of the noise were more severe in case of the axial inflow. Nevertheless, the values corresponding to the swirl generator presence were higher in case of the initial regime of cavitation similarly to the pipe-wall acceleration analysis.

Provide analysis of the pressure was slightly more complex. Beside the courses of time-averaged values of pressure fluctuations obtained using the Kistler pressure transducer, the time-averaged values of pressure captured using the BD transducers p1, p2 and p3 were described to discuss utilization of the p3 pressure transducer for the evaluation of the cavitation number and hydraulic loss coefficient. Regarding to the analysis of the pressure fluctuations, it can be stated that the presence of the cavitation leads to the significant increase of these values. Time-averaged values of the pressure fluctuations magnitude were higher in case of the axial inflow with exception of the initial cavitation similarly to the acoustic pressure and pipe-wall acceleration analysis. On the other hand, the values corresponding to the supercavitation were more or less same regardless the experimental configuration.

Dynamics of the pipe-wall acceleration, acoustic emission, acoustic pressure and static pressure affected by the cavitating flow were investigated using the analysis of the signal variance. In general, it can be stated that the fluctuations are more severe in case of the axial inflow, which is consequent to the nature of the cavitating flow patterns and typical courses of the cavitation cycles.

The investigation of the acoustic emission and pressure fluctuations were complemented by the spectral analyses of the captured signals.

The main purpose of the *AE* analysis was to describe the higher frequencies in order of thousands of hertz and more. The results were affected by the oversaturation of the AE transducer in case of the highest flowrates, especially in case of the axial inflow. Thus, 5 l/s flow rate was considered for the purpose of the discussion of the results. Since the results which are discussed are under the lower threshold of the recommended operational range of the transducer, the frequency response of this probe was provided. The cavitation inception was nicely captured using the acoustic emission probe in case of the SG presence. As it has been shown the cavitation regime significantly influenced the obtained frequency spectra. Nevertheless, with the occurrence of the cavitation it was possible to observe significant amount of the signal noise between the 5 kHz and 30 kHz frequencies. Beside that significant peaks between the 35 – 36 kHz occurred. Nevertheless, it was stated that these frequencies are not induced by the by the cavitation but correspond to the resonance frequency of the utilized transducer. It was shown that the maximum amplitudes are higher in case of the axial inflow, with exception of the less developed regimes of cavitation. This is in good agreement with the previous observations. The influence of the flow rate value was also discussed, and it was stated that the increase of the investigated discharge leads to the increase of the *AE* fluctuations.

Interesting observation was done in case of the pressure fluctuations variance. While the increase of the pressure variance with the decreasing value of the cavitation number was more or less gradual in case of the axial inflow, significant peaks of this value were found close to the transition from the initial stage of the cavitation to the fully developed regime and in case of the beginning of the transition to the supercavitation when the flow was affected by the introduced swirl.

The results of the whole range of the investigated flow rates were provided in this chapter. It was stated that the frequencies of the cavitation volume fluctuations were higher in case of the swirl generator presence, which is in good agreement with the previous results. The influence of the cavitation number was discussed using the different definitions of the cavitation number. It was stated, that the definition

σ_{vel} neglects significant radial and tangential component of the velocity in case of the SG presence, which was shown using the comparison of the dimensionless Strouhal numbers provided as a function of σ_{vel} utilizing the bulk velocity within the throat of the nozzle and σ_{pres} which was based on the pressure drop across Venturi nozzle. It was shown that the values of the Strouhal number corresponding to the similar cavitation numbers are higher in case of the SG presence, regardless the exploited definition of the cavitation number. Nevertheless, this difference was considerably more pronounced in case of the σ_{pres} utilization. It was shown that the decrease of the identified frequencies was gradual (with decreasing value of σ_{pres}), whereas it became considerably faster in case of the large cavitating structures presence.

The experimental investigation was complemented by the numerical analysis considering 6 l/s flow rate which was carried out using the OpenFoam v1606+ and its *interPhaseChangeFoam* solver. The numerical settings which were exploited during the investigation were based on the previous experience with the analysis of the cavitating flow within Venturi tube. The main purpose of the investigation was to verify capabilities of the chosen solver and setting from the cavitation dynamics and hydraulic loss points of view. In the first step, the full geometry including the swirl generator was utilized. The analysis was carried out using the different densities of the computational grid. It was stated that the results provided by the finer mesh are in better qualitative agreement with the observed cavitating structures. Above that, the prediction of the hydraulic loss coefficient was more precise in case of the finer grid. Thus, the further analysis was carried out using the finer computational grid. The influence of the cavitation number definition was discussed using the kinetic energy correction factor α_{corr} calculated close to the leading edge of the throat of the nozzle in case of the SG presence. The mean value of α_{corr} calculated using three different operating points was utilized for the correction of the experimental result considering same nominal discharge. It was shown that the corrected experimental results are in surprisingly good agreement with numerical data considering the velocity magnitudes for the calculation of σ_{vel} and ξ. It should be stated that the values of the hydraulic losses are slightly underpredicted in case of the SG presence which contrasts with the analysis of the axial inflow which provided slightly overpredicted results. Nevertheless, it can be stated that the predicted tendency and growth rate of the hydraulic losses with the gradual development of the cavitation were well-predicted regardless the experimental configuration.

The main disadvantage of the simulations considering the whole geometry including the SG was unbearable computational time. Thus, it was practically impossible to use this approach for the proper investigation of the cavitation dynamics considering wider range of operating points.

Therefore, the computational domain has been sliced downstream the spike of the swirl generator and pre-calculated profiles of the velocity components and turbulent quantities were used as a boundary conditions to mimic the upstream mounted swirl generator. This approach leads to 6.5 times faster computational times of the investigated cases. The cavitation cycles were shown and influence of the specific flow patterns on the cavitation dynamics was described. The same results were provided in case of the axial inflow, where the whole length of the test section was utilized. Different redistribution of the gaseous phase based on the experimental configuration was discussed.

The spectral analysis of the pressure signals was carried out in order to identify numerically predicted frequencies of pulsations of the cavitating structures. These results were correlated with the experimental results obtained using the POD analysis and analysis of the pressure fluctuations. It was stated that the numerically predicted frequencies agreed well with the experimental data regardless the experimental configuration.

Last part of the thesis is devoted to the experimental focused on the investigation of the cavitating flow using the computed tomography. The experimental investigation was carried out in the hydraulic laboratory of Technical University in Liberec using their EIT ITS p2+ electrical impedance tomography device. The tomography measurement was carried out in two cross-sections downstream the throat of the nozzle. The measurement was focused on the initial and fully developed stage of cavitation due to the characteristic of the test bench and utilized pump. The hydraulic losses during the transition between these regimes were discussed before the discussion of the EIT results.

The EIT investigation was divided into the two parts. First part was devoted to the investigation of the cavitation hysteresis during the transition of the cavitation regime and comparison of the obtained conductivity profiles based on the experimental configuration. Unfortunately, the time and spatial resolution of the exploited device was low. Thus, the time averaged profiles were created and used for discussion. From the qualitative point of view, it was possible to identify the redistribution of the gaseous phase over the measuring planes. Nevertheless, due to the low spatial resolution it was not possible to capture details of the observed flow patterns such as thin liquid layer close to the throat of the nozzle in case of the axial inflow. Therefore, it can be stated that the exploited EIT device is appropriate in a case where is no possibility of visual inspection of the cavitating flow to identify general properties of the cavitating structures, but the advantage of the application of this measurement in case of the transparent test section was minor.

The potential hysteresis of the cavitating structures was investigated during the transition from the cavitation-free regime and vice versa. This investigation complements the previously published results of the hysteresis analysis in case of the axial inflow and transition between the fully developed cavitation and supercavitation. Some of the identified differences based on the flow rate change direction suggest that small discrepancy between the corresponding operating points exist. Nevertheless, the actual presence of hysteresis cannot be confirmed based on the obtained results due to the above-mentioned shortcomings of the experimental device and since it was not possible to fully take into account the influence of the water temperature increase during the measurement.

The results of the EIT measurement considering 6 l/s flow rate were compared with the results of the CFD analysis for the selected operating points in the last part of the investigation. It should be noted that the malfunction of the P2 measuring plane occurred during the measurement. Thus, it was not possible to use these results and the results corresponding to the different flow rates with similar cavitation number were utilized for the discussion. In general, it can be stated that the distribution of the gaseous phase over the cross-section predicted by the CFD were in good agreement with the nature of the conductivity maps. On the other hand, it was not possible to capture some of the typical flow properties using the EIT due to its low spatial resolution as it was mentioned.

Literature

[1] FRANC J.P., MICHEL J.M., *Fundamentals of cavitation. Boston: Kluwer Academic Publishers*, xxii, 300 p., 2004, ISBN 14-020-2232-8.

[2] NOSKIEVIČ J., *Kavitace v hydraulických strojích a zařízeních*. 1st edition. SNTL Praha,. 336 s, 1989, ISBN 80-03-00206-0.

[3] RAYLEIGH L., *On the pressure developed in a liquid during the collapse of a spherical cavity*. Phil. Mag. 34. 94-98. 1919.

[4] PLESSET M.W., *The dynamics of cavitation bubble*. ASME J. Appl. Mech. 16: 228–231 19, 1949.

[5] BRENNEN Ch. E., *Cavitation and bubble dynamics*. 1st ed. New York: Oxford University Press, 613 s. 1995, ISBN 01-950-9409-3.

[6] DAVIDSON L., *Fluid mechanics, turbulent flow and turbulence modeling*, Chalmers University of Technology , 2015.

[7] ANSYS, Inc.: Fluent 12.0 Theory guide, 2009.

[8] RUDOLF P., HUDEC M., GRÍGER M., ŠTEFAN D., *Characterization of the cavitating flow in converging-diverging nozzle based on experimental investigations*, EPJ Web of Conferences 67 02101, 2014.

[9] SINGHAL A. K., LI H. Y., ATHAVALE M. M., JIANG Y., *Mathematical Basis and Validation of the Full Cavitation Model*. ASME FEDSM'01, New Orleans, Louisiana, 2001, DOI: 10.1115/1.1486223.

[10] ALEKSEENKO S.V.; KUIBIN, P.A.; OKULOV, V.L.: *Theory of Concentrated Vortices. First Edition*. Berlin: Springer, 487s, 2007, ISBN 978-3-540-73375-1.

[11] ŠTIGLER J., *Models of the vortex in real fluid*. Sborník konference ENGINEERING MECHANICS 2000, 1. vyd. Praha: Institute of theoretical and applied mechanics academy of sciences of the Czech Republic,. pp.156-160, 2000, ISBN 80-86246-07-8.

[12] ŠVAŇHAL R., *Vírové struktury s kavitujícím jádrem.* Brno: Vysoké učení technické v Brně, Master's thesis, 2010.

[13] STUPARU A., RESIGA R.S., ANTON L.E., MUNTEAN S., *New Approach in Numerical Assessment of the Cavitation Behaviour of Centrifugal Pumps*, International Journal of Fluid Machinery and Systems, 10.5293/IJFMS.2011.4.1.104 Vol. 4, No. 1, 2011, DOI: 10.5293/IJFMS.2011.4.1.104.

[14] ZWART P.J., GERBER A.G., BELAMRI T., *A Two-Phase Flow Model for Predicting Cavitation Dynamics*, 5th International Conference on Multiphase Flow, Yokohama, Japan, 2004

[15] SCHNERR G.H., Sauer J., *Physical and Numerical Modeling of Unsteady Cavitation Dynamics*. 4th International Conference on Multiphase Flow, NewOrleans, USA, 2001.

[16] KUNZ R.F., BOGER, D. A., STINEBRING D. R., CHYCZEWSKI, THOMAS S., GIBELING, HOWARD J., VENKATESWARAN S., GOVINDAN T.R., *A Predictioned Navier-Stokes Method for Two-Phase Flows with Application to Cavitation Prediction*. American Institute of Aeronautics and Astronautics. 1999.

[17] MERKLE C. L., FENG J., BUELOW P. E. O., *Computational modeling of the dynamics of sheet cavitation* ,in Proceedings Third International Symposium on Cavitation Grenoble, France 1998.

[18] Knapp R. T., Daily J. W., Hammit F.G., *Cavitation*, McGraw-Hill, 1970, ISBN 0070350809.

[19] KUNDU P.K., COHEN I. M., *Fluid Mechanics*. Fourth Edition. San Diego: Academic Press, 872s, 2008, ISBN 978-0-12-373735-9.

[20] RUDOLF P., HUDEC M., ZUBÍK P, ŠTEFAN D., *Experimental measurement and numerical modeling of cavitating flow in converging-diverging nozzle*, EPJ Web of Conferences 25 01081, 2012, DOI: 10.1051/epjconf/20122501081.

[21] DAVIDSON L., *Large Eddy Simulation*. MTF270 Turbulence Modelling. 2006

[22] SMAGORINSKY J., *General Circulation Experiments with the Primitive Equations. I. The Basic Experiment*. Month. Wea. Rev. 91. 99–164. 1963.

[23] GERMANO M., PIOMELLI U., MOIN P., CABOT W. H., *Dynamic Subgrid-Scale Eddy Viscosity Model*. In Summer Workshop. Center for Turbulence Research, Stanford, CA. 1996.

[24] NICOUD F., DUCROS F., *Subgrid-Scale Stress Modelling Based on the Square of the Velocity Gradient Tensor.Flow*. Turbulence, and Combustion. 62(3). 183–200. 1999.

[25] SHUR M. L., SPALART P. R., STRELETS M. K., TRAVIN A. K., *A Hybrid RANS-LES Approach With Delayed DES and Wall-Modelled LES Capabilities*. International Journal of Heat and Fluid Flow, 29:6, 1638-1649, 2008, doi.org/10.1016/j.ijheatfluidflow.2008.07.001.

[26] KOOP A. H., *Numerical simulation of unsteady three-dimensional sheet cavitation*, 2008, ISBN 978-90-365-2701-9.

[27] SEDLÁŘ, M, KOMÁREK M., RUDOLF P., KOZÁK J., HUZLÍK R., *Numerical and experimental research on unsteady cavitating flow around NACA 2412 hydrofoil*. IOP Conference Series: Materials Science and Engineering, vol. 72, issue 2, 2015, DOI: 10.1088/1757-899X/72/2/022014.

[28] RADON J., *Uber die Bestimmung von Funktionen durch ihre Integralwerte langs bestimmter Mannigfaltigkeit* Ber. Ver. Sachs. Akad. Wiss. Leipzig, 1917.

[29] HENDEE W.R., E RITENOUR E., *Medical imaging physics*, 4th ed. New York: Wiley-Liss, 2002, ISBN 04-713-8226-4.

[30] BAUER D., CHAVES H, ARCOUMANIS C., *Measurements of void fraction distribution in cavitating pipe flow using x-ray CT*, Measurement Science and Technology, vol. 23, issue 5, pp. 055302, 2012.

[31] KALENDER W.A., *Computertomographie-Grundlagen,Geratetechnik, Bildqualit at, Anwendungen*. Publics Publishing, 2000, ISBN 3895782157.

[32] HENDEE W., *Physical principles of computed tomography*, 1st ed. Boston: Little, Brown, 1983, ISBN 9780316355940.

[33] BRETT G., RIVELAND M., JENSEN C.T., HEINDEL J.T., *Cavitation From a Butterfly Valve: Comparing of 3D Simulations to 3D X-Ray Computed Tomography Flow visualization*, Joint Fluids Engineering Conference, 2011.

[34] GEORGE D.L., TORCZYNSKI J.R., SHOLLENBERGER K.A., O'HERN T.J., CECCIO S.L., *Validation of electrical-impedance tomography for measurements of material distribution in two-phase flows*, International Journal of Multiphase Flow 26, 2000, doi.org/10.1016/S0301-9322(99)00029-4.

[35] SUSAN-RESIGA R., MUNTEAN S., HASMATUCHI H., ANTON I., AVELLAN F., *Analysis and Prevention of Vortex Breakdown in the Simplified Discharge Cone of a Francis Turbine*. Journal of Fluids Engineering, Vol. 132, 2010, DOI: 10.1115/1.4001486.

[36] DÖRFLER P., SICK M., COUTU A., *Flow-induced pulsation and vibration in hydroelectric machinery: engineer's guidebook for planning, design and troubleshooting*. London: Springer, 2013, ISBN 978-1-4471-4251-5.

[37] LUCCA-NEGRO O., O'DOHERTY, T., *Vortex breakdown: a review*, Annual Review of Fluid Mechanics, 10, 221-246, 1978.

[38] AVELLAN F., *Flow investigation in a Francis draft tube: the FLINDT project*, 20th IAHR Symposium on Hydraulic Machinery and Systems, IAHR, Charlotte (NC), U.S.A., 2000.

[39] CHIRAG T., CERVANTES M.J., GANDHI B.K. AND DAHLHAUG O.G., *Experimental and numerical studies for a high head Francis turbine at several operating points*. Journal of Fluid Engineering, November 2013, Vol. 135.

[40] KIRSCHNER O., RUPRECHT A., SUSAN-RESIGA, R.F., MUNTEAN S., *Swirling Flow in a Straight Cone Draft Tube: Axi-Symmetric FFlow Analysis and Comparison with Circumferentially Averaged PIV Measurments*. 2nd IAHR International Meeting of the Workgroup on Cavitation and Dynamic Problems in Hydraulic Machinery and Systems, 2007. pp. 185-196.

[41] JOŠT D., LIPEJ A., *Numerical Prediction of the Vortex Rope in the Draft Tube*. 3rd IAHR International Meeting of the Workgroup on Cavitation and Dynamic Problem in Hydraulic Machinery and systems, 2009. pp. 75-85.

[42] FLEMMINGF., FOUST J., KOUTNIK J., FISHER R.K., *Overload Surge Investigation Using CFD Data*. International Journal of Fluid Machinery and Systems, vol. 2, issue 4, 2009, DOI: 10.5293/IJFMS.2009.2.4.315.

[43] DÖRFLER P. K., KELLER M., BRAUN O., *Francis full-load surge mechanism identified by unsteady 2-phase CFD*. IOP Conference Series: Earth and Environmental Science, vol. 12, 2010, DOI: 10.1088/1755-1315/12/1/012026.

[44] ŠTEFAN D., RUDOLF P., *Computational Fluid Dynamic Study of the Flow Downstream of the Swirl Generator Using Large Eddy Simulation*, technical report.

[45] ŠTEFAN D., RUDOLF P., HUDEC M., HABÁN V., *Comprehensive study of unsteady pressure pulsations induced by the spiral vortex structure in a conical diffuser*. 6th IAHR International Meeting of the Workgroup on Cavitation and Dynamic Problems in Hydraulic Machinery and Systems, At Ljubljana, Slovenia, 2015.

[46] GRÍGER M., *Hydraulické charakteristiky proudění v kavitačních tryskách*, master's thesis VUT, 2013.

[47] RUDOLF P., HUDEC M., ZUBÍK P., Štefan D., *Experimental measurement and numerical modeling of cavitating flow in converging-diverging nozzle*. EPJ Web of Conferences 25, 2012, DOI: 10.1051/epjconf/20122501081.

[48] ŠTEFAN D., RUDOLF P., SEBASTIAN M., RESIGA R., *Structure of Flow Fields*, Engineering mechanics, Vol. 20 No.5, 2013.

[49] KALAMUCK K.M., CHAHINE G.L., HASIO C-T, CHOI J-K. *Remediation and disinfection of water using jet generated cavitation*, 5th international Symposium on Cavitation, Japan, 2003.

[50] JANČURA D., MIKULA P., MARŠÁLEK B., RUDOLF P., POCHÝLY F., *Selective method for cyanobacterial bloom removal: hydraulic jet cavitation experience*, Aquaculture International 22(2), 2014, DOI 10.1007/s10499-013-9660-7.

[51] KOZÁK J., RUDOLF P., ŠTEFAN D., HUDEC M., GRÍGER M., *Analysis Of Pressure Pulsations Of Cavitating Flow In Converging-Diverging Nozzle*. 6th IAHR International Meeting

of the Workgroup on Cavitation and Dynamic Problems in Hydraulic Machinery and Systems, Slovenia, 2015.

[52] MADISETTI V., *Digital signal processing fundamentals*, 2nd ed. Boca Raton, FL: CRC Press, 2010, ISBN 978-142-0046-069.

[53] KOZÁK J., RUDOLF P., SEDLÁŘ M., HABÁN V., HUDEC M., HUZLÍK R., *Numerical simulation and experimental visualization of the separated cavitating boundary layer over NACA2412*. *EPJ Web of Conferences*, 2015, DOI: 10.1051/epjconf/20159202037.

[54] KOZÁK J., RUDOLF P., HUDEC M., URBAN O., ŠTEFAN D., HUZLÍK R., ČALA M., *Investigation Of The Cavitation Within Ventruri Tube: Influence Of The Generated Vortex*, In *Advances in Hydroinformatics*. Singapore: Springer Singapore, p. 1049-1067, 2018, ISBN: 978-981-10-7217-8.

[55] ZAREMBA M., KOZÁK J., MALÝ M., WEISS L., RUDOLF P., JEDELSKÝ J., JÍCHA M., *An Experimental Analysis of the Spraying Processes in Improved Design of Effervescent Atomizer*, International Journal of Multiphase Flow, vol. 1, no. 103, p. 1-15, 2018, ISSN: 0301-9322.

[56] BALASUNDARAM B., HARRISON S.T.L., *Disruption of Brewers- Yeast by Hydrodynamic Cavitation: Process Variables and Their Influence on Selective Release*, Department of Chemical Engineering, University of Cape Town, 2006, DOI: 10.1002/bit.20878.

[57] KOZÁK J., RUDOLF P., HUZLÍK R., HUDEC M., CHOVANEC R., MARŠÁLEK B., MARŠÁLKOVÁ E., URBAN O., *Transition of cavitating flow to supercavitation within Venturi nozzle – hysteresis investigation*. In *EPJ web of conferences. EPJ Web of Conferences*. p. 1-11, 2017, ISSN: 2100-014X.

[58] KOZÁK J., RUDOLF P., HUDEC M., ŠTEFAN D., FORMAN M., *Numerical and Experimental Investigation of the Cavitating Flow Within Venturi Tube*, Journal Of Fluids Engineering-Transactions Of The Asme, vol. 141, no. 4, p. 1-11, 2018, ISSN: 0098-2202.

[59] SIROVICH L., *Turbulence and The Dynamics of Coherent*, Structures Quarterly Of Applied Mathematics Volume Xlv, Number 3 October 1987, Pages 561-571.

[60] LUMLEY J. L., *Coherent structures in turbulence*. Transition and Turbulence, pp. 215–241. Academic, 1981.

[61] BERKOOZ G., HOLMES P., LUMLEY J., *The proper orthogonal decomposition in the analysis of turbulent flows*, Annual Rev. of Fluid Mechanics vol. 25(1), Pages: 539-575, 1993.

[62] ŠTEFAN D., RUDOLF P., *Proper Orthogonal Decomposition of Pressure Fields in a Draft Tube Cone of the Francis (Tokke) Turbine Model*, Journal of Physics: Conference Series, vol. 579, 2015, DOI:10.1088/1742-6596/579/1/012002.

[63] RUDOLF P., ŠTEFAN D., SEDLÁŘ M., KOZÁK J., HABÁN V., HUZLÍK R., *Spatio-temporal description of the cavitating flow behavior around NACA 2412 hydrofoil*, Journal of Physics: Conference Series, vol. 656, 2015, DOI: 10.1088/1742-6596/656/1/012168.

[64] TOMOV P., DANLOS A., KHELLADI S., RAVELET F., SARRAF C., BAKIR F., *POD study of aerated cavitation in a venturi nozzle*, Journal of Physics: Conference Series, vol. 656, 2015, DOI: 10.1088/1742-6596/656/1/012171.

[65] DANLOS A., RAVELET F., COUTIER-DELGOSHA O., BAKIR F., SARRAF C., BAKIR F., *Cavitation regime detection through Proper Orthogonal Decomposition:Dynamics analysis of the sheet cavity on a groovedconvergent–divergent nozzle*, International Journal of Heat and Fluid Flow, vol. 47, 2014, DOI :10.1016/j.ijheatfluidflow.2014.02.001.

[66] ŠTEFAN D., RUDOLF P., MUNTEAN S., RESIGA S.R., 2017, *Proper Orthogonal Decomposition Of Self-Induced Instabilities In Decelerated Swirling Flows And Their Mitigation Through Axial Water Injection*, Journal Of Fluids Engineering 139 (8): 081101., 2017, DOI:10.1115/1.4036244

[67] Saad J., Hogendoorn W., Poelma Ch., *Dynamics Of Partial Cavitation In An Axisymmetric Converging-Diverging Nozzle*. International Journal Of Multiphase Flow 106: 34-45. 2018, doi:10.1016/j.ijmultiphaseflow.2018.04.019.

Nomenclature

ACRONYM	UNIT	DESCTIPTION
p	Pa	Static pressure
T	K	Temperature
r	m	Radial coordination
σ	$N \cdot m^{-1}$	Surface tension
t	s	Time
v	$m \cdot s^{-1}$	Velocity
x,y,z	m	Coordinates
ρ	$kg \cdot s^{-3}$	Density
Ω	s^{-1}	Vorticity
Γ	$m^2 \cdot s^{-1}$	Circulation of the velocity
R	m	Radius
ν_t	$m^2 \cdot s^{-1}$	Eddy viscosity
k	$m^2 \cdot s^{-2}$	Turbulent Kinetic energy
ε	$m^2 \cdot s^{-3}$	Turbulent dissipation rate
V	m^{-3}	Volume
α	1	Volume fraction
nB	1	Number of bubbles
f	s^{-1}, Hz	Frequency
HU	1	Hundsen number
Sn	1	Swirl number
Q	$m^3 \cdot s^{-1}$, l/s	Discharge
Q_{11}	$m^3 \cdot s^{-1}$	Specific discharge
a	$m \cdot s^{-2}$	Acceleration, Mean values of the magnitude of the pipe wall acceleration fluctuation
ξ	1	Hydraulic loss coefficient
Lp	dB	Sound level

INDEX	Meaning
vap	Saturated vapor
l	Liquid
B	Bubbe
gas	Gas
sur	Surrounding
amb	ambient
sur	surrounding
0	Initial
i	Reference
tan	tangential
ax	axial
c	core, condensation
r	radius
e	evaporation
samp	sampling
ax	axial
tan	tangential
vel	velocity
pres	pressure
th	throat

ABBREVIATION	DESCTIPTION
CFD	Computational Fluid Dynamics
FFT	Fast Fourier Transform
ACC	Accelerometer
AE	Accoustic emission
DFT	Discrete Fourier transform
fps	frames per second
FSI	Fluid Structure Interaction
HS	High-speed
LDV	Laser Doppler Velocimetry
LED	Light-emmiting diode
LES	Large Eddy Simulation
Mic	Microphone
P1	Measurting plane 1, closer to throat of the nozzle (EIT measurement)
P2	Measurting plane 2, (EIT measurement)
PIV	Particle Image Velicimetry
POD	Proper Orthogonal decomposition
px	pixel
RMS	Value of the standard deviation of the pixel intensity fluctuations
ROI	Region of Interest
RSM	Reynolds Stress Model
SAS-SST	Scale-Adaptive Simulation - Shear Stress Transport
SG	Swirl Generator

List of publications

2018

KOZÁK J., RUDOLF P., HUDEC M., ŠTEFAN D., FORMAN M., *Numerical and Experimental Investigation of the Cavitating Flow Within Venturi Tube*, Journal Of Fluids Engineering-Transactions Of The Asme, vol. 141, no. 4, p. 1-11, 2018, ISSN: 0098-2202.

KOZÁK J., RUDOLF P., HUDEC M., URBAN O., ŠTEFAN D., HUZLÍK R., ČALA M., *Investigation Of The Cavitation Within Ventruri Tube: Influence Of The Generated Vortex*, In *Advances in Hydroinformatics*. Singapore: Springer Singapore, p. 1049-1067, 2018, ISBN: 978-981-10-7217-8.

ZAREMBA, M., KOZÁK, J., MALÝ, M., WEISS, L., RUDOLF, P., JEDELSKÝ, J., JÍCHA, M. *An Experimental Analysis of the Spraying Processes in Improved Design of Effervescent Atomizer*. INTERNATIONAL JOURNAL OF MULTIPHASE FLOW, 2018, č. 103, s. 1-15. ISSN: 0301-9322.

2017

KOZÁK, J., RUDOLF, P., HUZLÍK, R., HUDEC, M., CHOVANEC, R., MARŠÁLEK, B., MARŠÁLKOVÁ, E., URBAN, O. *Transition of cavitating flow to supercavitation within Venturi nozzle – hysteresis investigation*. In EPJ web of conferences. EPJ Web of Conferences. 2017. s. 1-11. ISSN: 2100-014X.

KOZÁK, J., KOTEK, M., PRIMAS, J. *Vyhodnocení měření kavitujícího proudění elektrickou impedanční tomografií a srovnání s vícefázovým CFD výpočtem v programu OpenFOAM*. Technická zpráva, Brno: 2017.

RUDOLF, P., KUBINA, D., KOZÁK, J., HUDEC, M., POCHYLÝ, F. *Dynamics of the Cavitating Flow Downstream of the Orifice Plate*. In AIP Conference Proceedings. AIP Conference Proceedings. AIP Publishing, 2017. s. 1-8. ISSN: 1551-7616.

RUDOLF, P., KUBINA, D., HUDEC, M., KOZÁK, J., MARŠÁLEK, B., MARŠÁLKOVÁ, E., POCHYLÝ, F. *Experimental investigation of hydrodynamic cavitation through orifices of different geometries*. In EPJ Web of Conf. EPJ Web of Conferences. EPJ Web of Sciences, 2017. s. 1-5. ISSN: 2100-014X.

2016

KOZÁK, J., RUDOLF, P., HUDEC, M., HUZLÍK, R., ČALA, M. Cavitation affected by the presence of the swirl within Venturi tube: preliminary study. In 2016. s. 40-42.

2015

KOZÁK, J., RUDOLF, P., SEDLÁŘ, M., HABÁN, V., HUDEC, M., HUZLÍK, R. Numerical simulation and experimental visualization of the separated cavitating boundary layer over NACA2412. *EPJ Web of Conferences*, 2015, roč. 2015, č. 92, s. 1-8. ISSN: 2100-014

KOZÁK J., RUDOLF P., ŠTEFAN D., HUDEC M., GRÍGER M., *Analysis Of Pressure Pulsations Of Cavitating Flow In Converging-Diverging Nozzle*. 6th IAHR International Meeting of the Workgroup on Cavitation and Dynamic Problems in Hydraulic Machinery and Systems, Slovenia, 2015

SEDLÁŘ, M, KOMÁREK M., RUDOLF P., KOZÁK J., HUZLÍK R. *Numerical and experimental research on unsteady cavitating flow around NACA 2412 hydrofoil*. IOP Conference Series: Materials Science and Engineering. 2015-01-15, vol. 72, issue 2, DOI: 10.1088/1757-899X/72/2/022014

RUDOLF, P., ŠTEFAN, D., SEDLÁŘ, M., KOZÁK, J., HABÁN, V., HUZLÍK, R. Spatio-temporal description of the cavitating flow behavior around NACA 2412 hydrofoil. In Journal of Physics: Conference Series. Journal of Physics: Conference Series. IOP Publishing, 2015. s. 1-5. ISSN: 1742-6596.

RUDOLF, P., ŠTEFAN, D., KOZÁK, J. Odborná zpráva o postupu prací v roce 2015 - Úprava experimentálního okruhu a příprava pro měření elektrickou impedanční tomografií a time-resolved PIV. Brno: 2015.

2014

KOZÁK, J., SOUKUP, L., ŠTIGLER, J. CFD analysis of the flow field sensitivity in suction pipe on the test well configuration. In *Hydroturbo 2014 - Zborník abstraktov*. 2014. s. 76-78. ISBN: 978-80-227-4249-8.

KOZÁK, J., RUDOLF, P., SEDLÁŘ, M., HABÁN, V., HUDEC, M., HUZLÍK, R. Numerical simulation and experimental visualization of the separated cavitating boundary layer over NACA2412. In *Proceedings of the International conference Experimental Fluid Mechanics 2014*. Polypress s.r.o., 2014. s. 284-291.

RUDOLF, P., ŠTEFAN, D., HUDEC, M., KOZÁK, J. Cavitation in swirling flows. In *Proceedings of Kolloquium Kavitation und Kavitations Erosion*. Bochum: RUB Bochum, 2014. s. 1-15.

RUDOLF, P., KOZÁK, J. Computational modelling of cavitation in simple geometries, but complex flows. In *Computational mechanics 2014, book of extended abstracts*. Plzeň: FAV ZČU Plzeň, 2014. s. 1-2. ISBN: 978-80-261-0429-2.

ŠTIGLER, J., KOZÁK, J., SOUKUP, L., RUDOLF, P. *Test Well CFD Analysis*. Brno, Czech Republic: Department of Fluid Engineering, Energy Institute, Faculty of Mechanical Engineering, Brno University of Technology, 2014. s. 1-77.